DEVELOPMENT OF METHODS FOR THE CHARACTERISATION OF ENGINEERED NANOPARTICLES USED FOR SOIL AND GROUNDWATER REMEDIATION

by

LAURA CHEKLI

A Thesis submitted in fulfilment for the degree of

Doctor of Philosophy

School of Civil and Environmental Engineering

Faculty of Engineering and Information Technology

University of Technology, Sydney (UTS),

New South Wales, Australia.

February 2015

CERTIFICATE OF AUTHORSHIP/ORIGINALITY

I certify that this thesis has not previously been submitted for a degree nor has it been submitted as part of requirements for a degree except as fully acknowledge within the text.

I also certify that the thesis has been written by me. Any help that I have received in my research work and the preparation of the thesis itself has been acknowledged. In addition, I certify that all information sources and literature used are indicated in the thesis.

Signature of candidate:

………………………..

Date:

I dedicate this thesis to my parents

Thierry and Nathalie Chekli

ACKNOWLEDGEMENTS

First of all, I would like to express my deepest gratitude to my principal supervisor, A/Prof. Hokyong Shon for his excellent advices, contagious passion for research and never-ending support throughout the course of my PhD. I thank you for guiding me on how to become a bright researcher. I also would like to thank my external supervisors from UniSA, Prof. Enzo Lombi and Dr. Erica Donner as I have always felt welcome every time I was coming to Adelaide. You have been wonderful supervisors and I thank you for all your support and advices during my PhD. Many thanks as well to my co-supervisors, Dr. Sherub Phuntsho and Dr. Leonard Tijing for your continuous help and support.

I also want to acknowledge the contribution I received from my colleagues and friends Dr. Gianluca Brunetti, Dr. Yanxia Zhao, Bita Bayatsarmadi and Adi Maoz Shen and external collaborator and friend Dr. Maitreyee Roy from the National Measurement Institute who helped me to design and carry out some of my experimental works.

I would like also to acknowledge Prof. Hu Hao Ngo, Rami Hadad and Johir for their support in the laboratories as well as Katie McBean and Mark Berkahn for their valuable help and knowledge in SEM analysis. I also acknowledge the administrative support from Phyllis, Craig, Van and Viona during my three years at UTS.

Special thanks as well to all my dear friends Fouzy Lofti, Jung Eun Kim, Mohammad Shahid, Soleyman Memesahebi, Kanupriya Khurana, Sotos Vasileiadis as well as Julie, Laure, Delphine, Simon and Thomas for their constant support, encouragement and friendship.

Finally, I would like to express my profound gratitude to my family, especially my parents who have always supported me and encouraged me during my study. Without their support,

Journal Articles Published or Submitted**

1. **Chekli, L.**, Phuntsho, S., Shon, H.K., Vigneswaran, S., Kandasamy J. and Chanan, A., A review of draw solutes in forward osmosis process and their use in modern applications, 2012, **Desalination and Water Treatment**, vol. 43, pp. 167-184.

2. ***Chekli, L.**, Phuntsho, S., Roy, M., Lombi, E., Donner, E. and Shon, H. K., Assessing the aggregation behaviour of iron oxide nanoparticles under relevant environmental conditions using a multi-method approach, 2013, **Water Research,** vol. 47, issue 13, pp. 4585-4599.

3. ***Chekli, L.**, Phuntsho, S., Roy, M. and Shon, H. K., Characterisation of Fe-oxide nanoparticles coated with humic acid and Suwannee River natural organic matter, 2013, **Science of the Total Environment**, vol. 461–462, pp. 19-27.

4. Park, S.M., **Chekli, L.**, Kim, J.B., Shahid, M., Shon, H.K., Kim, P.S., Lee, W.-S., Lee, W.E. and Kim, J.-H., NO_x removal on mortar mixed with titania produced from Ti-salt flocculated sludge, 2014, **Journal of Industrial and Engineering Chemistry,** vol. 20, issue 5, pp. 3851–3856.

5. ***Chekli, L.**, Zhao, Y.X., Tijing, L.D., Phuntsho, S., Donner, E., Lombi, E., Gao B.Y. and Shon, H.K. Aggregation behaviour of engineered nanoparticles in natural waters: Characterisation of aggregate structure by use of an on-line laser light scattering set-up, 2015, **Journal of Hazardous Materials,** vol. 284, pp. 190-200.

6. ***Chekli, L.**, Phuntsho, S., Tijing, L.D., Zhou, J., Kim J.-H., and Shon, H.K., Stability of Fe-oxide nanoparticles coated with natural organic matter (NOM) under relevant environmental conditions, 2014, **Water Science and Technology,** vol. 70, issue 12, pp. 2040-2046.

7. Shahid, M., El Saliby, I., McDonagh, A., **Chekli, L.**, Tijing, L.D., Kim, J.-H., and Shon, H.K., Adsorption and photocatalytic degradation of methylene blue using

potassium polytitanate and solar simulator, 2014, **Journal of Nanoscience and Nanotechnology.**

8. **Chekli, L.**, Galloux, J., Zhao, Y.X., Gao B.Y. and Shon, H.K., Coagulation performance and floc characteristics of polytitanium tetrachloride (PTC) compared with titanium tetrachloride (TiCl$_4$) and iron salts in humic acid-kaolin synthetic water treatment, 2015, **Separation and Purification Technology,** vol. 142, pp. 155-161.

9. ***Chekli, L.**, Roy, M., Tijing, L.D., Donner, E., Lombi, E. and Shon, H.K., Aggregation behaviour of titanium dioxide nanoparticles in river waters: Multi-method approach combining light scattering and field-flow fractionation techniques, 2015, **Journal of Environmental Management**, vol. 159, pp. 135-142.

10. ***Chekli, L.**, Bayatsarmadi, B., Sekine, R., Sarkar, B., Maoz Shen, A., Scheckel, K.G., Skinner, W., Naidu, R., Shon, H.K., Donner, E. and Lombi, E., Characterisation of nanoscale zero-valent iron for soil and groundwater remediation: A methodological review. Submitted to **Analytica Chimica Acta.**

11. Galloux , J., **Chekli, L.**, Phuntsho, S., Tijing, L.D., Jeong , S., Zhao, Y.X., Gao, B.Y. and Shon, H.K., Coagulation performance and floc characteristics of polytitanium tetrachloride and titanium tetrachloride compared with ferric chloride for coal mining wastewater treatment. Submitted to **Separation and Purification Technology**.

12. ***Chekli, L.**, Brunetti, G., Marzouk, E., Maoz-Shen, A., Naidu, R., Shon, H.K, Lombi, E. and Donner, E., Evaluating the mobility of polymer-stabilised zero-valent iron nanoparticles and their potential to co-transport contaminants in intact soil cores. Submitted to **Environmental Pollution**.

13. Majeed, T., Phuntsho, S., **Chekli, L.** and Shon H.K., Role of various physical and chemical techniques for hollow fiber forward osmosis membrane cleaning. Submitted to **Desalination and Water Treatment**.

**Publications made during the PhD candidature including articles not entirely related to the Thesis. *Articles related to the Thesis.

Conference papers and presentations

1. **Chekli, L.**, Phuntsho, S., Kandasamy, J., and Shon, H.K., An emerging method for the separation and characterization of manufactured nanoparticles in complex environmental samples, in: **Proceedings Nanotechnology 2013**: Advanced Materials, CNTs, Particles, Films and Composites (Volume 1), Chapter 1: Nanoscale Materials Characterization, Nano Science and Technology Institute, pp. 47-50, ISBN: 978-1-4822-0581-7.

2. **Chekli, L.**, Phuntsho, S. and Shon, H.K., Assessing the aggregation behaviour of Iron Oxide Nanoparticles by Flow Field-Flow Fractionation, in: the 5th conference of Challenges in Environmental Science & Engineering, Melbourne, 9-13 September 2012.

3. **Chekli, L.**, Phuntsho, S. and Shon, H.K., Characterisation of manufactured nanoparticles by flow field-flow fractionation, in: Communicate Conference 2012, Adelaide, 17-19 September 2012.

4. **Chekli, L.**, Phuntsho, S., Kandasamy, J., Shon, H.K., Assessing the aggregation behaviour of iron oxide nanoparticles by using a multi-method approach, in: TechConnect World 2013, Washington D.C., 12-16 May 2013.

5. **Chekli, L.**, Phuntsho, S., Roy, M. and Shon, H. K., Characterisation of Fe-oxide nanoparticles coated with humic acid and Suwannee River natural organic matter, in: CleanUp 2013, Melbourne, 15-18 September 2013.

6. **Chekli, L.**, Phuntsho, S., Tijing, L.D. and Shon, H.K., Characterizing Aggregate Structure in Natural Waters Using On-Line Laser Light Scattering, in: Goldschmidt 2014, Sacramento, 9-13 June 2014.

7. **Chekli, L.**, Donner, E., Lombi, E., Shon, H.K. and Naidu, R., Environmental risk assessment of nanomaterials for soil and groundwater remediation, in: Communicate Conference 2014, Adelaide, 15-17 September 2014.

8. Phuntsho, S., **Chekli, L.**, Tijing, L.D., Zhou, J., Kim J.-H., and Shon, H.K., Stability of Fe-oxide nanoparticles coated with natural organic matter (NOM) under relevant environmental conditions, in: IWA World Water Congress & Exhibition, Lisbon, 21-26 September 2014.

Presentations made during the PhD candidature including proceedings, oral and poster presentations.

LIST OF ABBREVIATIONS

AFM: Atomic Force Microscopy

BTC: Breakthrough Curve

CCA: Chromated-Copper-Arsenate

CCC: Critical Coagulation Concentration

CE: Capillary Electrophoresis

CMC: Carboxymethyl Cellulose

CNTs: Carbon Nanotubes

CPM: Count Per Minute

DLA: Diffusion-Limited Aggregation

DLS: Dynamic Light Scattering

DLVO: Derjaguin–Landau–Verwey–Overbeek

DO: Dissolved Oxygen

DOC: Dissolved Organic Carbon

DOM: Dissolved Organic Matter

EC: Electrical Conductivity

EXAFS: X-ray Adsorption Fine Structure

ENPs: Engineered Nanoparticles

FD: Fractal Dimension

FFF: Field-Flow Fractionation

FlFFF: Flow Field-Flow Fractionation

sFlFFF: Symmetrical Flow Field-Flow Fractionation

AsFlFFF: Asymmetrical Flow Field-Flow Fractionation

FTIR: Fourier Transform Infrared Spectroscopy

GZVI: Granular Zero Valent Iron

HA: Humic Acid

HMW: High Molecular Weight

IC: **I**on **C**hromatography

ICP-MS: **I**nductively **C**oupled **P**lasma **M**ass **S**pectrometry

IS: **I**onic **S**trength

LIBD: **L**aser-**i**nduced **B**reakdown **D**etection

MA(L)LS: **M**ulti **A**ngle (**L**aser) **L**ight **S**cattering

MWCNTs: **M**ulti-**w**alled **C**arbon **N**anotubes

NOM: **N**atural **O**rganic **M**atter

NTU: **N**ephelometric **T**urbidity

nZVI: **n**anoscale **Z**ero **V**alent **I**ron

ORP: **O**xydo-**r**eduction **P**otential

PAA: **P**olyacrylic **A**cid

PRBs: **P**ermeable **R**eactive **B**arriers

PSS: **P**olystyrene **S**ulfonate

PZC: **P**oint of **Z**ero **C**harge

QELS: **Q**uasi-**e**lastic **L**ight **S**cattering

RF: **R**ecovery **F**actor

RLA: **R**eaction-**l**imited **A**ggregation

RPs: **R**etention **P**rofiles

SAXS: **S**mall **A**ngle **X**-ray **S**cattering

SDBS: **S**odium **D**odecyl**b**enzene**s**ulfonate

(HP)SEC: (**H**igh **P**erformance) Size-Exclusion Chromatography

SEM: **S**canning **E**lectron **M**icroscopy

SF: **S**trength **F**actor

SLS: **S**tatic **L**ight **S**cattering

SPM: **S**canning **P**robe **M**icroscopy

SRNOM: **S**uwannee **R**iver **N**atural **O**rganic **M**atter

SWCNTs: **S**ingle-**w**alled **C**arbon **N**anotubes

TCE: **Tr**i**c**hloro**e**thylene

(S)TEM: (**S**canning) **T**ransmission **E**lectron **M**icroscopy

TOC: **T**otal **O**rganic **C**arbon

WWTPs: **W**astewater **T**reatment **P**lants

XANES: **X**-ray **A**dsorption **N**ear-**e**dge **S**tructure

XAS: **X**-ray **A**dsorption **S**pectroscopy

XEDS: **X**-ray **E**nergy **D**ispersive **S**pectroscopy

XPS: **X**-ray **P**hotoelectron **S**pectroscopy

XRD: **X-r**ay **D**iffraction

TABLE OF CONTENTS

LIST OF FIGURES

LIST OF TABLES

xxviii

ABSTRACT

In the past two decades, extremely rapid progress in the nanotechnology R&D sector has been met by equally rapid commercialisation of this new technology. As a consequence, engineered nanoparticles (ENPs) are increasingly released into the environment. For the purpose of soil and groundwater remediation, large amounts of nanomaterials are intentionally discharged to the environment. Risk assessment of these novel technologies is therefore required due to the uncertainties regarding their potential side effects. To support this, research into the environmental fate of ENPs is urgently needed but has been so far hindered by significant analytical challenges. Developing novel methodologies to better understand the ENPs behaviour in the environment is therefore crucial to assessing their potential risk.

Iron nanoparticles, and more specifically nanoscale zero-valent iron (nZVI), are becoming increasingly popular for the treatment of contaminated soil and groundwater; however, their mobility and reactivity in subsurface environments are significantly affected by their tendency to aggregate. Assessing their stability under environmental conditions is crucial for determining their environmental fate. A multi-method approach (including different size-measurement techniques and the DLVO theory) has been developed to thoroughly characterise the behaviour of iron oxide nanoparticles (Fe_2O_3NPs – used as a surrogate for nZVI) under environmentally relevant conditions. Although recent studies have demonstrated the importance of using a multi-method approach when characterising nanoparticles, the majority of current studies continue to use a single-method approach.

Under some soil conditions (i.e. pH 7, 10 mM NaCl and 2 mM $CaCl_2$) and increasing particle concentration, Fe_2O_3NPs underwent extensive aggregation to form large aggregates (> 1 μm). Coating the nanoparticles with dissolved organic matter (DOM) was investigated as an alternative "green" solution to overcoming the aggregation issue instead of using the

more commonly proposed polyelectrolytes. At high concentrations, DOM effectively covered the surface of the Fe_2O_3NPs, thereby conferring negative surface charge on the particles across a wide range of pH values. This provided electrostatic stabilisation and considerably reduced the particle aggregation effect. DOM-coated Fe_2O_3NPs also proved to be more stable under high ionic strength conditions. The presence of $CaCl_2$, however, even at low concentrations, induced the aggregation of DOM-coated Fe_2O_3NPs, mainly via charge neutralisation and bridging. This has significant implications in regards to the reactivity and fate of these materials in the environment.

Humic acid (HA) and Suwannee River natural organic matter (SRNOM) were tested and compared as surrogate for DOM to stabilise Fe_2O_3 NPs. The advantages of DOM over conventional organic surface modifiers are that DOM is naturally abundant in the environment, inexpensive, non-toxic and readily adsorbed onto the surface of metal oxide nanoparticles. The DOM-coated Fe_2O_3 NPs were characterised by developing a multi-method approach including various analytical methods: flow field-flow fractionation (FlFFF), high performance size exclusion chromatography (HPSEC) and Fourier transform infrared spectroscopy (FTIR). The stability of the coated NPs was also evaluated by assessing their aggregation and disaggregation behaviour over time.

Results showed that both HA and SRNOM were rapidly and readily adsorbed on the surface of Fe_2O_3 NPs, providing electrosteric stabilisation over a wide range of pH. HPSEC results showed that the higher molecular weight components of DOM were preferentially adsorbed onto the surface of Fe_2O_3. As SRNOM consists of macromolecules with a higher molecular weight than HA, the measured size of the SRNOM-coated Fe_2O_3 NPs was 30 % larger than the HA-coated Fe_2O_3 NPs. FTIR results indicated the occurrence of hydrogen bonding arising from electrostatic interaction between the DOM and Fe_2O_3 NPs. Finally, a stability study showed that after 14 days, small agglomerates and aggregates were formed. The HA-coated Fe_2O_3 NPs formed agglomerates which were easily disaggregated using a vortex

mixer, with the coated NPs returning to their initial size. However, SRNOM-coated Fe_2O_3 NPs were only partially disaggregated using the same method, which indicates that these aggregates have a more compact structure.

To date, research focusing on the development of novel surface modifiers to increase the mobility of iron-based nanoparticles has only been carried out in highly idealised systems which facilitated their detection and quantification. In fact, one of the main analytical challenges in characterising nanomaterials is related to the difficulty of quantifying nanomaterials once they are dispersed in complex environmental matrices. Finding new analytical methods to overcome this issue would significantly help in the development of effective remediation materials. A novel method based on radiolabelling has been therefore developed and enables the detection and quantification of iron-based nanoparticles in intact soil cores. The radioisotopes (i.e. ^{59}Fe) were incorporated in the core of the nanoparticles during its synthesis. The mobility of radiolabelled nanoparticles was assessed by gamma counting analysis and then compared with the mobility of commercialised nanoparticles which was determined by common ICP-MS method. Results showed limited mobility of both nanomaterials with less than 1% of the injected mass eluted from the columns. The use of specific isotopic signature allowed determining the retention profiles of radiolabelled nanoparticles which was a major advantage compared to conventional ICP-MS method. Results indicated that the majority (i.e. 80%) of the particles were retained in the first centimetres of the columns suggesting that rapid aggregation of iron-based nanoparticles after its injection was the main explanation of its limited mobility. The method was further developed by coupling gamma counting and ICP-MS measurements to evaluate both the mobility of radiolabelled nanoparticles and its potential to co-transport contaminants in contaminated soils. Results showed that, although the mobility of iron-based nanoparticles was limited, the breakthrough of both contaminants and iron-based nanoparticles occurred

simultaneously suggesting that iron-based nanoparticles has the potential to co-transport contaminants.

Adsorption of natural organic matter (NOM), aggregation and disaggregation have been identified as three of the main processes affecting the fate and behaviour of ENPs in aquatic environments. However, although several methods have been developed to study the aggregation behaviour of ENPs in natural waters, there are only a few studies focusing on the fate of such aggregates and their potential disaggregation behaviour. In this study, we developed and demonstrated a simple method, based on on-line light scattering measurement, for characterising the aggregation behaviour and aggregate structure of ENPs in different natural waters. Both the aggregate size of ENPs and their adsorption capacity for DOM were strongly related ($R^2 > 0.97$, $p < .05$) to the combined effect of initial concentration of DOM and the ionic strength of the natural waters. The structure of the formed aggregates was strongly correlated ($R^2 > 0.95$, $p < .05$) to the amount of DOM adsorbed by the ENPs during the aggregation process. Under high ionic strength conditions, aggregation is mainly governed by diffusion and the aggregates formed under these conditions showed the lowest stability and fractal dimension, forming linear, chain-like aggregates. In contrast, under low ionic strength conditions, the aggregate structure was more compact, most likely due to strong chemical binding with DOM and bridging mechanisms involving divalent cations formed during reaction-limited aggregation.

Finally, a multi-method approach combining the developed on-line light scattering method with off-line instruments such as field-flow fractionation techniques has been proposed to overcome the limitation of light scattering instruments related to the polydispersity of the samples. Results confirmed the benefits of using a multi-method approach. While the on-line light scattering method can provide information on the larger aggregates (i.e. size and structure), FlFFF proved to be a very accurate technique for characterising the smaller

particles remaining in suspension after sedimentation. When combined, these techniques can

offer complementary data on the particle size distribution of the samples.

UTS
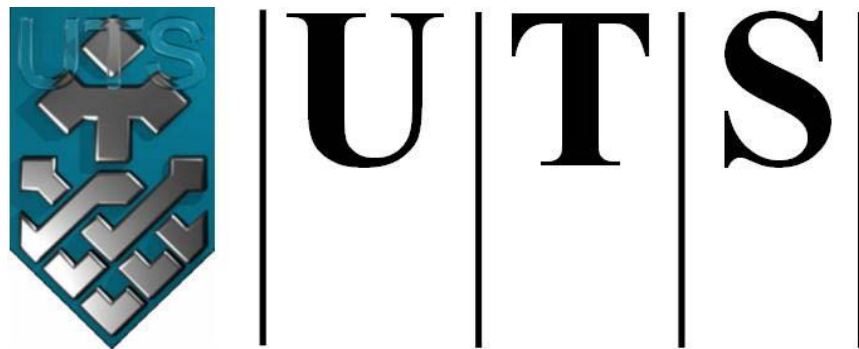
University of Technology Sydney
FACULTY OF ENGINEERING

CHAPTER 1   INTRODUCTION

1.1 Research background

Over the past two decades, extremely rapid progress in nanomaterial research and development has been met by equally rapid commercialisation of new products and technologies. As a result, engineered nanoparticles (ENPs) are increasingly released to the environment, both directly and indirectly, and this has produced a growing concern among the environmental science community (Ju-Nam and Lead 2008). With detrimental effects of nanomaterials reported for a number of environmental endpoints (Chae et al. 2009; Poynton et al. 2010), the need for appropriate risk assessment and policy development in this area is apparent. Research into the environmental fate of nanoparticles in the Australian environment is needed to support this (Batley et al. 2008).

To date, risk assessment of nanomaterials has largely focused on engineered zinc oxide (ZnO) and silver (Ag) nanoparticles as these materials contain metals that are known to be toxic. However, it is likely, given their commercial uses, that only a few amounts of these materials will be released in the environment. On the other hand, nanomaterials are also being developed for the remediation of contaminated soil and groundwater and, in this case, it is foreseen that large amounts of these materials will be directly added to environmental compartments. These nanomaterials may not pose a significant risk in their initial form but could acquire unwanted characteristics once reacting in the environment. Furthermore, due to their small size, their mobility and potential to transport targeted contaminants cannot be neglected. This situation is not different from what has been known for naturally occurring nanoparticles. In this latter case, evidence is mounting that the transport of low-solubility contaminants is facilitated by environmental colloids or nanoparticles (de Jonge et al. 2004). In fact, in recent years, colloidal-facilitated transport by natural iron nanoparticles has been identified as the key process underlying the unexpected appearance of low-solubility contaminants at considerable distances from known sources (Hassellöv and von der Kammer 2008). It is thus possible that engineered nanomaterials applied to soil and groundwater for

the remediation of contaminants may, as a side effect, also promote the movement and dispersion of these contaminants. This issue has been already recognised at European level (Mueller and Nowack 2009) and recent studies have demonstrated the high potential of ENPs to aggregate with both organic (e.g. humic acids) and inorganic (e.g. heavy metals) contaminants (Baalousha et al. 2008; Baalousha 2009; Plathe 2010).

However, to understand the fate of nanoparticles and its complex interactions with the environment, it is necessary to be able to separate and characterise these nanoparticles and this is one of the key challenges that hinder risk assessment of these materials. In fact, although, there are numerous techniques for producing, sorting and characterising "as-manufactured" nanoparticles in simple matrices, there is still a lack of standard measurement methods that can reliably characterise the nanoparticles in complex environmental samples and therefore new analytical methods are essential. Another pressing research needs are the development of methods that can differentiate between abundant, naturally occurring colloids, and engineered nanoparticles (von der Kammer et al. 2012).

1.2 Engineered nanoparticles used for soil and groundwater remediation

Historical and recent industrial and urban activities have led to the increased concentration of a wide range of pollutants in soils, river sediments and surface and ground waters. Therefore, the management of contaminated soil and groundwater is currently one of the major environmental issues (Cundy et al. 2008). As it is now well recognised that conventional methods, such as disposal to landfill, isolation or pump-and-treat, are not effective and sustainable in various situations, there has been a considerable increase in research for the development of novel in-situ remediation technologies.

Due to their subcolloidal size, ENPs have been proved to display better catalytic, chemical, optical, mechanical, electronic and magnetic properties over conventional macroscale materials (Jortner and Rao 2002). In fact, when particle size decreases, there is an increase in

the proportion of atoms present at the surface of the particle which enhances its propensity to interact and react with other atoms, molecules and complexes to stabilise its surface charge. Besides, due to their very small size, nanoparticles can be integrated in aqueous suspensions and thus behave as colloids (Crane and Scott 2012). These distinctive properties have shown particular advantages for a wide range of environmental applications ranging from water and air purification to hazardous waste treatment and environmental remediation (Li et al. 2006).

In the past decades, ENPs have particularly received an increase of interest for the treatment of contaminated soil and groundwaters. In comparison to traditional macroscale materials, nanomaterials possess significantly higher surface-to-volume ratio which can generate unexpected surface effects. Moreover, when using a smaller volume of material to produce the same objective, it can conceptually preserve both raw materials and energy and thus leads to significant cost savings (Masciangioli and Zhang 2003). In addition, by virtue to their size, nanomaterials can be used directly in field via injection at almost any location and depth in soil and groundwater systems (Crane and Scott 2012).

Theoretically, for in situ soil and groundwaters remediation, ENPs are required to feature several essential properties which are:

- High reactivity for the removal of targeted environmental contaminants;
- High mobility in porous media (especially soil);
- High reactive longevity after their injection;
- Low toxicity for the surrounding environment.

These properties are the main drivers when designing ENPs for the purpose of soil and groundwaters remediation. However, these nanoparticles must also be produced and delivered at a cost that remains sufficiently low to compete with other conventional technologies. So far, there are not many ENPs which gather all the above mentioned properties. For instance, silver nanoparticles exhibit high reactivity with aqueous

4

contaminants and also high stability as colloidal suspensions (Panacek et al. 2006). However, due to their high cost and their well-recognised environmental toxicity (Asharani et al. 2008), silver nanoparticles are not a suitable candidate for such environmental application.

Due to their purportedly low cost, suitable environmental compatibility and high reactivity, the most widely used and studied nanoparticles for soil and groundwater remediation are currently nanoscale zero-valent iron (nZVI) (Wang and Zhang 1997; Elliott and Zhang 2001; Zhang 2003; Quinn et al. 2005). Over the past few years, intensive research for the improvement of nZVI has been carried out and various studies have demonstrated the high performance of nZVI for the degradation, removal or stabilisation of a wide range of common environmental contaminants including chlorinated organic solvents (Elliott and Zhang 2001; Zhang 2003; Nutt et al. 2005), organic dyes (Liu et al. 2005), various inorganic compounds (Alowitz and Scherer 2002; Cao et al. 2005), including metals (Kanel et al. 2005; Xu et al. 2005). However, there are still some issues related to this remediation technology; which currently limit its widespread utilisation. First, many studies have demonstrated the limited mobility of nZVI in natural porous systems (e.g. soils), mainly due to particle aggregation; resulting in ineffective in-situ remediation (Schrick et al. 2004; Quinn et al. 2005; He and Zhao 2007; Saleh et al. 2008). In fact, previous studies reported transport distances ranging from few centimetres (Schrick et al. 2004) in lab-scale column experiments to just a few meters in a field-scale demonstration (Zhang and Elliott 2006). Besides, there are still some uncertainties regarding the risks associated with nZVI materials upon release to the environment; especially regarding their potential to co-transport contaminants (Mueller and Nowack 2009). In fact, the ability of nZVI to sorb contaminants upon oxidation has been already demonstrated for arsenic, chromium and other inorganic contaminants in soils (Schorr 2007). It is thus possible that nZVI may, as a side effect; act as a carrier for contaminants.

These different factors (e.g. tendency to aggregate and interact with the environment) mainly depend on the nanoparticle properties such as particle size, surface charge, bulk composition and surface chemistry. Furthermore, these properties change with time due to the reactive nature of the materials. Therefore, it is crucial to accurately characterise and understand the implications of these properties before deploying these materials into contaminated environments in order to ensure safe and efficient remediation. Although some studies have previously focused on the characterisation of nZVI (Li et al. 2006; Sun et al. 2006), it is increasingly recognised that the characterisation approaches used for ENPs are frequently inadequate and/or underdeveloped. Moreover, multiple and complimentary analytical methods are needed (von der Kammer et al. 2012) as the validity and accuracy of some results may be inadequate under some conditions (Baer et al. 2010).

1.3 Objectives and scope of the research

As discussed in the last section, there are two main issues related to the nanoremediation technology: (i) the aggregation of nanoparticles which limited both their mobility and reactivity; resulting in ineffective remediation and (ii) the uncertainties related to the potential of nanoparticles to transport contaminants far from the contaminated zone. To date, the research on the fate and behaviour of ENPs in the environment is still hindered by significant analytical challenges. Therefore, the main objective of this research is to develop novel analytical methods to better understand the behaviour of ENPs (e.g. aggregation behaviour and interaction with the environment) under various environmental conditions (e.g. groundwater and soil conditions). This will considerably help in reducing the uncertainties associated with risk assessment of ENPs used for environmental remediation. The knowledge gained from this project will support the future design of effective yet sustainable nanomaterials. It will also mitigate the risk that premature application of unsuitable nanomaterials could hinder future commercialisation of sustainable nanoproducts by generating negative public perceptions and undermining future innovation.

6

The proposed scope of the project can be summarised into different segments:

- Develop novel methods to effectively characterise the aggregation behaviour of iron-based nanoparticles, bare and stabilised with organic coating, under relevant environmental conditions.

- Develop a novel method based on radioisotope labelling to be able to differentiate between engineered and natural iron nanoparticles. This will enable to easily trace the mobility of ENPs in intact soil cores.

- Develop a novel analytical method based on light scattering techniques (i.e. the most widely use and accessible techniques to characterise nanoparticles) to characterise the behaviour of ENPs in different natural waters.

1.4   Structure of the study

This thesis comprises nine chapters with the research background, objectives and scope of the study included in Chapter 1 (Introduction).

Chapter 2 gathers a comprehensive literature review on the subject matter including a general introduction on nanoparticles and their interaction with the environment followed by a review on the characterisation methods for iron-based nanoparticles used for soil and groundwater remediation.

Chapter 3 describes the materials and analytical methods common to all chapters while experimental investigation of specific studies can be found in their respective chapters.

Chapter 4 presents a multi-method approach (i.e. combining theoretical and analytical methods) developed to study the aggregation behaviour of iron-based nanoparticles under relevant environmental conditions (i.e. soil and groundwater conditions). In fact, although the characterisation of ENPs can be considerably simpler than it is for natural particle samples, ENPs are also complex, and a multiple characterisation approach is necessary to

ensure the accuracy of the characterisation data. However, due to analytical challenges, the lack of appropriate characterisation data in environmentally realistic conditions is a major limitation of current research in this area.

Chapter 5 focuses on the characterisation of iron-based nanoparticles stabilised with organic coating. In fact, this is currently one of the most utilised methods to reduce the aggregation of nanoparticles. It is therefore crucial to effectively characterise the interactions between the organic coating and the iron nanoparticles to be able to predict their fate and behaviour once applied in the environment.

A novel method based on radioisotope labelling is investigated in Chapter 6 to assess the mobility of organic-coated iron-based nanoparticles in intact soil cores. This method was further developed and combined with elemental analysis method to investigate the potential of ENPs to co-transport contaminants in real contaminated soil cores.

A novel experimental setup based on on-line light scattering analysis is described in Chapter 7. ENPs used for environmental applications may ultimately end up in the entire aquatic environment. This novel setup was used to evaluate both the aggregation behaviour and aggregate structure of different ENPs in several natural waters. In fact, these are among the main factors affecting the fate and behaviour of ENPs in the aquatic environment.

This novel on-line setup was further developed and combined with different off-line analytical techniques to better assess the polydispersity of the samples (Chapter 8). In fact, it is well demonstrated that light scattering techniques suffer from the strong particle size dependence of the scattering intensity which leads to Z-average or intensity values being biased toward larger particles/aggregates.

Conclusions and recommendations are presented in Chapter 9.
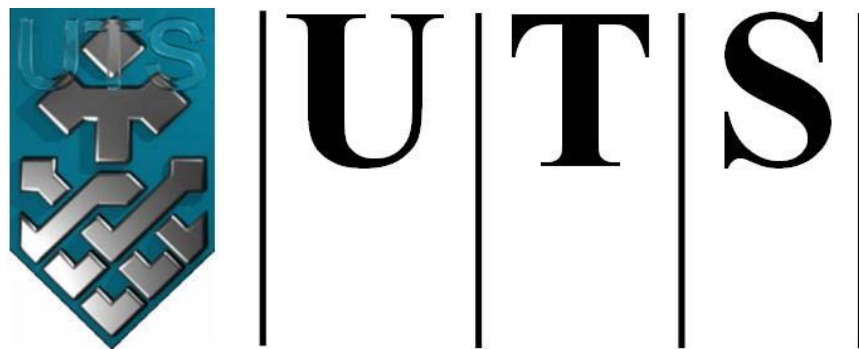
University of Technology Sydney
FACULTY OF ENGINEERING

CHAPTER 2   LITERATURE REVIEW

2.1 Nanoparticles: General introduction and behaviour in the aquatic environment

2.1.1 Definitions and classification

Nanomaterials are usually defined as particulate matter with at least one dimension which is less than 100 nm; where one nanometre is equal to one-billionth of a meter (i.e. 10^{-9} m) (Dowling et al. 2004). Materials that are less than 100 nm in only one dimension comprise thin films and surface coatings while materials that are less than 100 nm in two dimensions include nanotubes, nanowires and nanorods. Finally, materials that are nanoscale in three dimensions are defined as nanoparticles. Since colloids are, by definition, particles in the range of 1 nm to 1 μm, nanoparticles can be classified as a sub-fraction of colloids as shown in Figure 2-1. Therefore, fundamental and theoretical knowledge derived from the colloid science may also be applied to nanoparticle research (Lead and Wilkinson 2006). In this thesis, airborne particles and particulate matter are excluded as only the aquatic (and soil) system is of interest.
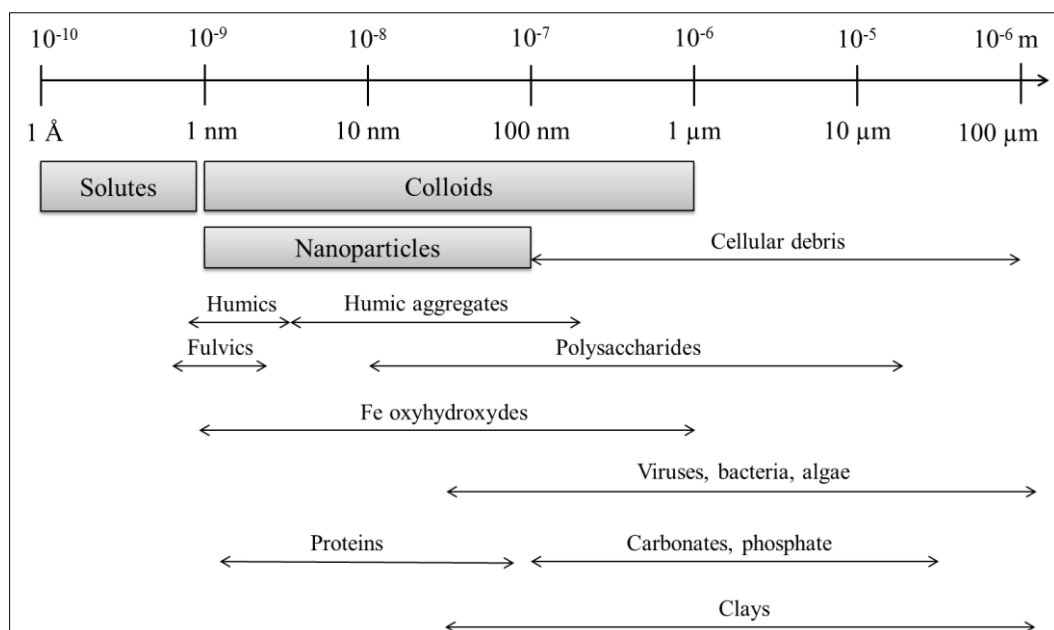
Figure 2-1: Size domains of some environmental colloids and nanoparticles [adapted from (Lead and Wilkinson 2006; Christian et al. 2008)].

Colloids are abundant in the environment and can be from either natural origin (i.e. formed by processes taking place for millions of years) or from anthropogenic origin (Nowack and Bucheli 2007). Depending on their origin, environmental colloids can be divided into four groups: natural colloids which can be divided into inorganic and organic colloids, anthropogenic colloids and finally engineered nanoparticles (ENPs) (Christian et al. 2008). The distinction between anthropogenic colloids and ENPs is based on their nature as either unintended by-product from technological processes or resulting from target-oriented manufacture. More details on this categorisation can be found in Table 2-1.

Table 2-1: Categorisation of environmental aquatic colloids.

Environmental aquatic colloids			
Natural colloids		Anthropogenic colloids	Engineered nanoparticles
Inorganic colloids - silicates (e.g. clays) - oxides/hydroxides - carbonates - phosphates - metal sulfides	**Organic colloids** - macromolecules (e.g. humic and fulvic acids) - bio-colloids (e.g. bacteria) - coal/soot/black carbon - cellular debris	- wear and corrosion products (e.g. from tire and brakes) - waste and combustion products (e.g. soot, fly ash)	- Carbon-based nanoparticles (e.g. fullerenes and CNTs) - Metal nanoparticles (e.g. silver and gold nanoparticles) - Metal oxides nanoparticles (e.g. TiO_2 nanoparticles)

ENPs can be classified into four different categories; as detailed below:

2.1.1.1 Carbon-based nanoparticles: Fullerenes and CNTs

Among the large family of fullerenes, the C_{60} molecule known as the buckminsterfullerene is the most widely studied (Kroto et al. 1985). Fullerenes are mainly used in combination with polymer, as thin films, in biological applications and in electro-optical devices (Prato 1999; Bosi et al. 2003). Other fullerenes such as carbon nanotubes (CNTs) have been discovered after C_{60} (Iijima 1991). There are various types of engineered CNTs including single-walled (SWCNTs) and multi-walled (MWCNTs). Depending on the synthesis method (e.g. arc evaporation, pyrolysis or laser ablation), the following purification methods and the various possible functionalization, a wide variety of CNTs can be engineered with different

properties depending on the targeting applications (Dai 2002; Niyogi et al. 2002). This will have important implications when investigating their environmental fate and behaviour.

2.1.1.2 Metal nanoparticles

Elemental metal nanoparticles such as gold and silver nanoparticles are already produced at industrial scale since they feature special size-related properties such as magnetic, optical and electronic properties (Zhou et al. 2009). Elemental silver nanoparticles are mainly used as bactericide in various consumer products such as textiles and disinfectant sprays (Morones et al. 2005) while elemental gold nanoparticles has been used for a broad range of applications (Brust and Kiely 2002).

Other important metal nanoparticle is nanoscale zero-valent iron (nZVI) which has been widely studied for environmental nanoremediation (Zhang 2003). This remediation technology has been or is currently utilised in about 30 contaminated site projects around the world (Li et al. 2006). More detailed on nZVI and its environmental applications can be found in section 2.2.

2.1.1.3 Metal oxides nanoparticles

Metal oxides nanoparticles are among the most utilised ENPs (Aitken et al. 2006). Bulk materials of several metal oxides including TiO_2, SiO_2 and iron and aluminium oxides have been already manufactured for several years. It is not until recently that they have been produced in the nanoscale form and have been commercialised (e.g. ZnO and TiO_2 NPs in sunscreens). TiO_2 is currently the most widely used NPs finding applications in paints, cosmetics and as photocatalyst for water and wastewater treatment.

2.1.1.4 Other engineered nanomaterials

Materials scientists investigated a broad range of other nanomaterials such as nano-sized zeolites (Larlus et al. 2006), clays (Yaron-Marcovich et al. 2005) and ceramics (Cain and Morrell 2001). Also, some non-carbon nanotubes have been developed (Pokropivny 2001), including silica/titania (Zhang et al. 2006). There is also an increased interest in the areas of information technology, medicine and molecular biology for the development of quantum dots which are fabricated from semiconductor materials such as CdTe, CdSe or ZnS (Gao et al. 2004).

2.1.2 Nanoparticle structure

Nanoparticle structure is quite complex but can be divided into three layers: the surface which can be functionalised, the shell material which can be purposely added and the core material (Christian et al. 2008).

2.1.2.1 The nanoparticle surface

The surface of a nanoparticle can be functionalised and the composition of the surface will be closely related to the targeted application. Since most nanoparticles lose their properties once they aggregate or precipitate; many researchers are focusing on finding appropriate surface coating which can facilitate the dispersion of nanoparticles. These surface coatings are usually a small molecule that will bind to the nanoparticle surface via a covalent-like bond and often carry a charge to provide electrostatic repulsive forces between the coated particles (see Figure 2-2). Silver nanoparticles are, for instance, generally stabilised with citrate (Henglein and Giersig 1999). The use of surfactant, such as sodium dodecylsulfate, is another method to stabilise nanoparticles in suspension (Qiu et al. 1999). Another type of surface stabiliser includes long-chain molecules with high molecular weight which can

provide both electrostatic and steric repulsive forces between the coated particles as depicted in Figure 2-2.
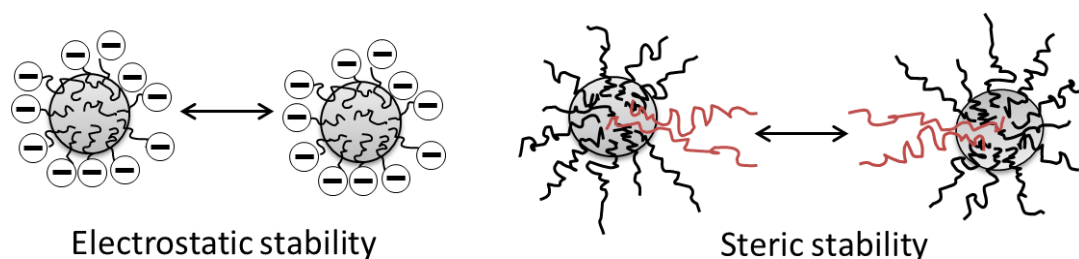
Figure 2-2: Schematic representation of charge-stabilised nanoparticles (left) and sterically stabilised nanoparticles (right)

2.1.2.2 *The nanoparticle shell*

The nanoparticle shell usually represents the top layer of the nanoparticle and is often composed of a chemically different structure from that of the core material. One good example of an intentionally engineered core/shell structure is the quantum dots which usually have a core made of one material (e.g. cadmium selenide) and a shell of another (e.g. zinc sulphide) (Malik et al. 2002).

However, the formation of core/shell structure can also occur via other processes such as the alteration (e.g. chemical reactions) of the core material when exposed to the environment. For instance, nZVI are known to rapidly oxidise in the presence of oxygen which creates layers of iron oxides at their surface (Sun et al. 2006).

2.1.2.3 *The nanoparticle core*

The core generally refers to the centre of the nanoparticle and it commonly designates the nanoparticle itself. In most cases, the nanoparticle properties of interest are mostly determined by the properties of the core.

It is important to note that for inorganic nanoparticles, the core may exist in more than one phase (e.g. anatase and rutile for TiO_2 NPs) even if the nanoparticle has been synthesised in a pure single phase. It is therefore important to carefully analyse all prepared materials as it is very likely that the fate of nanoparticles will be dependent on the phase of the core (Rempel et al. 2006).

Finally, the core may present different morphologies; although most of the nanoparticles are nominally isotropic (i.e. identical in all directions such as the spherical shape). The most common non-isotropic shape is a simple rod or wire such as the CNTs. Some other structures (e.g. tetrapod, dendrite, tear drop…etc.) have also been synthesised [e.g. (Manna et al. 2000)].

2.1.3   Nanoparticle intrinsic properties

The nanoparticle intrinsic properties will be the main factors affecting their fate and behaviour in the environment. In the next paragraphs, we intend to give a simple description of some important nanoparticles properties. More detailed explanations can be found elsewhere (Shaw 1992).

2.1.3.1   Nanoparticle reactivity

Due to their small size, nanoparticles possess a very high surface to volume ratio. The surface to volume ratio is proportional to the inverse of the radius which indicates that the ratio of atoms at the surface of a particle available for reaction is also proportional to the inverse of the radius. In other words, the smaller the nanoparticle, the higher number of atoms will be present at the surface for reaction. An example given by Christian et al. (2008) showed that a gold nanoparticle with a 5 nm diameter will have 31% of its atoms at the surface whereas a 50 nm gold nanoparticle will only possess 3.4% of its atoms at the surface and this percentage drops to 0.2% for a 1 μm gold particle.

Apart from the number of atoms available for reaction, the chemistry of these sites will also affect the nanoparticle reactivity because of the differences from the bulk material. In fact, materials engineered in a nanoscale form may have a much higher catalytic activity than the bulk material (Yoo 1998). A good example of material which shows poor catalytic activity in the bulk form and excellent catalytic properties when prepared in the nanoscale form is gold (Sau et al. 2001).

2.1.3.2 *Nanoparticle colloidal stability*

The dispersion of nanoparticles in an aqueous solution will result in particle-particle collision which will likely result in their agglomeration. Single particles are often referred as primary particles while agglomerates referred to primary particles held together with weak attractive forces such as Van der Waals forces (Jiang et al. 2009).

Particle-particle collision is controlled by three distinct processes: (i) Brownian motion, (ii) shear flow and (iii) differential settling related to the size, shape and density of the particles (Handy et al. 2008). The rate of collision will mainly depend on the particle size and dispersion homogeneity. In fact, monodispersions are more stable than polydispersions. Besides, the particle-particle collision frequency will also depend on Brownian motion temperature and particle concentration (Phenrat et al. 2007).

In order to form stable dispersions, it is therefore crucial to provide a repulsive barrier between two approaching particles. There are two typical barriers which are based either on charge or steric stabilisation as shown previously in Figure 2-2. For charge stabilisation, a surface charge is present and associated with counter ions and some solvent molecules which are bound to the surface of the particle: this corresponds to the Stern layer (Stern 1924). The charge present at the particle surface will cause repulsion of like charges according to Coulombs laws and therefore providing a barrier to agglomeration. For steric stabilisation, a long-chain molecule is attached to the particle surface. The long-chain

molecule will present a high affinity for the solvent and thus, the barrier to aggregation is caused by the interactions of the long chain molecule with itself and with the solvent. This will cause entropically unfavourable conditions when the particles come closer to one another and prevent the coated nanoparticles to agglomerate (Tiller and O'Melia 1993).

These two barriers (i.e. charge and steric stabilisation) may behave differently depending on the physico-chemical properties of the solvent. For instance, an increase in the ionic strength of the solvent will have much more effect on the aggregation of charged-stabilised nanoparticles than of sterically-stabilised ones. This can be accounted by the fact that an increase in the ionic strength will lead to a decrease in the double layer thickness of particles and thus shield the charge of two approaching particles. This will reduce the effectiveness of the Coulomb repulsive forces and thus promote the agglomeration of nanoparticles. Moreover, tri- and divalent ions may also exchange with monovalent ions on the nanoparticle surface of charge-stabilised particles. This usually leads to rapid agglomeration and precipitation of nanoparticles whereas sterically-stabilised nanoparticles are much less affected.

2.1.4 Behaviour of nanoparticles in the aquatic environment

To date, only few studies have investigated the behaviour of ENPs in the aquatic environment, and little is known about their transport, fate, and probable concentrations in different environmental compartments. A recent modelling study by Keller et al. (2013) estimated that in 2010, 63% to 91% of the global ENP production ended up in landfills; 8% to 28% was released into soils; 0.4% to 7% into water bodies; and 0.1% to 1.5% into the atmosphere. Among the ENPs considered, titanium dioxide (TiO_2) was released to the environment in the largest quantities, followed by iron and zinc (Keller et al. 2013).

ENPs are increasingly release to the environment, both unintentionally and intentionally. Intentionally release of ENPs is mainly related to their use in soil and groundwater

remediation whereas unintentional release includes atmospheric emission as well as soil or liquid waste streams from manufacture facilities (Tungittiplakorn et al. 2004; Limbach et al. 2008). Depending on their dispersion state, ENPs will then be transported or immobilised within the different environmental compartments as depicted in Figure 2-3.
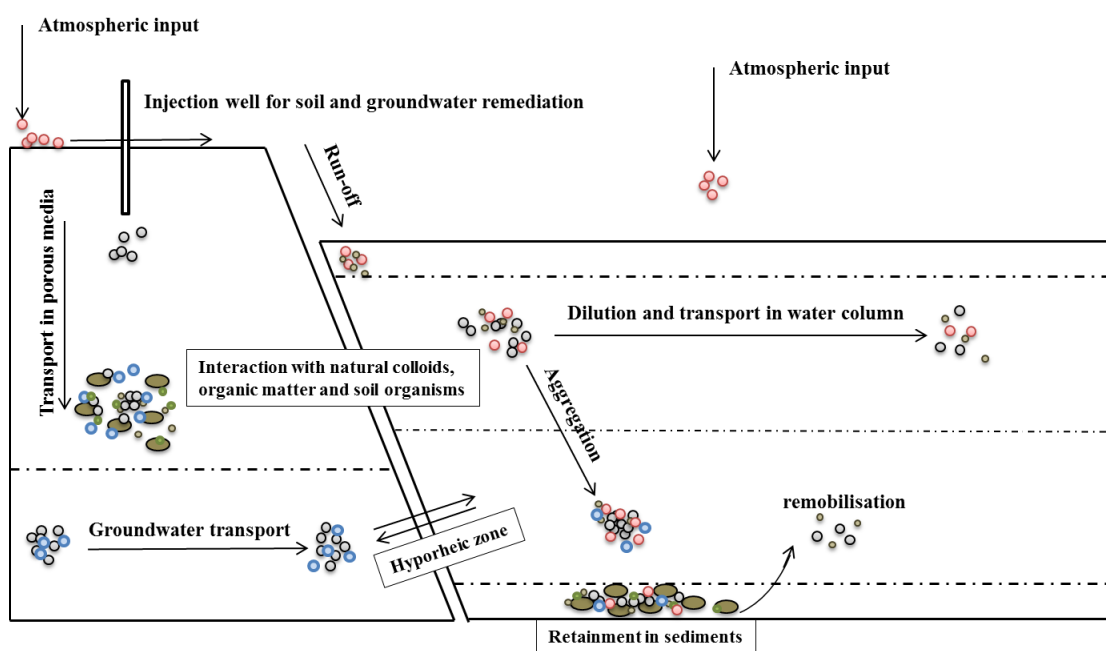
Figure 2-3: Schematic diagram of the possible pathways and potential interactions of ENPs in the environment [adapted from (Ottofuelling 2010)].

The fate and behaviour of ENPs will then greatly depend on their transport characteristics (i.e., aggregation, sedimentation or adsorption) and transformation (i.e., dissolution or chemical transformation) in the environment (Lowry et al. 2012). Agglomeration/aggregation and sedimentation are the major processes affecting the behaviour of ENPs in aquatic systems and results suggest they are mainly controlled by the combined effects of pH, ionic strength, salt composition and the presence and concentration of natural organic matter (NOM) (Phenrat et al. 2007; Christian et al. 2008).

For instance, it is well demonstrated that the stability of nanoparticles is strongly affected by the pH in aqueous systems. Many metal oxide nanoparticles have a positive surface charge under acidic conditions and a negative surface charge under basic conditions (Imae et al.

1991; Kosmulski 2006; Baalousha et al. 2008). The point of zero charge (PZC) is defined as the pH when the net surface charge density is equal to zero. Around the PZC, there is no net positive energy barrier which promote the formation of very large aggregates since the only factor controlling aggregation is Brownian motion (Hu et al. 2010). Natural surface coating by NOM has also been shown to influence the surface charge of ENPs by neutralising the positive charge and thus enhancing the negative surface charge of ENPs depending of the nanoparticle PZC and the solution pH. Surface coating by NOM is thus likely to affect the stability of ENPs by either reducing their aggregation through charge and steric stabilisation (Tipping and Higgins 1982; Jekel 1986) or enhance their aggregation through charge neutralisation and bridging mechanisms with divalent cations (Buffle et al. 1998).

Different experimental approaches have been tested to predict the behaviour of ENPs in aquatic systems. One approach is to consider the individual effects of different physical and chemical components (i.e., the effect of pH, a single electrolyte, organic matter, etc.) in order to identify the main factors affecting the stability of ENPs. A more realistic, yet more complex, approach investigates the behaviour of ENPs under environmentally-relevant conditions and ultimately in natural waters. Several recent studies have used these approaches to understand and predict the behaviour of ENPs once they enter the environment (Phenrat et al. 2007; Zhang et al. 2008; Baalousha 2009; Badawy et al. 2010; Hu et al. 2010; Keller et al. 2010; Huynh and Chen 2011; Ottofuelling et al. 2011; Baalousha et al. 2013; Brunelli et al. 2013; Dobias and Bernier-Latmani 2013; Romanello and de Cortalezzi 2013; Yang et al. 2013). Results from these studies confirmed the role of pH, electrolyte composition and the presence of organic matter in the aggregation or stabilization of ENPs.

2.2 Iron-based nanoparticles used for soil and groundwater remediation

2.2.1 Introduction: From permeable reactive barriers to nanoscale particles

The use of iron-based materials and especially zero-valent iron for soil and groundwater remediation has started in the early 1990s. Granular zero-valent iron particles (GZVI) have firstly been proposed in 1994 by Gillham and O'Hannesin and applied for environmental remediation. The main application for GZVI was their installation in permeable reactive barriers (PRBs) for the treatment of groundwater plumes. A PRB is defined as an engineered zone of reactive materials designed to intercept and treat contaminated groundwater. GZVI has been used successfully as a reactive media for the treatment of chlorinated organic compounds, heavy metals and radionuclide contamination (Scherer et al. 2000; Deng and Hu 2001; Lo et al. 2007). However, GZVI applications have been limited to shallow groundwater plumes in unconsolidated aquifers and the use of PRBs requires intrusive engineering methods for installation and the need for well-constrained and discrete groundwater flow paths. Moreover, many authors have reported significant loss of reactivity and build-up of mineral precipitates within the PRBs over time (Phillips et al. 2003; Liang et al. 2005; Morrison et al. 2006; Henderson and Demond 2007). The introduction of nanoscale ZVI (nZVI) within the past 15 years has led to a wider range of applications due to easier deployment via direct injections, degradation of a broader range of contaminants and faster degradation rates (Grieger et al. 2010). Therefore, nZVI is currently the most widely studied nanomaterial for environmental remediation of soil and groundwater.

2.2.2 Properties of nZVI

2.2.2.1 The core-shell structure

Microscopic and spectroscopic studies have revealed that nZVI possess a core-shell structure (Liu et al. 2005; Nurmi et al. 2005; Sun et al. 2006; Yan et al. 2010) as displayed in

Figure 2-4. The core consists primarily of zero-valent or metallic iron while the shell is largely iron oxides/hydroxides formed from the oxidation of the metallic iron. The shell of iron oxides may compose 40 to 86% of apparent nZVI (Phenrat et al. 2007).
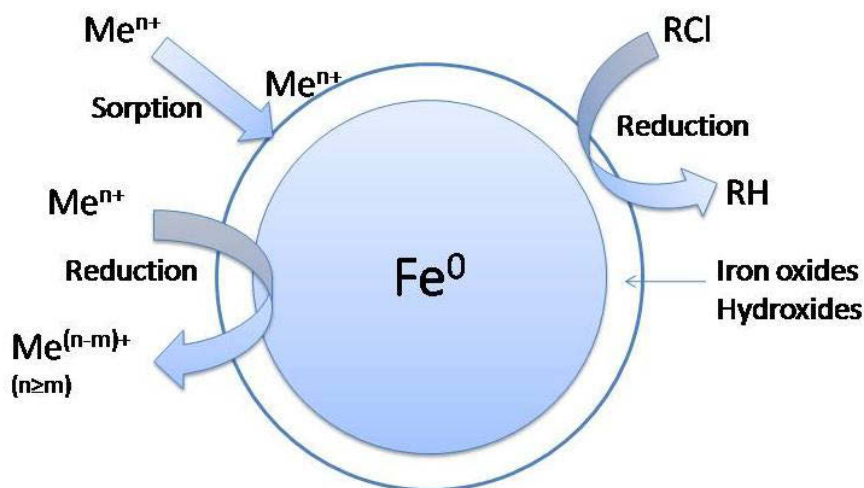
Figure 2-4: The core-shell model of zero-valent iron nanoparticles.

This specific core-shell structure will have important significance for the chemical properties of nZVI. In fact, the nature of the oxide shell makes it more reactive than a simple passive oxide layer that may form on bulk iron materials (Wang et al. 2009). The composition of the oxide shell and the metal in nZVI is also significantly different from that of bulk ZVI. This makes the core-shell structure a crucial aspect to examine when investigating the reactivity of nZVI for environmental remediation. In fact, nZVI exhibits characteristics of both iron oxides and metallic iron. While the metallic iron acts as the electron source and exhibits a reducing character, the oxide shell will promote contaminant sorption via surface complexation and electrostatic interactions and at the same time, allows electron passage from the metallic core.

2.2.2.2 The aqueous corrosion of zero-valent iron

Metallic or zero-valent iron (i.e. Fe^0) is well-known to be highly exposed to corrosion in aqueous solution. The corrosion of metallic iron occurs primarily via an electrochemical

process with anodic and cathodic components (Crane and Scott 2012). The anodic reaction mainly includes the dissolution of Fe^0 which involves the formation of soluble ionic products or insoluble oxide/hydroxide. This reaction is generally coupled with the reduction of redox species at the cathode. In natural waters, both dissolved oxygen (DO) and water (H_2O) are the primary components responsible for the corrosion of metallic iron with the reaction with H_2O being thermodynamically favoured:

$$2Fe^0_{(s)} + 4H^+_{(aq)} + O_{2(aq)} \rightarrow 2Fe^{2+}_{(aq)} + 2H_2O_{(l)} \ E^0 = +1.67 \text{ V} \tag{1}$$

$$2Fe^0_{(s)} + 2H_2O_{(l)} \rightarrow 2Fe^{2+}_{(aq)} + H_{2(g)} + 2OH^-_{(aq)} \ E^0 = -0.39 \text{ V} \tag{2}$$
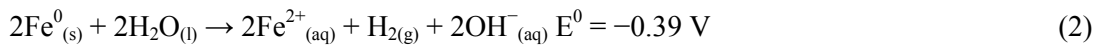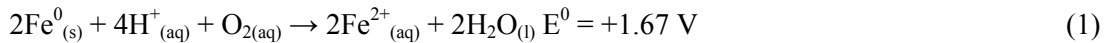
Ferrous iron (i.e. Fe^{2+}) can also undergo further oxidative transformation:

$$2Fe^{2+}_{(aq)} + 2H^+_{(aq)} + \tfrac{1}{2}O_{2(aq)} \rightarrow 2Fe^{3+}_{(aq)} + H_2O_{(l)} \ E^0 = +0.46 \text{ V} \tag{3}$$

$$2Fe^{2+}_{(s)} + 2H_2O_{(l)} \rightarrow 2Fe^{3+}_{(aq)} + H_{2(g)} + 2OH^-_{(aq)} \ E^0 = -1.60 \text{ V} \tag{4}$$
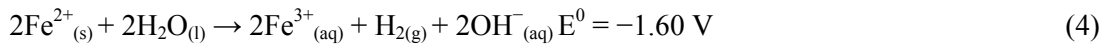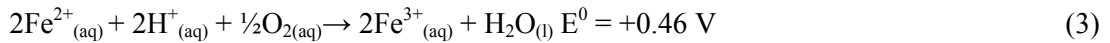
Li et al. (2006) performed detailed X-ray Photoelectron Spectroscopy (XPS) analysis on nZVI and found that ferric iron (i.e. Fe^{3+}) may also react with OH^- and H_2O to yield iron hydroxides (i.e. $Fe(OH)_3$) or iron oxyhydroxide (i.e. $FeOOH$) which are believed to be the main components of the oxide shell:

$$Fe^{3+}_{(aq)} + OH^-_{(aq)} \rightarrow Fe(OH)_3 \tag{5}$$

$$Fe^{3+}_{(aq)} + H_2O_{(aq)} \rightarrow FeOOH + 3H^+_{(aq)} \tag{6}$$

Equations (1) to (4) are the typical electrochemical/corrosion reactions by which nZVI is oxidised when exposed to oxygen and water. These corrosion reactions can be accelerated or inhibited by changing the solution chemistry and/or metal composition (Zhang 2003). It is also clear from these equations that nZVI oxidation will produce a characteristic increase of solution pH as either protons are consumed or hydroxyl ions are produced. A highly

reducing environment is also created through the rapid consumption of oxygen and production of hydrogen. Zhang (2003) and Sun et al. (2006) observed a pH increase of 2-3 units and a reduction in the oxydo-reduction potential (ORP) in the range of 500-900 mV in closed batch reactor experiments. This ability of nZVI to rapidly reduce groundwater redox potential has been proved to be not only crucial for chemically induced degradation of environmental contaminants but also useful for stimulating reductive biodegradation of chlorinated solvents (Cundy et al. 2008).

2.2.2.3 *Degradation of organic and inorganic contaminants*

Many recent studies have demonstrated that nZVI is highly effective for the removal or degradation of a wide range of common environmental contaminants including chlorinated organic solvents (Elliott and Zhang 2001; Zhang 2003; Nutt et al. 2005), organic dyes (Liu et al. 2005), various inorganic compounds (Alowitz and Scherer 2002; Cao et al. 2005), including metals (Kanel et al. 2005; Xu et al. 2005). Examples are given in Table 2-2.

Table 2-2: List of some of the common environmental contaminants removed by nZVI.

	Family of contaminants	Contaminants
Organic	Chlorinated methanes	Carbon tetrachloride
		Chloroform
		Chloromethane
	Chlorinated benzenes	Dichlorobenzene
		Tetrachlorobenzene
		Pentachlorobenzene
		Hexachlorobenzene
	Pesticides	DDT
		Lindane
	Organic dyes	Acid orange
		Acid red
		Chrysoidine
	Trihalomethanes	Bromoform
		Dibromochloromethane
		Dichlorobromomethane
	Chlorinated ethenes	Tetrachloroethene
		Trichloroethene
		Vinyl chloride
	Other organic contaminants	PCBs
		Dioxins
		TNT
Inorganic	Heavy metal ions	Mercury
		Nickel
		Silver
		Cadmium
	Inorganic anions	Dichromate
		Arsenic
		Perchlorate
		Nitrate

Because there are significant variations in contaminant chemistry, several pollutants removal pathways have been identified and include complexation, sorption, precipitation and surface mediated chemical reduction (Miehr et al. 2004). For instance, for the treatment of organic contaminants such as chlorinated solvents, removal usually occurred via the reductive degradation of the chemical implying that the contaminant is physically destroyed. For

inorganic pollutants, especially for the treatment of heavy metals, removal generally occurs via immobilisation on the surface of the oxide shell without physical degradation (Crane and Scott 2012).

Li et al. (2006) demonstrated that nZVI exhibit either metal-like or ligand-like coordination properties depending on the solution chemistry, and especially on the solution pH. In fact, at low pH (i.e. below the PZC which occurs at around pH 8), iron oxides are positively charged and will have a tendency to attract anionic ligands such as key environmental species (e.g. chloride and phosphate). However, when the solution is above the PZC, the oxide surface becomes negatively charged and the oxide shell will likely form surface complexes with cations (e.g. metal ions).

2.2.3   Synthesis of nZVI

Nanoparticle synthesis methods are usually classified as either top-down or bottom-up approaches. The top-down strategy starts with large-size bulk materials (e.g. microscale or granular) and the production of nanoscale particles is generated by mechanical or chemical steps. For the bottom-up approach, nanoparticles are produced by the assemblage of atoms or molecules via chemical synthesis (Li et al. 2006). The synthesis methods are determining factors in preparing nanoparticles with different sizes and shapes. Researchers have developed different synthesis methods for nZVI that can be classified as either physical or chemical methods as shown in Table 2-3.

Some of the most widely employed synthesis methods for application in environmental remediation (i.e. borohydride reduction of ferrous salts, gas-phase reduction and high-energy ball mining) will be developed in the next sections.

Table 2-3: Summary table of nZVI synthesis methods

	Synthesis methods	References
Physical synthesis methods	Inert gas condensation	(Sanchez-Lopez et al. 1997; Nakayama et al. 1998; Choa et al. 1999; Nakayama et al. 2000; Wang et al. 2004)
	Severe plastic deformation	(Valiev et al. 2000; Sus-Ryszkowska et al. 2004)
	High-energy ball milling	(Del Bianco et al. 1998; Malow et al. 1998)
	Ultrasound shot peening	(Tao et al. 1999)
Chemical synthesis methods	Liquid-phase reduction or borohydride reduction of ferrous salts	(Glavee et al. 1995; Wang and Zhang 1997; Choe et al. 2000; Elliott and Zhang 2001; Zhang 2003; Liu et al. 2005; Nurmi et al. 2005; Sun et al. 2006; Celebi et al. 2007; Sun et al. 2007; Hoch et al. 2008; Scott et al. 2010)
	Gas-phase reduction	(Uegami et al. 2004; Nurmi et al. 2005)
	Microemulsion	(Wiggins et al. 2000; Carpenter 2001; Li et al. 2003; Song et al. 2004)
	Controlled chemical co-precipitation	(Liu et al. 2004)
	Chemical vapour condensation	(Choi et al. 2001)
	Pulse electrodeposition	(Natter et al. 2000; Choi et al. 2001)
	Liquid flame spray	(Makela et al. 2004)
	Thermal reduction of ferrous iron	(Hoch et al. 2008; Bystrzejewski 2011)
	Electrolysis	(Chen et al. 2004; Wang et al. 2008)
	Polyphenolic plant extract	(Hoag et al. 2009)

2.2.3.1   *Liquid-phase reduction or borohydride reduction method*

The borohydride reduction method is currently the most widely employed synthesis method within academia (Wang and Zhang 1997). The basic concept of this method is to add a strong reductant (e.g. sodium borohydride) into a metallic ion solution (e.g. $FeCl_3$) to reduce it to nanoscale metal particles (Li et al. 2006). For the production of nZVI by liquid-phase reduction, $NaBH_4$ is commonly used as reductant to reduce either ferric (Fe(III)) or ferrous (Fe(II)) salts. This method has been used by many research groups since one of its major

advantages relies on its relative simplicity with the need of only two common reagents and no need for any specific lab equipment (Li et al. 2006).

Typically, nZVI can be prepared by slowly adding 1:1 volume ratio of 0.25 M sodium borohydride into 0.045 M ferric chloride solution ($FeCl_3.6H_2O$). Ferric iron is reduced by the borohydride following this reaction (Wang and Zhang 1997):

$$4Fe^{3+}_{(aq)} + 3BH_4^-_{(aq)} + 9H_2O_{(aq)} \rightarrow 4Fe^0\downarrow + 3H_2BO_3^-_{(aq)} + 12H^+_{(aq)} + 6H_{2(aq)} \tag{7}$$

Ferrous sulfate ($FeSO_4.7H_2O$) has been also used successfully as the aqueous-phase iron solution (Ponder et al. 2000; Wang et al. 2006):

$$Fe^{2+}_{(aq)} + 2BH_4^-_{(aq)} + 6H_2O_{(aq)} \rightarrow Fe^0\downarrow + 2B(OH)_{3(aq)} + 7H_2O_{(aq)} \tag{8}$$

Most of the studies using this method obtained similar results in term of particle size and specific surface area. The borohydride method typically produces polydispersed nZVI ranging over tens to hundreds of nanometres in size with specific surface area of 20-40 m^2/g (Li et al. 2006).

Nevertheless, although this method produces highly reactive nZVI, it also presents some disadvantages. First, this synthesis method is associated with important health and safety consideration. In fact, the synthesis needs to be conducted in a fume hood as the chemical reactions produce large volumes of hydrogen gas as a by-product. This drawback associated with the use of expensive reagents preclude its industrial application (Hoch et al. 2008). Moreover, nZVI produced with this method are highly polydispersed and thus highly prone to agglomeration as shown in Figure 2-5 (Nurmi et al. 2005; Sun et al. 2006; Scott et al. 2010).
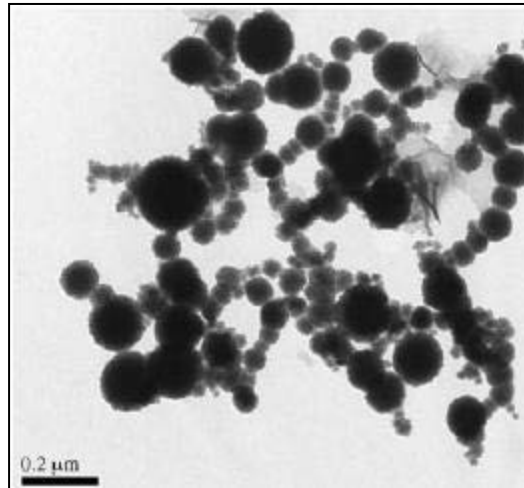
Figure 2-5: TEM images of nZVI synthesised by the borohydride reduction method [From (Sun et al. 2006)].

2.2.3.2   Gas-phase reduction method

In 2006, Toda Kogyo Ltd. developed a commercial nZVI product known as RNIP. This product is widely used in environmental applications and is synthesised by gas-phase reduction (Uegami et al. 2004). The nZVI generated by this method are produced by heat-reducing goethite or hematite particles with hydrogen gas at very high temperature (i.e. 350-600°C). After cooling, the iron particles are transferred into water in a gas phase which producing an oxidised shell on the particle surface in water. The synthesised nanoparticles are then dried and ready for use in diverse applications. The nZVI produced by this method are generally composed by a two-phase material consisting of Fe_3O_4 and α-Fe^0 with a Fe content of no less than 65% by weight (Uegami et al. 2004). The particles have an average particle size ranging from 50 to 300 nm with a specific area of about 7.55 m^2/g.

2.2.3.3   High-energy ball milling

In recent years, Golder Associates Inc. has become the market leader for large-scale field application of nZVI. They are producing large quantities of this nanomaterial using the ball milling method (Müeller and Nowack 2010). This method uses conventional mechanical attrition techniques to break macroscale Fe^0 into nanoscale particles. Australia's Advanced

Powder Technology Pty. Ltd. has also successfully produced and commercialised a wide range of nZVI powders synthesised with the ball mining method (Dallimore 1999). However, although being straightforward, this method is highly energy demanding and synthesised particles generally exhibit a very high surface energy which promotes their aggregation.

2.2.4 Transport and reactivity of nZVI in environmental media

As discussed in the previous sections, nZVI has attracted increased attention in the past years for the treatment of contaminated soil and groundwater as many researchers demonstrated its high performance for the removal of a wide range of common environmental pollutants. However, the major obstacles to its field-scale application remains its limited mobility and reactivity once applied to the environment, resulting in ineffective in-situ remediation (Schrick et al. 2004; Quinn et al. 2005; He and Zhao 2007; Saleh et al. 2008). Both transport and reactivity are affected by several factors and many researchers have focused on finding solutions to control or reduce these factors in order to improve nZVI mobility and reactivity in environmental media.

2.2.4.1 Factors affecting the mobility and reactivity of nZVI

There is a broad consensus that the mobility and reactivity of nZVI is very limited in environmental media this can be explained by three basic mechanisms (Elimelech et al. 1998; Kanel et al. 2008; Scott 2011):

- Due to its magnetic properties (Phenrat et al. 2007), nZVI have a natural tendency to aggregate which generates significant losses in reactivity and decreases environmental mobility in porous media (e.g. soil) (Theron et al. 2008);
- Because of the surface particles oxidation, there are formation of large corrosion product precipitates (including $Fe(OH)_2$, $Fe(OH)_3$, Fe_3O_4, Fe_2O_3, $FeOOH$,

Fe$_5$HO$_8$.4H$_2$O and green rusts) which considerably limits direct Fe^0-contaminant interactions.

- Due to interaction with the subsurface environment (mainly via attachment to mineral surfaces and carbonaceous materials or microbial removal), nZVI become easily inert and fairly immobile.

Aggregation is considered as the primary cause of reduced mobility and reactivity and many studies have demonstrated that this phenomenon depends on many factors which are mainly: particle size, solution pH, ionic strength, soil composition (e.g. the presence of organic matter) and groundwater flow velocity (Ponder et al. 2000; Zhang et al. 2002; Schrick et al. 2004; He and Zhao 2005; Lien and Zhang 2005; Saleh et al. 2005; Sun 2006). For instance, groundwater usually has high ionic strength which tends to reduce the electrostatic repulsion among particles which then increases particle aggregation. Environmental conditions such as the presence of humic acids in soil or groundwater are also well known to affect the stability of nZVI (Saleh et al. 2008).

The reactivity of nZVI has also been shown to be pH dependant. In fact, Giasuddin et al. (2007) demonstrated that the adsorption of humic acids is fairly high in the pH range 3.0-9.0 and decreases considerably at a pH over 10.0. This is consistent with the electrostatic interaction mechanism since nZVI will remain attractive to negatively charged humic acids as long as it is positively charged. The results of Giasuddin et al. (2007) can be explained by the fact that nZVI are positively charged below the PZC which was shown in previous studies to be around pH 8.0 (Sun et al. 2006).

Other studies focused on the influence of oxyanions and divalent cations on nZVI sorption capacity (Ali and Dzombak 1996; Geelhoed et al. 1998; Mylon et al. 2004; Peng et al. 2005; Guan et al. 2006; Giasuddin et al. 2007). For instance, Giasuddin et al. (2007) studied the effect of oxyanions and divalent cations on the adsorption of humic acids onto nZVI. They

found that the presence of highly concentrated (i.e. 10 mM) oxyanions H_4SiO_4, HCO_3^- and $H_2PO_4^{2-}$ reduces the adsorption capacity of nZVI up to 100% due to competition between these anions and humic acids for sorption sites. However, they also found that the presence of 2 mM Mg^{2+} and Ca^{2+} enhances humic acid removal from 17 mg.g^{-1} to 55 mg.g^{-1} and 76 mg.g^{-1} respectively. This was explained by the compression of the diffuse double layer and charge neutralisation of both absorbate and adsorbent by the divalent cations (Peng et al. 2005) because interaction between salts and organics generally generates a change in organic matter properties. Murphy et al. (1990) also explained that the presence of divalent cations promotes the formation of a complex nZVI-mineral-humic acid which significantly enhance the nZVI adsorption capacity.

2.2.4.2   *Methods to enhance nZVI mobility*

Many studies suggested that the key to enhance particle mobility is in modifying their surface properties to improve their colloidal stability (i.e. reducing particle aggregation to maintain discrete particles) and reduce their adherence to porous media solids (Quinn et al. 2005; Phenrat et al. 2009; Crane and Scott 2012). This is usually done by surface coatings with surfactants, polymers or polyelectrolytes. These coatings help to increase the steric and/or electrostatic repulsion between nanoparticles to counterbalance the attractive van der Waals and magnetic attractive forces (He and Zhao 2007; He et al. 2007; Saleh et al. 2008; Cirtiu et al. 2011). Moreover, it has been demonstrated that the presence of a stabiliser during the synthesis of nanoparticles may facilitate its nucleation and growth (Shimmin et al. 2004). Different surface coatings have been proposed for nZVI which includes polyacrylic acid (PAA) (Schrick et al. 2004; Kanel et al. 2008; Lin et al. 2010), polystyrene sulfonate (PSS) (Phenrat et al. 2009), carboxymethyl cellulose (CMC) (He and Zhao 2007; He et al. 2007; Lin et al. 2010), triblock copolymers (Saleh et al. 2005), polyeletrolyte block polymers (Sirk et al. 2009), cellulose acetate (Wu et al. 2005), polyasparate (Phenrat et al.

2008; Tiraferri et al. 2008), polysorbate 20 (also known as Tween® 20) (Kanel et al. 2007), xanthan gum (Vecchia et al. 2009) and many others.

Polymer coatings and surfactants

Particle stabilisation through the use of surfactants or polymer coatings is achieved by controlling the surface particle charge. As mentioned before (i.e. section 2.1.2.1), the steric hindrances provided by these coatings counteract the electrical and dipolar attractions that occur naturally between particles. However, this is only achieved when a sufficient mass of surfactants or polymer coating material is applied to form a complete micelle around the nanoparticles (Crane and Scott 2012). Therefore, the use of these coatings in environmental remediation is unlikely to provide complete stabilization if there is insufficient surface coverage (Cirtiu et al. 2011).

Polyelectrolyte coatings

The surface coating of nZVI by high molecular weight hydrophilic polyelectrolytes may be considered irreversible and therefore may be a more suitable method (compared to surfactants) for increasing mobility of nZVI in subsurface systems (Crane and Scott 2012). Polyelectrolytes coatings work in the same way as surfactants to enhance colloidal stability (i.e. steric hindrances); however these polymers are chemically or physically grafted to the particle surface (Saleh et al. 2005). Other benefits of this type of coating include promotion of microbial activity which may improve contaminant removal in carbon limited environments and high resistance in a wide range of groundwater conditions for very long periods (up to several months) (Phenrat et al. 2009).

The two principal studied materials are guar gum and CMC which are formed from guar beans and cellulose respectively. Both species are very cheap, non-toxic, naturally water-soluble, and biodegradable and remain neutrally charged and unaffected by ionic strength or

pH in water across an environmentally relevant range (i.e. pH 5-9) (Tiraferri et al. 2008; He et al. 2010).

Protective shells and solid supports

The use of protective shells, firstly designed for magnetic applications, has been also used to improve the mobility and longevity of nZVI. The different protective shells tested so far include silica (Tang et al. 2006), polymers (Wilson et al. 2004) and carbon (Hoch et al. 2008; Zhang et al. 2010), and have been observed to improve nZVI stability to a level comparable with polyelectrolyte coatings. The use of carbon has usually been preferred over other protective shells since it has higher stability in acidic or basic media and was proved not having toxic or injurious effects on biological systems.

The use of solid supports has also been tested by scientists at the Helmholtz Centre for Environmental Research in Germany (Bleyl et al. 2012; Kopinke and Mackenzie 2012). They developed a method to combine nZVI with activated carbon to produce "Carbo-Iron" platelets with diameters varying between 50 and 200 nm. The sorbent properties of the activated carbon combined with the reductive capacity of the Fe^0 was proved to exhibit hydraulic mobility comparable to surfactants and polyelectrolyte coatings whilst enhancing the reduction of a range of chlorinated organics (e.g. trichloroethylene (TCE)) as shown in Figure 2-6.

Figure 2-6: Picture showing the high affinity of nZVI for hydrophobic compounds (i.e. TCE) when combined with activated carbon (Kopinke and Mackenzie 2012).

Increasing the particle size

One of the main challenges with nZVI surface modification is in maintaining the reactive performance of the nZVI. An alternative method to enhance the particle mobility without affecting the surface properties is to increase the particle size. It has been demonstrated that particles within the size range of 0.1-2 µm (depending on the soil type) have the highest mobility (EPA 2005; Müeller and Nowack 2010). Moreover, by using larger particles, any nano eco-toxicological issues will be excluded. Finally, particles larger than 0.5 µm can be handled as powder which reduces material volume.

2.2.4.3   Methods to enhance nZVI reactivity

One of the most applied methods to increase nZVI reactivity is to alloy it with a noble metal (e.g. Pd, Pt, Ag, Ni, Cu, etc.). Advantages of bimetallic nZVI include cost effectiveness, good corrosion stability and faster contaminant degradation than uncoated nZVI (Lien and Zhang 1999; Kim et al. 2008). The bimetallic nZVI are simply prepared by soaking the freshly produced nZVI in a solution containing the noble metal salt (Li et al. 2006).

In the past few years, several studies of bimetallic nZVI for environmental remediation have been made and include mainly Fe/Pd (Grittini et al. 1995; Zhang et al. 1998; Lien and Zhang 1999; Elliott and Zhang 2001; Lien and Zhang 2005; Lien and Zhang 2007), Fe/Ni (Zhang et al. 1998; Schrick et al. 2002; Tee et al. 2009; Barnes et al. 2010; Barnes et al. 2010), Fe/Pt (Zhang et al. 1998) and Fe/Ag (Xu and Zhang 2000). In these different combinations, Fe^0 is considered to behave as an anode and thus undergoes oxidation to protect the noble metal. The chemical reduction of sorbed contaminants at the surface of the bimetallic nZVI surface is believed to occur through direct electron transfer with the noble metal or through reaction with hydrogen produced by the oxidation of the zero-valent iron (Zhang et al. 1998). Experiments have yielded many different results regarding bimetallic nZVI performance but Fe-Pd (Pd 0.1-1 wt. %) generally performed better than the other combinations (Elliott and Zhang 2001; Henn and Waddill 2006).

2.3 Characterisation of iron-based nanoparticles for soil and groundwater remediation: A methodological review

As discussed in the previous section, the mobility and reactivity of nZVI in subsurface environments are significantly affected by their tendency to aggregate. Both the mobility and reactivity of nZVI mainly depends on properties such as particle size, surface chemistry and bulk composition. In order to ensure efficient remediation, it is thus crucial to accurately assess and understand the implications of these properties before deploying these materials into contaminated environments.

The purpose of this section is therefore to present the different analytical tools available to characterise the different properties of nZVI and to discuss their advantages and limitations. Examples of characterisation methods of commercial nZVI/ZVI will be also provided. Finally, the challenges of characterising nZVI in groundwater will be also discussed.

The following section is part of a review paper submitted by the author in Analytica Chimica Acta.

2.3.1 Particle size, size distribution and aggregation state analysis

Particle size, size distribution and aggregation state are important parameters to evaluate before deploying nZVI in the subsurface environment to ensure efficient site remediation. Many studies have demonstrated that both the reactivity and mobility of metal nanoparticles can be dependent on particle size (Nurmi et al. 2005; Christian et al. 2008; Hassellöv et al. 2008). For instance, a recent study by Signorini et al. (2003) demonstrated that the composition of the oxide shell, which significantly impacts on nZVI reactivity (Kim et al. 2010), is influenced by the size of the particle. Another important characteristic of nZVI particles that can impact on their remediation efficiency is their strong tendency to aggregate due to their magnetic properties and tendency to remain in the most thermodynamically favourable state (Saleh et al. 2005; Kanel et al. 2007). Importantly, the formation of highly aggregated particles will reduce the available reactive surface sites compared to dispersed nano-sized particles (Nurmi et al. 2005).

Several analytical methods are available to measure the particle size, size distribution and aggregation state of a sample. In the case of nZVI, most published studies rely on one single method; primarily using transmission electron microscopy (TEM) (Nurmi et al. 2005; Giasuddin et al. 2007; Yan et al. 2010) or a combination of TEM with one other size-measurement technique (He and Zhao 2007; He et al. 2007; Tiraferri et al. 2008; Lin et al. 2010; Cirtiu et al. 2011; Hwang et al. 2011). However, many recent studies have emphasised the importance of using a multi-method approach when characterising nanoparticles to ensure the accuracy of the characterisation data (Lead and Wilkinson 2006; Domingos et al. 2009). Analytical methods suitable for providing particle size data are presented and discussed below, together with some nZVI demonstration data.

2.3.1.1 Microscopy techniques

Microscopy techniques provide some of the most direct methods for ENP characterisation; enabling the determination of fundamental parameters such as size, shape and aggregation state by direct visualisation. Traditional optical microscopes do not offer adequate spatial resolution: they are diffraction limited (for visible light $d \approx \lambda/2 \approx 250$ nm), so electron microscopy techniques are required to examine ENPs at the single particle level. The acquired images can be post-processed to obtain a number-weighted size distribution of the ENPs that can assist in confirming the results obtained from other bulk size-measurement techniques (e.g. Dynamic Light Scattering - DLS, Field Flow Fractionation - FFF). As microscopy methods are effectively single particle counting methods, a large number of particles needs to be analysed in order to acquire statistically representative results. The required number of particles to be analysed is dependent on the distribution and the desired accuracy (Jillavenkatesa et al. 2001), but is typically in the several hundreds to thousands of particles (Klein et al. 2011; Singh et al. 2011). This can be largely automated by the use of image processing programs such as ImageJ (Rasband 1997-2012). However, some manual intervention is often necessitated by the limited ability of programs to recognise dimers or larger aggregates, even with the use of various boundary metrics (e.g. circularity). Furthermore, appropriate sample preparation is critical in determining accurate sizes and distributions from these methods. For the characterisation of nZVI, the most commonly applied microscopy techniques are TEM (Nurmi et al. 2005; Giasuddin et al. 2007; Yan et al. 2010), scanning electron microscopy (SEM) (Shi et al. 2011; Yuvakkumar et al. 2011) and atomic force microscopy (AFM) (Kanel et al. 2005; Choi et al. 2007; WooáLee and BináKim 2011).

Transmission electron microscopy (TEM)

Transmission electron microscopy is a single particle characterisation technique that uses an accelerated beam of electrons to illuminate thin samples (typically <100 nm). In the commonly applied bright-field TEM, the transmitted electrons produce a 2D projection of the specimen on to an imaging device such as a charge coupled device (CCD). Due to the short de Broglie wavelength of electrons, TEM can image particles beyond the diffraction limit of light microscopies and provide direct visual information about size, shape and aggregation state; as well as information about crystallinity and lattice spacing when using high resolution TEM (Cha et al. 2007; Wang et al. 2007; Wang et al. 2007). This ability to directly image nanoscale materials such as nZVI is a powerful advantage over other methods of particle characterisation such as DLS or FFF, and TEM and its variants have been widely used for nanoparticle characterisation (Sun et al. 2006; Wang et al. 2009; Wang et al. 2010). For example, while DLS can be used to derive the hydrodynamic diameter of particles, this technique requires an inherent assumption that the diffusing "particles" are spherical, which may not necessarily be the case. TEM can offer irrefutable evidence of the nZVI core shape and aspect ratio that can assist in the appropriate interpretation of complementary data. It is also important to note that TEM measures the hard particle limits defined by the iron components (in the case of nZVI), rather than the hydrodynamic diameter which extends to include the adsorbed organic stabilisers with low TEM contrast. On the other hand, inorganic surface layers can also be examined, and this may be very useful in examining core-shell structures of nZVI such as oxide minerals (Martin et al. 2008; Kim et al. 2010; Yan et al. 2010) (Figure 2-7), or palladium used for enhancing nZVI environmental stability or catalytic reactivity (Yan et al. 2010).
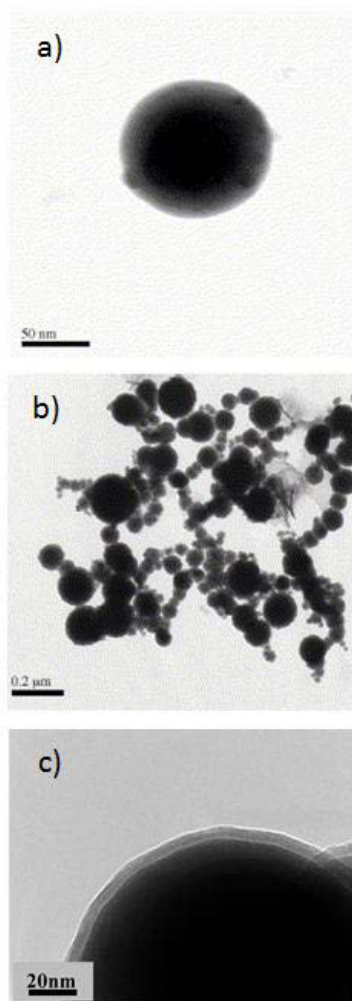
Figure 2-7: Bright-field TEM images of a) a single nZVI, b) an aggregate of nZVI and c) TEM image showing the oxide layer at the surface of an nZVI. [a) and b): Reprinted with permission from ref. (Sun et al. 2006) Copyright 2006 Elsevier; c): Reprinted with permission from ref. (Martin et al. 2008), Copyright 2008 American Chemical Society]

Other modes of TEM can be used to provide additional physicochemical information about the samples. For example, dark-field imaging, which produces contrast by electron density differences, may reveal the individual particles within nZVI agglomerates linked by oxide layers (Yan et al. 2010; Yan et al. 2012), and even internal grain structures (Nurmi et al. 2005). X-ray energy dispersive spectroscopy (XEDS) can provide further details, such as semi-quantitative information about the elemental composition of a collection of nZVI particles, and can be used to map single particles with scanning TEM (STEM) – XEDS (Figure 2-8), which may be valuable in assessing the spatial distribution of bimetallic nZVI

dopants, or the mechanisms of reactions and effectiveness of remediation at the nanoscopic level (Wang et al. 2010; Yan et al. 2010; Ling and Zhang 2014). One of the advantages of TEM-XEDS is that the thin specimens lead to greater spatial resolution than that achieved with SEM-XEDS, as the large sub-surface interaction volume can limit the SEM-XEDS resolution at high voltages.
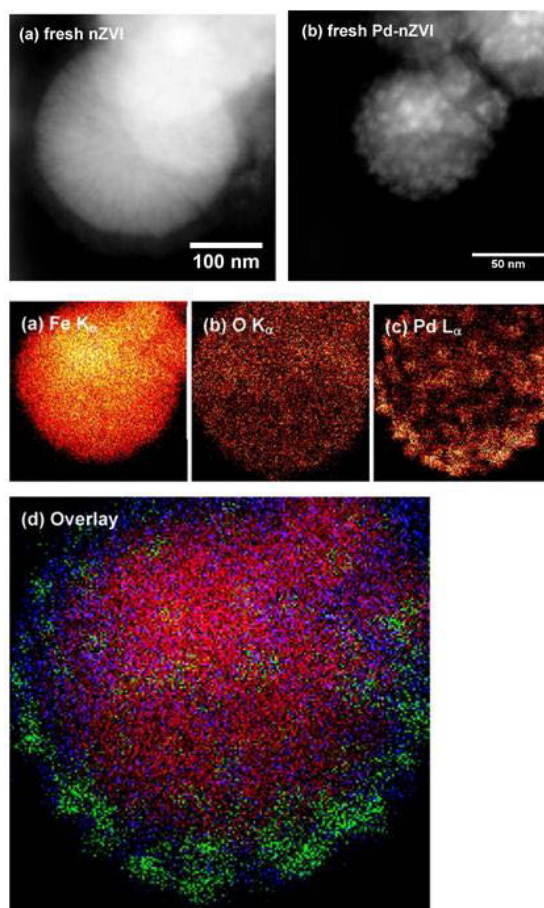
Figure 2-8: *Top:* **High-angle annular dark field (HAADF) images of a) fresh ZVI nanoparticle and b) fresh Fe/Pd bimetallic nanoparticle;** *Bottom:* **Corresponding TEM-XEDS intensity map of a) Fe, b) O and c) Pd in fresh Fe/Pd bimetallic nanoparticles; d) a false colour image of the three components overlayed. [Reprinted with permission from ref. (Yan et al. 2010) Copyright 2010 American Chemical Society]**

Further speciation of the crystalline components can be achieved by electron diffraction. Techniques such as select area electron diffraction (SAED) and convergent beam electron diffraction (CBED) can determine the lattice parameters of nanomaterials (Martin et al. 2008; Yan et al. 2010), even enabling speciation of nZVI at the single particle level (Wang

et al. 2007). Electron energy loss spectroscopy (EELS) can also reveal the electronic structure, and hence identify, different iron/oxide phases at the single particle level (Liu et al. 2005; Wang et al. 2009), although the interpretation of spectra may require further expertise.

Sample preparation is one of the challenging aspects of TEM analysis. For the determination of particle size distributions using TEM, the specimen needs to be thin (typically < 100 nm) and should ideally consist of well separated monolayers of particles in a uniform focal plane. The microscopes operate under high vacuum and the samples must be dried prior to analysis. This presents a challenge due to the high reactivity of nZVI with oxygen under normal atmospheric conditions and the magnetic properties of nZVI also complicate matters. Furthermore, slow drying processes can induce aggregation or agglomeration as a result of the increase in absolute particle concentrations and increased ionic strength. Sample preparation techniques are thus ideally fast (e.g. flash drying) and should avoid contact with oxygen rich atmospheres by the use of anaerobic chambers or vacuum desiccators. One approach may be to immobilise nanoparticles on to carbon coated grids with a functionalised polymer (e.g. poly-L-lysine – see later example for SEM, Figure 2-10e), from which excess sample can be removed prior to drying, and the immobilised fraction bound to the surface can be dried without the risk of inducing aggregation. There is also need for caution to minimise damage to the samples from the high energy electrons, which may for example, contrary to expectation, induce oxidation of the outer layers of nZVI (Wang et al. 2007; Latham and Williams 2008). Therefore, it is recommended that acquisition parameters be optimised in regions that are close to, but not directly aligned with, the actual regions of interest. Finally, once prepared, samples should be stored appropriately in a dry, inert environment (e.g. a vacuum desiccator) and analysed within a short timeframe to minimise transformation artefacts (Glover et al. 2011).

Scanning electron microscopy (SEM)

Scanning electron microscopy (SEM) is a technique whereby finely focused electron beams are raster scanned to image the surface of samples. Rather than imaging the transmitted electrons as in TEM, SEM utilises electrons that are generated when the beam interacts with the sample surface (Figure 2-9). Thus, it is a surface sensitive imaging technique. Three phenomena are routinely used in different modes of analysis: secondary electron (SE) mode, backscattered electron (BSE) mode, and XEDS mode (as in TEM). SE are low energy electrons that are generated from the material in response to the beam and the contrast is obtained using several different factors. For example, edges or sharp features appear brighter due to greater number of SE escaping from these areas and is useful for acquiring information regarding the surface structure. On the other hand, BSE are electrons that have been near-elastically scattered in the backward direction by electrons in the material and therefore contrast is generated by the electron density (which generally correlates with atomic number, Z, and the mass density) of the materials. This is similar to dark-field imaging in TEM. BSE and XEDS are thus able to offer information regarding the elemental composition of ENPs.
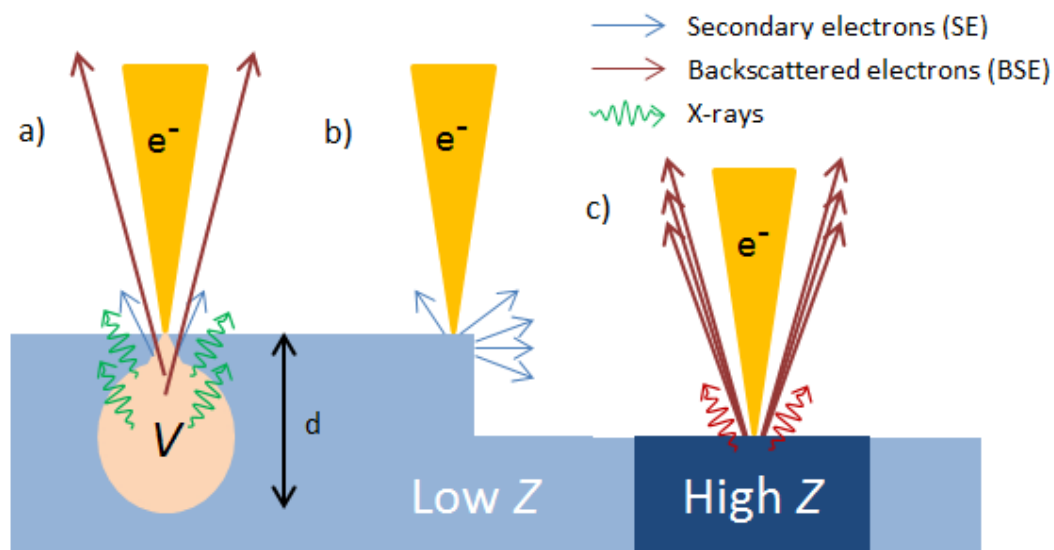
Figure 2-9: a) Focused electron beam interacts over volume V and depth d and generates secondary (SE) and backscattered (BSE) electrons, and X-rays characteristic of elements; b) greater number of SE are able to escape from edges and sharp features creating topographic contrast in the image; c) higher atomic number or density result in greater BSE providing Z contrast in the image. Different Z also result in the emission of different X-ray energies.

SEM have been used to examine the aggregation state, surface morphology (Kanel et al. 2006; Su et al. 2011) (see also Figure 2-10), and spatial distribution of nZVI on solid substrates (Bezbaruah et al. 2009; Üzüm et al. 2009; Su et al. 2011; Wu et al. 2013), and, less frequently, for size determination. While SEM is generally more accessible than TEM (i.e. more common in research laboratories), spatial resolution is poorer in SEM than in TEM, even for SEMs with a field-emission source (FEG-SEM). This is dependent on several factors such as the acceleration voltage of the beam, working distance and the atomic number and density of the material. While the best SEMs can achieve sub-nanometre resolution in SE/BSE modes and resolve sub-100 nm ENPs in X-ray imaging modes, in practice, accurate size determination with commonly available microscopes using SE mode is limited to *ca*. 10 nm and slightly worse for BSE mode. SEM-XEDS images have even higher limits for accurate sizing due to the large sub-surface interaction volume, which is highly dependent on the beam energy and sample density (Figure 2-11). Typically, a beam energy of approximately twice that of the desired X-ray emission line is used. For Fe L-edge emission (6.4 keV) this is 12.8 keV, and a beam of this energy at a spot size of 1 nm would

provide a lateral resolution of *ca.* 0.5 μm. Unlike TEM, SEM cannot accurately determine the oxide layer thickness in nZVI, unless for example, the particles have a thick oxide layer, such as that more commonly found on ZVI microparticles. In such cases, comparing the BE and BSE images may reveal regions of different electron density (Figure 2-10c), or XEDS may be acquired for qualitative element/composition identification.
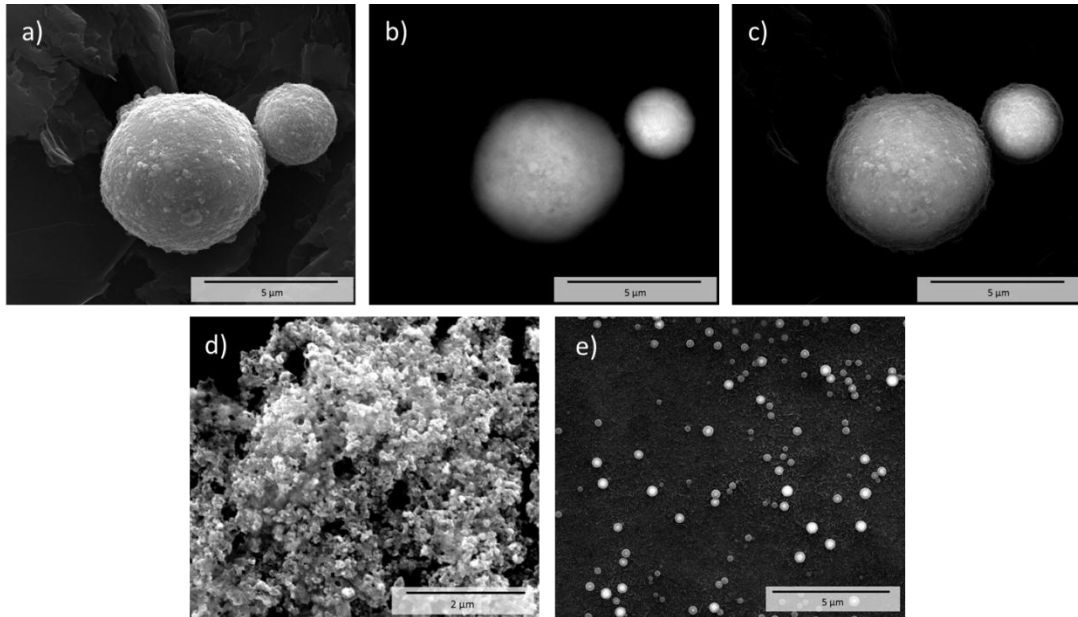
Figure 2-10: Examples of SEM images of a commercialised sample of ZVI at pH 2: a microparticle imaged in a) SE mode clearly showing the surface features, b) imaged in BSE mode showing less contrast in the core, c) an overlay of SE and BSE, suggestive of a lower density surface layer such as a stabiliser or an oxide layer; d) aggregated nZVI sample; e) nZVI particles isolated for size determination by adsorbing them onto a poly-L-lysine coated graphite substrate. (FEI Quanta 450 ESEM with FEG source under high vacuum; a) – c) HV = 20 kV, d) HV = 15 kV, e) HV = 30 kV; WD = 5-10 mm).
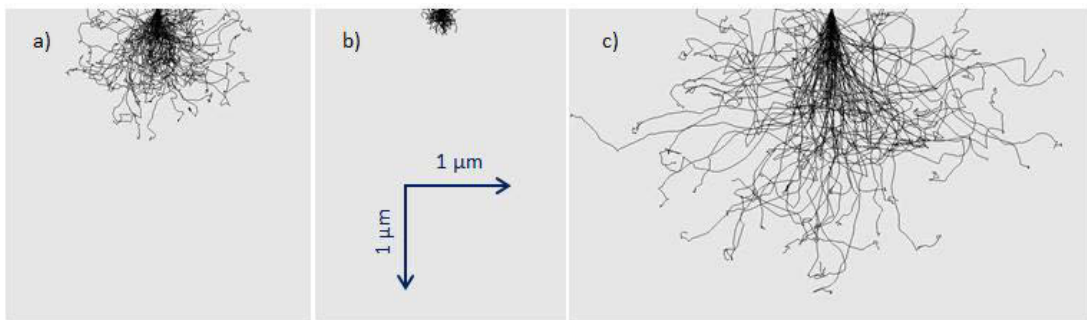
Figure 2-11: Simulated sub-surface trajectories (that collectively map the interaction volume) of 100 electrons from a 10 nm beam of a) 20 kV on Fe, b) 5 kV on Fe$_2$O$_3$, and c) 20 kV on Fe$_2$O$_3$ (Monte Carlo simulations performed using the CASINO program (Drouin et al. 2011)).

Sample preparation for SEM is comparatively easier than for TEM because the specimens do not need to be so thin. However, as with TEM, care is still required in minimising exposure to air, while ensuring that the samples are dry. Furthermore, they need to be electrically conductive: non-conductive samples require surface coating via sputtering or evaporative processes to impart surface conductivity and this may be necessary for samples with high organic stabiliser content. Alternatively, environmental SEM (ESEM) provides a route to examine "wet" and non-conductive samples by operating the SEM in a low vacuum environment (ca. 1-15 Torr, cf. $< 10^{-3}$ Torr in high vacuum). Coating is thus not required in an ESEM and reduces any changes that may be manifest through the coating, handling, evacuating and imaging processes. Finally, a variation in the image collection geometry of SEM has led to the invention of "Wet STEM", which in essence, is an ESEM operating in transmission (Bogner et al. 2005). This is a method that offers significant potential as it minimises potential aggregation effects induced by complete drying and can be used to observe ENPs in the bulk of the solution, not just those sitting near the surface.

Scanning probe microscopy (SPM)

Scanning probe microscopy (SPM) is a technique that utilises a sharp tip (probe) to scan over the surface of a sample. There are many types of SPM available including for example, atomic force microscopy (AFM), scanning tunnelling microscopy (STM) and scanning near-field optical microscopy (SNOM or NSOM); however, the application of SPM to nZVI in the literature is limited. In AFM, the interaction force between a sharp tip (located on the end of a cantilever) and the sample surface are monitored using an optical system that detects for example, minute deflections of the cantilever (contact mode) or changes in the resonant oscillation amplitudes (non-contact or tapping modes). This provides a height profile of the surface and under carefully controlled conditions, topographic images of the nanomaterials can be obtained at atomic resolution. It is thus capable of providing quantitative information about the particle height ($\approx$ size, if spherical) and morphology of

nZVI (Lin et al. 2008; Kiruba Daniel et al. 2012), and its aggregation state or distribution over a flat surface. Unlike conventional TEM and SEM, AFM can be conducted under a wider range of conditions (e.g. in vacuum, liquid or moist conditions, or in other controlled environments), and as it does not involve the use of high energy electron beams, it could be advantageous in the case of nZVI characterisation with respect to minimising sample damage and oxidation. For conductive samples, STM can be used to image the topography at atomic resolution by exploiting the tunnelling current generated between an electrically biased sharp tip and the sample surface. It has been applied to study the change in surface profiles after reaction with Cr(III) and Se(IV), where they found that roughness (protrusions) on the surface had smoothed out as a result of the reaction (Qiu et al. 2000).

Other microscopy methods with potential applications

Several novel method developments have recently occurred that have potential applications in nanomaterials analysis. For example, hyperspectral dark-field imaging with the aid of multivariate classification algorithms (Badireddy et al. 2012) had the potential to provide information on the size, aggregation state, and compositional differentiation of Ag, CeO_2 and TiO_2 nanoparticles when these were analysed in representative environmental media. This technique may offer an avenue to explore iron-based nanoparticles in environmental waters, although there may be difficulties arising from the presence of naturally occurring colloids which may also contain iron. Furthermore, light microscopy has been revolutionalised in the last decade with the birth of super-resolution microscopy (SRM) that offers spatial resolution surpassing the classical diffraction limit. There are several examples of SRM such as structured illumination microscopy (SIM) (Gustafsson 2000), spatially modulated illumination microscopy (SMI) (Baddeley et al. 2007), and stochastic optical reconstruction microscopy (STORM) (Rust et al. 2006), but so far, no applications for the characterisation of nZVI could be found in the literature. They offer spatial resolution down to <100 nm but many methods (e.g. SMI and STORM) require labelling with a fluorophore.

SIM and near-field optical microscopy (SNOM or NSOM) are two methods that do not require such labels; they work by exploiting interference imagery and evanescent waves, respectively, and may have potential in nZVI imaging. Finally, helium ion microscopy (HeIM or SHOM), is also an imaging technique that is becoming accessible, where He ions are used as the probe instead of electrons (Ward et al. 2006). This results in improved surface sensitivity (reduced interaction volume), better spatial resolution (shorter de Broglie λ) and larger depth of field (lower beam divergence), and has been used to examine the surface deposition morphologies of nanocluster deposits (Kaur et al. 2012).

2.3.1.2 *Light scattering techniques*

Light scattering techniques are commonly used to determine the size and aggregation behaviour of nanoparticles in suspensions (Schurtenberger and Newman 1993). The light source can be laser light, X-rays or neutrons and the choice of the light source will depend on the size range and particle compositions of the sample to be analysed (Hassellöv et al. 2008). Nowadays, dynamic light scattering (DLS) is the most commonly utilised techniques for sizing nanoparticles (Farré et al. 2011) as it offers several advantages, such as rapid analysis, simple operations and minimum perturbation of the samples (Ledin et al. 1994). Other commonly used light scattering techniques for the characterisation of ENPs include small angle X-ray scattering (SAXS) which enables the characterisation of both monodispersed and polydispersed samples, laser-induced breakdown detection (LIBD), which is able to detect trace amount of NPs in aqueous suspensions, and static light scattering (SLS), also called multi angle (laser) light scattering (MALS or MALLS) which can provide valuable information on particle shape factors when combined with DLS (Hassellöv et al. 2008). To date, few studies have reported the use of light scattering techniques to measure the size and aggregation behaviour of nZVI (He and Zhao 2007; He et al. 2007; Phenrat et al. 2007; Saleh et al. 2007; Tiraferri et al. 2008; Phenrat et al. 2009; Fatisson et al. 2010; Shih et al. 2011; Honetschlagerova et al. 2012; Kim et al. 2012; Kocur

et al. 2012). This is largely due to inherent analytical challenges. The detailed discussion about light scattering techniques below is limited to DLS, since this is the only light scattering technique used for characterising nZVI.

Characterisation of nZVI using dynamic light scattering

Table 2-4 summarises results from all of the studies which have used DLS to characterise nZVI and places particular focus on the reported methods of sample preparation and data processing.

DLS measures the diffusion coefficient of particles by correlating the fluctuations of the scattered light intensity over time. These fluctuations come from the Brownian motion of the particles and from the fact that neighbouring particles can have constructive or destructive interference on the scattered light intensity in a certain direction (Phenrat et al. 2007; Hassellöv et al. 2008). DLS gives an intensity weighted correlation function which can be then converted to a Z-average (intensity weighted) diffusion coefficient. If the particles are spherical, the Stokes-Einstein relation can then be applied to derive the hydrodynamic diameter of the particles.

The limitations of this technique mainly relate to the analysis and interpretation of the data obtained, especially for polydispersed samples (Filella et al. 1997). DLS is known to be very sensitive to larger particles and a very small number of large particles sedimenting during the analysis (e.g. due to aggregation processes) can induce biased results (Domingos et al. 2009). This is mostly due to the strong particle size dependence of the scattering intensity. In fact, according to the Rayleigh approximation, the intensity of light scattered by a particle is proportional to the sixth power of its diameter. This causes large particles to scatter far more light than small particles (Hiemenz and Rajagopalan 1997). Therefore Z-average or intensity values tend to overweight the contribution of larger particles/aggregates (Domingos et al. 2009). In addition, for multimodal size distributions, the conversion of the autocorrelation

function to a diffusion coefficient poses a major mathematical problem (i.e. small variations can give large deviations in the output). For this reason but also due to the fact that the signal from larger particles dominates over smaller ones, a common rule is that DLS cannot be applied to samples with polydispersity indices above ~1.5–1.7 (Hassellöv et al. 2008).

Previous studies using nZVI have demonstrated that this class of nanoparticle has a great tendency to aggregate, especially when particles are not surface stabilised (i.e. coated). This often results in samples having high polydispersity with the presence of substantially large aggregates (Ponder et al. 2000; Schrick et al. 2004; Quinn et al. 2005; Saleh et al. 2005; He and Zhao 2007; Saleh et al. 2007). In order to obtain more accurate and reliable data with DLS, the polydispersity of the sample can be reduced by using different sample preparation methods and data processing. Sample preparation methods are documented in Table 1. The most simple and applied sample preparation method to break down nanoparticle aggregates (i.e. aggregates formed during storage) is sonication (Phenrat et al. 2007; Saleh et al. 2007; Tiraferri et al. 2008; Phenrat et al. 2009; Honetschlagerova et al. 2012; Kim et al. 2012). Different sonication times may be used depending on the aggregation state of the sample prior to measurement. Honetschlägerová et al. (Honetschlagerova et al. 2012) applied different sonication times and found that above 15 minutes, no further change was observed. Saleh et al. (Saleh et al. 2007) combined sonication with an ultrasonic probe for 30 minutes and rotator mixing for 72 hours and obtained fairly stable samples.

The particle concentration of the sample is also important and this may need to be adjusted by dilution. In fact, for charged particles, the electrostatic forces arising between particles can have an effect on their diffusive behaviour and this effect is concentration dependant, with a maximum occurring at a point called "gel-formation" (Hassellöv et al. 2008). Phenrat et al. (Phenrat et al. 2007) tested different nanoparticle concentrations and found that aggregation rate increased with increasing particle concentration. This issue can generally be overcome by diluting the sample (e.g. with MQ water) but this will affect the aggregation

state of the sample. It is quite clear though that due to the limitations of DLS, this technique cannot be successfully used to assess primary particle size in commercial nZVI concentrated products as they are generally too concentrated. Hence, if the purpose of the analysis is to measure the aggregation behaviour of the sample, then it is more relevant to report the diffusion coefficient rather than the size, without diluting the sample.

As aggregation of charged particles is also pH-dependant with maximum aggregation occurring at the point of zero charge (PZC) (i.e. around pH 8 for nZVI (Sun et al. 2006)), reducing or increasing the pH far away from the PZC could be one way to form stable dispersions. Kim et al. (Kim et al. 2012) investigated the aggregation behaviour of two polymer-coated nZVI materials at two different pH values (pH 6 and pH 8) and found that aggregation increased with decreasing pH.

Pre-fractionation of the sample can also be used to obtain more accurate characterisation. Phenrat et al. (Phenrat et al. 2009) prepared three different intrinsic particle size distributions by sequential, gentle sedimentation. They found a bimodal size distribution for unfractionated samples while samples collected in the supernatant showed a monomodal size distribution with smaller particle size.

Another way to reduce the polydispersity of the sample which has not yet been tested for nZVI is to couple DLS with a size fractionation technique such as Flow Field-Flow Fractionation (FlFFF). In this way, more complex characterisation of size fractions can be potentially achieved (Weinberg et al. 2011). More details on FlFFF and its potential for the characterisation of nZVI are given in a later section. To date, only one study has been reported on the use of this combination for the characterisation of C_{60} nanoparticles (Isaacson and Bouchard 2010).

As discussed previously, the data derived from DLS measurements are intensity-based distributions or averages which tend to overweight the contribution of larger aggregates and

hence overestimate particle size (Domingos et al. 2009). Nowadays, mathematical conversion to volume or number distributions are quite often used as they can correct for overestimation to some extent (Hanus and Ploehn 1999). However, these conversions should be made only with good knowledge of the particle shapes, polydispersity and relevance of other key assumptions (Finsy 1994).

Table 2-4: Summary of the different studies that have used DLS to characterise nZVI.

nZVI source	Coating material(s)	Sample preparation before measurement	Concentration	Type of size average	Hydrodynamic diameter (nm)		Observations	Ref.
NANOFER 25 provided by NANOIRON Ltd.	Tetraethyl orthosilicate (TEOS)-PVP	Samples were sonicated for different time periods	Not specified	Not specified	~ 300		No further effect of sonication when applied for more than 15 minutes	(Honet schlage rova et al. 2012)
Reactive nanoscale iron particle (RNIP) provided by Toda Kyogo	PSS (3 different PSS-coated nZVI were prepared)	Solution was pre-fractionated and then diluted in DI water and sonicated for 3 minutes	5 mg/L	Volume weighted	1	45.6 (6%)/328 (94%)	Bimodal size distribution was observed for samples containing larger aggregates. Number weighted data reached lower particle size.	(Phenr at et al. 2009)
					2	25 (40%)/367 (60%)		
					3	24 (100%)		
				Number weighted	1	26 (98%)/263 (2%)		
					2	15 (100%)		
					3	16 (100%)		
Bare and sodium polyaspartate-coated reactive nanoscale iron particle (RNIP and MRNIP) provided by Toda Kyogo	PMAA-PMMA-PSS triblock copolymers or SDBS surfactant	Solution was sonicated with ultrasonic probe for 30 minutes and then rotated at 30 rpm with an end-over-end rotator for at least 72 hours before measurements	30 mg/L	Intensity weighted	Bare RNIP	146 ± 4	Larger size than the average primary particle size determined from TEM measurements	(Saleh et al. 2007)
					MRNIP	66 ± 3	Stable	
					SDBS-RNIP	36/220	Bimodal size distribution was observed due to the presence of SDBS micelles	
					Polymer-RNIP 1	212 ± 21	Stable	
					Polymer-RNIP 2	178 ± 11	Stable	

Material	Coating	Sample preparation	Concentration	Measurement	Particle	Hydrodynamic diameter (nm)	Findings	Reference
Bare and sodium polyaspartate-coated reactive nanoscale iron particle (RNIP and MRNIP) provided by Toda Kyogo	PMAA-PMMA-PSS	Samples were sonicated in a water bath for 5 minutes just prior to measurement	300 mg/L in 1 mM NaHCO$_3$ and 10 mM NaCl	Intensity weighted	MRNIP	1100 (pH 8)/ 2000 (pH 6)	Aggregation increased with decreasing pH	(Kim et al. 2012)
					Polymer-RNIP	1000 (pH 8)/ 1500 (pH 6)		
Reactive nanoscale iron particle (RNIP) provided by Toda Kyogo	None	Each samples were sonicated for 1 minute prior to measurement (N.B. the stock solution was pre-settled for 5 minutes to remove the largest particles (i.e. > 2 μm))	2 mg/L	Intensity weighted	RNIP	125 after 10 minutes	Aggregation rate increased with increasing particle concentration	(Phenrat et al. 2007)
			60 mg/L			1200 after 10 minutes and reached 20-70 μm after 30 minutes		
Bare and sodium polyaspartate-coated reactive nanoscale iron particle (RNIP and MRNIP) provided by Toda Kyogo	Guar gum	Each samples were sonicated for 30 minutes prior to measurement	231 mg/L	Intensity weighted	MRNIP	375.4 ± 19.2	Guar gum effectively reduced the aggregation of RNIP	(Tiraferri et al. 2008)
			231 mg/L RNIP and 0.5 g/L guar gum		Guar gum-RNIP	162.8 ± 5.7		
Lab-made using the sodium borohydride reduction method	None	Not specified	Not specified	Intensity weighted		67	-	(Shih et al. 2011)

Lab-made using the sodium borohydride reduction method	Carboxymethyl cellulose (CMC) at different CMC/Fe^{2+} molar ratio	Measured as prepared	0.1 g/L	Volume weighted	CMC/Fe^{2+}: 0.0062	> 3 μm (92.4%)	Large aggregates observed as the ratio CMC/Fe^{2+} was too low to stabilise the particles	(He and Zhao 2007)
					CMC/Fe^{2+}: 0.0124	18.6 (81%)/ 161 (5.1%)/ 1460 (13.9%)	Trimodal size distribution	
					CMC/Fe^{2+}: 0.0186	17.6 (89.5%)	-	
					CMC/Fe^{2+}: 0.0248	15.3 (90.3%)	-	
			1 g/L	Volume weighted	CMC/Fe^{2+}: 0.0025	37.2 (45%)	CMC is more effective at higher iron concentration as nucleation of Fe atoms is accelerated at elevated reagent concentrations (i.e. Fe^{2+})	
					CMC/Fe^{2+}: 0.0031	22.8 (84%)		
					CMC/Fe^{2+}: 0.0050	19.6 (89.9%)		
	Carboxymethyl cellulose (CMC) used a stabiliser to prepare Fe-Pd nanoparticles	Measured as prepared	0.1 g/L	Number weighted	CMC-stabilised Fe-Pd nanoparticles	17.2 ± 3.2	Good agreement observed among TEM and DLS measurements	(He et al. 2007)
	Carboxymethyl cellulose (CMC)	Samples were vortex mixed for 30 seconds prior to measurement	150 mg/L	Intensity weighted	Bare nZVI	~ 400	-	(Fatisson et al. 2010)
					CMC-nZVI	135	-	
	Carboxymethyl cellulose (CMC)	Measured as prepared	0.1 g/L (0.2 wt.% CMC)	Intensity weighted	0.1 g/L	61 to 123 (after 1 h)	-	(Kocur et al. 2012)
			2.5 g/L (0.8 wt.% CMC)		2.5 g/L	25 to 109 (after 1 h)	-	

2.3.1.3   Chromatographic and separation techniques

Conventional chromatographic methods and separation techniques used for characterising nanoparticles include size-exclusion chromatography (SEC), capillary electrophoresis (CE) and flow field-flow fractionation (FlFFF). These methods can generally be coupled with different types of detection systems such as inductively coupled plasma mass spectrometry (ICP-MS), UV-visible spectroscopy, and light scattering techniques to further extend their applications. They are becoming increasingly popular for nanoparticle characterisation due to their wide size separation range (e.g. from 1 nm to several μm in the case of FFF), and relatively low sample perturbation (Stolpe et al. 2005; Helfrich et al. 2006; Yegin and Lamprecht 2006; Dubascoux et al. 2010). However, to date, none of these techniques have yet been applied to characterise nZVI, probably due to the difficulties in maintaining oxygen-free systems during analysis.

<u>*Size-exclusion chromatography (SEC)*</u>

Size-exclusion chromatography (SEC) is a chromatographic technique in which molecules or particles in solution are separated by their size or molecular weight. SEC resolution is estimated to be in the range from 20-60 nm. During SEC analysis, the sample passes through a column made with a porous packing material incorporating a distribution of pore sizes in the size range of the particles to be fractionated (Barth and Boyes 1992). The particles in the sample are thus separated by their ability to enter the porous structure of the packing material. Smaller particles enter the pores easily whereas the bigger particles will be excluded and eluted earlier from the column. Size-exclusion chromatography has been applied to studies involving a wide range of ENPs, including carbon nanotubes (Duesberg et al. 1998; Yang et al. 2005; Sánchez-González et al. 2012), fullerenes (Treubig Jr and Brown 2002) and gold nanoparticles (Helfrich et al. 2006).

However, traditional liquid chromatography techniques like SEC suffer from stationary phase interactions. In fact, because of the low charge of nanoparticles compared to biomolecules of the same size, nonspecific affinity with the stationary phase usually results in strong interactions, and in some cases, irreversible binding (Liu and Wei 2004; Farré et al. 2011). Any interaction between the NPs and the stationary phase will lead to a slower elution time which may bias the results. To avoid these unwanted interactions, additives can be added to block the active sites. Aggregation of NPs inside the column should also be controlled and avoided, as it will also alter the results if large aggregates block and stick in the pores of the packing material. The choice of a suitable mobile phase (i.e. pH, ionic strength, addition of surfactants) is therefore crucial as this will affect the stability of the NPs during analysis. In the case of nZVI, oxidation within the column also has to be prevented as this may alter the stationary phase.

Capillary electrophoresis (CE)

Capillary electrophoresis is a separation method that allows fractionation of particles in a sample based on their size to charge ratio in the interior of a small capillary filled with an electrolyte (Pyell 2010). Particle separation will be dependent on the differential migration of charged particles in an applied electric field. Generally, capillary electrophoresis has better separation efficiency than SEC but only allows a very small volume of sample to be analysed (i.e. 10 nl) (Liu and Wei 2004). Capillary electrophoresis has been successfully applied to different ENPs, including gold nanoparticles (Hwang et al. 2003; Liu and Wei 2004), silver nanoparticles (Liu et al. 2005) and CdSe quantum dots (Carrillo-Carrión et al. 2011). The addition of anionic surfactants such as sodium dodecyl sulphate (SDS) to the running electrolytes can help prevent NP aggregation and thus enhance the separation of NPs by CE. Liu and Wei (Liu and Wei 2004) also demonstrated that at sufficient concentration (i.e. when the whole surface area of the NPs is coated with surfactant), there is

a linear relationship between the electrophoretic mobility/zeta potential and nanoparticle size.

Flow field-flow fractionation (FFFF)

Flow field-flow fractionation is a chromatography-like separation technique based on laminar flow in a very thin (i.e. ~250 μm) channel, with a cross flow applied perpendicular to the channel flow. The channel flow has a parabolic velocity profile (i.e. the maximum velocity is at the centre of the channel). The cross flow forces the particles to move toward a membrane at the channel wall, from where they can move back into the channel as a result of diffusion forces in the normal elution mode (i.e. for particles smaller than 1 μm). The smallest particles, having the highest diffusion coefficient, will migrate farther into the channel at higher flow rates and will thus elute first. Flow field-flow fractionation can be used for the separation and characterisation of a wide range of components ranging from macromolecules up to 50 μm in diameter to colloids and nanoparticulates down to 0.001 μm in diameter (Beckett and Hart 1993). Moreover, it provides great flexibility with respect to sample types, carrier liquids (also known as the mobile phase), pH and ionic strength (Li et al. 1997). It also offers high speed measurement and selectivity, simple on-line hyphenation to a wide range of detectors and ready collection of sample fractions for further off-line analysis (Giddings 1993; Baalousha et al. 2011). In the past few years, FlFFF has been applied to a variety of ENPs, including TiO_2 NPs (Contado and Pagnoni 2008), carbon nanotubes (Chun et al. 2008), SiO_2 NPs (Zattoni et al. 2009), Ag NPs (Poda et al. 2011), ZnO NPs (Gimbert et al. 2007) and a variety of iron oxides (Baalousha et al. 2008; Chekli et al. 2013). However, one of the main limitations of FlFFF is related to material losses during analysis. These generally occur via particle-membrane interaction and adsorption and may represent up to 50% of the injected mass (Hasellöv and Kaegi 2009). The particle-membrane interaction is mainly due to attractive forces (e.g. Van der Waals), hydrophobic and charge interactions which are all dependent on the mobile phase characteristics. As for

SEC, on-channel oxidation of nZVI should be avoided; otherwise it could damage the membrane. This could be achieved by putting the FlFFF system in an anaerobic chamber, or a cheaper alternative could be to thoroughly purge the mobile phase with N_2.

2.3.2 Bulk composition and surface chemistry analysis

Bulk composition and surface chemistry are also important characteristics that need to be rigorously determined in any nZVI materials during experimentation and before they are deployed into the environment. In fact, the metallic iron content as well as the composition of the oxide shell at the time of delivery will have a substantial impact on the nZVI performance (O'Carroll et al. 2012).

Among different analytical techniques which have been applied to determine these properties, X-ray diffraction (XRD) (Ponder et al. 2001; Sun et al. 2006; Lin et al. 2008; Zheng et al. 2008; Li et al. 2009; Wang et al. 2009; Baer et al. 2010; Dickinson and Scott 2010; Kim et al. 2010; Xi et al. 2010; Shi et al. 2011), X-ray adsorption spectroscopy (XAS) (Ponder et al. 2001; Sun et al. 2006; Lin et al. 2008; Kim et al. 2010; Reinsch et al. 2010; Leveneur et al. 2011; Yan et al. 2012) and X-ray photoelectron spectroscopy (XPS) (Ponder et al. 2001; Li et al. 2006; Sun et al. 2006; Sun et al. 2007; Li et al. 2009; Üzüm et al. 2009; Baer et al. 2010; Dickinson and Scott 2010; Kim et al. 2010; Xi et al. 2010; Yan et al. 2010; Leveneur et al. 2011; Liu and Yan 2011) are the most common X-ray techniques used to characterise nZVI.

2.3.2.1 X-ray diffraction (XRD)

X-ray diffraction (XRD) is a simple, versatile, non-destructive and comparatively inexpensive technique for identifying the phases of crystalline materials. Broad applications include assessment of percentage crystallinity; identification of fine-grained minerals such as nanoparticles, nano-clays and mixed layer clays that are difficult to distinguish optically;

determination of unit cell dimensions; and evaluation of sample purity. If the sample is finely ground and homogenised; the bulk compositional chemistry of the material can be obtained through XRD (Lin et al. 2008; Wang et al. 2009; Wang et al. 2009; Kim et al. 2010; Wang and Hong 2011).

For determining the crystal structure and quantifying the different phases, additional advanced numerical technique such as Rietveld refinement is often required. This method can also be applied to indirectly analyse the composition of major elements (constituting the crystalline phases); however, the sensitivity is much lower than with other elemental analytical techniques such as inductively coupled plasma mass spectrometry (ICP-MS). The detection limit of an individual phase present in a mixed material is about 2 – 3 % and this quantification is limited to well crystalline phases. In most previous studies where XRD was used as an nZVI characterisation tool, the researchers were confined only to identification of iron phases and evaluation of crystallinity (Table 2-5). Iron phases in nZVI samples identified by XRD patterns include Fe0, ferrihydrite, magnetite (Fe_3O_4)/maghemite (γ-Fe_3O_4), lepidocrocite (γ-FeOOH) and wuestite (FeO) (Table 2-5). The presence of Fe0 and oxides and/or hydroxides of iron support the core-shell structure model of nZVI (Yan et al. 2012). The extent of oxides/hydroxides present in an nZVI sample depend on its synthesis and storing conditions, duration of ageing, presence of other chemical elements/compounds, etc. (Table 2-5).

The principle of XRD is based on Bragg's Law ($n\lambda = 2d \sin \theta$; where λ is the wavelength of the X-rays, n is the order of diffraction, d is the spacing between consecutive parallel planes of a crystal and θ is the complement of the angle of X-ray incidence) in which monochromatic X-rays constructively interfere with a crystalline sample and produce diffracted X-rays. Scanning the sample within a range of 2θ angles, a random orientation of the powdered sample allows diffraction from all possible directions of the lattice. After the diffracted X-rays are detected and processed a diffraction pattern is obtained. The position of

peaks in the diffraction pattern (2θ angles) gives the d-spacings (or lattice spacings) which is the signature for a particular crystal phase. The phase is then identified by comparing the d-spacings with standard reference patterns. Often nZVI samples may provide very broad XRD peaks due to the short range order structure (i.e. amorphous nature) of the iron nano-phases, including the Fe0 phase (Wang et al. 2009; Fang et al. 2011). Peak broadening can also occur due to surfactant artefacts in surfactant stabilised nZVI samples (Kanel et al. 2007). Some polymer (e.g., polyacrylic acid, polyvinylpyrrolidone) stabilised nZVI samples may show no XRD peak of iron phases due to this combination of amorphous and non-crystalline nature and surfactant artefacts (Esfahani et al. 2013).

Valuable information about the particle size of a material might be derived from XRD patterns of crystallites less than about 100 nm in size. These nano crystallites provide appreciable broadening (FWHM – Full Width at Half Maxima) of the XRD peaks. By entering a corrected peak broadening value (corrected for instrumental contribution and crystal strain; β) in Scherrer's equation ($D = 0.9 \lambda/\beta \cos \theta$) the average particle size can be estimated. The size can be estimated from a single diffraction peak if particle stress is absent, but several diffraction peaks should be involved if stress is present. However, most published studies using XRD for nZVI characterisation have not used this method for nZVI particle size determination (Table 2-5), probably because of the ambiguity in the reasons for peak broadening. Rather TEM, SEM or DLS is more commonly used for this purpose.

The main limitation of the XRD technique resides in the fact that it only detects crystalline phases and is characterised by detection limits of ~ 2 – 3 % for mixed materials (Üzüm et al. 2008). That is why most previous studies did not report the quantification of iron phases present in nZVI samples (Table 2-5). Furthermore, while identification of a homogeneous and single phase material by XRD is simple, resolving the mineralogical composition of a heterogeneous unknown sample is difficult. The technique requires access to standard reference spectra of inorganic compounds (d-spacings) for identification of unknown phases.

The unit cell determinations and indexing of patterns for non-isometric crystal systems is also highly complicated. The required sample volume for conventional XRD analysis is large (tenths of a gram) and it must be ground into a fine powder for analysis. Modern high end instruments can deal with smaller sample volumes, but selection of a representation sample is also a challenge. In addition, peak overlay in the pattern of a multi-phase sample (which worsens for high angle reflections) can create difficulties in identification and quantification. In these cases, the XRD analysis needs to be supported by additional analytical techniques such as elemental analysis by ICS-MS, AES or EDAX.

As ZVI nanoparticles are reactive, there is also the possibility of sample oxidation during the XRD run time, because a good quality pattern takes about 40 minutes to obtain when scanning in the range 10° to 90° 2θ with a step size of 0.013^{o} and around 100 sec per step. Even short exposures to air of one minute or less can significantly affect the speciation of nZVI (Baer et al. 2008), therefore an appropriate covering technique should be employed during sample preparation in order to prevent the oxidation of nZVI during the test period. Also, samples need to be prepared and stored under anaerobic conditions or an inert atmosphere prior to XRD analysis.

Table 2-5: Summary of different studies which used XRD for nZVI characterisation.

nZVI source	Experimental conditions/sample preparation	Fe-phases identified and quantification	Other observation	Ref.
Lab made nZVI from FeCl₃ through borohydride reduction	nZVI particles (2 -5 g/L) reacted with an aqueous As(III) solution (1.33 mM) for 24 h; powder diffraction in ambient air	Fe^0 and ferrihydrite; not quantified	No significant change in core–shell configuration due to reaction with As (III); surface of nZVI particles was decorated with loose debris of ferrihydrite; grain size of Fe^0 core 1 nm	(Yan et al. 2012)
nZVI (RNIP-10DS) purchased from Toda Kogyo Corp., Japan	Pristine nZVI particles reacted with air under controlled exposure (4 to 50 mL/min for 24 h) or rapid atmosphere exposure for 5 min; powder diffraction in ambient air	Fe^0, magnetite (Fe_3O_4) and maghemite (r-Fe_3O_4); not quantified	Intensities of the Fe^0 peaks for the modified particles were weaker than those for pristine nZVI particles due to transformation of Fe^0 to magnetite and maghemite	(Kim et al. 2010)
Lab made nZVI from FeCl₃ through borohydride reduction	nZVI particles synthesised under aqueous ethanol conditions (0, 30, 70, 90, and 100% by volume); powder diffraction in ambient air	Fe^0, iron oxides (magnetite and maghemite) and iron hydroxides (lepidocrocite, bernalite, akaganéite, and goethite); not quantified	Increasing ethanol concentrations provided gradually decreasing particle sizes (20 – 50 nm in no ethanol, 10 – 30 nm in 30% ethanol, 10 – 20 nm in 70% ethanol, 5 – 20 nm in 90% ethanol and 2 – 5 nm in 100% ethanol) and irregular amorphous structure	(Wang et al. 2009)
nZVI purchased from Nanostructured and Amorphous Materials, Inc. (Houston, TX)	nZVI reacted with dithionite (0.2, 0.9, 1.8 and 3.7 g dithionite/g of nZVI); powder diffraction in ambient air	Fe^0, lepidocrocite and magnetite; not quantified	High dithionite concentration caused green rust formation	(Xie and Cwiertny 2010)

Lab made nZVI from FeCl$_3$ through borohydride reduction	nZVI synthesised in aqueous ethanol solutions (70 or 90% ethanol by volume); powder diffraction in ambient air	Fe^0 and iron oxides; not quantified	Appearance of broad α-Fe^0 peak due to short range order structure (amorphous)	(Wang et al. 2009)
Lab made nZVI from FeCl$_3$ through borohydride reduction	Surfactant (Tween®80) modified nZVI (2 mg) reacted with trichloroethylene (TCE) (20 mL of 29 mg/L); powder diffraction in ambient air	Fe^0 and γ-Fe$_2$O$_3$; not quantified	Reaction with TCE caused disappearance of Fe^0 peak and prominence of γ-Fe$_2$O$_3$ peak	(Lee et al. 2009)
Lab made nZVI from FeCl$_2$ through borohydride reduction	nZVI particles sprinkled on to adhesive carbon tapes supported on metallic disks	Fe^0, Fe$_3$O$_4$ and γ-Fe$_2$O$_3$; not quantified	Fresh nZVI provided prominent Fe^0 peak, oxide peaks dominated with ageing of the sample	(Karabelli et al. 2008)
Lab made nZVI from FeCl$_3$ through borohydride reduction and commercial nZVI product from Kanto Chemical Co., Inc., Japan	nZVI (50 g/L) reacted with As (III) (100 mg/L) in 0.01 M NaCl for 1 – 60 days; powder diffraction in ambient air	Fe^0, magnetite/maghemite (Fe$_3$O$_4$/ɤ-Fe$_2$O$_3$), lepidocrocite (ɤ-FeOOH); not quantified	Reactions provided a mixture of amorphous Fe-oxide/hydroxide (Fe (II) and Fe (III)) as the corrosion products of nZVI; crystalline magnetite and lepidocrocite replaced amorphous phases over 2 months period	(Kanel et al. 2005)
Lab made nZVI from FeSO$_4$ through borohydride reduction facilitated by dispersant polyvinylpyrrolidone	Powder diffraction in ambient air	Fe^0	Only evidence of Fe^0 formation shown; broad Fe^0 peak appeared due to amorphous structure	(Fang et al. 2011)
Lab made nZVI from FeSO$_4$ through borohydride reduction	nZVI (20 g/L) reacted with trinitrotoluene (TNT) (around 3 g/L) for 1 h; powder diffraction in ambient air	Fe^0 and magnetite/maghemite (Fe$_3$O$_4$/ɤ-Fe$_2$O$_3$); not quantified	nZVI corrosion products consisted a mixture of Fe$_3$O$_4$ and ɤ-Fe$_2$O$_3$	(Zhu et al. 2012)

nZVI purchased from Tianjin Kermel Chemical Co., Ltd., China	nZVI (3 g/L) reacted with acid orange II (100 mg/L) at pH 3.0, 7.0 and 11.0; powder diffraction in ambient air	Fe^0 and lepidocrocite; not quantified	Ferric hydroxides (lepidocrocite – FeOOH) formed on the surface of the reacted nZVI powder	(He et al. 2013)
Lab made nZVI from FeSO$_4$ through borohydride reduction	nZVI stabilised with polyacrylic acid and polyvinylpyrrolidone; powder diffraction in ambient air	Fe^0, FeOOH and FeO; not quantified	Polymer stabilised nZVI showed no iron peak due to amorphous and non-crystalline nature	(Esfahani et al. 2013)
nZVI (Nanofer 25 and Nanofer 25S) purchased from NANOIRON® Company, Czech Republic, EU	Nanofer 25 (150 mg/L) reacted with As (V) (5 mg/L) at pH 5 and 9 for 90 min and aged for 30 and 60 days; powder diffraction in ambient air after freeze drying	Fe^0, magnetite/maghemite, lepidocrocite, hematite in Nanofer 25; not quantified; no obvious peak for iron oxide appeared in the XRD profile of Nanofer 25S	Hematite formed at pH 5, but not at pH 9; lepidocrocite and magnetite/maghemite were the main corrosion products after 30 days, whereas lepidocrocite predominated after 60 days	(Dong et al. 2012)
Lab made nZVI from FeCl$_3$ through borohydride reduction	nZVI (50 g/L in 0.01 M NaCl at pH 7) reacted As (V) (100 mg/L) for 7, 30, 60 and 90 days; powder diffraction in ambient air	Fe^0, magnetite/maghemite, lepidocrocite; not quantified	Appearance of magnetite/maghemite and lepidocrocite and appearance of amorphous region in the expense of Fe^0 peak after 7 days of ageing; sharp crystalline peaks of lepidocrocite and magnetite/ maghemite appeared after 30 days; lepidocrocite disappeared after 60 days onwards	(Kanel et al. 2006)

Lab made nZVI from FeCl₃ through borohydride reduction	Surfactant (Tween 20) stabilised nZVI; powder diffraction in ambient air	Fe^0; no other peak identified	Surfactant stabilised nZVI showed peak broadening due to surfactant artefact	(Kanel et al. 2007)
Lab made nZVI by evaporation of Fe in tungsten (W) boat at 1773° K under He environment (133 Pa)	nZVI treated under different residual vacuum pressures and temperatures; powder diffraction in ambient air	Fe^0, γ-Fe_2O_3 and/or Fe_3O_4; not quantified	Presence of oxide species at the surface of the passivated nanocrystalline powders	(Rojas et al. 2004)
Lab made nZVI from FeCl₃ through borohydride reduction	Powder diffraction of ethanol stored sample in ambient air	Fe^0 and FeO; not quantified	Broad peak due to amorphous Fe^0 and sharp peak due to crystalline FeO observed	(Sun et al. 2006)
Lab made nZVI from FeCl₃ through borohydride reduction	Powder diffraction in ambient air	Fe^0, hematite and magnetite; not quantified	Freshly prepared sample showed only Fe^0 peak; oxides peak appear after 2 months of ageing; oxides could not be quantified due to limitation of detection limit	(Üzüm et al. 2008)
Lab made nZVI from FeSO₄ through borohydride reduction with ultrasound assistance	Powder diffraction in ambient air	Fe^0 and FeO; not quantified	Ultrasound assisted synthesis provided more crystallinity to Fe^0	(Jamei et al. 2014)
Lab made nZVI from FeCl₃ through borohydride reduction	Powder diffraction in ambient air	Fe^0	Fresh nZVI with high reductive and adsorptive activity has low crystallinity of the metal phase and highly disordered iron oxides	(Zhang et al. 2013)

2.3.2.2   X-ray photoelectron spectroscopy (XPS)

X-ray photoelectron spectroscopy (XPS) is an ultra-high vacuum, surface sensitive technique in which a sample is irradiated with X-rays of known energy and the kinetic energies of emitted photoelectrons and Auger electrons are measured. Elements present are identified by the characteristic binding energies, of their atomic orbitals, and determined from Equation 1:

$$h\nu = BE + KE + \phi \tag{1}$$

where $h\upsilon$ is the incident X-ray energy, BE is the photoelectron binding energy, KE the measured kinetic energy of the emitted photoelectron and ϕ is an instrumental work function (energy loss).

Typical X-ray source energies are <2000 eV ($K\alpha$ line), with the commonest anodes being Mg (1253.6 eV) and Al (1486.6 eV), with monochromatic Al $K\alpha$ sources fitted to high (spectral) resolution instruments.

Useful for a wide range of materials and sample types (Baer and Engelhard 2010; Baer et al. 2010), XPS provides elemental concentration and, for many elements, chemical environment and/or oxidation state information in the top-most few nanometres of surfaces, whether organic (Kempson et al. 2003) or mineral with inorganic (Grano et al. 1997) or organic adsorbates (Grano et al. 1997). Surface concentrations of elements, relative to the bulk concentrations, can give valuable indicators of specific absorption of solution-borne species, while oxidation state may suggest potential impacts of redox changes, re-mobilisation and bioavailability. In the context of fine particles, the last is extremely important when examining toxicity (e.g. (Karakoti et al. 2006)). For particles such as ZVI, XPS can monitor surface composition and chemistry as a function of time and environmental exposure (Turner et al. 1984; Baer and Engelhard 2010; Baer et al. 2010). Through the use of ion

66

etching of surfaces and/or examination of photoelectron escape depths, information about the thickness of particle coatings, contamination or reaction layers may be gleaned (Venezia 2003; Baer et al. 2008; Baer and Engelhard 2010; Baer et al. 2010; Baer et al. 2012).

2.3.2.3   *X-ray adsorption spectroscopy (XAS)*

X-ray adsorption spectroscopy (XAS) uses synchrotron radiation to obtain information about the oxidation state, identity of nearest neighbours, bond length, coordination number and electronic configuration of an element of interest in virtually any sample (see (Grafe et al. 2014) for review). Using this technique the valence and chemical state of Fe on both the particle surface and in the bulk volume can be determined (Sun et al. 2006; Kim et al. 2010; Leveneur et al. 2011).

In an XAS experiment, the energy of the incident X-ray beam is progressively increased across the relevant range for the element of interest and the fluorescence signal is collected incrementally. This obviously requires a tunable energy source, hence the necessity of performing XAS investigations at synchrotrons. As the energy approaches the binding energy of the core electrons of the element of interest, the absorption of the incident beam progressively increases and so does the emitted fluorescence. XAS spectra are therefore generated by detecting and recording the absorption or fluorescence at each energy point. XAS spectra are typically divided into two parts: the X-ray adsorption near-edge structure (XANES) region extends from approximately -50 to +200 eV from the absorption edge and the X-ray adsorption fine structure (EXAFS) region extends to about 800-1000 eV above the absorption edge. XANES is particularly sensitive to the oxidation state of the element of interest and the electronegativity of the ligand(s) while the EXAFS portion of a spectrum contains information regarding the coordination chemistry of an element (e.g. identity and coordination number of surrounding atoms and inter-atomic distances).

One of the most important advantages of this technique is the possibility of speciation analysis in any sample under almost any environmental condition (without the need of separating the element of interest through an extraction procedure) (Prietzel et al. 2007; Feldmann et al. 2009). This is a particular advantage in the case of nZVI as samples can be analysed as slurries (or frozen) or as dry powders as long as they are mounted in a way that prevents their contact with oxygen. This is easily achievable by sandwiching the sample between two layers of a material such as polyimide, which is virtually transparent to the X-rays of interest.

On the other hand, the interpretation of XANES/EXAFS spectra can be very intricate and time-consuming in samples with complex mixture of chemical species, because the spectra obtained represent the weighted sum of all the species in the analysed volume (Lombi and Susini 2009). Consequently, the quantification of a very thin layer of oxidised Fe on the surface of nZVI particles, which is easily detected by XPS, would be difficult to quantify by XAS unless it represented at least a few percentage of the total Fe.

2.3.3   Characterisation of commercial products

To demonstrate some of the advantages and limitations of the major techniques described above we used them to characterise a number of commercial ZVI/nZVI products. Five different commercial products with different physicochemical properties, including three powders and two slurries, were examined. Major physical and chemical properties of the materials reported according to the manufacturers' specifications are shown in Table 2-6.

Table 2-6: Physical and chemical properties of commercial nanoparticles as reported by the manufacturers.

N#	Form	Colour	Fe content (%)	Density (gr/cm^3)	Particle Size (μm)	Sold as nZVI
P1	Powder	Black	98	7.87	0.1-0.25	Yes
P2	Powder	Dark grey	95.5	7.8	70-80	No
P3	Powder	Dark grey	99	7.87	5-50	No
S1	Slurry	Black	20	1.15-1.25	<0.1	Yes
S2	Slurry	Black	20	1.15-1.25	<0.1	Yes

All sample preparation steps for the following analyses were conducted under anaerobic conditions, and anaerobic conditions were also maintained during analysis as detailed below.

DLS analysis was attempted using a Nicomp 280 instrument. In order to improve the dispersion of the particles the samples were diluted up to 100 times in degassed milli-Q water and sonicated for 10-75 minutes. The samples were transferred under anaerobic conditions to cuvettes that were subsequently sealed to prevent oxidation during analysis. Despite the dilution and sonication steps, sedimentation of particles was visible in all samples during the analysis period. As DLS measurements are based on the Brownian motion of the particles, evidence of sedimentation indicated that this technique would not produce reliable or reproducible results for these materials (results not shown). In order to further investigate the true particle size the samples were then examined by SEM. Figure 2-12 shows SEM images of 2 commercialised ZVI products (i.e. one powder and one slurry). It is clear from these images that both products were dominated by micron scale aggregates rather than well dispersed primary particles.
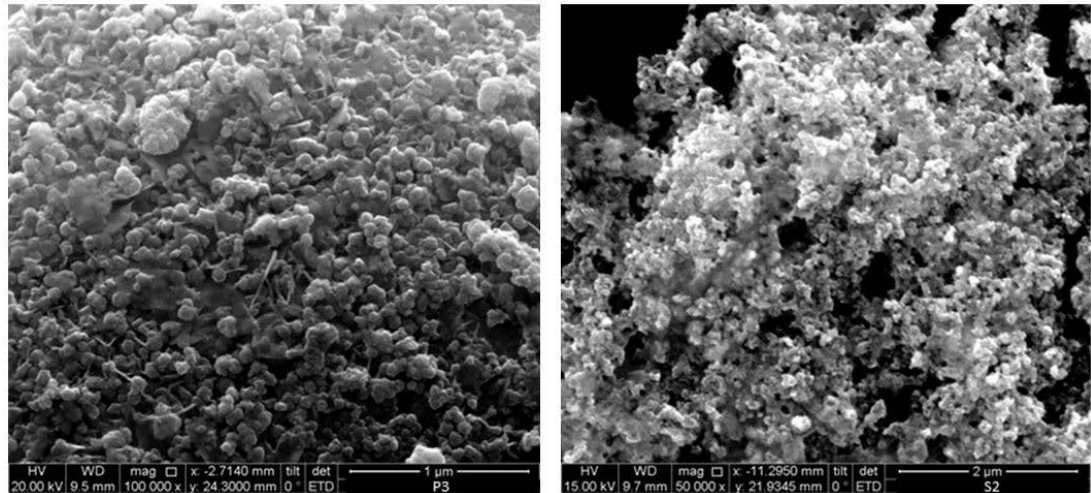
Figure 2-12: Examples of SEM images of commercialised ZVI samples at pH 2.

XRD analysis was conducted in order to assess the relative proportion of ZVI in the materials and the identity of any other major Fe species or Fe corrosion products. The XRD patterns were obtained by capping the samples (prepared under anaerobic conditions) with polyimide film in order to prevent oxidation during the analysis (Figure 2-13). The thickness of the polyimide film used was 8 μm, (note that thicker, 1 mm, polyimide film obscured the diffraction region of the sample at 2θ values 10 – 30°).
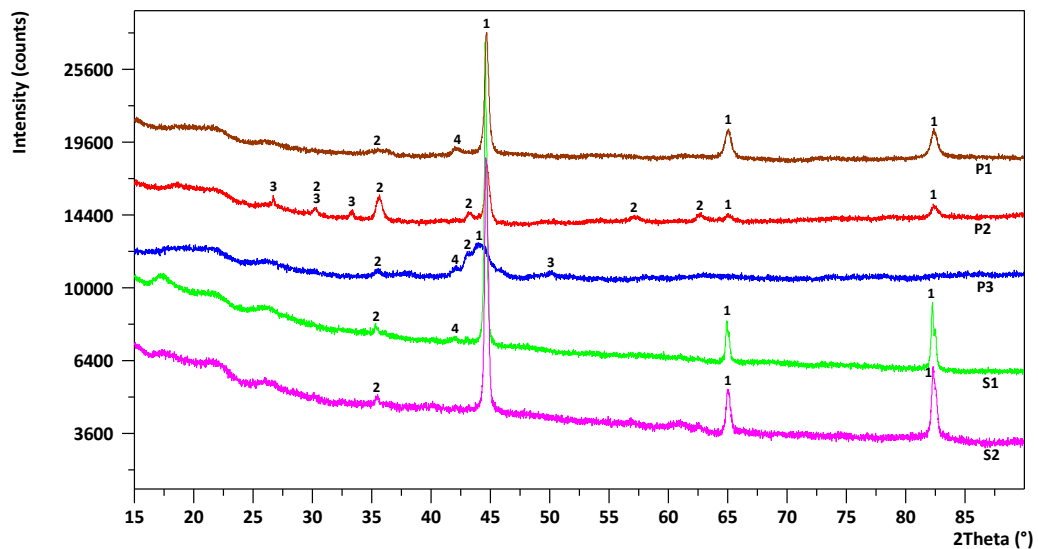
Figure 2-13: XRD patterns of commercial ZVI/nZVI particles. Numbers indicate peaks respective to iron phases; 1 – ZVI (Fe), 2 – magnetite (Fe$_3$O$_4$) and/or maghemite (ɣ-Fe$_2$O$_3$), 3 – lepidocrocite (ɣ-FeOOH), 4 – wuestite (FeO).

70

The XRD quantification results indicated a significant disparity in the contents of ZVI and iron oxide-hydroxide in the measured samples as compared to the values reported in the manufacturers' specifications (Table 2-7). The oxide and hydroxide phases of iron in the samples included magnetite (Fe_3O_4) and/or maghemite (γ-Fe_2O_3), lepidocrocite (γ-FeOOH) and wüstite (FeO) (Figure 2-13) (Kanel et al. 2005; Greenlee et al. 2012). Zero-valent iron is characterised by peaks appearing at 2θ values of 44-45°; 65-66° and 82-85° (Liu et al. 2005; Nurmi et al. 2005; Sun et al. 2006; Giasuddin et al. 2007; Lin et al. 2008; Wang et al. 2009; Wang et al. 2009; Xi et al. 2010). We note that the ZVI contents in some samples (P2 & P3) were remarkably less than that specified in the manufacturers' reports. This may be partly due to oxidation of ZVI particles occurring during storage and transportation.

Table 2-7: Iron content of the 5 commercial nZVI/ZVI products: Comparison between the manufacturers' data and XRD analysis.

Commercial nZVI	Form	Fe(0) as per manufacturer	Iron content analysed using XRD	
			Zero-valent Iron	Iron oxides/hydroxides (Fe(II), Fe (III))
P1	Powder	98	92	8
P2	Powder	95.5	47	53
P3	Powder	99	34	66
S1	Slurry	100	98	2
S2	Slurry	100	91	9

Figure 2-14 shows the Fe 2p photoelectron emission spectra of the five commercially-available ZVI particles obtained for this study. Once again, we note that these materials were prepared in an anaerobic chamber and an anaerobic transfer chamber was used to transfer the materials into the XPS instrument, thus preventing oxidation of the products prior to measurement. As can be seen, metallic Fe, Fe(0), was only present in the surface layers of samples S1 and S2. No Fe(0) was evident on the surfaces of the other three products. The majority of intensity contributions, however, derive from Fe(II) and Fe(III) associated with oxygen on all sample surfaces (Allen et al. 1974; Fiedor et al. 1998; Sun et al. 2006; Wang

et al. 2009; Baer et al. 2010; Leveneur et al. 2011), with P1, P2 & P3 all apparently identical in Fe oxidation product exposure.
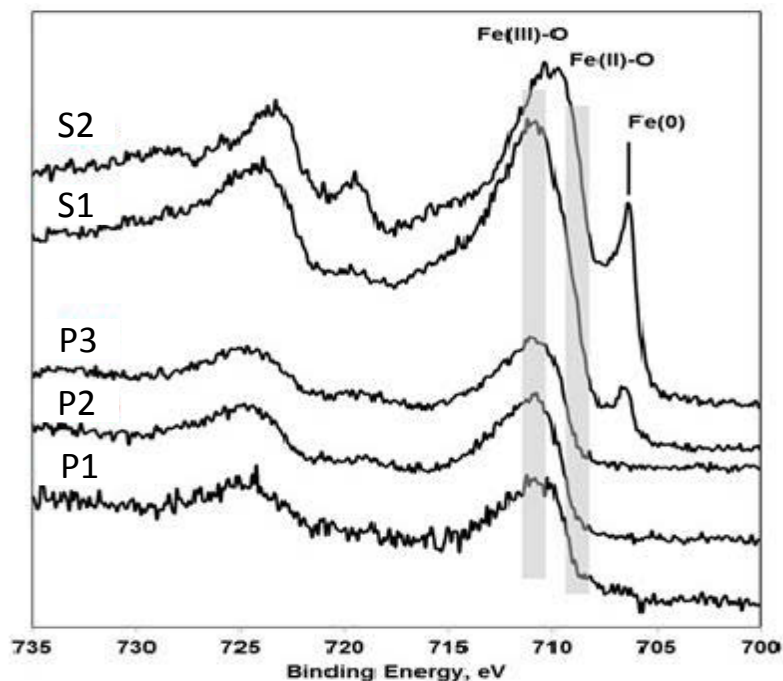
Figure 2-14: Fe 2p XPS analysis of commercialised ZVI particles.

XAS studies were conducted in quick-scan transmission mode at the Materials Research Collaborative Access Team (MRCAT) beamline 10-ID, Sector 10, at the Advanced Photon Source of the Argonne National Laboratory, U.S.A. The storage ring operated at 7 GeV in top-up mode. Calibration was performed by assigning the first derivative inflection point of the absorption K-edge of Fe metal (7112 eV), and each sample scan was collected simultaneously with an Fe metal foil. The collected spectra were analysed using the Athena software program in the computer package IFEFFIT (Ravel and Newville 2005) for data reduction and WinXAS 3.0 (Ressler 1998) for data fitting. The data were converted from energy to photoelectron momentum (k-space) and weighted by k3 using WinXAS. Linear combination fitting (LCF) was performed on the data using a dataset of reference spectra including metallic Fe as well as a number of iron oxy/hydroxides minerals. Furthermore, extended X-ray absorption fine structure spectra were calculated over a typical k-space range

72

with a Bessel window. Fourier transforms were performed to obtain the radial distribution function in R-space. Plotted R-space (Å) data are not phase shift corrected. The results of the LCF procedure (Table 2-8, Figure 2-15) indicated that most of the Fe was present in metallic form in samples P1, S1 and S2; with the remaining Fe in these samples present as magnetite and maghemite. In samples P2 and P3 most of the Fe was oxidised, with maghemite, magnetite and wuestite dominating the Fe speciation.

Table 2-8: Linear combination fitting of the XAS data for the 5 commercial nZVI/ZVI products tested. Species proportions are presented as percentages. Goodness of fit is indicated by the χ^2 value.

Commercial nZVI	Fe(0)	Magnetite	Maghemite	Lepidocrocite	Wuestite	χ^2
P1	79	12		9		0.0001
P2	49	15	36			0.0005
P3	24	28	8		40	0.0040
S1	85	15				0.0001
S2	76	8	8	8		0.0001
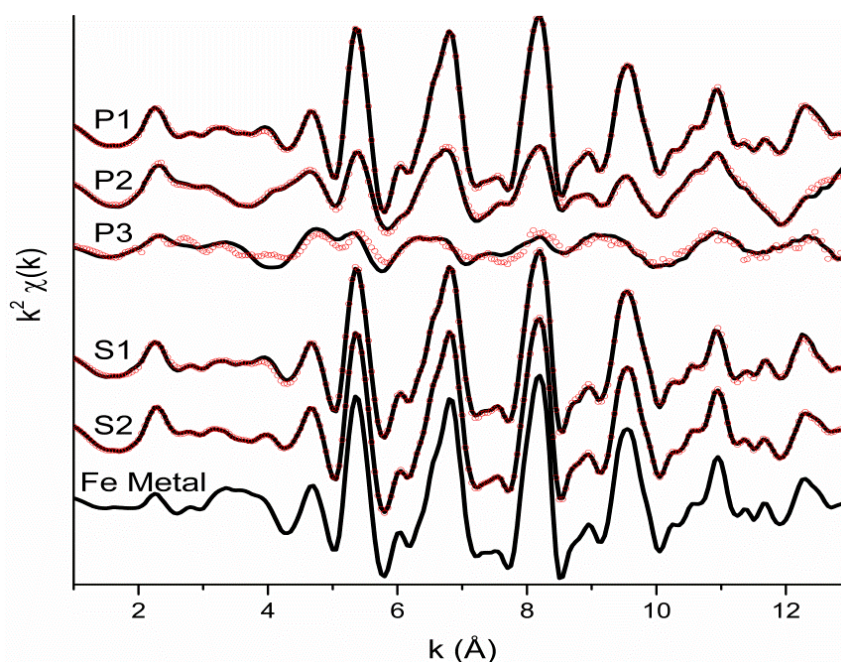
Figure 2-15: Normalised Fe K-edge k^3-weighted EXAFS of the 5 commercial nZVI/ZVI products tested. Dotted lines show the best 4-component linear combination fit of reference spectra as documented in Table 2-6.

Figure 2-16 shows the Fourier transformed radial distribution functions (RDFs) of the five samples and an iron metal foil. The fit data (Table 2-9) shows the coordination parameters of Fe in the samples. Metallic Fe is present in each sample and results of the Fe metal foil show

the basic parameters expected for Fe(0) with paths of Fe-Fe1 (CN: 8, R: 2.49Å), Fe-Fe2 (CN: 6, R: 2.87Å), Fe-Fe3 (CN: 12, R: 4.06Å), and Fe-Fe4 (CN: 24, R: 4.76Å), along with multi-scattering paths to accurately fit the spectrum. The fitting of the Fe metal foil involved fixing the CN of each path determined by *ab initio* calculations by FEFF8 and allowing atomic distance to float, resulting in R values close to theoretical calculations (Fe-Fe1 – 2.4855 Å; Fe-Fe2 – 2.8700 Å; Fe-Fe3 – 4.0588 Å; and Fe-Fe4 – 4.7594 Å). Despite LCF results indicating minor portions of Fe-III (oxy)hydroxides in samples P1, S1, and S2, the EXAFS fitting was unable to accurately fit components for Fe-III (oxy)hydroxides. The transformed RDFs represent the average of all signals in a given sample, which may inhibit identification of some low quantity phases. The results for samples P1, S1, and S2 indicate the presence of Fe(0) as the primary phase with CN and R values representative of the Fe metal foil and *ab initio* data noted above. Samples P2 and P3 added complexity to the fitting process with the presence of oxidized iron minerals. The LCF results of P2 indicate the presence of Fe(III) oxide minerals and Fe(0). The components of Fe(0) metal in P2 (Fe-Fe1; Fe-Fe2; Fe-Fe3; and Fe-Fe4) align well with parameters of the iron metal foil results. The Fe(III) mineral components of P2 yield an Fe-III-O path with CN of 6 at 1.94 Å and an Fe-Fe2 Oxide path with CN of 6 at 2.94 Å (Table 2-9). These fit parameters for the Fe(III) mineral components in P2 align well with *ab initio* calculation for LCF determined minerals of magnetite (FeIII-O – CN: 6, R: 2.00 Å; Fe-Fe2 Oxide – CN: 6, R: 2.89 Å), maghemite (Fe-III-O – CN: 6, R: 2.08 Å; Fe-Fe2 Oxide – CN: 6, R: 2.94 Å), and lepidocrocite (Fe-III-O – CN: 6, R: 1.99 Å; Fe-Fe2 Oxide – CN: 6, R: 3.04 Å). The LCF results for P3 indicate the presence of wuestite (Fe-II-O) in addition to Fe(III) oxide minerals and Fe(0). EXAFS fitting results (Table 2-9) for P3 demonstrate an additional path of Fe-II-O with a CN of 6 at 2.19 Å relative to P2, which supports the presence of wuestite (Fe-II-O – CN: 6, R: 2.15 Å). However, the Fe-Fe2 Oxide R value is larger than the 3.24 Å Fe-Fe bond distance in wuestite and larger than the average second shell Fe-Fe distance of the oxidize Fe minerals determined by LCF for P3 (magnetite, maghemite, and wuestite). Overall, the EXAFS fitting

results (Table 2-8) support the LCF information (Table 2-7) as well as visual evidence in Figure 2-16 where P1, S1, and S2 possess similar RDFs to the Fe metal foil. The Fe metal foil peaks are observable in P2 in addition to peaks associated with Fe-III (oxy)hydroxides. For P3, the Fe metal foil peaks are less obvious and the presence of wuestite yields an RDF that is different than that of the other four samples.
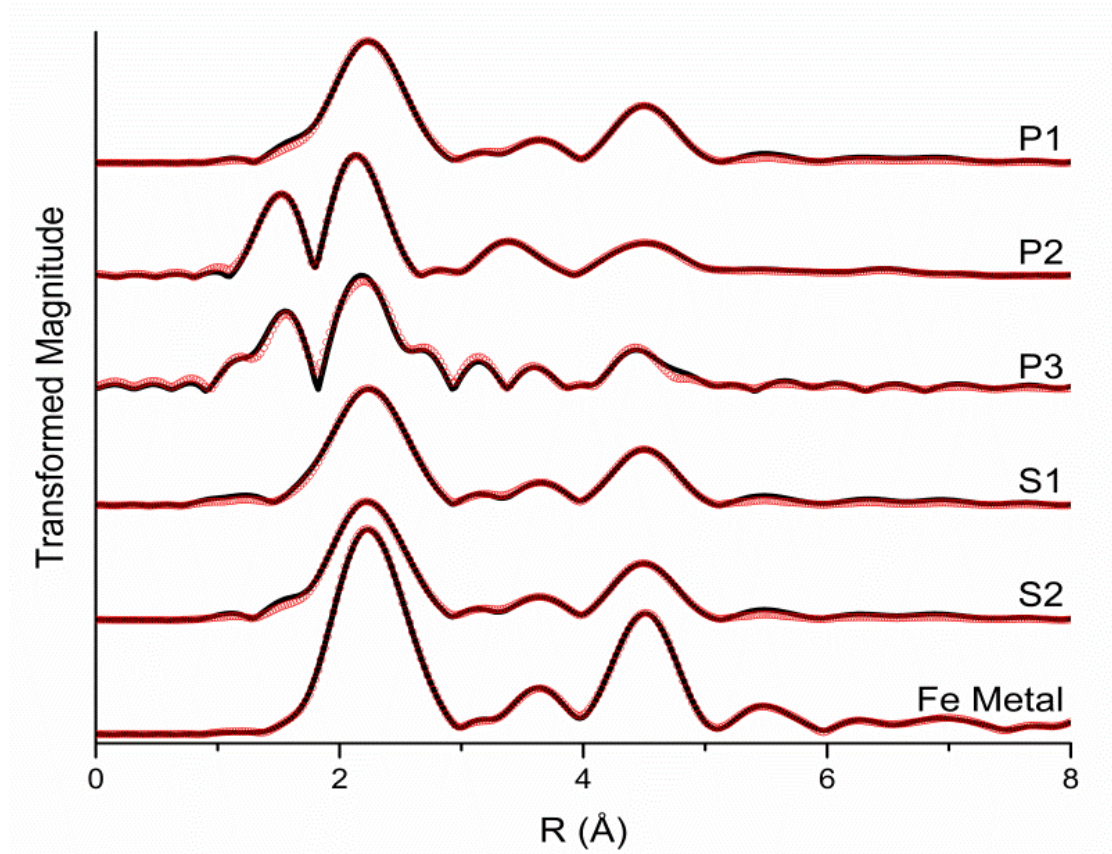
Figure 2-16: Fourier transformed radial distribution functions (RDFs) of the five samples and an iron metal foil. The black lines represent the sample data and the red dot curve represents the non-linear fitting results of the EXAFS data.

Table 2-9: Coordination parameters of Fe in the samples.

Sample	Energy shift DE (eV)	Shell	Coordination Number CN	Interatomic bond distance R (Å)	Debye-Waller factor s^2	Error R^2
P1	2.87	Fe-Fe$_1$	8	2.49	0.007	4.26
		Fe-Fe$_2$	6	2.84	0.012	
		Fe-Fe$_3$	12	4.10	0.011	
		Fe-Fe$_4$	24	4.79	0.007	
P2	1.19	Fe$_{III}$-O$_1$	6	1.94	0.013	4.75
		Fe-Fe$_1$	8	2.55	0.015	
		Fe-Fe$_{2\ Metal}$	6	2.79	0.002	
		Fe-Fe$_{2\ Oxide}$	6	2.94	0.003	
		Fe-Fe$_3$	12	4.04	0.013	
		Fe-Fe$_4$	24	4.73	0.017	
P3	1.44	Fe$_{III}$-O$_1$	6	1.97	0.018	5.76
		Fe$_{II}$-O$_1$	6	2.19	0.002	
		Fe-Fe$_1$	8	2.51	0.015	
		Fe-Fe$_{2\ Metal}$	6	2.72	0.016	
		Fe-Fe$_{2\ Oxide}$	6	3.32	0.021	
		Fe-Fe$_3$	12	3.99	0.020	
		Fe-Fe$_4$	24	4.83	0.030	
S1	1.91	Fe-Fe$_1$	8	2.49	0.006	5.47
		Fe-Fe$_2$	6	2.83	0.010	
		Fe-Fe$_3$	12	4.10	0.010	
		Fe-Fe$_4$	24	4.77	0.007	
S2	2.02	Fe-Fe$_1$	8	2.49	0.006	4.16
		Fe-Fe$_2$	6	2.84	0.012	
		Fe-Fe$_3$	12	4.10	0.011	
		Fe-Fe$_4$	24	4.78	0.007	
Fe Metal	1.02	Fe-Fe$_1$	8	2.49	0.003	2.37
		Fe-Fe$_2$	6	2.87	0.004	
		Fe-Fe$_3$	12	4.06	0.005	
		Fe-Fe$_4$	24	4.76	0.005	

These results indicate that in all cases the content of Fe(0) present in the materials was less than that reported by the manufacturers. However, in three cases (P1, S1 and S2) both XRD and XAS analysis showed that metallic Fe comprised the large majority of the materials with the rest composed of magnetite, maghemite and lepidocrocite. In the case of the S1 and S2 materials, XPS analysis showed that Fe(0) was present on the surface of the particles, while in the case of P1 the lack of a peak indicative of Fe(0) indicates that a continuous shell of oxidised Fe was present. In the case of P2 and P3, all techniques showed that oxidised forms of Fe were dominant both on the surface and in the core of the particles. This characterisation study clearly demonstrates the complementarity of the techniques employed, and shows the importance of a thorough characterisation not only for laboratory

experiments but also in the context of understanding the performance and characteristics of commercial materials proposed for use in field applications.

2.3.4 Analytical challenges for characterizing nZVI in real groundwater samples

To date, most nZVI studies have focused on the characterisation of freshly synthesised nanomaterials in simple matrices. However, the high reactivity of nZVI particles makes them highly dynamic in complex environmental systems such as groundwater (Lowry et al. 2012). Understanding their behaviour under environmental conditions is crucial for determining their long-term environmental fate and performance once they are injected into contaminated groundwaters. Furthermore, because of the large quantity of nZVI required for injection in remediation applications, risk assessment of these materials needs to be conducted, and this requires the measurement of nZVI in groundwaters.

At present, the direct measurement of engineered nanoparticles in the environment is still limited by significant analytical challenges (Gottschalk et al. 2010). In fact, the different characterisation methods described in this review can provide accurate information for "as-manufactured" nanoparticles in simple matrices but they all present significant limitations when it comes to the detection and quantification of ENPs in more complex samples (von der Kammer et al. 2012).

Various analytical techniques and experimental methods have been tested to predict the behaviour (i.e. aggregation/sedimentation/deposition, mobility and reactivity) of nZVI in groundwater. Some examples are given in Table 2-10. One simple approach consists of studying the individual or combined effects of different physical and chemical groundwater components (e.g. effect of a single electrolyte, pH, organic matter concentration etc.) in order to understand how these different factors can affect the mobility and reactivity of nZVI (e.g. (Tiraferri et al. 2008; Johnson et al. 2009; Raychoudhury et al. 2012; Xie and Cwiertny 2012; Yin et al. 2012; Adeleye et al. 2013; Dong and Lo 2013)). Results from these studies

are generally easily reproducible and can help in gaining quantitative data but they are only valid for the limited conditions examined in the experiments and cannot necessarily be extrapolated to predict behaviour in natural systems. A more realistic approach would be to investigate the behaviour of nZVI directly in natural groundwater samples. However, further research in this area is required, partly because this type of investigation faces significant analytical challenges.

Various field-scale studies of nZVI injection have been reported in the literature (Elliott and Zhang 2001; Quinn et al. 2005; Bennett et al. 2010; He et al. 2010; Wei et al. 2010; Johnson et al. 2013; Kocur et al. 2014) but due to a lack of appropriate analytical methods that can directly measure and detect nZVI on site, most field studies have relied on indirect methods to quantify nZVI transport and reactivity. For instance, both a decrease in ORP and a change in solution pH are widely reported upon nZVI injection, and this is seen as evidence of the presence of nZVI and its mobility. However, a recent study (Shi et al. 2011) showed that the interpretation from ORP measurements is quite complex as the response of ORP electrodes to nZVI suspensions is not linearly correlated to nZVI concentration. For instance, at low nZVI concentration (< 50 mg/L), the measured ORP likely represents a mixed potential including the contributions from nZVI, dissolved Fe^{2+} and H_2. ORP changes have also been reported as an indicator of nZVI reactivity. Elliot and Zhang (2001) reported a good correlation between TCE degradation and ORP reduction at the closest monitoring well from the injection point. However, this correlation was less obvious at monitoring wells located further away from the injection point, where a lag period of one to several days was observed between the ORP reduction and TCE decline. To circumvent the limitations of individual methods, Johnson et al. (2013) utilised a number of complimentary techniques to ensure that nZVI transport and reactivity were adequately characterised. They developed a spectrophotometric method combining visual inspection (i.e. change in colour), UV-vis absorbance measurements and the use of a tracer to directly quantify the transport of nZVI

as well as to detect any flow changes during the injection. They concluded that the use of indirect indicators such as ORP, DO or pH is only relevant when they are used to supplement direct characterisation methods.

Table 2-10: Examples of characterisation studies investigating the behaviour of nZVI in different aqueous media.
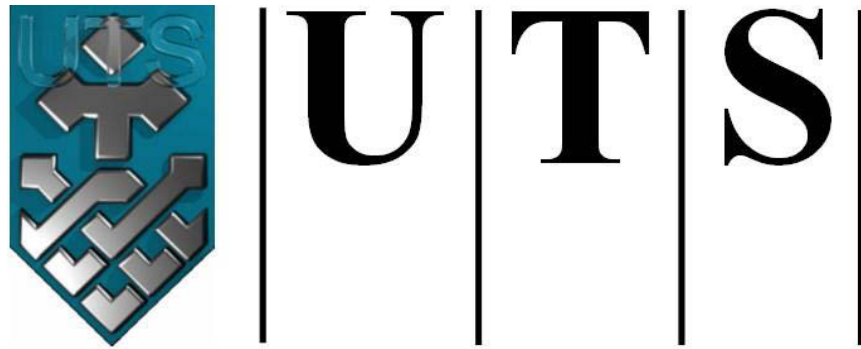
nZVI source	nZVI concentration	Environmental media	Analytical methods	Observation(s)	Ref.
One lab-made nZVI using the sodium borohydride reduction method and 2 commercial nZVI provided by NANOIRON Ltd. (NANOFER 25 and 25S)	150 mg/L	**pH 8.5**, **1-50 mgNaCl/L** for aggregation study; **Synthetic groundwater** with different concentration of humic acid for As/Cr desorption study	**Laser Light Scattering** (LLS) for aggregation study; **Atomic Absorption Spectroscopy** (AAS) for desorption study	Slight variations in particle size with increased ionic strength. Authors explained that the size measured by LLS is the size of the particles remaining in suspension (i.e. first measurement was only taken after 30 minutes) (rest of the particles sedimented in the cuvette). No information on the sedimented particles were provided (e.g. mass fraction).	(Yin et al. 2012)
Bare and guar gum-coated reactive nanoscale iron particle (RNIP) (Bare RNIP were provided by Toda Kyogo)	154 mg/L for aggregation study and 385 mg/L for sedimentation study	**pH 7.0, 10 mM NaCl, 0.5 M NaCl and 3 mM CaCl₂** for aggregation study; **pH 7.0, 100 mM NaCl and 3 mM CaCl₂** for sedimentation study	**Dynamic light scattering** (DLS) for aggregation study; **UV-vis spectrophotometer** for sedimentation study	During aggregation study, sedimentation of the larger aggregates (sedimentation rate of 0.27 mm/min calculated by the authors) likely affected the DLS measurement. Results from DLS and UV-vis measurements are not comparable since different concentrations were used. The electrolyte concentrations tested in this study were much higher than the ones found in groundwater.	(Tiraferri et al. 2008)
NANOFER 25S (PAA-coated nZVI) from NANOIRON Ltd. and Starch and Tween 20 coated nZVIs prepared in lab from commercial nZVI NANOFER 25 (NANOIRON Ltd)	100 mg/L	**0-20 mgHA/L** for aggregation study; **0-10 mgHA/L** for sedimentation study	**DLS** for aggregation study; **UV-vis spectrophotometer** for sedimentation study	Both aggregation and sedimentation studies showed enhanced stability of nZVI at higher HA concentration. A two-phase aggregation/sedimentation regime was observed with rapid sedimentation of large aggregates in the first few minutes followed by slow aggregation/sedimentation with time of the remaining particles in suspension.	(Dong and Lo 2013)

Source of nZVI	Concentration	Conditions	Analytical methods	Findings	Reference
NANOFER STAR, NANOFER 25S and NANOFER 25SS provided by NANOIRON Ltd.	3 g/L	The three commercial products were aged for 28 days in **NanoPure water, 10 mM CaCl$_2$, 100 mM CaCl$_2$ and one groundwater sample** under both anaerobic and aerobic conditions for each media	**Inductively coupled plasma atomic emission spectroscopy** (ICP-AES) for total iron concentration; **DLS** for particle size; **Colorimeter** to determine the ferrous ion concentration; **Oxidation-Reduction potential** (ORP) measured with a portable meter	A decrease in particles/aggregates size was observed in the supernatant over time. DLS only measured the smaller particles remaining in suspension while the larger aggregates quickly sedimented in the measurement cell. Reduction in particle size was also explained by the rapid oxidation of nZVI particles. Particles/Aggregates size as large as 7 μm was reported in this study which is far beyond the limit of detection of DLS (i.e. 5 μm).	(Adeleye et al. 2013)
Commercial nZVI powder provided by Nanostructured and Amorphous Materials, Inc.	2 g/L	nZVI suspensions were aged for 1 month in **5, 25 and 100 mN Cl$^-$, SO$_4^{2-}$ and ClO$_4^-$ and in 5 and 25 mN HCO$_3^-$ and NO$_3^-$**	**X-ray diffraction** (XRD) and **Transmission electron microscopy** (TEM) for mineralogy study	Both XRD and TEM results confirmed the development of corrosion products in aged samples with the formation of magnetite, carbonate green rust and iron carbonate hydroxide which resulted in decreasing the reactivity of nZVI toward different contaminants.	(Xie and Cwiertny 2012)
Lab-made CMC-nZVI using the sodium borohydride reduction method	200 mg/L	**0.1 mM and 10 mM NaHCO$_3$** for transport and deposition study	**AAS** for Fe concentration in the effluent samples	Increased ionic strength enhanced particle deposition of CMC-nZVI.	(Raychoudhury et al. 2012)
Lab-made PVP and PAA stabilised nZVI using the sodium borohydride reduction method	200 mg/L	**pH 7.5; 1, 10 and 100 mM NaCl**	**Scanning Electron Microscope** (SEM) and **Energy Dispersive X-Ray Spectrometer** (EDS) to determine the deposition mechanism of nZVI and **AAS** for Fe concentration in the effluent samples	Increased ionic strength enhanced aggregation and particle deposition of both polymer stabilised nZVI. SEM-EDS results confirmed the attachment of nZVI aggregates onto the sand grains.	(Esfahani et al. 2013)
Lab-made Pd/nZVI using the sodium borohydride reduction method	1.7 kg injected over a 2-day period	**Real field scale study in a TCE-contaminated site** (Trenton, New Jersey)	**ORP** and **pH** measured on site with a portable meter; **Certified analytical laboratory using US EPA standard protocols** for **total and dissolved iron, TCE and its daughter compounds** concentration	The TCE reduction observed on site correlated well with the change in ORP at the monitoring location close to the injection well. The correlation was less obvious for the monitoring points located further where a lag period of one to several days was observed between the ORP and TCE decline.	(Elliott and Zhang 2001)

Lab-made CMC-nZVI using the sodium borohydride reduction method	900 mgFe/L	**Field-scale study in a model aquifer**	Multi-method approach to monitor the **total and dissolved iron, dissolved oxygen** (DO), **specific conductance**, **pH**, **ORP**	Total unoxidized nZVI was only transported in the first meter and less than 2% of the total injected nZVI reached this distance. Conventional indicators used in field scale studies such as DO, ORP and pH may not necessarily measure the presence of nZVI.	(Johnson et al. 2013)
On-site synthesis of CMC-nZVI using the sodium borohydride reduction method	1 g/L	**Real field-scale study** (Sarnia, Ontario)	**Inductively coupled plasma-optical emission spectroscopy** (ICP-OES) for total iron concentration; **TEM** and **EDS** to characterise the change in nZVI before and after injection	After 10 days, only 1% of the total injected nZVI was detected from the monitoring well (1 m from injection well) which most likely indicated the deposition of particles on the subsurface porous medium. Measurements of total iron concentration after 48h is believed to be related to dissolved iron in low concentration rather than mobile iron nanoparticles. TEM-EDS measurements showed no morphological changes between the injected particles and the ones recovered from the monitoring well.	(Kocur et al. 2014)

2.4 Conclusions

A thorough understanding of nanoparticle fate and behaviour in the environment can only be achieved by ensuring that experimental results are always reported in conjunction with appropriate and detailed characterisation data. This requirement is not limited to experimental and laboratory work but extends to pilot and field scale remediation efforts. A large number of analytical techniques can be employed to determine the physico-chemical characteristics of these materials. While these techniques, especially when used in combination, can provide a thorough characterisation of nanomaterials, their detection, quantification and characterisation in the environment continue to pose considerable challenges that should be the focus of future research efforts.

University of Technology Sydney
FACULTY OF ENGINEERING

CHAPTER 3

MATERIALS AND METHODOLOGIES

3.1 Introduction

This chapter aims to describe the general experimental procedures carried out within the scope of this study, including materials and analytical methods used to characterise nanoparticles. Some experimental procedures and particular materials and analytical and theoretical methods which are only specific to some chapters are described in their respective chapters and not included in the present chapter.

3.2 Materials

3.2.1 Commercialised engineered nanoparticles

3.2.1.1 Iron oxide nanoparticles as a surrogate for nZVI

Commercially available α-Fe$_2$O$_3$NPs (20 wt. % dispersed in water at pH 4) were obtained from Sigma Aldrich Australia. The average particles size is about 30 nm (based on TEM measurements) and the specific surface area ranges from 50 to 245 m^2/g (as provided by the manufacturer). Their surface charge is positive at pH 4 and shifts to negative at pH above 7.5 (Figure 3-1). This nanoparticle was used as a surrogate for nZVI in Chapters 4, 5, 7 and 8. In fact, nZVI particles have been shown to have substantial shells of iron oxide (Phenrat et al. 2007). Therefore, Fe$_2$O$_3$NPs demonstrate various similar properties to nZVI when they are used to treat contaminated soil and groundwater and can thus be used as a model system for understanding behaviour in the environment (He et al. 2008).
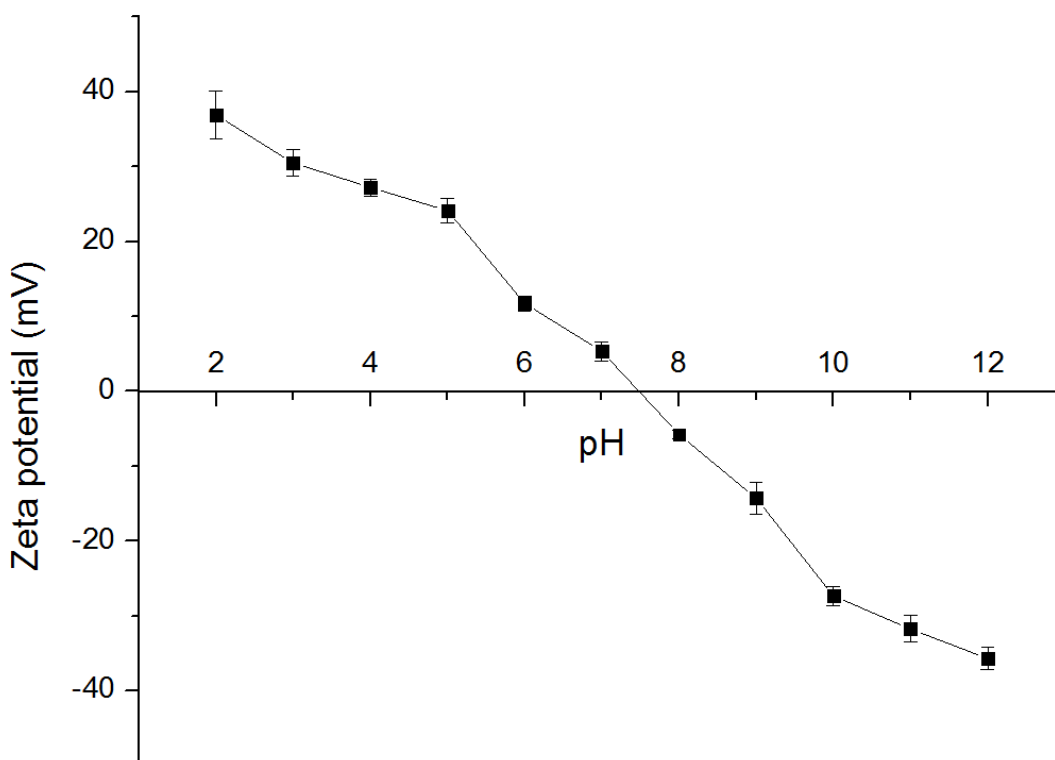
Figure 3-1: Zeta potential profile of Fe$_2$O$_3$ NPs dispersion (10 mg/L) as a function of pH.

3.2.1.2   Titanium dioxide nanoparticles

Commercial Aeroxide P25 TiO$_2$ NPs were obtained from the Evonik Degussa Corporation (Parsippany, NJ, USA). The mean particles size is around 30 nm and the specific surface area ranges from 47 to 52 m^2/g (as provided by the manufacturer). The surface charge of P25 is positive at pH values below 5.8 and negative at higher pH as shown in Figure 3-2. TiO$_2$ NPs were used in Chapters 7 and 8 in which a novel method was developed and optimised to characterise the aggregation behaviour and aggregate structure of ENPs in various natural waters. TiO$_2$ NPs were chosen among various ENPs as a recent study by Keller et al. (2013) showed that this nanoparticle was released to the environment in the largest quantities, followed by iron.
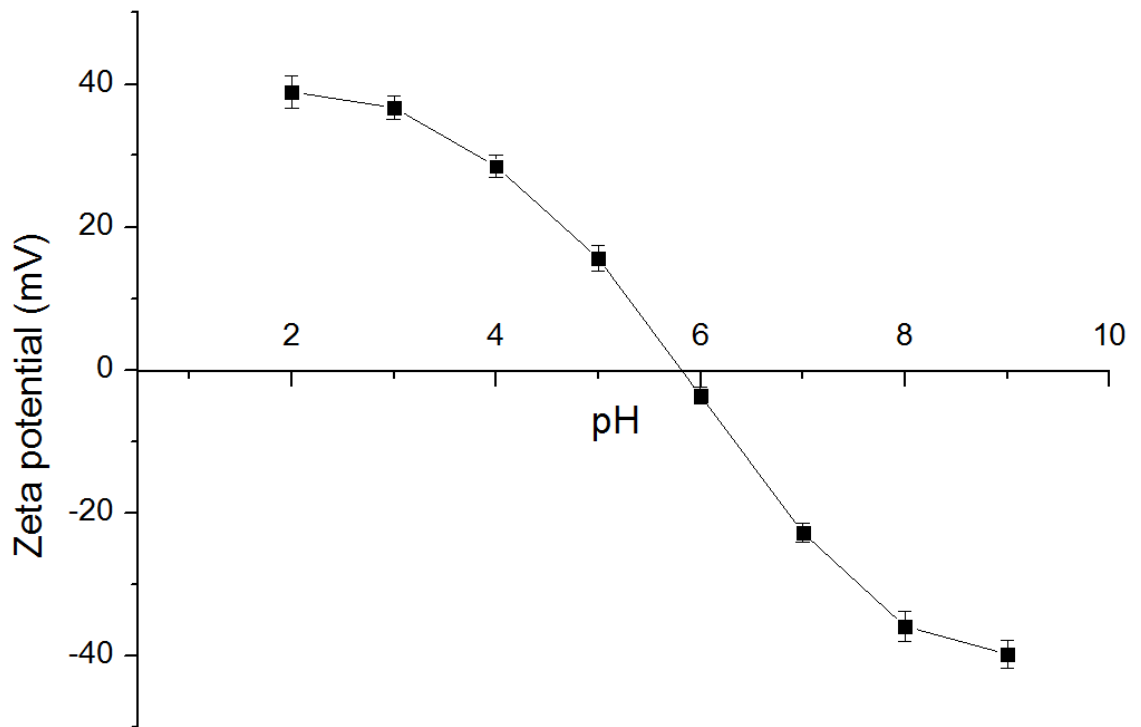
Figure 3-2: Zeta potential profile of TiO$_2$ NPs dispersion (12.5 mg/L) as a function of pH.

3.2.2 Chemicals

The list of chemicals used in this study for the preparation of solutions and reagents are gathered in Table 3-1.

Table 3-1: List of chemical used in this study.

Generic name	Purity (%)	Supplier	Main purpose
Calcium Chloride (CaCl$_2$)	99.9	Sigma Aldrich	Effect of divalent cation (i.e. Ca^{2+})
FL70	-	Fisher Scientific	FFF mobile phase to reduce interaction between FFF membrane and nanoparticles
Humic acid (HA)	-	Sigma Aldrich	Surrogate for natural organic matter (NOM)
Hydrochloric acid (HCl)	37	ANALAR, VWR	pH adjustment
Sodium azide (NaN$_3$)	99	Sigma Aldrich	Bactericide for FFF membrane
Sodium chloride (NaCl)	99.9	Sigma Aldrich	Effect of monovalent cation (i.e. Na$^+$)
Sodium hydroxide (NaOH)	97	Chem Supply	pH adjustment
Suwannee River Natural Organic Matter (SRNOM)	-	IHSS	Surrogate for natural organic matter (NOM)

3.3 Analytical methods for the characterisation of nanoparticles

3.3.1 Flow Field-Flow Fractionation

FlFFF is a chromatography-like separation technique based on laminar flow (so-called channel flow) in a very thin (i.e. ~250 μm) channel with a cross flow applied perpendicular to the channel flow. The channel flow has a parabolic velocity profile (i.e. the maximum velocity is at the centre of the channel). The cross flow forces the particles to move toward a membrane at the channel wall, from where they can move back into the channel as a result of diffusion forces in the *normal* elution mode (i.e. for particles smaller than 1 μm). The smallest particles, having the highest diffusion coefficient, will migrate farther into the channel at higher flow rates and will thus elute first. The theory and principles of FlFFF can be found elsewhere (Giddings 2000; Phuntsho et al. 2011).

There are two major FlFFF techniques: Symmetrical FlFFF (sFlFFF) and Asymmetrical FlFFF (AsFlFFF) which can be differentiated by the way that the perpendicular crossflow is produced (Kammer et al. 2011). In this study, we used two different AsFlFFF systems.

In the AsFlFFF setup (Figure 3-3), the top wall of the channel is impermeable and generally made of a transparent glass plate and the crossflow is generated by an excess flow rate at the channel inlet. The shape of the AsFlFFF channel is trapezoidal, in contrast to the ribbon-like shape of the sFlFFF channel, in order to avoid constant loss of axial flow occurring with the transport of carrier liquid along the channel (Litzen and Wahlund 1991). The sample injection is followed by a focusing step where a well-balanced opposing flow is generated from the inlet and outlet of the channel.
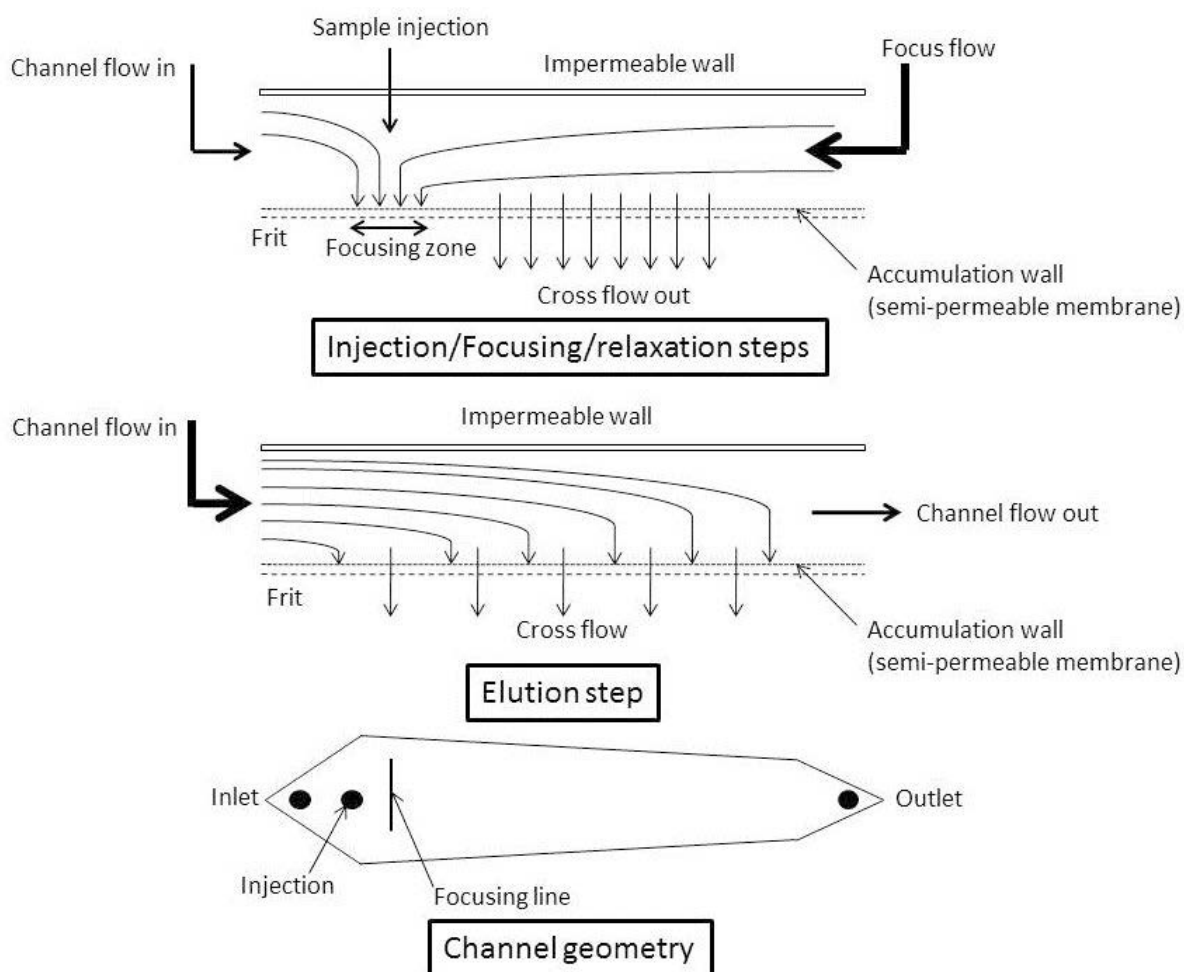
Figure 3-3: Schematic representation of AsFlFFF flow schemes: injection, focusing and relaxation steps (top), elution step (middle) and trapezoidal shape channel geometry (bottom).

AsFlFFF is one of the preferred systems today (Kowalkowski et al. 2006). In fact, this technique provides several advantages over sFlFFF. First the transparent top-wall allows checking the channel contents and the flow streams, especially when using coloured polymers. Secondly, the channel handling and membrane replacement are simpler. Then, thanks to the focusing step, sample volume does not have any effects on the fractionation and the fractionation resolution is better. Finally, this technique provides better detection limits due to less sample dilution and there are lower risks of contamination from the bottom frit when it is coupled to other detectors (Baalousha et al. 2011). However, there are still some drawbacks, including irregular separation behaviour started with particles having

diameters above 500 nm, more complex fractionation theory and potential contamination from previous runs during the focusing step especially when using old membrane.

In this study, two different FlFFF systems were used. FlFFFa was an asymmetrical AF2000 Focus (Postnova Analytics, Germany) with channel length of 29.8 cm (tip to tip), channel width of 2 cm and channel thickness of 0.025 cm as shown in Figure 3-4. The detection system comprised a UV/Vis detector operating at a 254 nm wavelength (SPD 20A from Shimadzu, Japan). The software AF2000 Control, version 1.1.0.23 (Postnova Analytics) was used to control the FlFFF system. A regenerated cellulose membrane (Z-AF4-MEM-612-10KD, Postnova Analytics, Germany) with a molecular weight cut-off of 10 kDa was used as a channel wall. Sodium azide (0.1 mM) was used as bactericide in the mobile phase for all experiments. The sample volumes were all 20.8 µL and were injected using 50 µL sample loop (Rheodyne Corporation, CA, USA).
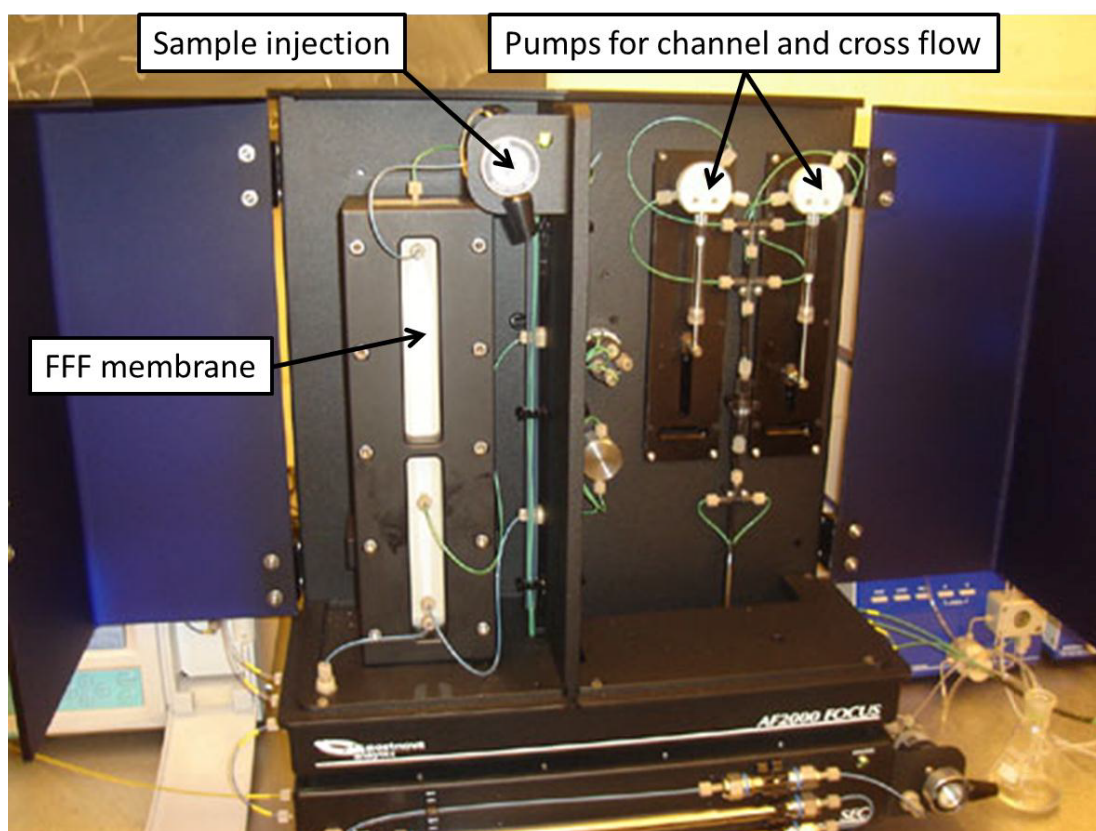
Figure 3-4: Schematic picture of one of the FlFFF systems used in this study.

The second FlFFF system, FlFFFb, consisted of an Eclipse 3+ system (Wyatt Technology, Dernbach, Germany) with channel length of 26.55 cm (tip to tip) and channel thickness of 0.035 cm, equipped with an Agilent 1200 HPLC system (Agilent technologies, Santa Clara, CA, USA). The Agilent 1200 HPLC system comprised an in-line degasser and an autosampler for the delivery of the carrier liquid and the injection of samples. A regenerated cellulose membrane (Millipore PLGC, 10KD, Wyatt Technology, Dernbach, Germany) with a molecular weight cut-off of 10 kDa was used as a channel wall. The on-line detection system for eluted particles consisted of a UV/Vis absorbance diode array detector (DAD1200, Agilent Technologies) with a spectral range from 190 nm to 950 nm and a quasi-elastic light scattering detector (QELS, Dawn HELEOS II, Wyatt Technology Corporation, Santa Barbara, CA) operating at a wavelength of 658 nm. The software ChemStation, version B.04.02 SP1 (Agilent Technology) was used to control the delivery flow of the FlFFF system. Data acquisition and data processing were done using Astra, version 6.0.2 software (Wyatt Technology).

Latex beads of 22 nm, 58 nm and 100 nm (Postnova Analytics, Germany) were used to create calibration curves from which hydrodynamic diameters of the particles were determined. These curves correlated the retention time to particle size. Calibration curves were regularly (i.e. once a week) re-drawn to check the accuracy of data. An example of calibration curve can be found in Figure 3-5.
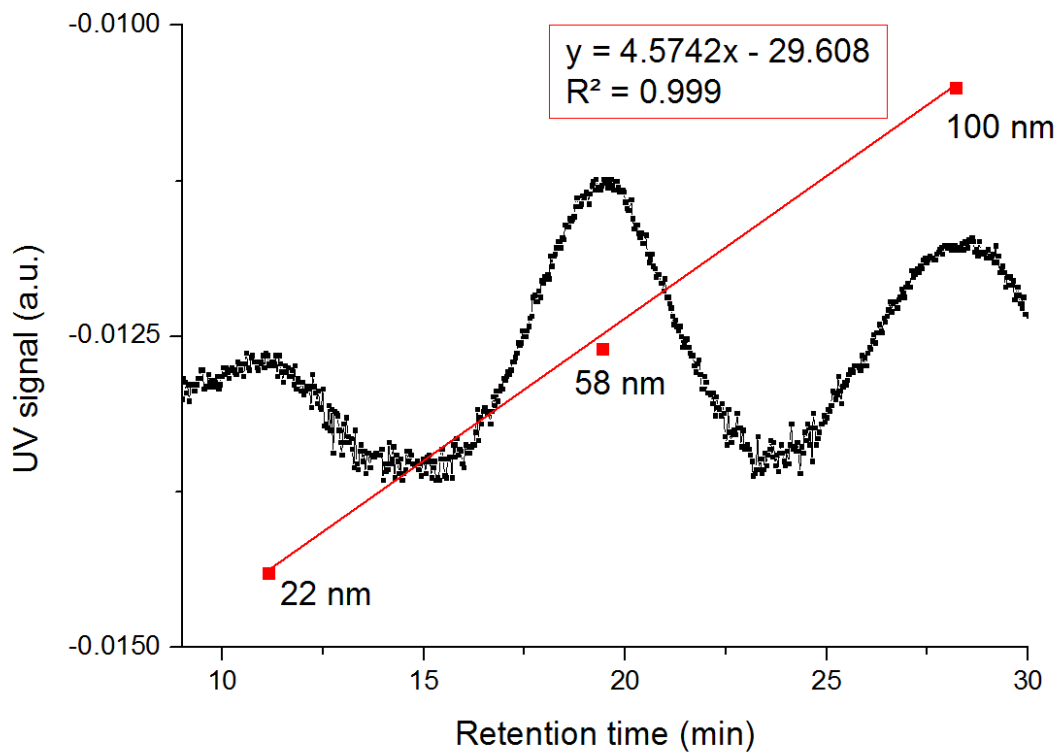
Figure 3-5: Example of FFF calibration curve using latex beads of 22, 58 and 100 nm as standard materials.

3.3.2   Dynamic light scattering

Dynamic light scattering technique measures the diffusion coefficient of particles by correlating the fluctuations of the scattered light intensity over time as shown in Figure 3-6. These fluctuations come from the Brownian motion of the particles and from the fact that neighbouring particles can have constructive or destructive interference of the scattered light intensity in a certain direction (Hassellöv et al. 2008). The Z-average hydrodynamic diameter can then be calculated by applying the Stokes-Einstein equation. Detailed information on this method, including physical principles, mathematical models, and limitations can be found elsewhere (Filella et al. 1997).
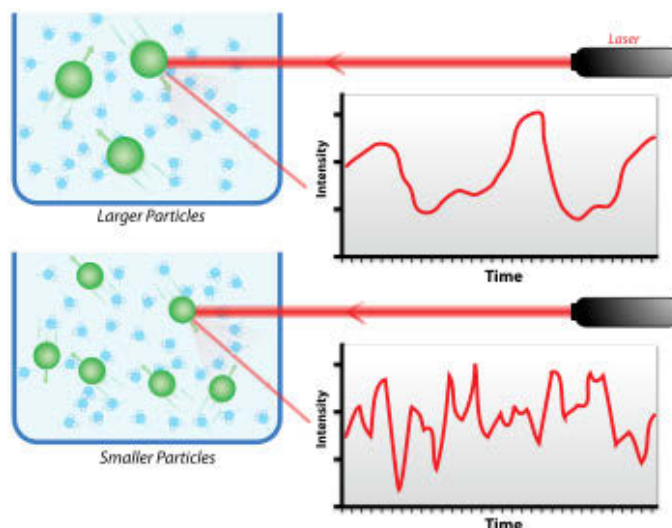
Figure 3-6: Principles of dynamic light scattering for the determination of particles hydrodynamic diameter.

A Zetasizer (model ZEN3600; Malvern Instruments, Worcestershire, UK) operating with a He-Ne laser at a wavelength of 633 nm was used in this study to determine both the zeta potential and hydrodynamic diameter of the different samples.

The measurement of zeta potential is achieved by a combination of laser Doppler velocimetry and phase analysis light scattering (PALS) in Malvern's patented M3-PALS technique. The instrument is a combination of an optical measurement unit and a computer that controls the measurement and allows data analysis and presentation. A blank consisted of ultrapure water (MilliQ, Millipore, USA) was run systematically before the samples to calibrate the instrument. Zeta potential was measured within the range of -50 mV to +50 mV.

3.3.3   Static light scattering

A static light scattering (SLS) instrument (Malvern Mastersizer 2000, Malvern Instruments, Worcestershire, UK) was employed in Chapters 7 and 8 to investigate the aggregate size and aggregate structure of different ENPs in natural waters.

The principle of Mastersizer 2000 is based on the laser diffraction technique to measure the size of particles in suspension. Laser diffraction measures the particle size distributions of a sample by measuring the angular variation in intensity of light scattered as a laser beam passes through a sample containing particles in suspension. Large particles will theoretically scatter light at small angles relative to the laser beam whereas small particles will scatter light at larger angles. The angular scattering intensity data is then analysed to calculate the size of the particles using the Mie theory (Mie 1976). The particle size is then reported as a volume equivalent sphere diameter.

The Malvern Mastersizer has also an array of photosensitive detectors positioned at different angles between 0.01° and 40.6° which detect the light scattered by the sample and enable the determination of the aggregate fractal dimension (FD). Previous studies have reported the determination of aggregate FD using a Mastersizer 2000 (Rieker et al. 2000; Jarvis et al. 2005; Zhao et al. 2012). The method is based on the fact that the total scattered light intensity I is related to the scattering vector Q and the FD (Gregory and Duan 2001):

$$I \propto Q^{-FD} \tag{1}$$

The scattering vector Q is the difference between the incident and scattered wave vectors of the radiation beam in the medium (Rieker et al. 2000):

$$Q = \frac{4n\pi \sin(\theta/2)}{\lambda} \tag{2}$$

where, n, λ and θ are the refractive index of the medium, the laser light wavelength in vacuum, and the scattering angle, respectively.

The floc structural information are obtained from the Mastersizer in the form of raw output data which are then converted to provide the angle of each detector and the intensity of light at each detector by use of a spreadsheet provided by Malvern Instruments (Malvern, UK).

The FD value equates to the slope of a linear regression line fitting a plot of I against Q values (on a log-log scale) measured at different angles as shown in Figure 3-7.
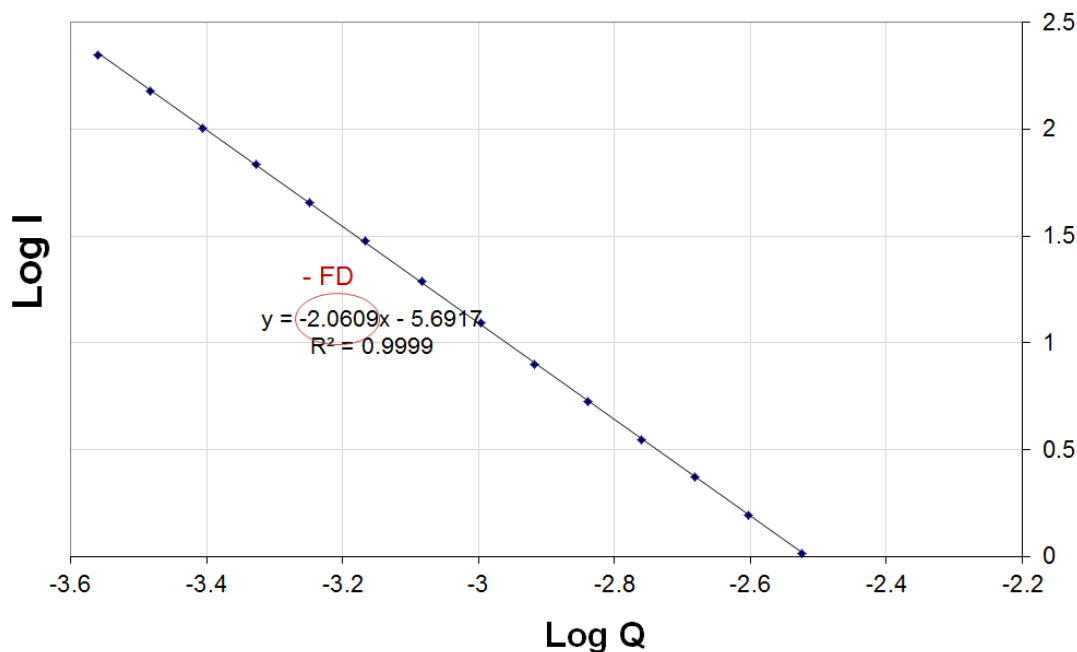
Figure 3-7: Relationship between the scattered light intensity (I) and the scattering vector (Q) on a log-log scale for the determination of the fractal dimension of ENPs aggregates.

Densely-packed aggregates will display a higher FD value, while lower FD values indicate linear and loosely bound aggregates.

3.3.4   Scanning electron microscope

Nanoparticle size distribution and shape were also obtained by performing Scanning Electron Microscopy (SEM) analysis. Images were obtained from a Zeiss Supra 55VP SEM operating at 15-20 kV (Carl Zeiss AG, Germany). Silicon wafers attached on carbon stubs were used for measurements.

Prior to imaging, about 10 μL of sample were deposited on a silicon wafer and left to dry completely. The samples were then placed in the vacuum chamber of the SEM and images

were recorded using SmartSEM® software. The mean equivalent circular diameters were
determined from these images from the analysis of at least 200 nanoparticles.

3.4   Other analytical methods

3.4.1   Total organic carbon analyser

A total organic carbon (TOC) analyser (Multi N/C 3100, Analytic Jena AG, Germany) was
used to determine the total carbon content of the samples. Prior to measurements, all
samples were filtered through 0.45 µm syringe filters. Therefore, the obtained values
represent the dissolved organic carbon (DOC) only. This instrument uses thermocatalytic
decomposition in the presence of a specific catalyst, with synthetic air used as a carrier gas.
Data were recorded and processed on a computer via the Multiwin software package
provided by the manufacturer. Standard DOC solutions were used to draw calibration curves
prior to measurement. An example of such calibration curve is given in Figure 3-8.

The plotted regression line shows:

$$y = 0.968x + 1.094$$
$$R^2 = 0.9988$$
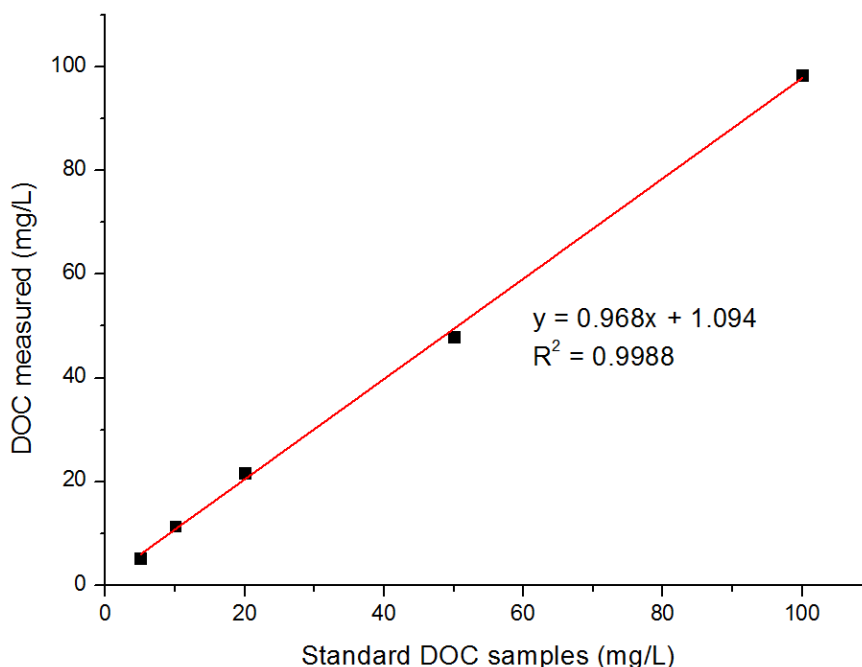
Figure 3-8: Example of calibration curve for TOC instrument.

For measurement, at least 10 mL of samples were placed in 30 mL vial in the auto-sampler (APG-64). Injection volume was set to 500 μL using a pre-selected TOC measurement method. The sample is pumped to the combustion tube, pyrolysed and oxidised within the carrier gas flow, which also acts as an oxidising agent, with the aid of the catalyst. The gas which is then formed (i.e. CO_2) is directed to the Non-Dispersive Infra-Red (NDIR) detector where a signal sequence is generated and used to obtain a time integral. This integral is proportional to the concentration of carbon in the sample. A previously determined calibration function (from the manufacturer manual) is then used to calculate the carbon content of the sample.

3.4.2 Ion chromatography

The concentration of the bromide tracer used in Chapter 6 as well as the ionic composition of the natural waters used in Chapters 7 and 8 was determined by the Metrohm ion chromatograph (790 IC) equipped with a Metrosep A Supp 5-150 (150 x 4.0 mm, 5 μm) column. The mobile phase consisted of 1 mM of sodium hydrogen carbonate and 3.2 mM of sodium carbonate, dissolved in Milli Q water. The injection volume was 5 mL and running time was 22 min per sample. The concentration of bromide and other major ions (e.g. Ca^{2+}, Mg^{2+}, Na^+, NO_3^-, SO_4^{2-}) was determined from a calibration curve that enables to convert the peak area (μS/cm.sec) to ion concentration (mg/L). An example of such calibration curve is given in Figure 3-9.
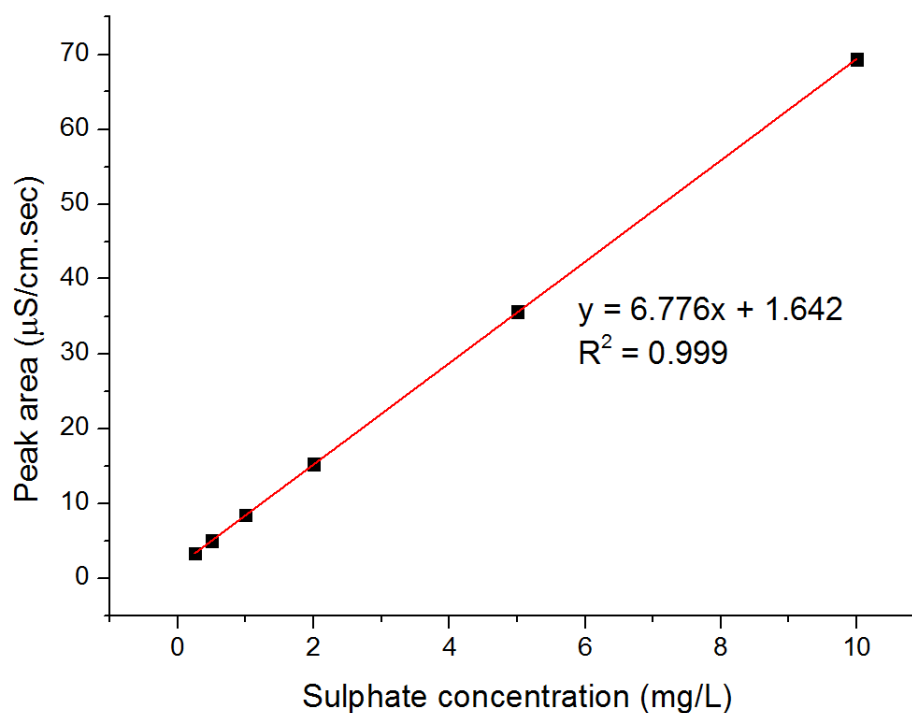
Figure 3-9: Example of IC calibration curve for SO$_4^{2-}$ anion.

3.5 Auxiliary laboratory instruments

The separation of the nanoparticles from the unadsorbed organic matter (i.e. HA or SRNOM – Chapters 5, 7 and 8) was achieved by centrifugation (Model 2040, Centurion Scientific Ltd, UK). The samples were placed in 50 mL conical centrifuge tubes (Axygen, SCT-50ML-R-S) and the centrifugation was carried out for 10 minutes at 3500 rpm.

The concentration of TiO$_2$ NPs in synthetic and natural water samples (Chapters 7 and 8) was determined by measuring the nephelometric turbidity (NTU) (2100P turbidimeter, Hanna, HI93414) as described by Battin et al. (Battin et al. 2009). The correlation between NTU and TiO$_2$ concentration is shown in Figure 3-10.
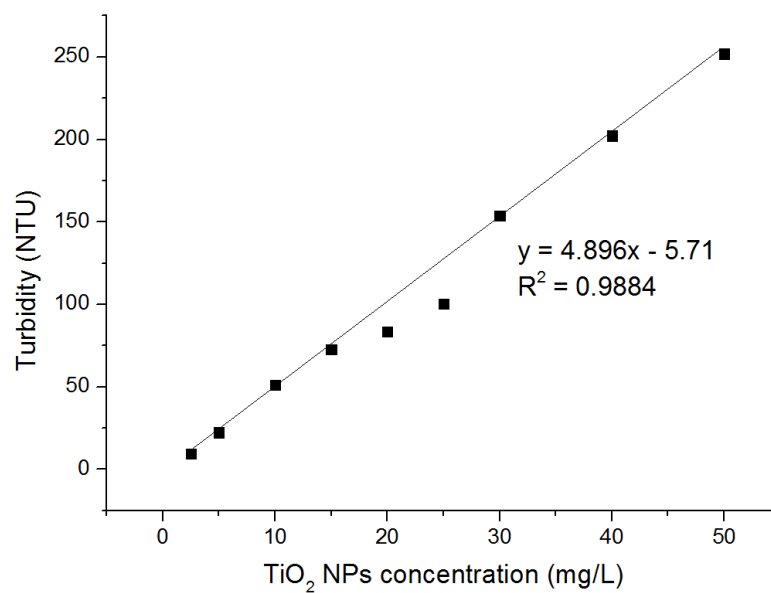
Figure 3-10: Correlation between turbidity (NTU) and TiO$_2$ concentration.

The pH of the solutions was monitored using a TPS 90FL pH meter (TPS Pty Ltd, Australia). The instrument was calibrated regularly using two buffer solutions: pH 6.88 (TPS 121380) and pH 4 (TPS 121382).
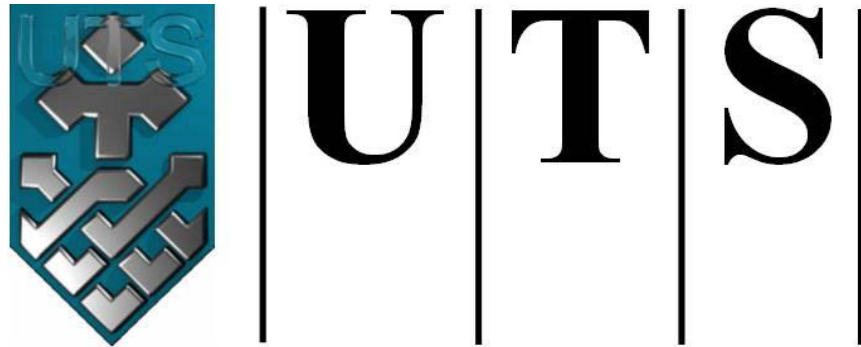
University of Technology Sydney
FACULTY OF ENGINEERING

CHAPTER 4

ASSESSING THE AGGREGATION BEHAVIOUR OF IRON OXIDE NANOPARTICLES UNDER RELEVANT ENVIRONMENTAL CONDITIONS USING A MULTI-METHOD APPROACH

4.1 Introduction

Due to their low cost, highly reactive surface sites and high *in-situ* reactivity, the most widely studied engineered nanoparticles (ENPs) for soil and groundwater remediation are nanoscale zero-valent iron (nZVI) (Wang and Zhang 1997; Elliott and Zhang 2001; Zhang 2003). Numerous studies have shown that nZVI are highly effective for the removal/degradation or stabilisation of a wide range of common environmental contaminants including chlorinated organic solvents (Elliott and Zhang 2001; Zhang 2003), organic dyes (Liu et al. 2005), various inorganic compounds (Alowitz and Scherer 2002), and even some metals(Kanel et al. 2005). In the past few years, a variety of iron oxide nanoparticles have also been investigated for environmental remediation purposes. Despite the potential efficacy of these materials, many laboratory and pilot-scale field studies have demonstrated that the mobility and reactivity of iron-based nanoparticles are substantially limited in natural porous systems (e.g. soils and groundwater aquifers) (Schrick et al. 2004; Quinn et al. 2005; He and Zhao 2007; Saleh et al. 2007). Aggregation is considered to be the primary cause of reduced mobility and reactivity, and this phenomenon is the result of many factors including solution pH, ionic strength and the presence of organic matter (Ponder et al. 2000; Saleh et al. 2005). In the case of iron-based nanoparticles, previous studies have demonstrated that these nanoparticles have pH-dependant surface charges and that extensive aggregation due to charge neutralisation occurs near the point of zero charge (PZC) (Sun et al. 2006; Baalousha et al. 2008; Baalousha 2009; Hu et al. 2010). Furthermore, soil and groundwater conditions are often characterised by high ionic strength and high concentrations of monovalent (e.g., Na^+, K^+) and divalent (e.g., Ca^{2+}, Mg^{2+}) cations in the mM range; factors that are known to reduce electrostatic repulsion between particles and thereby enhance aggregation (Saleh et al. 2008).

To optimise the use of ENPs for environmental remediation it is necessary to understand the factors that cause aggregation under environmentally relevant conditions with the aim of

enhancing their mobility while still maintaining good reactivity (Saleh et al. 2007). Surface modifications using charged polymers, polyelectrolytes or surfactants are now widely used to disperse nanoparticles in environmental matrices such as soil and water (Zhang et al. 1998; Schrick et al. 2004; Saleh et al. 2005; He et al. 2007; Saleh et al. 2007; Hajdú et al. 2009; Phenrat et al. 2009; Sirk et al. 2009; Cirtiu et al. 2011). These modifications can theoretically provide both electrostatic and steric (so-called electrosteric) stabilisation to prevent particles from aggregating and can also reduce the propensity for surface attachment (Saleh et al. 2005; Saleh et al. 2008). Unfortunately, although these different surface coatings can enhance nanoparticle stability, they can also be expensive, have toxic effects on the environment, and alter the interaction of ENPs with contaminants (Tiraferri et al. 2008). Natural surface coating by the adsorption of dissolved organic matter (DOM) such as humic and fulvic acids on the surface of nanoparticles has also been studied as an alternative "green" surface coating, and has been demonstrated to enhance nanoparticle stability through electrosteric stabilisation (Mylon et al. 2004; Illes and Tombácz 2006; Hu et al. 2010). The advantage of DOM over conventional surface modifiers is that DOM is ubiquitous in the environment, cheap, non-toxic, and not only has the ability to adsorb onto metal oxide nanoparticles but is also able to complex with heavy metals (Liu et al. 2008; Dickson et al. 2012). A recent study by Chen et al. (Chen et al. 2011) demonstrated that DOM–coated nZVI may significantly mitigate bacterial toxicity due to the electrosteric hindrance preventing direct contact.

In this chapter, characterisation of bare Fe_2O_3NPs and the aggregation behaviour of these nanoparticles under relevant environmental conditions (i.e. pH, particle concentration and ionic strength) were performed using flow field-flow fractionation (FlFFF), dynamic light scattering (DLS) and scanning electron microscopy (SEM). Although the characterisation of ENPs can be considerably simpler than it is for natural particle samples, ENPs are also complex, and a multiple characterisation approach is necessary to ensure the accuracy of the

characterisation data (Lead and Wilkinson 2006; Domingos et al. 2009). In fact, due to analytical challenges, the lack of appropriate characterisation data in environmentally realistic conditions is a major limitation of current research in this area. As such, there is clearly a need for useful characterisation tools that can assist in assessing ENP behaviour under relevant environmental conditions. Flow field-flow fractionation (FlFFF) is well suited to measuring ENP behaviour under relevant conditions simply by modifying the mobile phase used during characterisation. However, one of the main limitations of FlFFF is related to material losses during analysis. These generally occur via particle-membrane interaction and adsorption and may represent up to 50% of the injected mass (Hassellöv and Kaegi 2009). The particle-membrane interaction is mainly due to attractive forces (e.g. Van der Waals), hydrophobic and charge interactions which are all dependent on the mobile phase characteristics.

This is the first time that FlFFF has been applied to study the aggregation behaviour of Fe_2O_3NPs under relevant environmental conditions. The results have been compared with those from other size-measurement techniques and theoretical models to provide increased confidence in the outcomes. The stability of the DOM-coated Fe_2O_3NPs was also assessed under relevant conditions using FlFFF and DLS. Although many studies have demonstrated that DOM-coated Fe_2O_3NPs can be stable under a wide range of pH and NaCl concentrations, there is a lack of data in regard to the effect of divalent cations, especially Ca^{2+}, which is known to complex easily with organic matter (Hong and Elimelech 1997).

This chapter is an extension of the research article published by the author in Water Research (Chekli et al. 2013).

4.2 Theoretical method: The DLVO theory

The Derjaguin–Landau–Verwey–Overbeek (DLVO) theory (Derjaguin and Landau 1941; Verwey 1947; Verwey and Overbeek 1948) was employed in this study to model the

interactions between Fe_2O_3NPs at different particle concentrations, pH and ionic strength. This theory provides the classical explanation for the stability of colloids in suspension. It states that the stability of nanoparticles can be explained by the sum (i.e. total interaction energy) of the van der Waals attractive forces (V_{vdw}) and the electrostatic repulsive forces (V_{el}). The total interaction energy (V_T) is experienced by a nanoparticle when approaches another particle, and determines whether the net interaction between the particles is repulsive or attractive (Zhang et al. 2008; Dickson et al. 2012).

DLVO calculations were performed according to the following equations (Elimelech et al. 1998):

$$V_{vdw} = \frac{-A}{6}\left[\frac{2R^2}{h(4R+h)} + \frac{2R^2}{(2R+h)^2} + ln\frac{h(4R+h)}{(2R+h)^2}\right] \tag{1}$$

$$V_{el} = 2\pi\varepsilon R\delta^2 ln[1 + e^{-kh}] \tag{2}$$

$$V_T = V_{vdw} + V_{el} \tag{3}$$

where A (J) is the Hamaker constant (1.10^{-9} J for iron nanoparticles (Phenrat et al. 2009)); R (m) is the radius of particles; h (m) is the distance between the surfaces of two interacting particles; $\varepsilon=\varepsilon_r\varepsilon_0$ is the dielectric constant where ε_r (78.54 for water at 25°C) is the relative dielectric constant of the medium and ε_0 ($8.85.10^{-12}$ C^2/J.m) is the permittivity in vacuum; δ, the zeta potential of the charged particles; k (1/m) is the reciprocal of the thickness of the double layer with $k=2.32\times10^9$ $(\Sigma C_i Z_i^2)^{1/2}$ where C_i is the concentration of ion, i, and Z_i is its valency value.

The following assumptions/measurements are used in this study:

(1) Particle diameter is 30 nm (average size of the primary particles provided by Sigma Aldrich).

(2) When not specified, ionic strength is assumed to be 1 mM NaCl. In fact, when no electrolytes are used (i.e. when using ultrapure water), equation 2 is reduced to zero and calculations cannot be performed.

(3) Zeta potentials are experimentally determined.

4.3   Experimental

4.3.1   Chemicals and reagents

Commercially available Fe_2O_3NPs (α-Fe_2O_3, average particle size 30 nm, BET 50-245 m^2/g, 20 wt. % dispersed in water at pH 4), humic acid (HA) (technical grade), NaCl and $CaCl_2$ (99.99% purity) were all supplied by Sigma-Aldrich Australia. HA was employed as a surrogate DOM since HA and more generally humic substances represent an important fraction of DOM in soils, surface and groundwater (Aiken et al. 1985) and have been demonstrated to play a key role in water quality for various pollutants such as trace metals and some organic compounds (Murphy et al. 1990; Maurice and Namjesnik-Dejanovic 1999).

4.3.2   Sample preparation

Fe_2O_3NPs were suspended in ultrapure water to obtain a set of solutions in the range 10-200 mg/L at pH 4 ± 0.1. Solution pH was adjusted using 0.1 M HCl and 0.1 M NaOH solutions and left for 24 hours to equilibrate, after which the pH was re-measured and adjusted if necessary for all experiments. No buffers were used in this study because they usually have a high ionic strength and thus may alter the surface chemistry of the Fe_2O_3NPs and enhance their aggregation (Baalousha 2009).

HA was dissolved in ultrapure water with a resistivity of 18 MΩ/cm (MilliQ, Millipore, USA) to obtain a stock solution with a concentration of 500 mg/L. This was then filtered

through a 0.45 μm filter using vacuum suction to retain only the 'dissolved' organic matter, and stored at 4°C prior to experimental use. The total organic content (TOC) of the stock solution (dilution 1:10) was measured as 19.1 mgC/L using a TOC analyser (Multi N/C 3100, Analytic Jena AG, Germany).

HA-coated Fe_2O_3NPs were prepared by mixing 10 mL of concentrated Fe_2O_3NPs (i.e. 2 g/L) with either 1, 2, 4, 10 or 20 mL of HA (initial concentration of the stock solution: 500 mg/L) for one hour before diluting in ultrapure water to obtain five solutions with Fe_2O_3NP concentration of 200 mg/L and HA concentration of 5, 10, 20, 50 and 100 mg/L. All solutions were then brought to pH 4 ± 0.1 using either 0.1 M HCl or 0.1 M NaOH and stored at 4°C for 24 hours before measurements were taken.

NaCl and $CaCl_2$ were also dissolved in ultrapure water to obtain stock solutions with a concentration of 500 mM. The stock solutions were filtered through a 0.45 μm filter using vacuum suction to avoid dust contamination before being used as the mobile phase in FlFFF experiments or to prepare samples for FlFFF and DLS measurements.

4.3.3   FlFFF analysis

Particle size analysis using FlFFF was carried out by following the methods described in Chapter 3. FlFFFa (Postnova Analytics, Germany) was used in this particular study. The final solution concentration of Fe_2O_3NPs for all FlFFF experiments was 50 mg/L for the aggregation study and 200 mg/L for the DOM coating stability study to give satisfactory separation and detection. These concentrations are necessary to ensure suitable detection by UV detectors because the sample becomes considerably diluted in the FlFFF channel during the elution stage.

Latex beads of 22 nm, 58 nm, 100 nm and 410 nm (Postnova Analytics, Germany) were used to create calibration curves from which hydrodynamic diameters of Fe_2O_3NPs were determined. These curves correlate the retention time to particle size. Calibration curves were established for all mobile phases and conditions (change in cross flow or channel flow) used in this study and regularly (i.e. once a week) re-drawn to check the accuracy of sizing. An example of the calibration curves used for the pH effect study can be found in Figure 4-1.
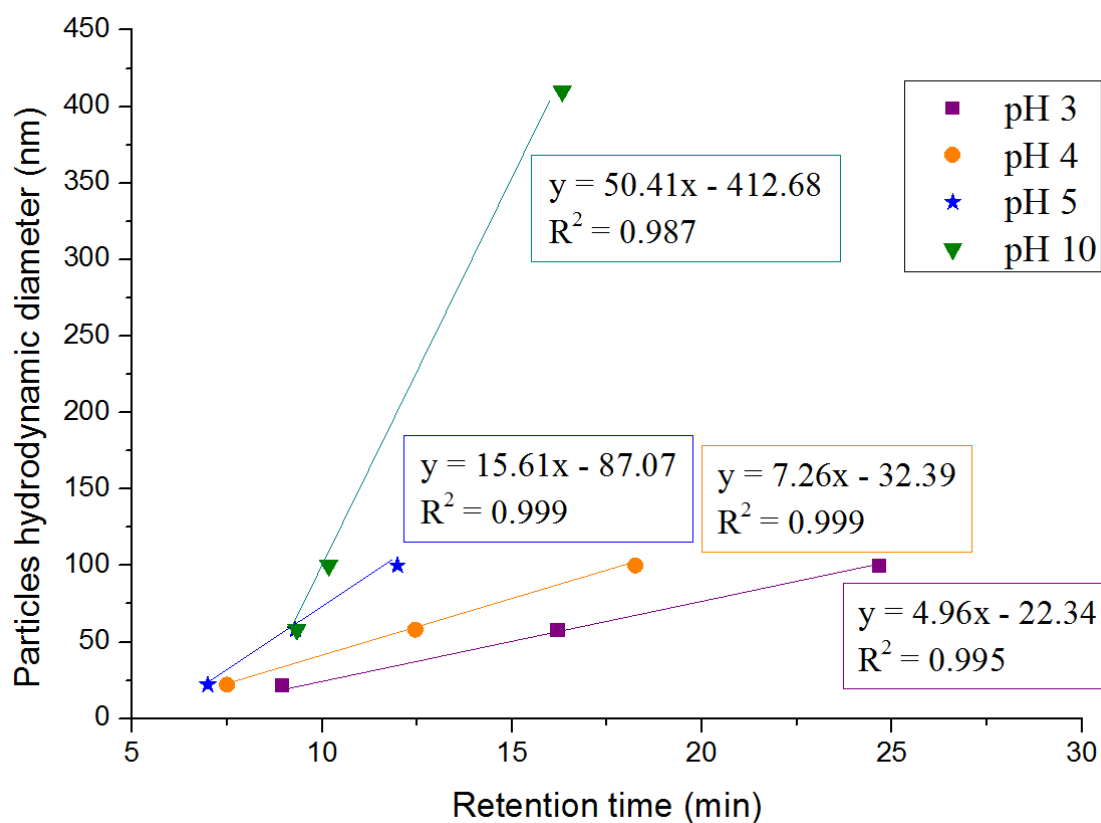
Figure 4-1: Calibration curves at different pH obtained with latex beads standards. Channel flow: 1 mL/min; Cross flow: 0.15 mL/min (pH 5 and pH 10), 0.30 mL/min (pH 4) and 0.50 mL/min (pH 3).

4.3.3.2 pH effect

To investigate the effect of pH on the aggregation of Fe_2O_3NPs, samples of 50 mg/L of NPs were pH-adjusted and equilibrated for 24 hours prior to analysis. The mobile phase consisted of ultrapure water prepared at different pH values ranging from pH 3 to pH 10. This is the range of pH tolerance for the FFF membrane; outside this range the membrane may be altered. For pH 2, 11 and 12, only DLS measurements were performed. The FlFFF measurement conditions are summarised in Table 4-1.

Table 4-1: Summary of the different FFF operating conditions used in this study.

Study		Channel Flow (mL/min)	Cross Flow (mL/min)	Mobile phase
Effect of pH	pH 3	1	0.5	Ultrapure water at pH 3
	pH 4		0.3	Ultrapure water at pH 4
	pH 5		0.15	Ultrapure water at pH 5
	pH 10			Ultrapure water at pH 10
Effect of Ionic Strength	Ultrapure water	1	0.3	Ultrapure water at pH 4
	1 mM NaCl			1 mM NaCl at pH 4
	5 mM NaCl			5 mM NaCl at pH 4
	10 mM NaCl			10 mM NaCl at pH 4
	0.5 mM $CaCl_2$			0.5 mM $CaCl_2$ at pH 4
	2 mM $CaCl_2$			2 mM $CaCl_2$ at pH 4
Effect of HA concentration	HA alone (100 mg/L)	1	0.5	Ultrapure water at pH 4
	Fe_2O_3NPs alone (200 mg/L)			
	HA/Fe_2O_3NPs 5 mgHA/L			
	HA/Fe_2O_3NPs 50 mgHA/L			
	HA/Fe_2O_3NPs 100 mgHA/L		0.15	
Stability of HA-coated Fe_2O_3NPs	pH 4	1	0.5	Ultrapure water at pH 4
	pH 7			Ultrapure water at pH 7
	pH 7/10 mM NaCl			10 mM NaCl at pH 7
	pH 7/0.5 mM $CaCl_2$			0.5 mM $CaCl_2$ at pH 7

4.3.3.3 Ionic strength effect

The effect of Na^+ and Ca^{2+} on Fe_2O_3NPs aggregation was investigated as follows. NaCl and $CaCl_2$ solutions were prepared at 1mM, 5mM and 10 mM, and 0.5 mM and 2 mM, respectively, by diluting the 500 mM stock solutions using ultrapure water and adjusting to pH 4 before being used as the mobile phase. Fe_2O_3NPs samples of 50 mg/L were suspended

in solutions having the same ionic strength as the different mobile phase solutions (i.e. 1 mM, 5 mM and 10 mM NaCl and 0.5 mM and 2 mM $CaCl_2$) and equilibrated for 24 hours before measurements. These ions were chosen because they are abundantly present in soil and in groundwater aquifers in this typical concentration range (Saleh et al. 2008). The operating conditions are presented in Table 4-1.

4.3.3.4 *Stability of DOM-coated Fe_2O_3 NPs*

HA-coated Fe_2O_3NPs at five different HA concentrations were analysed by FlFFF for size determination using ultrapure water at pH 4 as the mobile phase. The operating conditions are displayed in Table 4-1.

The most stable DOM-coated Fe_2O_3NPs (i.e. mixture of 50 mg/L HA and 200 mg/L Fe_2O_3NPs) were then tested under environmentally relevant conditions by modifying the mobile phase and the solution where the particles were suspended (i.e. pH 7, 10 mM NaCl and 0.5 mM $CaCl_2$). The operating conditions are summarised in Table 4-1.

A solution of 100 mg/L of HA was also analysed by FlFFF for molecular weight determination using sodium salt of Polystyrene sulfonates-PSS (Polysciences, Inc., PA, USA) of four different molecular weights (4600, 8000, 18000 and 35000 Da, as provided by the manufacturer, with a polydispersity of 1.1) to create a calibration curve (Figure 4-2). The operating conditions were 0.5 mL/min for the channel flow and 3 mL/min for the cross flow.
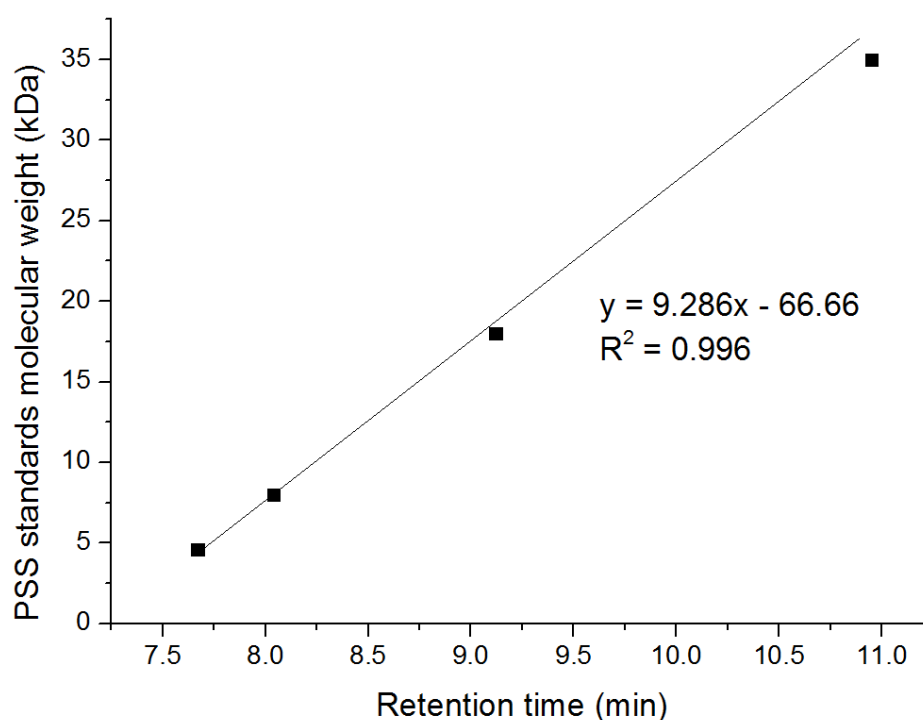
Figure 4-2: Calibration curve obtained with sodium salt of polystyrene sulfonates (PSS).

4.3.4 DLS analysis

The DLS instrument (i.e. model ZEN3600; Malvern Instruments, Worcestershire, UK) used in this study has been already described in Chapter 3. Samples used in DLS experiments were the same as for FlFFF experiments to ensure data comparability except for the study of concentration effect.

4.3.4.1 Concentration effect

Five solutions of Fe_2O_3NPs were prepared at pH 3 with concentrations of 10, 20, 50, 100 and 200 mg/L. The pH was raised slowly from pH 3 to 5 by adding drops of 0.1 M NaOH, and the Z-average hydrodynamic diameter was measured without further modifications. The pH was then brought directly to pH 10 to overcome the aggregation occurring around the PZC, before being raised slowly to pH 12. Finally, solutions were brought from pH 9 to 6 by adding drops of 0.1 M HCl.

4.3.5   SEM analysis for the effect of pH

Silicon wafers attached on carbon stubs were used for SEM measurements. About 10 μL of sample was deposited on a silicon wafer and left to dry completely. Images were obtained from a Zeiss Supra 55VP variable pressure SEM (Carl Zeiss AG, Germany) and recorded using SmartSEM® software. The mean equivalent circular diameter was determined from these images. Samples used for SEM measurements were the same as those analysed in the FlFFF and DLS experiments for the study of pH effect.

4.4   Results and discussion

4.4.1   Characterisation of Fe_2O_3 NPs

SEM was used to identify the general characteristics of the Fe_2O_3NPs. At pH 3, the Fe_2O_3NPs were spherical and present as single independent particles, as illustrated in Figure 4-3a. Analysis of 212 particles by SEM yielded a mean equivalent circular diameter of 25 nm with a very low polydispersity (i.e. standard deviation: ± 3.5 nm, Figure 4-3b).

a)
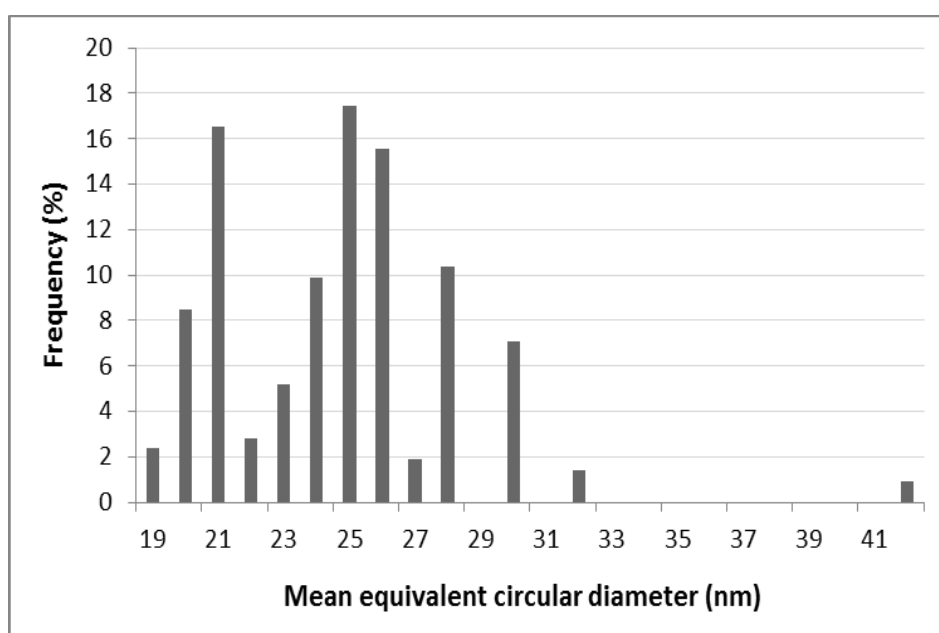
b)

Figure 4-3: (a) SEM image of Fe$_2$O$_3$NPs (50 mg/L; pH 3) and (b) particle size distribution of the same sample determined from SEM images.

Zeta potential measurements carried out at different particle concentrations (Figure 4-4) suggested that Fe$_2$O$_3$NPs are highly positively charged at low pH values (i.e. pH 2-5). The zeta potential decreased as pH increased from 5 to 9 and became highly negative from pH 10

with a PZC at around pH 7 for all particle concentrations. This value is within the range of PZC values (i.e. pH 6.8 to 8.1) found in the literature for iron oxide nanoparticles (Tombácz et al. 2004; Illes and Tombácz 2006; Baalousha et al. 2008; Baalousha 2009; Hu et al. 2010).
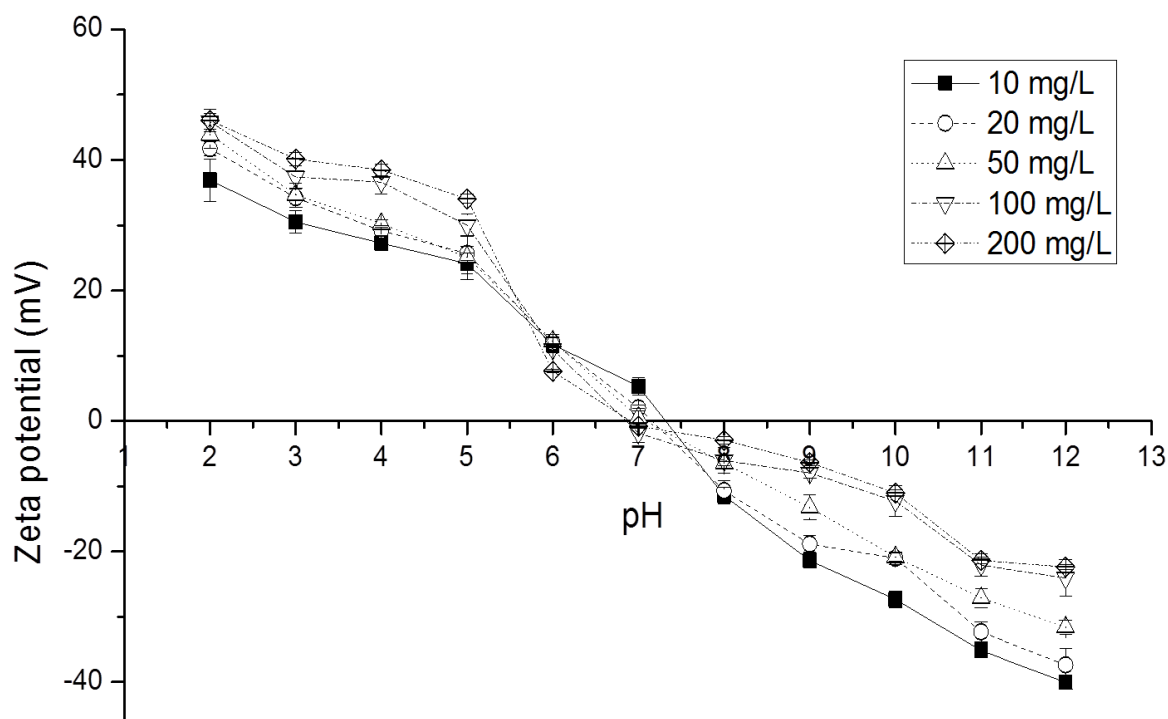
Figure 4-4: Zeta potential of Fe$_2$O$_3$NPs (10-200 mg/L) as a function of pH.

4.4.1.1 *Effect of particle concentration on the aggregation behaviour of Fe$_2$O$_3$ NPs*

Size measurements by DLS were performed at different particle concentrations ranging from 10 to 200 mg/L, and different pH values from pH 2 to 12 (all data are presented in Table 4-2). It should be noted that samples with particles having Z-average hydrodynamic diameter > 1,000 nm were settling during the analysis; however, DLS can only be used when particles are strictly subjected to Brownian motion. Thus, these data are only indicative of the agglomeration trend and cannot be used as accurate or absolute measurements.

At all particle concentrations, maximum aggregation was reached at the PZC where the net particle surface charge was reduced to zero, as shown in Figure 4-5. Far from this point,

particle aggregate sizes decrease because particles are stabilised by electrostatic repulsion forces.

Table 4-2: Summary of Z-average hydrodynamic diameter of Fe$_2$O$_3$NPs at variable pH and particle concentration, as determined by DLS.

pH	10 mg/L Z- average diameter (nm)	20 mg/L Z- average diameter (nm)	50 mg/L Z- average diameter (nm)	100 mg/L Z- average diameter (nm)	200 mg/L Z- average diameter (nm)
2	51.8 ± 0.6	54.6 ± 1.5	53.2 ± 4.1	55.2 ± 1.2	63.0 ± 0.3
3	52.9 ± 1.2	55.1 ± 2.3	55.3 ± 2.4	59.2 ± 1.3	64.8 ± 0.9
4	55.6 ± 4.2	56.9 ± 4.0	63.0 ± 3.9	64.9 ± 1.5	65.9 ± 0.3
5	102.8 ± 1.7	103.9 ± 1.4	106.1 ± 3.6	112.9 ± 3.1	131.0 ± 1.3
6	*1102.7 ± 4.2**	*1107.7 ± 5.5**	*1157.7 ± 12.5**	*1161.0 ± 2.6**	*5209.3 ± 609.0**
7	*1582.7 ± 100.3**	*1862.0 ± 37.0**	*2186.0 ± 240.0**	*2681.7 ± 587.4**	*4746.0 ± 845.9**
8	*1360.3 ± 111.2**	*1674.0 ± 65.1**	*1948.0 ± 146.7**	*2607.3 ± 578.5**	*4644.7 ± 698.6**
9	*1046.2 ± 60.9**	*1312.3 ± 66.5**	*1357.3 ± 155.0**	*3004.7 ± 418.9**	*4000.3 ± 263.8**
10	357.3 ± 3.6	360.0 ± 4.7	377.5 ± 3.6	*2635.3 ± 319.6**	*3531.3 ± 400.1**
11	108.6 ± 3.8	116.7 ± 7.3	173.6 ± 19.5	*2584.0 ± 213.9**	*3279.3 ± 130.0**
12	66.8 ± 6.6	72.8 ± 22.1	109.6 ± 14.7	*2105.7 ± 185.8**	*2735.3 ± 477.0**

* When a value is displayed in italics, it means that the result is not meaningful as sample was sedimenting during analysis. These values are only indicative of the agglomeration trend.

The results also show a particle size/concentration dependence at nanoparticle concentrations above 50 mg/L, especially at pH > 5. This is presumably due to the fact that when particle concentration increases, the distance between the particles in the sample is reduced, which increases the chance of collision between particles and hence, their aggregation. Previous studies (Baalousha 2009; Dickson et al. 2012) indicated similar findings for this concentration range. It should be noted here that injected concentrations of Fe$_2$O$_3$NPs on contaminated sites are generally between 1 to 10 g/L (Saleh et al. 2008), and aggregation phenomena are expected to be even more exacerbated in this high concentration range.
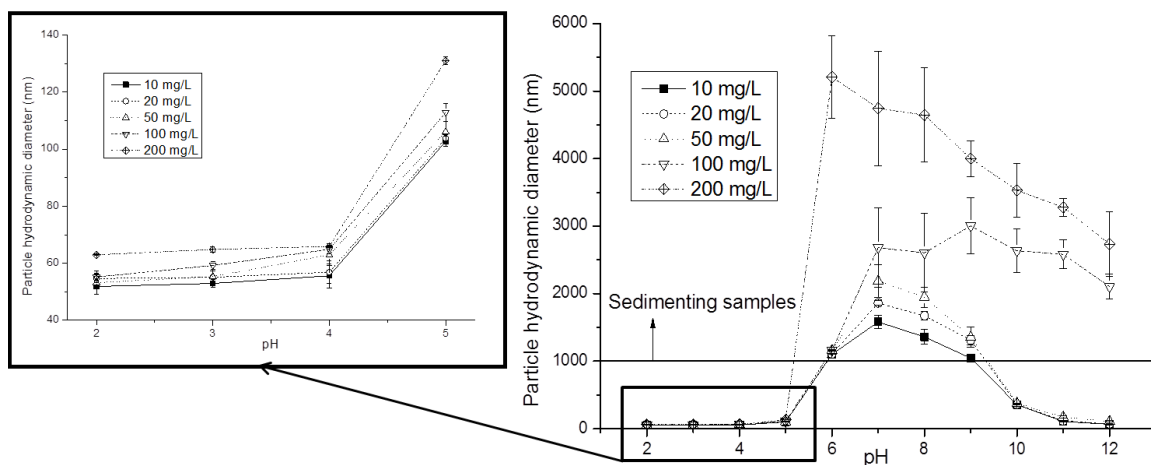
Figure 4-5: Influence of particle concentration on the Z-average hydrodynamic diameter of Fe$_2$O$_3$NPs at different pH, as measured by DLS.

These results can also be explained by the DLVO theory. Figure 4-6 shows the interaction forces that arise between two nanoparticles at concentrations of 10 and 200 mg/L, respectively. At 10 mg/L and high pH values (i.e. pH 10, 11 and 12), a net positive energy barrier prevents particles from aggregating. Because this barrier decreases from pH 12 to pH 10, we observe an increase in particle aggregate sizes. However, at 200 mg/L and pH 10, the net energy between particles is attractive which induces the aggregation of particles. At pH 11 and pH 12, the net positive barrier, although existing, is too low to prevent the particles from aggregation.
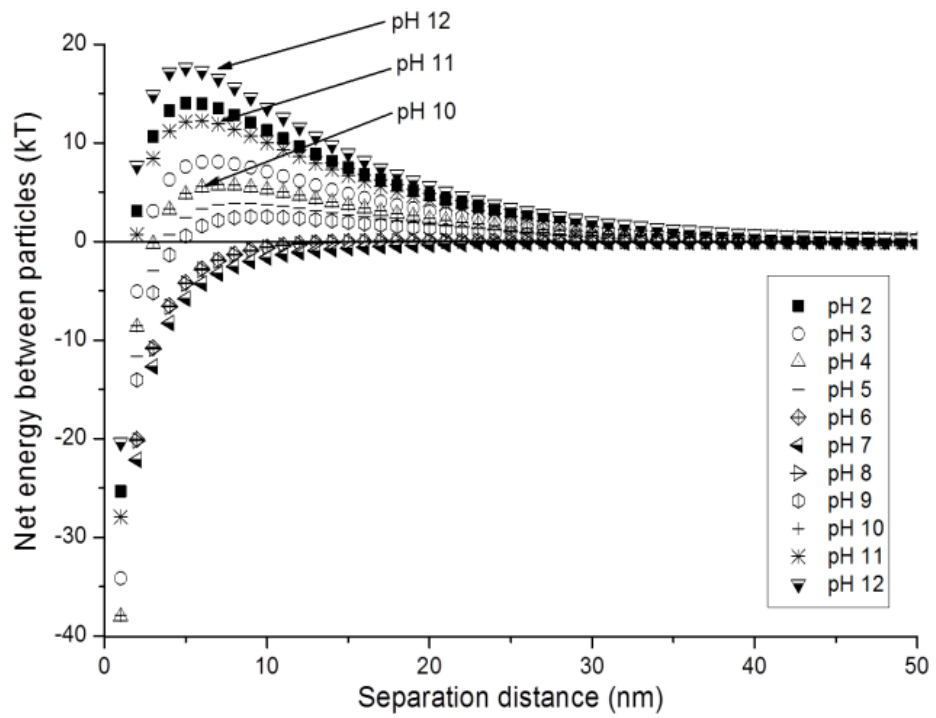
a)
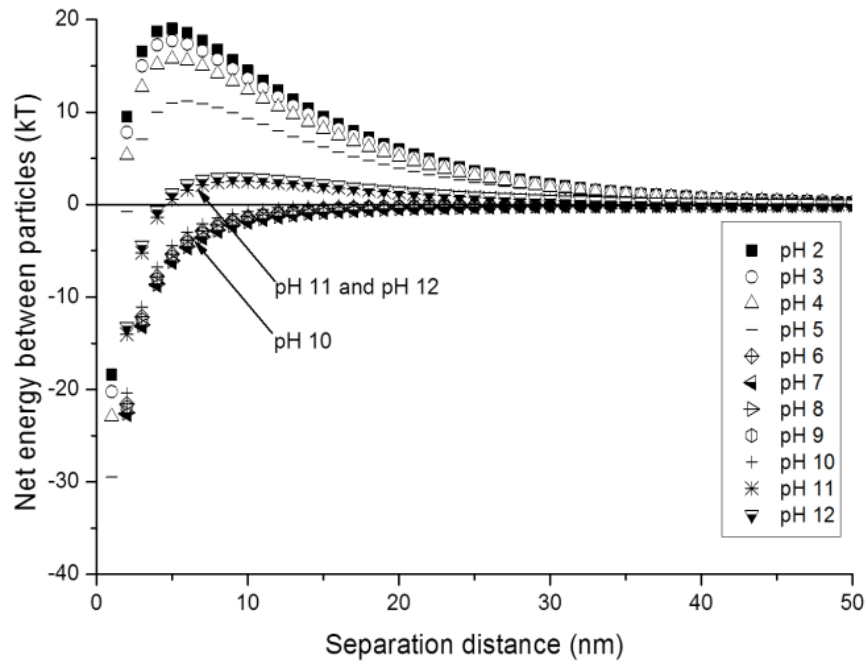
b)

Figure 4-6: Interaction forces between two spherical Fe$_2$O$_3$NPs (30 nm diameter) as a function of pH at (a) 10 mg/L and (b) 200 mg/L concentration according to the DLVO theory.

The effect of pH on the aggregate size of Fe_2O_3NPs at a concentration of 50 mg/L is shown in Table 4-3 for FlFFF, DLS and SEM measurements. The size analysis showed a good agreement among the three measurement techniques. In general, the sizes measured by SEM were comparable to FlFFF sizes, while the sizes measured by DLS were generally larger than FlFFF. DLS is known to be very sensitive to larger particles and a very small number of large particles (e.g. formed during the aggregation process) can induce a substantial shift toward larger sizes (Domingos et al. 2009). Moreover, it has also been demonstrated that the diffusion coefficient, from which the Z-average hydrodynamic diameter is determined, may show angular dependence and that lower angles yielded more precise values than those obtained at one angle only, which is the case with DLS (Takahashi et al. 2008).
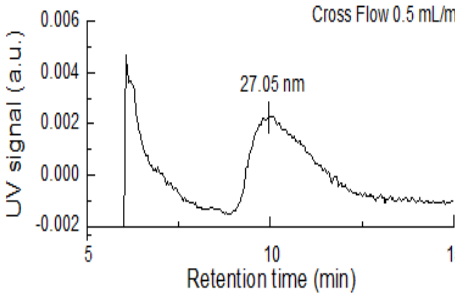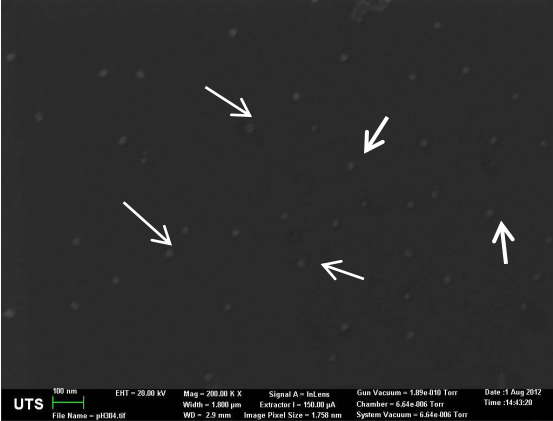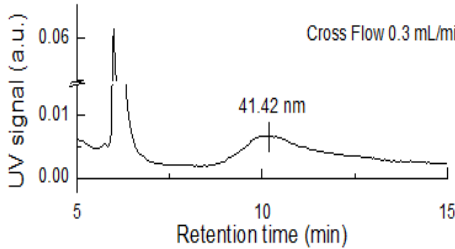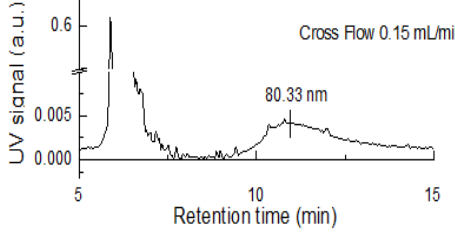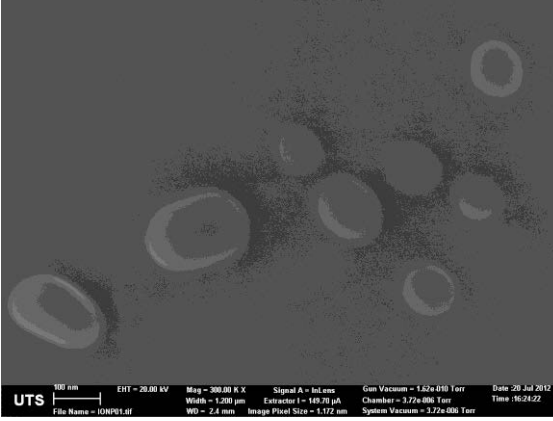
At pH 10, a significant difference in size was observed using the SEM, FlFFF and DLS techniques; the FlFFF results in particular, were much lower than those from other techniques showing the limitation of this technique. This could be explained by the fact that, at this pH, both the FFF membrane and Fe_2O_3NPs are negatively charged. Thus, in addition to the concentration gradient effect that drives the diffusion of particles back into the channel, electrostatic repulsive forces also arise between particles and the membrane, causing lower retention times than expected and translating into an underestimation of particle size.

Another limitation of the FlFFF techniques simulating environmental conditions is related to the recovery of the injected sample. FlFFF fractograms show that the majority of the samples are eluted in the void region (except at pH 3) and only a small fraction of the injected sample (i.e. < 5%) is detected during the elution time. This can probably be explained by the fact that when pH increases, some large aggregates may be formed (> 1 μm). These aggregates (even though not representative of the whole sample) are much larger

than the rest of the sample and are eluted in the void peak in *steric* elution mode. To reduce the intensity of the void peak signal, pre-fractionation of the sample could be used to increase the sample concentration and recovery during the elution.

Despite differing in absolute values, size measurements by FlFFF and DLS did show similar trends. Both the hydrodynamic diameter (from FlFFF) and Z-average hydrodynamic diameter (from DLS) increased slightly from pH 3 to 5 with the formation of doublets, triplets or larger aggregates (as illustrated by the SEM images) and then increased significantly at higher pH values, up to a maximum at pH 7 (i.e. at the PZC) with the formation of very large aggregates (cf. SEM image). Around the PZC, aggregation was so extensive that the samples could not be measured by FlFFF and DLS. At pH values above the PZC, aggregate sizes started to decrease but not at the same rate. As discussed previously, at high particle concentration (i.e. 200 mg/L), the chance of collision is enhanced, as is the potential for aggregation due to lower interparticle repulsive forces according to the DLVO theory. However, below 50 mg/L, far from the PZC (i.e. pH 10 to 12), Fe_2O_3NPs remained stable and the average particle size became closer to the original size (i.e. as measured at pH 3).

Table 4-3: Summary of the hydrodynamic diameter of Fe2O3NPs at variable pH as determined from FlFFF/UV, DLS and SEM at 50 mg/L.

pH	FlFFF/UV fractograms and hydrodynamic diameter (nm)	Hydrodynamic diameter as determined by DLS (nm)	Corresponding SEM images (50 mg/L)
3	27.05 ± 0.16	55.3 ± 2.4	Approximated size: 25 nm
4	41.42 ± 0.04	63.0 ± 3.9	Approximated size: 35 nm
5	80.33 ± 0.74	106.1 ± 3.6	Approximated size: 80 nm
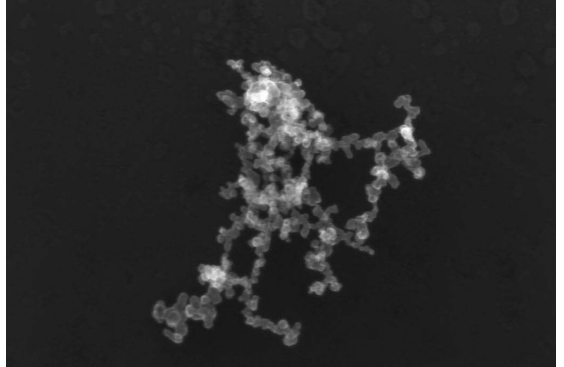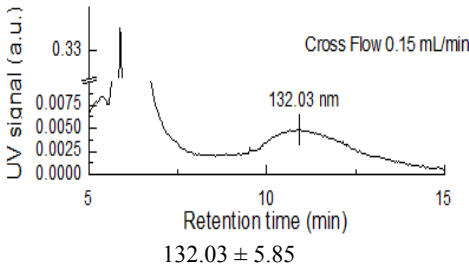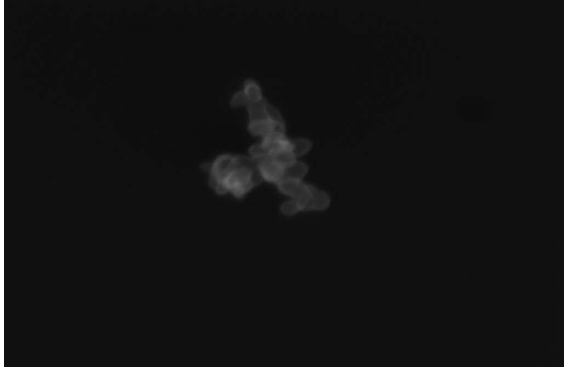
7	Samples settled down rapidly to the bottom of the vial and could not be analysed by FlFFF and DLS.		Approximated size: 1500 nm
10	132.03 ± 5.85	377.5 ± 3.6	Approximated size: 250 nm

Figure 4-7 shows the DLVO energy profiles for particle-particle interactions as a function of pH at 50 mg/L. From pH 2 to 7, there is a significant decrease in the repulsive forces between particles due to the decrease in particle surface charge to zero at the PZC (Figure 4-4). Around the PZC there is no net positive energy barrier promoting the formation of very large aggregates (i.e. up to several micrometres) since the only factor controlling aggregation is Brownian motion (Hu et al. 2010). At higher pH, starting at pH 10, the particles become highly negatively charged; giving rise to repulsive forces, and a net positive energy barrier once again prevents particles from aggregating.
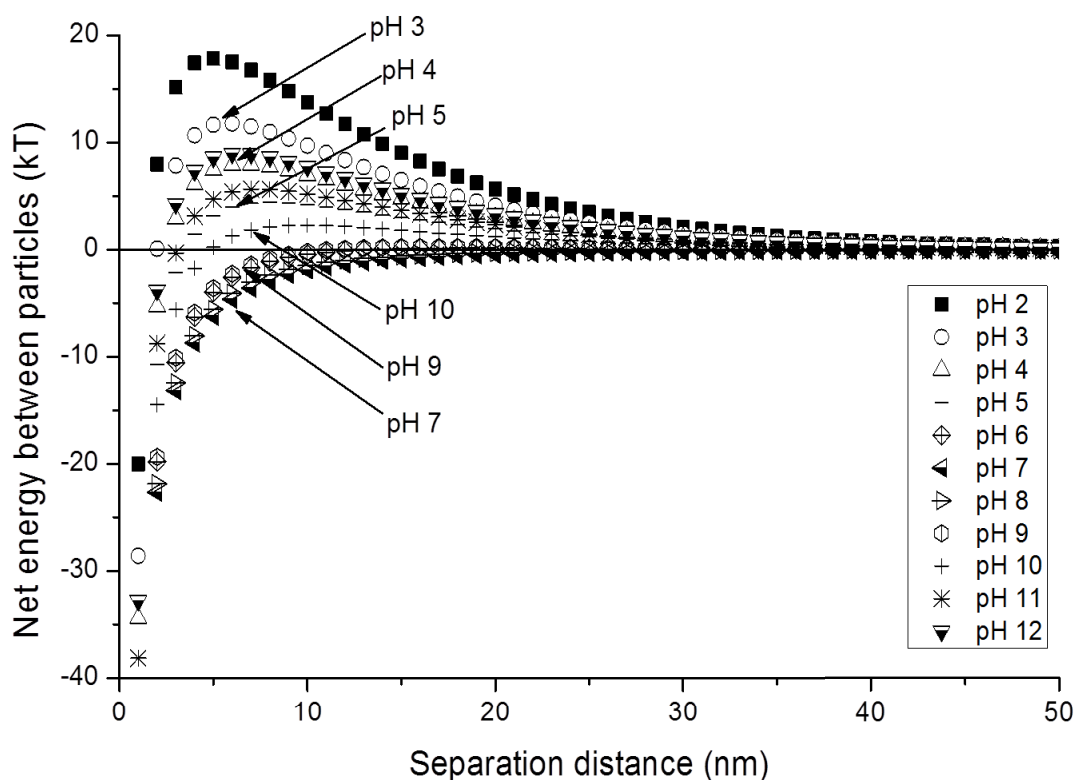
Figure 4-7: Interaction forces between two spherical iron oxide nanoparticles (30 nm diameter, 50 mg/L) as a function of pH according to the DLVO theory.

4.4.1.3   Effect of ionic strength

Figure 4-8 shows the FlFFF/UV fractograms of Fe_2O_3NPs as a function of ionic strength, and Table 4-4 gives the corresponding hydrodynamic diameters obtained from the FFF fractograms as well as the Z-average hydrodynamic diameters obtained by DLS measurements.

The DLS results show an increase in particle aggregate sizes with increasing ionic strength. At low ionic strength (1 mM-5 mM NaCl and 0.5 mM $CaCl_2$), the Z-average hydrodynamic diameter varies slightly from 63.19 to 64.92 nm. This is not significantly different from the size of nanoparticles measured in ultrapure water. This indicates that at low ionic strength, electrostatic repulsive forces are dominant over the attractive forces, preventing particles from aggregation. However, the use of 10 mM NaCl or 2 mM $CaCl_2$ resulted in particle

aggregation, probably due to the reduction in repulsive forces between particles as shown in Figure 4-9.

The FlFFF fractograms (Figure 4-8) show no change in the retention times with increased ionic strength but a significant decrease in the UV signal intensity is observed. The constant elution time is expected as it has been demonstrated in previous studies that ionic strength has no effect on retention time of particles of the same size (Dubascoux et al. 2008; Shon et al. 2009).
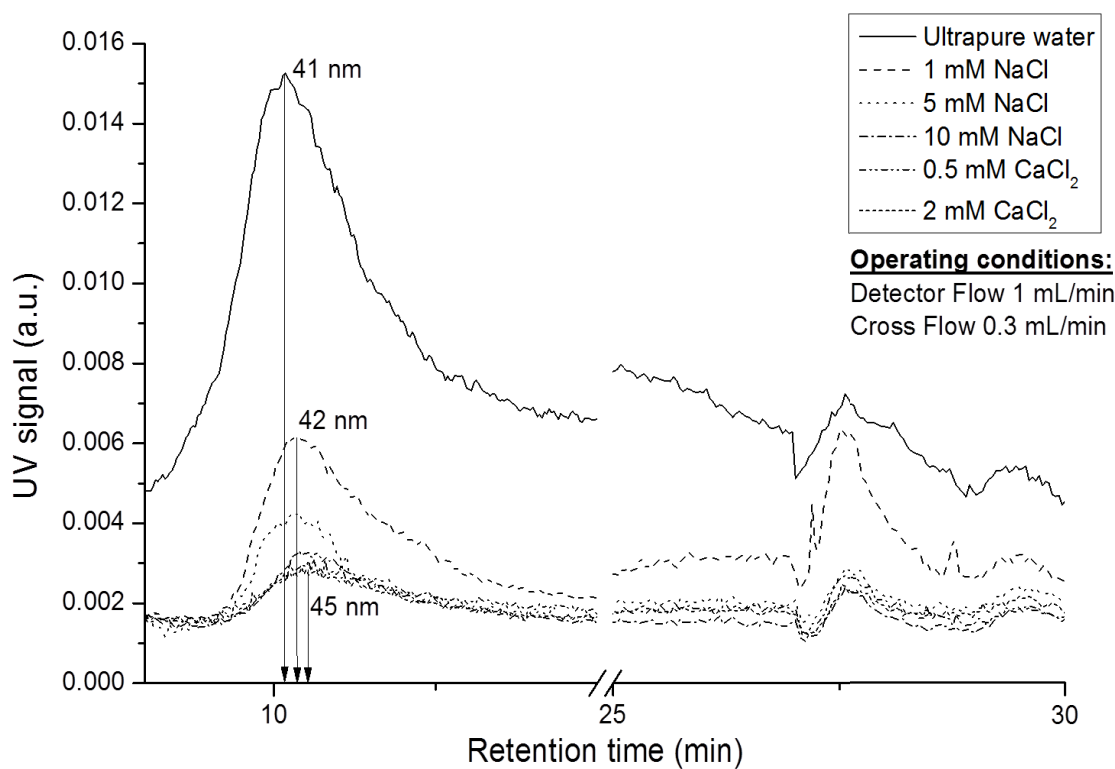
Figure 4-8: FlFFF fractograms of Fe$_2$O$_3$NPs (50 mg/L; pH 4) at variable ionic strength.

Table 4-4: Hydrodynamic diameter (FFF) and Z-average hydrodynamic diameter (DLS) of Fe$_2$O$_3$NPs as a function of ionic strength.

Ionic strength	Particle size (nm)	
	FlFFF/UV	DLS
Ultrapure water	41.4 ± 0.1	61.4 ± 1.4
1 mM NaCl	42.3 ± 0.1	63.2 ± 3.6
5 mM NaCl	42.8 ± 1.7	64.4 ± 5.2
10 mM NaCl	44.7 ± 2.5	312.4 ± 10.7
0.5 mM CaCl$_2$	44.4 ± 0.6	64.9 ± 4.9
2 mM CaCl$_2$	44.8 ± 2.7	438.7 ± 18.1

However, the decrease in UV signal points to a lower recovery at higher ionic strength, which could be explained by the DLVO theory and DLS results. Figure 4-9 shows that increasing ionic strength leads to a significant decrease in the repulsive forces between particles, which could lead to the formation of larger particle aggregates. Dubascoux et al. (2008) explained that an increase in ionic strength leads to a decrease in the double layer thickness of particles, which promotes the formation of larger aggregates. These larger clusters of particles will be located closer to the FFF membrane which will increase the interactions between the membrane and these larger aggregates. Thus, they could be irreversibly adsorbed onto the membrane explaining the observed decrease in the UV signal.
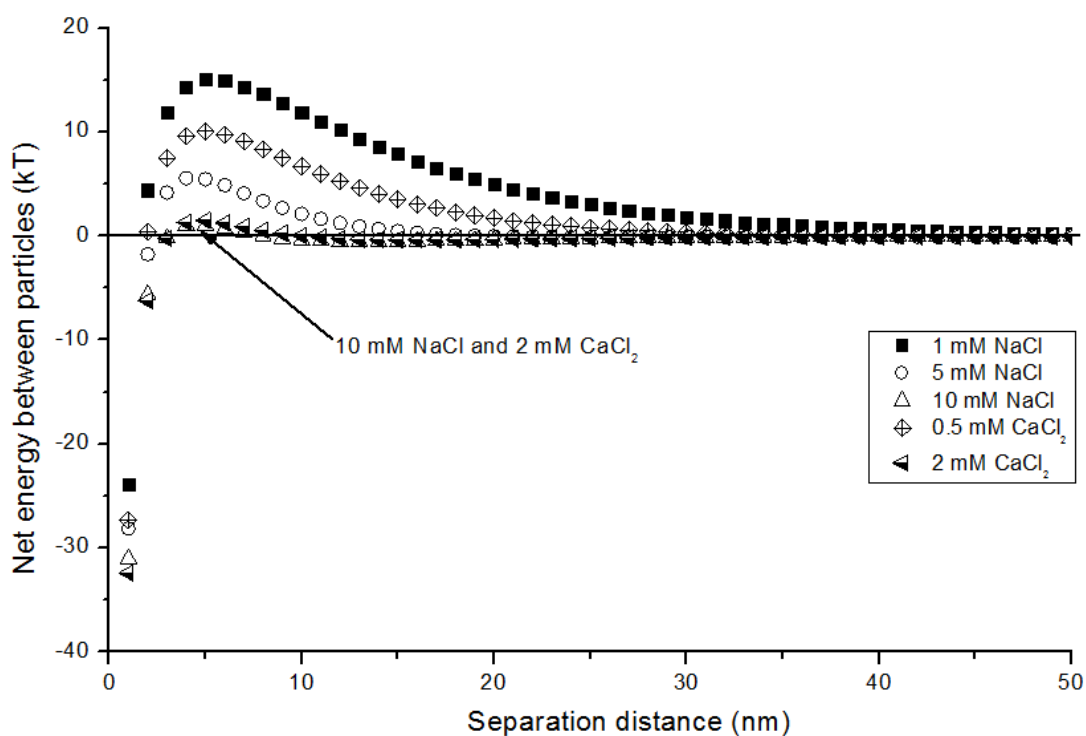
Figure 4-9: Interaction forces between two spherical Fe$_2$O$_3$NPs (30 nm diameter; 50 mg/L; pH 4) at variable ionic strength according to the DLVO theory.

4.4.2 Stability of DOM-coated Fe$_2$O$_3$ NPs under environmentally relevant conditions

4.4.2.1 Effect of DOM on particle surface charge

Figure 4-10 shows the zeta potential profiles of Fe$_2$O$_3$NPs alone (200 mg/L), HA-coated Fe$_2$O$_3$NPs at variable HA concentration and HA alone (50 mg/L) plotted as a function of pH, ranging from 3 to 10.

At low HA concentrations (i.e. from 5 to 20 mg/L), the zeta potential of Fe$_2$O$_3$NPs decreases, resulting in the PZC occurring at lower pH values (i.e. from pH 7 for 0 mg/L HA to pH 4 for 20 mg/L HA). This shift in the pH of the PZC is probably due to the adsorption of HA on the surface of Fe$_2$O$_3$NPs causing a change in their surface charge. The zeta potential of HA indicates that it is negatively charged over the whole pH range. This is due to the fact that HA macromolecules carry many functional groups, including carboxylic and

124

phenolic groups (Hajdú et al. 2009; Hu et al. 2010; Dickson et al. 2012). At concentrations above 20 mg/L, the zeta potential of HA-coated Fe_2O_3NPs remained negative across the whole pH range tested. At pH values greater than the PZC of the uncoated Fe_2O_3NPs, both Fe_2O_3NPs and HA are negatively charged and adsorption of HA is not expected to occur. Thus, the decrease in zeta potential values is probably due to the increased HA concentration which brings more negative charges into solution and shifts the zeta potential downwards.
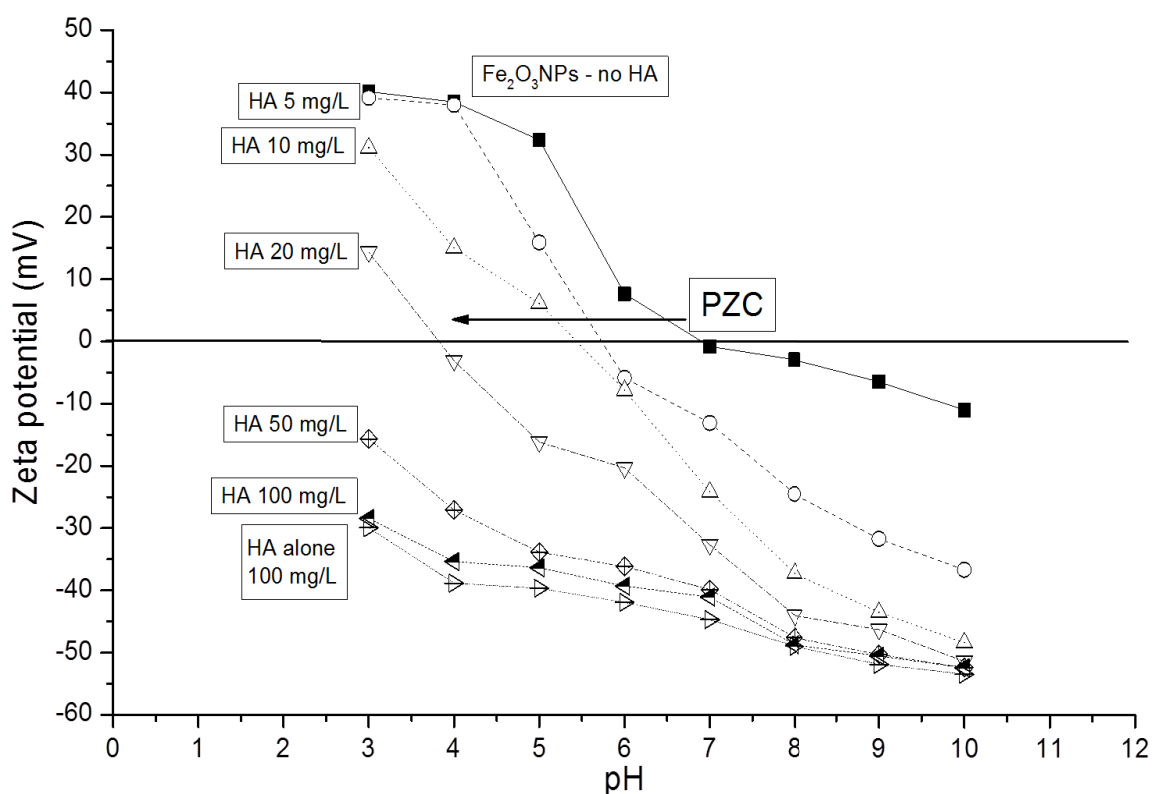
Figure 4-10: Effect of HA concentration on the zeta potential profile of Fe_2O_3NPs as a function of pH.

4.4.2.2   Effect of DOM concentration on particle aggregation

The effect of HA concentration on the aggregation of HA-coated Fe_2O_3NPs was investigated by FlFFF and DLS (Figure 4-11) at pH 4. At this pH, Fe_2O_3NPs are strongly positively charged (i.e. zeta potential of +38.5 mV, Figure 4-10) and HA is still strongly negatively charged (i.e. zeta potential of -38.8 mV, Figure 4-10). As the adsorption of DOM on the surface of Fe_2O_3NPs is mainly governed by Coulombic interactions via ligand-exchange

reactions, this provides the most favourable conditions for sorption (Filius et al. 2000; Chorover and Amistadi 2001; Illés and Tombácz 2004).
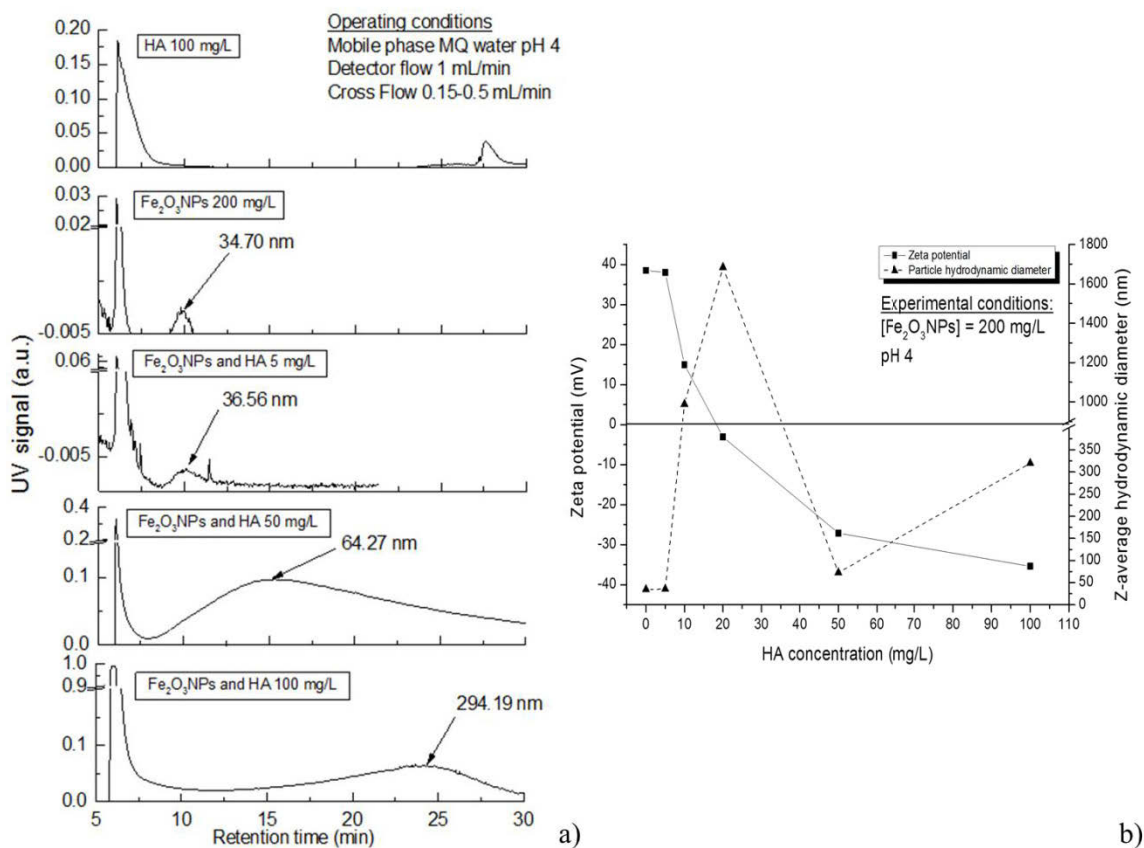
Figure 4-11: (a) FlFFF fractograms and (b) DLS results of HA-coated Fe₂O₃NPs at variable DOM concentrations (5-100 mg/L).

At low concentration (i.e. < 20 mgHA/L), HA partially neutralises the positive charges on Fe₂O₃NPs as shown in the zeta potential profile in Figure 4-10. Thus, aggregation takes place and extends with increasing HA concentration to reach a peak at 20 mgHA/L at which point the zeta potential is reduced to almost zero. At HA concentrations of 10 and 20 mg/L, very large aggregates were formed (see Figure 4-11b) and due to their rapid sedimentation on the bottom of the vial, FlFFF analysis could not be performed. From the FlFFF fractogram of the mixture of Fe₂O₃NPs with 5 mg/L of HA, the following observations can be made. Compared to the fractogram of Fe₂O₃NPs alone, there is a slight increase in the void peak UV signal which is probably due to the loss of sample during the injection and

126

focusing step and because HA is better adsorbed by UV as shown on the fractogram of HA alone. The second observation is that no apparent shift toward larger retention times is observed because the difference in size obtained from both fractograms is very low. This can be explained by the fact that at 5 mgHA/L, there is a very low amount of HA in the solution; thus, the number of coated nanoparticles is very low and they were not detected during the FFF analysis.

At higher HA concentrations (i.e. $\geq$ 50 mg/L), the surface of the Fe_2O_3NPs becomes negatively charged (i.e. -27.1 mV at 50 mgHA/L, Figure 4-10) providing electrostatic stabilisation of the particles and reducing their aggregation (i.e. from almost 1700 nm at 20 mgHA/L to 85.2 nm at 50 mgHA/L as measured by DLS as shown in Figure 4-11b). A significant increase in the void peak UV signal can be observed on the FFF fractograms of 50 mgHA/L and 100 mgHA/L (Figure 4-11a). This can be caused by the unadsorbed HA macromolecules. In fact, HA has a molecular weight of 38.7 kDa (as measured by FlFFF – see Figure 4-12) which corresponds to approximately 1.7 nm (conversion based on (Shon et al. 2006)) and is considerably smaller than the Fe_2O_3NPs. Therefore, the applied cross flow was too low to retain the unadsorbed HA molecules, and the elution of unretained HA is indicated by the larger void peak. FFF results also showed a shift toward higher retention times (compared to the FlFFF fractogram of bare Fe_2O_3NPs), indicating the formation of small aggregates of coated-particles. The broadening of the peak is probably caused by aggregates having different size and conformation. At a HA concentration of 100 mg/L, both DLS and FFF measurements indicate an increase in the particle size, which is probably due to the formation of larger aggregates. This consideration is supported by the fact that a small fraction of the sample settled on the bottom of the vial.

Finally, by comparing DLS and FFF results, it is clear that FFF, as a fractionation method, can provide not only the hydrodynamic diameter of the coated particles but also valuable information on the coating itself. For instance, the FFF results may be used to assess the

amount of HA coated onto the nanoparticles by comparing the intensity of the void peak on the fractograms of HA alone and HA-coated Fe_2O_3NPs. This demonstrates the versatility of FFF over conventional size-measurement techniques.
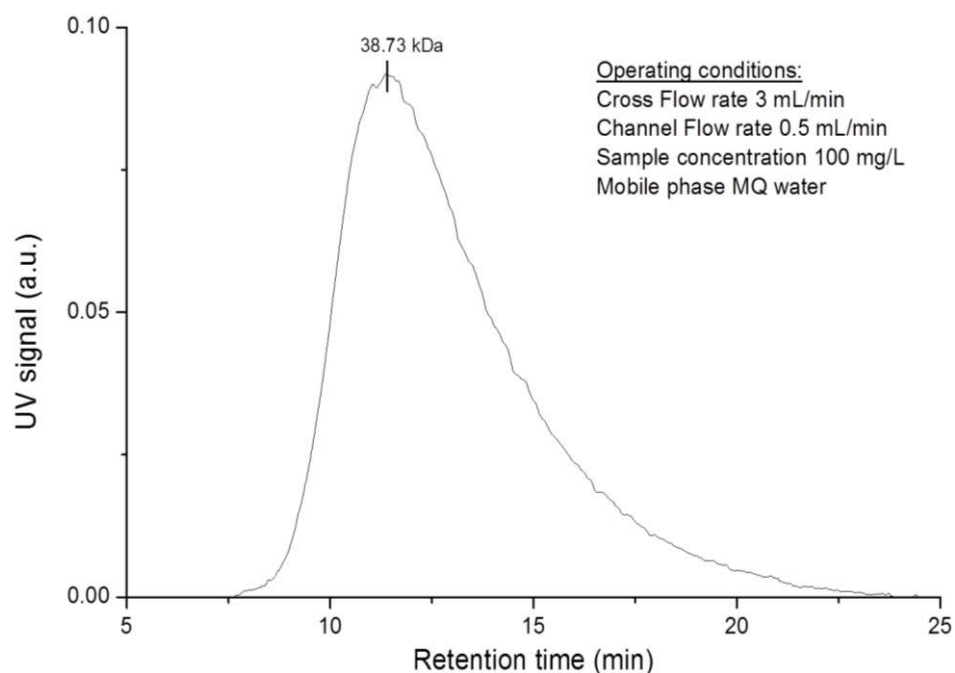
Figure 4-12: FlFFF-UV fractograms of HA (100 mg/L) for molecular weight determination.

4.4.2.3 *Stability under realistic conditions of pH and ionic strength*

The stability of HA-coated Fe_2O_3NPs was tested under realistic environmental conditions (i.e. pH 7, 10 mM NaCl and 0.5 mM $CaCl_2$) to verify whether or not this coating could be used effectively in the field. Figure 4-13 shows the FFF and DLS results for the stability study of a mixture of Fe_2O_3NPs (200 mg/L) coated by HA (50 mg/L).

Compared to bare Fe_2O_3NPs, HA-coated Fe_2O_3NPs were less affected by an increase in pH and were much more stable under neutral pH conditions. In fact, for the bare nanoparticles, an increase in pH to pH 7 (i.e. the PZC) resulted in extensive aggregation with the formation of large aggregates that were thirty-five times larger than at pH 4 (Figure 4-13b). However, when the nanoparticles were coated with HA, the same increase in pH resulted in a size

increase of less than 15%. This is most likely due to the negatively charged HA layer on the Fe_2O_3NPs surface which prevents particles from aggregating through electrostatic repulsion. Moreover, the macromolecular layer can also provide steric stabilisation by causing entropically unfavourable conditions when the particles come closer to one another (Tiller and O'Melia 1993; Illés and Tombácz 2004).
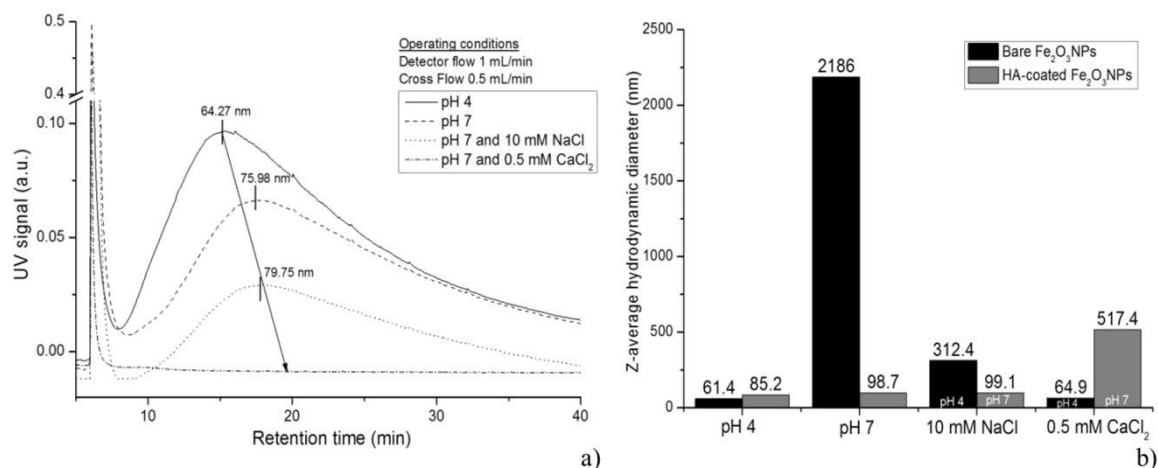
Figure 4-13: (a) FlFFF fractograms and (b) DLS results of HA-coated Fe_2O_3NPs (50 mg/L HA and 200 mg/L Fe_2O_3 NPs) at environmentally relevant conditions.

Regarding the effect of NaCl on the stability of HA-coated Fe_2O_3NPs, FFF and DLS results (cf. Figure 4-13) showed that increasing the NaCl concentration to 10 mM does not result in aggregation or sedimentation of the sample in comparison to bare Fe_2O_3NPs. In fact, it has been demonstrated in previous studies (Illés and Tombácz 2004; Hajdú et al. 2009) that HA-coated Fe_2O_3NPs are more stable under high NaCl concentration due to the electrosteric stabilisation providing by HA coating.
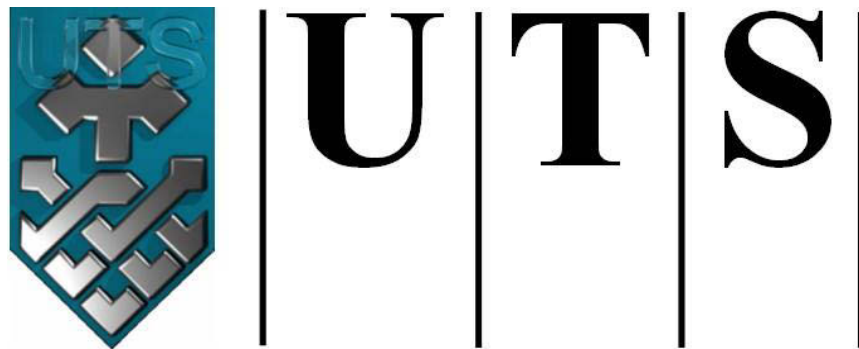
In the presence of $CaCl_2$ at 0.5 mM, HA-coated Fe_2O_3NPs became unstable and formed large aggregates (greater than 500 nm when measured by DLS). The effect of increasing the $CaCl_2$ concentration on FFF results is that no peaks were observed, which is most likely to be the results of aggregation and consequently much longer retention times. This aggregation behaviour could be attributed to the formation of complexes between Ca^{2+} and

HA, which neutralises the negative charge imparted by the HA coating on the Fe_2O_3NPs and thus, reduces the electrostatic stabilisation which previously arose between the coated nanoparticles. In addition, the presence of Ca^{2+} cations may promote the formation of complexes Fe_2O_3NPs-HA-Ca^{2+}-HA- Fe_2O_3NPs (Chen et al. 2006). It has also been reported that other alkaline earth metal divalent cations such Ba^{2+} and Sr^{2+} could accelerate hematite aggregate growth at very low concentrations, whereas Mg^{2+} showed no effect on aggregation even at high concentrations (Chen et al. 2007).

4.5 Conclusions

The stability of both coated and uncoated Fe_2O_3NPs has been investigated under different environmental conditions by using several analytical techniques and a theoretical method. The need for a multi-method approach has been clearly demonstrated by highlighting the limitations of each method.

The pH and ionic strength are important environmental conditions that need to be carefully considered before releasing nanoparticles into the environment. In the case of Fe_2O_3NPs, commonly encountered soil and groundwater conditions (i.e. pH 6-8 and high ionic strength) can induce extensive aggregation and can thus considerably reduce their mobility and reactivity once injected into subsurface environments. Finding solutions to reduce or suppress particle aggregation is therefore crucial in optimising remediation strategies using these materials. Surface coating is one of the preferred methods used to enhance the stability of the Fe_2O_3NPs. The choice of surface modifier is important and this will depend on the soil conditions and the target contaminants. This study has demonstrated the performance of DOM as a surface coating under conditions similar to the natural soil environment. DOM-coated nanoparticles were observed to show higher stability than bared Fe_2O_3NPs under most studied conditions.

University of Technology Sydney
FACULTY OF ENGINEERING

CHAPTER 5

MULTI METHOD APPROACH TO ASSESS

THE BEHAVIOUR OF IRON OXIDE

NANOPARTICLES STABILISED WITH

ORGANIC COATING

131

5.1 Introduction

nZVI is currently the most widely studied ENPs for soil and groundwater remediation as many studies have demonstrated that these nanoparticles exhibit high reactivity in remediating aquifers contaminated by non-aqueous phase liquids, hazardous element ions, and many other hazardous compounds (Elliott and Zhang 2001; Cundy et al. 2008; Geng et al. 2009). Delivering the nZVI to the contaminant source zone is essential for the success of *in-situ* remediation. However, many laboratory and pilot-scale field studies have demonstrated that the mobility and reactivity of iron-based nanoparticles are substantially limited in natural porous systems such as soils and groundwater aquifers (Schrick et al. 2004; Quinn et al. 2005; He and Zhao 2007; Saleh et al. 2007).

Aggregation is considered to be the primary cause of this reduced mobility and reactivity, and is the result of many factors including solution pH, ionic strength, and the presence of organic matter as demonstrated in the previous chapter. To overcome this limitation, surface modification using charged polymers, polyelectrolytes or surfactants is now widely used to disperse nanoparticles in environmental matrices of soil and water (Zhang et al. 1998; Schrick et al. 2004; Saleh et al. 2005; He et al. 2007; Saleh et al. 2007; Hajdú et al. 2009; Phenrat et al. 2009; Sirk et al. 2009; Cirtiu et al. 2011). These modifications can theoretically provide both electrostatic and steric (so-called electrosteric) stabilisation to prevent particles from aggregating and can also reduce the propensity for surface attachment (Saleh et al. 2008). Although these different surface coatings can enhance nanoparticle stability, unfortunately, they can also be expensive, have toxic effects on the environment, and alter the interaction of ENPs with contaminants (Tiraferri et al. 2008).

Natural surface coating by the adsorption of dissolved organic matter (DOM), such as humic and fulvic acids, on the surface of nanoparticles has also been studied as an alternative "green" surface coating, and has been demonstrated to enhance nanoparticle stability

through electrosteric stabilisation (Mylon et al. 2004; Illes and Tombácz 2006; Hu et al. 2010). The advantage of DOM over conventional surface modifiers is that DOM is naturally abundant in the environment, inexpensive, non-toxic, and has the ability to both adsorb onto metal oxide nanoparticles and complex with heavy metals (Liu et al. 2008; Dickson et al. 2012). A recent study by Zhang et al. (2013) has also demonstrated the capacity of humic acid (HA) coated iron oxide nanoparticles to remove organic dyes from wastewater. Finally, a study by Chen et al. (2011) demonstrated that DOM - coated nZVI may significantly mitigate bacterial toxicity due to the electrosteric hindrance preventing direct contact.

In this chapter, Fe_2O_3 NPs coated with DOM were characterised using modern analytical methods: flow field-flow fractionation (FlFFF), high performance size exclusion chromatography (HPSEC) and Fourier transform infrared spectroscopy (FTIR), in order to understand with greater confidence the interaction between DOM and Fe_2O_3 NPs. The use of a multi-method approach for the characterisation of ENPs has been demonstrated in the previous chapter and by other researchers (Domingos et al. 2009; Cerqueira et al. 2011; Cerqueira et al. 2012). Several characteristics were investigated in terms of surface charge, size, adsorption capacity and chemical bonds. The aggregation and disaggregation behaviour of the coated NPs was also investigated with FlFFF to assess their stability over time. Disaggregation is another important factor for predicting the fate and behaviour of NPs once released into the environment (Christian et al. 2008), however, there are only few studies available on the disaggregation of NPs (Baalousha 2009) and this is mainly due to analytical challenges. The use of FlFFF to study the aggregation and disaggregation behaviour of nanoparticles presents several advantages over conventional size-measurement techniques. In particular, compared to dynamic light scattering which only measures an average particle size, FlFFF is a fractionation method and separation of the sample allows accurate determination of the particle size distribution which is very useful for aggregation/disaggregation studies.

This chapter is an extension of the research article published by the author in Science of the Total Environment (Chekli et al. 2013).

5.2 Experimental

5.2.1 Chemicals and reagents

Commercially available Fe_2O_3 NPs (α-Fe_2O_3, average particle size 30 nm, BET 50-245 m^2/g, 20 wt. % dispersed in water at pH 4) and humic acid (HA) (technical grade) were supplied by Sigma-Aldrich Australia. SRNOM was obtained from the International Humic Substances Society (IHSS, St. Paul, USA). HA and SRNOM were employed as the DOM sources.

5.2.2 Sample preparation

Fe_2O_3 NPs were suspended in ultrapure water with a resistivity of 18 MΩ cm (MilliQ, Millipore, USA) to obtain a final concentration of 2 g/L at pH 4 $\pm$ 0.1. Solution pH was adjusted using 0.1 M HCl and 0.1 M NaOH solutions and left for 24 hours to equilibrate, after which the pH was re-measured and adjusted if necessary for all experiments. No buffers were used in this study, as their ionic strength may alter the surface chemistry of the Fe_2O_3 NPs, enhancing their aggregation (Baalousha 2009).

HA and SRNOM were dissolved in ultrapure water to obtain solutions with a concentration of 500 mg/L. These were then filtered through a 0.45 μm filter using vacuum suction. The filtrate was retained as the stock solution, and stored at 4°C prior to experimental use. The total organic content (TOC) of the DOM solutions (dilution 1:10 of the stock solutions) was measured as 19.1 mgC/L and 18.9 mgC/L, for HA and SRNOM respectively, using a TOC analyser (Multi N/C 3100, Analytic Jena AG, Germany).

DOM-coated Fe_2O_3 NPs were prepared by mixing (i.e. using a magnetic stirrer) 10 mL of concentrated Fe_2O_3 NPs (i.e. 2 g/L) with 10 mL of DOM stock solution and diluted with ultrapure water to obtain solutions with Fe_2O_3 NP concentrations of 200 mg/L and DOM concentration of 50 mg/L. While stirring, the solutions were constantly kept at pH 4, as a previous study demonstrated that this is a favourable pH for DOM adsorption (Illés and Tombácz 2004). Solutions were stirred for 24 h, and samples were taken at different time intervals and measured by the different analytical methods. The final solutions were then stored for 14 days at ambient temperature for the stability study.

5.2.3 Characterisation of DOM-coated Fe_2O_3 NPs

5.2.3.1 *Adsorption experiments*

The Fe_2O_3 NPs (200 mg/L) were equilibrated with HA and SRNOM solutions (50 mg/L) for 24 h at ambient temperature as described in the previous section. Samples were taken at different time intervals (i.e. 1 min, 2 min, 5 min, 10 min, 20 min, 30 min, 1 h, 2h, 5 h, 10 h and 24 h) and then centrifuged for 10 min at 3500 rpm (Model 2040, Centurion Scientific Ltd, UK) to separate the solution from the solid particles. The total organic carbon (TOC) content of the supernatant was then measured via a TOC analyser (Multi N/C 3100, Analytic Jena AG, Germany). The amount of DOM adsorbed on the surface of Fe_2O_3 NPs was calculated from the following equation:

$$q(t) = (C_0 - C_t)\frac{V}{m} \tag{1}$$

Where, C_0 and C_t (mg/L) are the initial and concentration at time t of DOM in solution, V (L) is the solution volume and m (g) is the mass of the Fe_2O_3 NPs.

Adsorption data were fitted to the pseudo first and pseudo second-order kinetic models using linearized parameter estimations. The pseudo-second order kinetic model showed good

correlations while the pseudo first-order model showed significantly low fit ($R^2 < 0.5$). Therefore, in this study, the pseudo second-order kinetic model was employed for data analysis. The linear form of this model can be described as (Febrianto et al. 2009):

$$\frac{t}{q(t)} = \frac{1}{kq_e^2} + \frac{1}{q_e} \qquad (2)$$

Where, k (g/(mg.min)) is the rate of the pseudo second-order and q_e (mg/g) is the amount of DOM adsorbed on the surface of Fe_2O_3 NPs at equilibrium. The k and q_e values were calculated from the slope and intercept of the y-axis obtained after plotting t/q(t) against t respectively.

5.2.3.2   Surface charge, average hydrodynamic diameter and particle size distribution

A Zetasizer (ZEN3600; $\lambda = 633$ nm; Malvern Instruments, UK) was used to determine zeta potential and Z-average hydrodynamic diameter of the samples, as described in Chapter 3. Zeta potential as a function of pH was measured in the range pH 3-10 for the Fe_2O_3 NPs (200 mg/L), HA (50 mg/L) and SRNOM (50 mg/L). At the end of the adsorption experiment (i.e. after 24h stirring), solutions of DOM-coated Fe_2O_3 NPs were pH adjusted (i.e. from pH 3 to pH 10) and zeta potential measurements were carried out at different pH.

The average hydrodynamic diameter of the DOM-coated Fe_2O_3 NPs was measured at 1 h, 2 h, 5 h and 10 h time intervals. Three aliquots were measured per sample, to obtain the reported values and associated standard deviations.

FlFFFa (Postnova analytics, Germany) was used to assess the distribution of hydrodynamic diameters in the samples. FlFFF principles and methods are described in Chapter 3. At least three independent replicates were run per sample and the data were averaged. In general, good agreement among the replicates was observed (i.e. peak heights differing by less than

5 % and peak maxima differing by less than 2 %). The FlFFF operating conditions are summarised in Table 5-1.

Measurements were conducted after 1h, 2h, 5h and 10h of stirring time using ultrapure water at pH 7 for the mobile phase for all samples except the bare Fe_2O_3 NPs which were run in ultrapure water at pH 4 due to their instability at pH 7. This pH (i.e. pH 7) was chosen for the DOM-coated Fe_2O_3 NPs as it falls within the range of groundwater pH (i.e. about 5.5 to 8.5) (Chi and Amy 2004) and this coated nanoparticles are likely to be used for the purpose of soil and groundwater remediation. FlFFF measurements were made on the same samples at the same time points as for DLS experiments to ensure data comparability.

Table 5-1: Summary of the different FlFFF operating conditions used for particle size determination.

Sample	Channel flow (mL/min)	Cross flow (mL/min)	Mobile phase
Fe_2O_3NPs – 200 mg/L			Ultrapure water at pH 4
HA and SRNOM – 50 mg/L	1	0.5	Ultrapure water at pH 7
HA-coated Fe_2O_3NPs			Ultrapure water at pH 7
SRNOM-coated Fe_2O_3NPs		0.15	Ultrapure water at pH 7

Latex beads of 22 nm, 58 nm and 100 nm (Postnova Analytics, Germany) were used to create calibration curves from which hydrodynamic diameters of the particles were determined. These curves correlated the retention time to particle size. Calibration curves were established for all mobile phases and conditions (change in cross flow or channel flow) used in this study and regularly (i.e. once a week) re-drawn to check the accuracy of data.

5.2.3.3 *Extended stability of DOM-coated Fe_2O_3 NPs and disaggregation study*

The stability of DOM-coated Fe_2O_3 NPs was assessed by measuring their size distribution by FlFFFb (Wyatt Technology, Dernbach, Germany) after 14 days, without any perturbation, following first measurements.

After measuring the size of the aggregates formed during this 14-day period, a vortex mixer (VELP Scientifica, 1 min, 3000 rpm) was used to induce disaggregation to assess the

stability of the formed aggregates and agglomerates. The mobile phase used for the disaggregation study was ultrapure water at pH 7. Operating conditions were channel flow of 1 mL/min and crossflow of 0.5 mL/min.

5.2.3.4 *Characterisation of binding properties between Fe_2O_3 NPs and DOM*

HPSEC analysis

The size distributions of DOM solutions before and after adsorption on Fe_2O_3NPs were determined by HPSEC. HPSEC is a low resolution chromatography technique which separates particles on the basis of molecular hydrodynamic size. In an HPSEC column, the smaller molecules are trapped in the pores of the gel. The larger molecules simply pass by the pores as they are too large to enter it. Therefore, the larger molecules will elute quicker than smaller ones (Mori and Barth 1999). HPSEC used in this study (Shimadzu, Japan) consisted of a glycol-functionalised silica gel column (Protein-Pak 125, Waters, USA) with fluorescence detector (RF-10A, Shimadzu, Japan). Standard polystyrene sulfonates (PSS: 210, 1800, 4600, 8000, and 18000 Da, Polymer Standards Service, Germany) were used to calibrate the equipment. Details of the measurement methodology are given elsewhere (Shon et al. 2004). A flow rate of 0.7 mL/min was used. All injection volumes of the samples were 100 μL. Samples used in HPSEC experiments were the same as for DLS and FlFFF experiments to ensure data comparability.

FTIR analysis

Chemical bonding information on metal-oxygen, hydroxyl, and other functional groups was obtained with FTIR spectroscopy using the IRAffinity-1 (FTIR-8400S, Shimadzu, Japan). Infrared spectra were recorded on ZnSe through plate (PIKE technologies, USA). Each spectrum is the sum of 25 scans at a resolution of 2 cm^{-1}. Samples of bare and coated Fe_2O_3 NPs (after 24 h stirring) were completely dried before performing measurements. For

the coated NPs, samples were first centrifuged and the supernatant discarded to remove the excess of DOM.

5.3   Results and discussion

5.3.1   Surface charge of DOM-coated Fe_2O_3 NPs

Figure 5-1 shows the zeta potential profiles of Fe_2O_3 NPs alone (200 mg/L), DOM-coated Fe_2O_3 NPs and DOM alone (50 mg/L), as a function of pH, ranging from 3 to 10. The zeta potential profile of Fe_2O_3 NPs showed that the nanoparticles were highly positively charged at low pH values (i.e. pH 3-5). The zeta potential decreased as pH increased from 5 to 9 and became highly negative above pH 10 with a point of zero charge (PZC) at around pH 7. This value is within the range of PZC values found in the literature for Fe_2O_3 NPs (Tombácz et al. 2004; Illes and Tombácz 2006; Baalousha et al. 2008; Baalousha 2009; Hu et al. 2010).

The zeta potential profiles of HA and SRNOM indicate that they are negatively charged over the whole pH range. This is due to the fact that DOM macromolecules carry several negatively charged functional groups, including carboxylic and phenolic groups (Hajdú et al. 2009; Hu et al. 2010; Dickson et al. 2012). The zeta potential profiles of DOM-coated Fe_2O_3 NPs also remain negative across the whole pH range tested and are quite similar to the zeta potential profiles of the DOM. This indicates that both HA and SRNOM cover the surface of the bare Fe_2O_3NPs, providing electrostatic stabilisation over a wide range of pH.
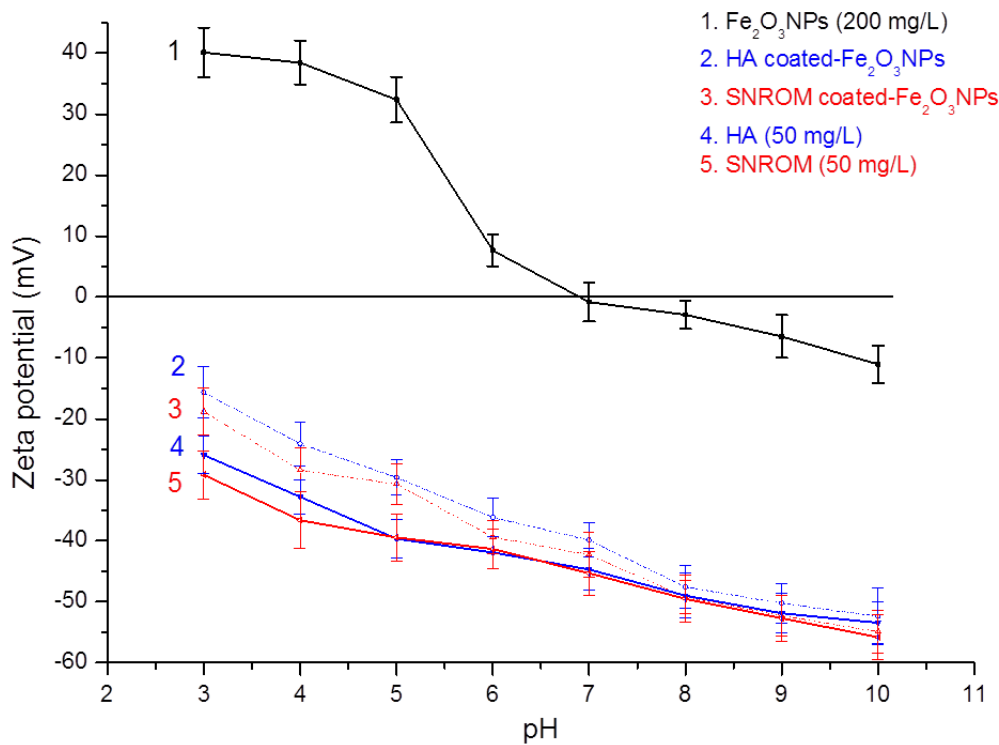
Figure 5-1: Zeta potential profiles of Fe$_2$O$_3$NPs, DOM-coated Fe$_2$O$_3$NPs, HA and SRNOM.

5.3.2 Particle size and size distribution analysis by FlFFF and DLS

The hydrodynamic sizes of the bare and DOM-coated nanoparticles were firstly determined by FlFFF (Figure 5-2). Measurements were made at pH 7 for the DOM-coated Fe$_2$O$_3$ NPs to assess their stability under groundwater conditions (i.e. groundwater pH are usually within the range 5.5-8.5 (Chi and Amy 2004)). Moreover, at this pH, the DOM-coated Fe$_2$O$_3$ NPs are highly negatively charged (as displayed in Figure 1) which should theoretically enhance electrostatic stabilisation compared to pH 4.

The FlFFF data allow a direct comparison between the bare and coated particles. By comparing the fractograms of the bare and coated Fe$_2$O$_3$ NPs (Figure 5-2), two key observations can be identified. Firstly, there was a significant increase in the void peak UV signal (i.e. from 0.06 a.u. for the bare nanoparticles to about 0.35 a.u. and 0.75 a.u. for all HA-coated and SRNOM-coated nanoparticles respectively). This may be caused by

unadsorbed DOM macromolecules which are considerably smaller than the Fe_2O_3 NPs. The applied cross flow was too low to retain the unadsorbed DOM, and so the elution of unretained DOM was indicated by the larger void peak. When the stirring time increased from 1 h to 10 h (i.e. labelled (c) to (f) on Figure 5-2), a decrease in the void peak signal was observed on the fractograms of both DOM-coated Fe_2O_3 NPs. This decrease in the void peak signal can be explained by the increasing adsorption of DOM onto the surface of the Fe_2O_3 NPs resulting in decreasingly fewer free DOM species in the solution and therefore less eluted DOM in the void peak.
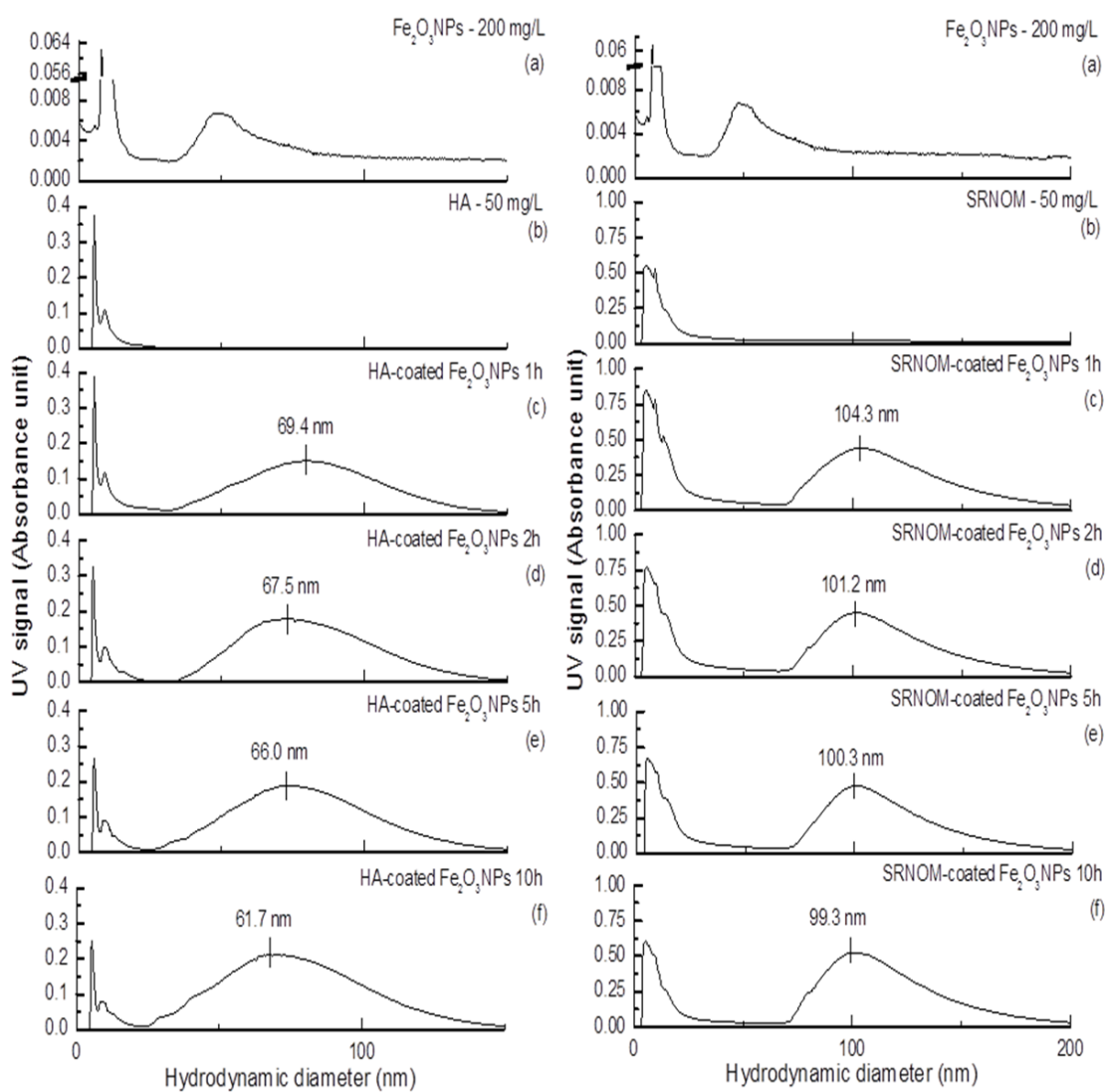
Figure 5-2: FlFFF fractograms of HA-coated and SRNOM-coated Fe_2O_3NPs after different mixing time at pH 4.

141

The second observation identified in the FlFFF data is a small shift toward smaller sizes of the peak maxima (by comparing fractograms (c) with fractograms (d) to (f) for both coated nanoparticles), probably indicating the formation of more stable coated particles. The shift is more important for the HA-coated Fe_2O_3 NPs (i.e. peak maxima decreasing by 11.1 % against 4.8 % for the SRNOM-coated Fe_2O_3 NPs), which may indicate that the SRNOM-coated Fe_2O_3 NPs reach equilibrium more rapidly (which was confirmed by the adsorption experiments displayed on Figure 3a and 3b). The broadening of the peak by comparing the fractograms of the bare (i.e. fractograms (a)) and coated Fe_2O_3 NPs (i.e. fractograms (c) to (f)) may be caused by the coated particles having different size and conformation. It should also be noted that the peaks in the fractograms of HA-coated Fe_2O_3 NPs are broader than those of SRNOM-coated Fe_2O_3 NPs. This may indicate that SRNOM-coated Fe_2O_3 NPs are more stable since the size distribution of the coated particles is narrower, indicating less aggregation. On the fractograms of both coated Fe_2O_3 NPs, a second peak was observed between the void peak and the elution peak. This can be attributed to the formation of small aggregates of DOM macromolecules. In fact, the coated-particles were prepared at pH 4 and at this pH, both HA and SRNOM are less negatively charged than at higher pH (as displayed in Figure 5-1) which could promote their aggregation.

These FlFFF results were compared with those from DLS. In general, the sizes measured by DLS (Table 5-2) were larger than FlFFF, which is in accordance with the results obtained in Chapter 4. DLS is known to be extremely sensitive to larger particles and a very small number of large particles (e.g. due to the formation of aggregates), can induce a substantial shift toward larger sizes (Domingos et al. 2009). Moreover, DLS measurements were made at pH 4, pH at which the coated nanoparticles are less negatively charged which might promote the formation of some aggregates.

Table 5-2: Z-average hydrodynamic diameter of bare Fe$_2$O$_3$NPs, HA-coated Fe$_2$O$_3$NPs and SRNOM-coated Fe$_2$O$_3$NPs as determined by DLS (at pH 4 for bare Fe$_2$O$_3$NPs and at pH 7 for DOM-coated Fe$_2$O$_3$NPs).

	Z-average hydrodynamic diameter (nm)	
Bare Fe$_2$O$_3$NPs	63 ± 4	
Mixing time	**HA-coated Fe$_2$O$_3$NPs**	**SRNOM-coated Fe$_2$O$_3$NPs**
1h	95 ± 4	127 ± 5
2h	91 ± 3	124 ± 4
5h	90 ± 3	124 ± 3
10h	89 ± 2	122 ± 3

Despite differing in absolute values, size measurements by FlFFF and DLS show similar trends. Both the hydrodynamic diameter (from FlFFF) and z-average hydrodynamic diameter (from DLS) of the coated particles slightly decreased with increasing stirring time. Also, both FlFFF and DLS results indicate that the size of the SRNOM-coated NPs is larger than those of HA-coated NPs. This is consistent with SRNOM having a larger molecular weight than HA (as shown on the HPSEC chromatograms in Figure 5-4).

5.3.3 DOM adsorption to Fe$_2$O$_3$ NPs

The adsorption kinetics of both HA and SRNOM to Fe$_2$O$_3$ NPs (Figure 5-3a) show a steep initial slope before reaching a plateau at equilibrium, implying a high affinity of binding sites for both HA and SRNOM at pH 4 (Kang and Xing 2008). Illés and Tombácz (2004) demonstrated that the adsorption of DOM is favourable under acidic conditions where negatively charged functional groups of DOM are attracted by the positively charged Fe$_2$O$_3$ NPs.

The adsorption data were then fitted with the pseudo second-order kinetic model as shown in Figure 5-3b. The results indicated that the correlation coefficient (i.e. R^2) for both DOM was higher than 0.999 and the calculated equilibrium adsorption capacity (i.e. q_e) was consistent with the experimental results for both HA and SRNOM. This suggested that kinetic data are

well described with pseudo second-order kinetic model, indicating that the rate-limiting step may be chemical sorption (Wu et al. 2001).

Finally, the adsorption of SRNOM onto Fe_2O_3 NPs was faster than the adsorption of HA (Figure 5-3), as equilibrium was reached after only 60 minutes compared with 120 minutes for HA and as indicated by the higher value of the constant k related to the adsorption rate which is consistent with the FlFFF data.
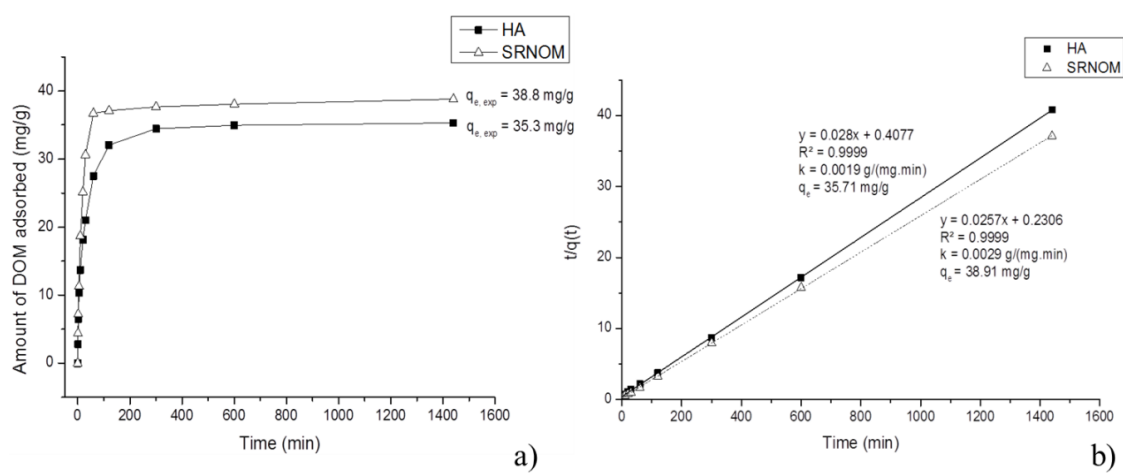
Figure 5-3: Adsorption kinetics of HA and SRNOM on Fe_2O_3NPs at pH 4 (a) experimental results and (b) pseudo second-order kinetic model.

5.3.4   Characterisation of Fe_2O_3 NPs-bound DOM

DOM is a mixture of heterogeneous components having different molecular weight and chemical composition. The polydispersity of DOM is supposed to be responsible for the adsorption of a preferential size fraction of DOM (Gu et al. 1995). It is thus interesting to investigate which fraction of DOM is preferentially adsorbed onto the Fe_2O_3 NPs surface. A possible approach is to compare the size distribution of the original DOM with the DOM-coated particles using HPSEC.

Figure 5-4 displays the HPSEC chromatograms of HA, SRNOM, and both HA-coated and SRNOM-coated Fe_2O_3NPs. The chromatograms of both HA and SRNOM have multiple peaks, indicating the polydispersity of the DOM. The molecular weights of SRNOM range

144

from 250 Da (organic acids) to 20,000 Da (high molecular weight compounds (HMW), such as colloids) against 250 Da to 1,000 Da for HA, with the highest fraction at 850-1,000 Da (humic substances) for both. This is in accordance with the general feature of DOM (Shon et al. 2005). The peak at a retention time of 10 minutes, which only appeared in the SRNOM chromatograms, suggests that SRNOM does possess higher molecular weight than HA. The peak at 250 Da, present in both chromatograms, has a higher intensity for HA indicating that HA has a greater amount of low-molecular weight components. The peak at 36,000 Da appearing only on the HPSEC chromatograms of the DOM-coated NPs can be attributed to the coated Fe_2O_3 NPs. Finally, the peak at 250,000 Da is probably related to the formation of small aggregates of coated particles and has higher intensity in the HA chromatograms. This can be related to the broader peaks in the FlFFF fractograms (Figure 5-2).

By comparing the chromatograms between DOM and DOM-coated nanoparticles, the intensity of the peaks ranging from 850 Da to 20,000 Da (i.e. humic substances and HMW molecules) decreased significantly, while the peak at 250 Da (i.e. organic acids) remained relatively high. As the measured fluorescence response is proportional to the DOM concentration, the concentrations of both HMW compounds and humic substances showed a significant decrease during adsorption. This demonstrated the preferential adsorption of both high molecular weight DOM and low molecular weight humic substances on the metal oxide surface. However, the smallest molecular weight compounds in the range of 250 Da were not adsorbed onto Fe_2O_3 NPs. Previous studies also indicated the preferential adsorption of high molecular weight DOM onto metal oxide surfaces (McKnight et al. 1992; Vermeer and Koopal 1998; Zhou et al. 2000).
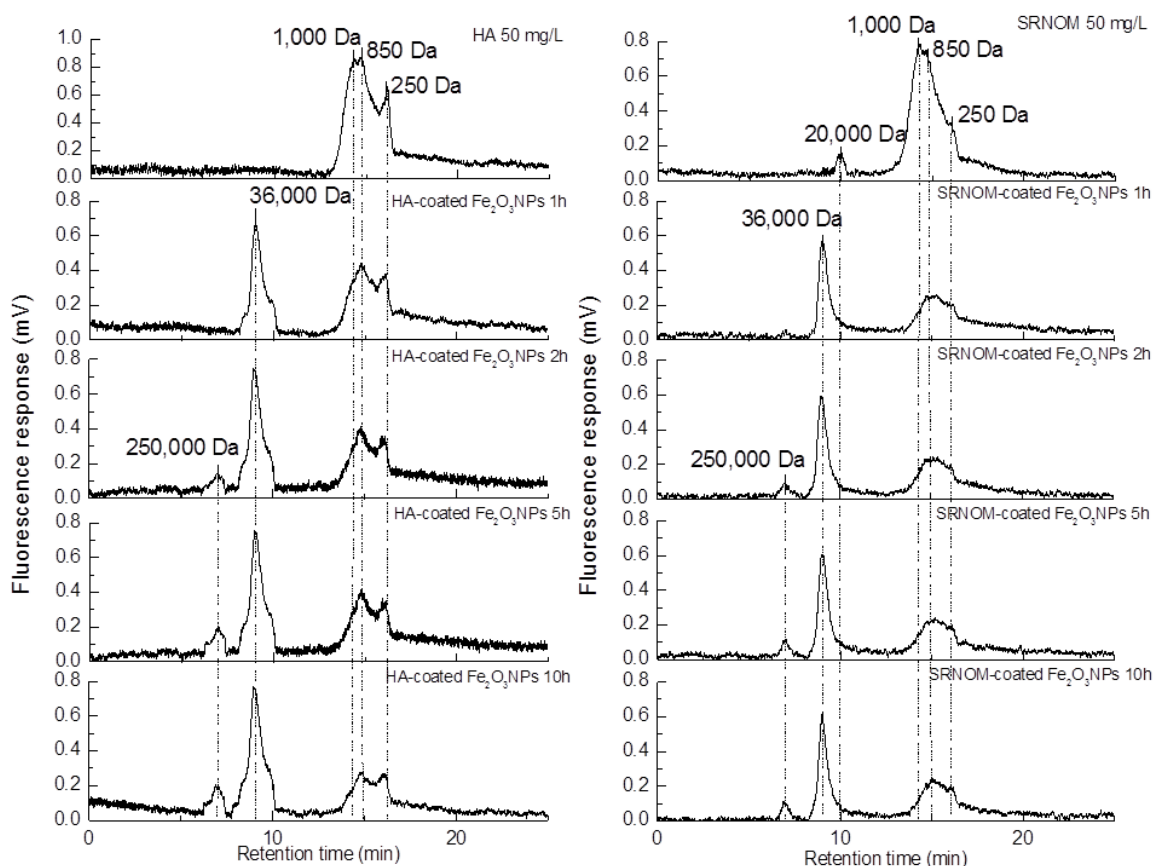
Figure 5-4: HPSEC chromatograms of HA-coated Fe₂O₃NPs and SRNOM-coated Fe₂O₃NPs after different mixing time at pH 4.

To further investigate the interactions between DOM and Fe_2O_3 NPs, FTIR spectra of bare and coated Fe_2O_3NPs were used to identify the physico-chemical binding mechanisms (Figure 5-5).

No apparent peaks can be assigned in the bare Fe_2O_3 NP spectra. The O-H stretch observed at about 3400 cm^{-1} may be due to the presence of small amount of water in the sample during analysis. The spectra of both DOM-coated Fe_2O_3 NPs show a C=O stretch at apprroximatley 1600 cm^{-1} which may indicate the carboxylate anion interacting with the iron oxide surface, since the C=O stretches in free carboxylic acid would be above 1700 cm^{-1} (Yantasee et al. 2007). As the peak of the C=O stretches in the SRNOM-coated Fe_2O_3 NPs spectrum have higher intensity (i.e. compared to the spectrum of HA-coated Fe_2O_3 NPs), it may be concluded that this type of bond is more pronounced between SRNOM and

146

Fe$_2$O$_3$ NPs than between HA and Fe$_2$O$_3$ NPs. The broad O-H stretch peak present in both DOM-coated Fe$_2$O$_3$ NPs spectra could indicate the occurrence of hydrogen bonding resulting from the interaction between the positively charged Fe-OH$^+$ and the negatively charged DOM in acidic conditions (Lin et al. 2010). In fact, many studies have demonstrated that the adsorption of DOM on the surface of Fe$_2$O$_3$ NPs is mainly governed by Coulombic interactions via ligand-exchange reactions below the pH of PZC (Filius et al. 2000; Illés and Tombácz 2004).
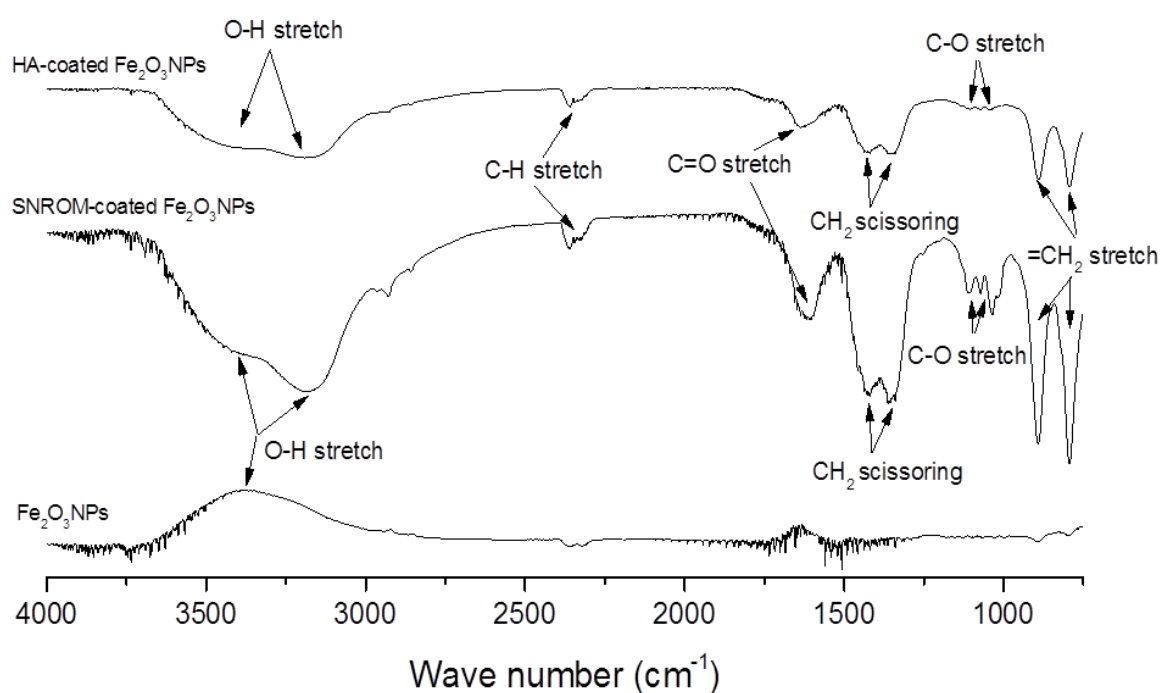
Figure 5-5: FTIR spectra of bare Fe$_2$O$_3$NPs, HA-coated Fe$_2$O$_3$NPs and SRNOM-coated Fe$_2$O$_3$NPs.

5.3.5 Stability of DOM-coated Fe$_2$O$_3$ NPs

The stability of the coated particles was assessed by measuring their size 14 days after the preparation of the "fresh coated nanoparticles" (i.e. 14 days after the 24 hours mixing time) without any modifications. Figure 5-6 shows the FlFFF fractograms of both DOM-coated Fe$_2$O$_3$ NPs. The size of the HA-coated Fe$_2$O$_3$ NPs was approximately 200 nm for all the samples, while SRNOM-coated Fe$_2$O$_3$ NPs were larger at 250 nm for all samples. These

147

values are greater than the size obtained with "fresh samples" (i.e. around 60-70 nm for HA-coated Fe_2O_3 NPs and around 100-105 nm for SRNOM-coated Fe_2O_3 NPs), indicating the formation of some aggregates with time. This also suggests that the stirring time has no influence on the stability of the coated nanoparticles. Increasing the stirring time after one hour did not improve the stability of the coating by providing increased steric stability, which would have caused entropically unfavourable conditions and prevented the coated nanoparticles from aggregation (Tiller and O'Melia 1993; Illés and Tombácz 2004; Silva et al. 2012; Silva et al. 2012; Silva et al. 2012).
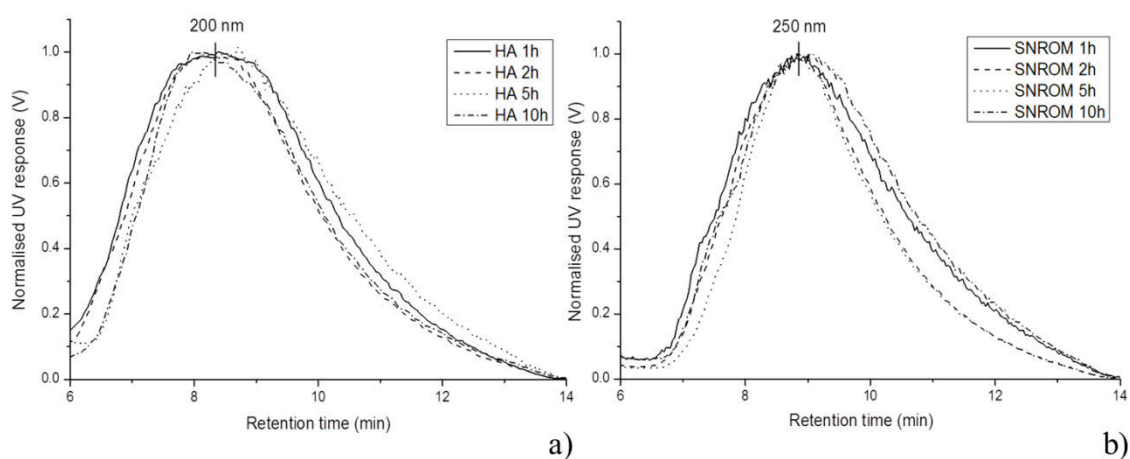
Figure 5-6: FlFFF fractograms of (a) HA-coated Fe_2O_3 NPs and (b) SRNOM-coated Fe_2O_3 NPs after 2 weeks.
(N.B.: 1 h, 2 h, 5 h and 10 h denote the mixing time originally used to prepare the different samples)

The stability of the formed aggregates was then assessed by studying the effect of vortex mixing on the disaggregation of the coated nanoparticles aggregates. Studying the stability of the formed aggregates is crucial for application in soil and groundwater remediation. In fact, for this application, nanoparticles are usually applied directly on-site via injection (Cundy et al. 2008). We demonstrated that after a short period of time (i.e. few days), the coated-particles aggregated slightly which could decrease their mobility once injected in the subsurface. Therefore, finding simple and rapid methods to disaggregate and stabilise the prepared coated-particles prior to their injection on-site is essential.

For HA-coated NPs (Figure 5-7a), the effect of vortex mixing was that the size of the aggregated samples decreased from 200 nm to 70 nm i.e. back to the initial size of the HA-coated sample, after 1 min of vortex mixing. This indicates that the HA-coated Fe_2O_3 NPs were agglomerated rather than aggregated and they were only held by weak van der Waals forces (Jiang et al. 2009). The results also suggests that the bonding of HA-Fe_2O_3 NPs is strong, otherwise vortex mixing the sample would have also broken the bonds between HA and the surface of Fe_2O_3 NPs.

For SRNOM-coated Fe_2O_3 NPs (Figure 5-7b), the same conditions were used and the results showed the presence of 2 peaks in the fractogram of the coated nanoparticles after vortex mixing. This indicates that only a fraction (about 50 %) of the sample was disaggregated (i.e. same size as the original samples) but the rest remained unchanged. This could be explained by the structure of the aggregates which may have a substantial influence on the disaggregation of nanoparticles (Christian et al. 2008). In fact, the aggregate structure (i.e. the conformation and porosity) can vary significantly with the concentration and type of DOM. A recent study by Baalousha et al. (2008) demonstrated that, in the absence of HA, Fe_2O_3 NPs formed open and porous aggregates, whereas in the presence of HA, they formed compact aggregates which were difficult to disaggregate without applying any exterior mechanical forces. SRNOM has a more complex structure than HA, with more HMW molecules; therefore the structure of the formed aggregates may be even more complex, making the disaggregation process more difficult.
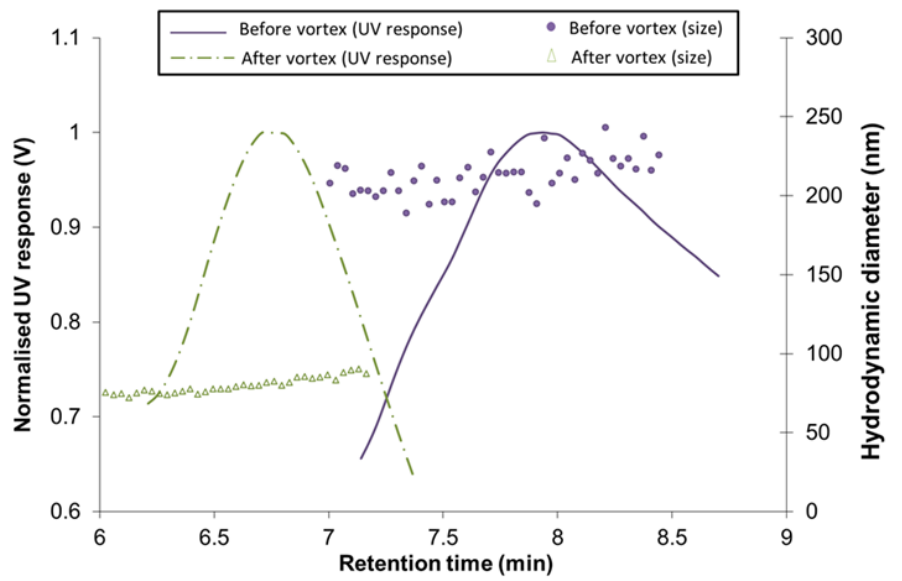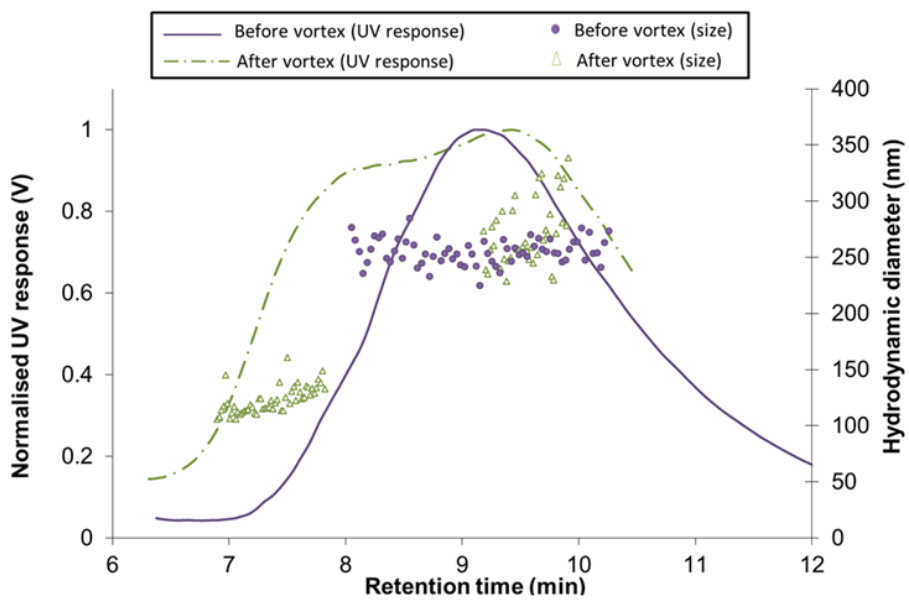
Figure 5-7: Effect of vortex on the disaggregation of (a) HA-coated Fe$_2$O$_3$NPs and (b) SRNOM-coated Fe$_2$O$_3$NPs.

5.4   Conclusions

Understand the interactions between DOM and Fe$_2$O$_3$ NPs is essential to be able to predict their fate and behaviour once applied in the environment. In this study, DOM-coated

Fe_2O_3 NPs were characterised with a range of techniques. Fe_2O_3 NPs proved to be a particularly good adsorbent for both HA and SRNOM under acidic conditions. The main interaction arises from a ligand exchange reaction between oppositely charged particles; however, carboxylate anions interacting with the iron oxide surface was also important between SRNOM and Fe_2O_3 NPs. Preferential adsorption for higher molecular sized components was observed which could potentially lead not only to electrostatic stabilisation but also to steric stabilisation by causing entropically unfavourable conditions when the coated particles come closer to one another.

Finally, an aggregation and disaggregation study revealed that after 14 days, small aggregates were formed but they remained in the nanosize range. HA-coated Fe_2O_3NPs formed agglomerates which were easily disaggregated using a vortex mixer and returned to their initial state. The SRNOM-coated Fe_2O_3 NPs formed more stable aggregates, where only a fraction of the coated nanoparticles were recovered.
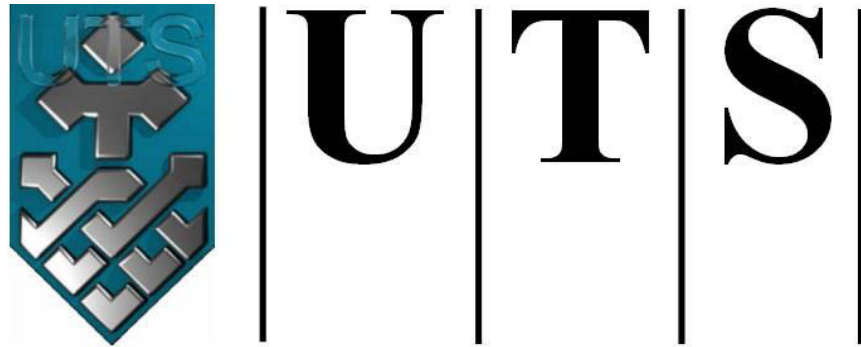
University of Technology Sydney
FACULTY OF ENGINEERING

CHAPTER 6

RADIOISOTOPE LABELLING COMBINED WITH ELEMENTAL ANALYSIS TO INVESTIGATE THE MOBILITY OF IRON-BASED NANOPARTICLES AND ITS POTENTIAL TO CO-TRANSPORT CONTAMINANTS

6.1 Introduction

One of the obstacles impeding more widespread utilisation of nZVI for *in situ* remediation is its limited mobility in natural porous systems such as soils, regolith, and aquifers. This is mainly due to particle aggregation and sedimentation, and related problems such as pore blocking and deposition of nZVI onto the granular porous matrices. Together, these processes can limit the effectiveness of *in situ* remediation (Schrick et al. 2004; Quinn et al. 2005; He and Zhao 2007; Saleh et al. 2008), making nZVI mobility and transport a topic of current research interest. Although increasing the mobility of nZVI may be desirable in order to maximise the zone of remediation influence, it also raises the possibility for undesirable side-effects; in particular, the potential for nZVI to adsorb and transport contaminants away from the primary zone of contamination (Mueller and Nowack 2009). In fact, while the efficiency of a remediation treatment requires sufficient mobility of substantial nZVI, the enhanced transport of contaminant off site, even in small quantities, is of concern. Previous research has demonstrated enhanced transport of low-solubility contaminants by naturally occurring nanoparticles (i.e. colloids) (de Jonge et al. 2004) and the ability of nZVI to sorb soil contaminants has already been reported for As, Cr and other inorganic contaminants (Schorr 2007). Together, these findings suggest that nZVI could, in some cases, promote the subsurface movement and dispersion of contaminants; a possibility that requires further assessment.

Many studies have focused on the use of surface modifiers such as polymers, polyelectrolytes or surfactants to decrease the aggregation and deposition of nZVI and enhance particle mobility (De Gennes 1987). Surface modification provides electrostatic and/or steric forces that counter the strong inter-particle magnetic attractive forces and thereby increase colloidal stabilisation (Wiesner and Bottero 2007). Various surface modifiers have been proposed to improve nZVI stability, including carboxymethyl cellulose (CMC) (e.g. (Kocur et al. 2012; Raychoudhury et al. 2012; Basnet et al. 2013; Jung et al.

2014; Raychoudhury et al. 2014)), poly(acrylic acid) (PAA) (e.g. (Jiemvarangkul et al. 2011; Laumann et al. 2013; Laumann et al. 2014)), poly(styrenesulfonate) (PSS) (Phenrat et al. 2008; Cirtiu et al. 2011), surfactant sodium dodecylbenzenesulfonate (SDBS) (Saleh et al. 2007; Saleh et al. 2008) and triblock copolymer (Saleh et al. 2007; Saleh et al. 2008; Kim et al. 2012). Many studies have already demonstrated reduced aggregation and/or improved transport in saturated porous media when polymers, polyelectrolytes or surfactants are used to stabilise nZVI suspension (e.g. (He et al. 2007; Saleh et al. 2007; Phenrat et al. 2008; Saleh et al. 2008; Tiraferri et al. 2008; Tiraferri and Sethi 2009; Cirtiu et al. 2011; Basnet et al. 2013; Laumann et al. 2014; Raychoudhury et al. 2014)).

Most studies have investigated nZVI transport in highly idealised systems consisting of repacked, homogeneous, coarse texture porous media (e.g. (Kocur et al. 2012; Raychoudhury et al. 2012; Basnet et al. 2013; Raychoudhury et al. 2014)) or even glass beads (e.g. (Kanel et al. 2007; Lin et al. 2010)). Furthermore, cleaning and drying procedures are often used to remove both metallic and organic impurities (e.g. (Raychoudhury et al. 2012; Basnet et al. 2013)). These "ideal" conditions, although not representative of real natural conditions, facilitate the detection and quantification of nZVI mobility. Only a few studies have considered the heterogeneity of natural porous media and focused on the individual or combined effects of different physical and chemical components (i.e., the effect of pH, natural organic matter (NOM), clay content, etc.) in order to understand factors affecting the mobility of nZVI. These studies showed that the presence of NOM can enhance the mobility of polymer-stabilised nZVI due to repulsive electrosteric forces between the NOM macromolecules and the negatively-charged surface coating (Johnson et al. 2009; Jung et al. 2014). Kim et al. (2012) demonstrated that in the pH range 6-8, there was greater deposition of CMC-nZVI onto clay minerals due to the charge heterogeneity on clay mineral surfaces. Finally, Laumann et al. (2013) studied the effect of

carbonate minerals, which often predominate in aquifers, and found reduced mobility of PAA-nZVI in the presence of carbonate minerals.

A more realistic, yet more complex, approach would be to assess the mobility of polymer-stabilised nZVI in real intact soil cores. This would help significantly in the development of effective remediation materials as well as in risk assessment. However, this task remains extremely challenging due to the high background of natural iron colloids present in soils and other environmental systems. This impasse can be overcome however by labelling the ENPs in order to differentiate them from the natural colloids. This approach can make the ENP of interest easily detectable even in complex matrices containing relevant concentrations of environmental nanoparticles (Zänker and Schierz 2012). Possible labelling methods for ENP tracking include fluorescence labelling where a dye is attached to the surface of the ENPs (Kirchner et al. 2005), radiolabeling with γ or β emitters (Ferguson et al. 2008; Oughton et al. 2008; Petersen et al. 2008; Abbas et al. 2010; Gibson et al. 2011; Hildebrand and Franke 2012), and isotope labelling with stable isotopes (Gulson and Wong 2006; Croteau et al. 2011; Dybowska et al. 2011). The labelling process can be performed directly during the nanoparticle synthesis by using a labelled precursor or via post-synthesis manipulation (Zänker and Schierz 2012), however labelling during synthesis is preferable.

The overall objectives of this study were:

- To synthesise radiolabelled ^{59}Fe-CMC-nZVI and compare its mobility with commercially available PAA-nZVI in intact soil cores. The mobility of the commercial nZVI was investigated using an ICP-MS method while ^{59}Fe-CMC-nZVI mobility was assessed by gamma counting; allowing the evaluation and comparison of both methods.

- To determine the retention profiles of radiolabelled nZVI in the soil columns after the mobility experiments.

- To assess the potential of nZVI to co-transport contaminants in Chromated-Copper-Arsenate (CCA)-contaminated soil by coupling gamma counting and ICP-MS measurements.

This chapter is an extension of a research article submitted by the author in Environmental Pollution.

6.2 Experimental

6.2.1 Commercial N25S and ^{59}Fe-CMC-nZVI synthesis

Commercial NANOFER 25S (N25S) was supplied by NANOIRON, s.r.o. (Czech Republic) in the form of a slurry with a mean primary particle diameter below 50 nm and a total iron concentration of 20 % (w/w) (as provided by the manufacturer). These iron particles are modified by an inorganic iron oxide layer and an organic PAA coating as described by Kadar et al. (2011). Prior to the experiments, a freshly received stock solution was prepared under anoxic atmosphere with a final concentration of 50 g/L and sealed in a glass bottle.

CMC-nZVI was synthesised according to the methods described by Cirtiu et al. (2011). The isotopic labelling was done during the first stage of the synthesis by spiking 160 μL (i.e. 260 MBq) of ^{59}FeCl$_3$ solution (Perkin Elmer, radionuclide purity of 99%, specific activity: 1623.88 MBq/mL) into 800 mL of 0.125 M FeSO$_4$.7H$_2$O (Sigma Aldrich, Australia) solution. The resulting specific activity of the labelled nZVI was 61.5 Bq/mg. This solution was then mixed for 5 minutes before adding 800 mL of a 1.75% (w/v) Na-CMC (90 K, Sigma Aldrich, Australia) solution which was mixed thoroughly for 30 minutes. NaBH$_4$ (Sigma Aldrich, Australia) solution was then added drop wise at a rate of 5 mL/min under anoxic atmosphere. The ratio of [Fe^{2+}]/[BH$_4^-$] was set at 1:2. The mixture was stirred for an additional 30 minutes. The final nZVI solution was sealed in a bottle under anoxic conditions and mixed at 135 rpm on a shaker overnight.

In order to remove the excess chemicals from the synthesis, the final nZVI solution was placed on a magnet for 5 hours to settle and the supernatant was discarded to obtain a concentrated "purified" stock solution. The recovery rate was determined by analysing both the supernatant and the stock solution with a gamma radiation counter (2480 Wizard[2]-3, Perkin Elmer). The recovery was 81% and the final stock solution concentration was adjusted to 50 g/L.

^{59}Fe-CMC-nZVI stock solution was characterised in terms of particle size, morphology and specific activity as described below.

Particle size distribution of the freshly prepared and purified CMC-nZVI was determined using dynamic light scattering (380ZLS, Nicomp, USA). Results are gathered in Table 6-1. Measurements were also repeated after 3 days and did not show significant differences, with the dominant pick (99% - number-weighted) ranging from 40 to 87 nm.

The morphology of the particles was also examined using scanning electron microscopy (Quanta 450, FEI, USA) with FEG source under high vacuum (operating conditions: HV = 10 kV; WD = 5-15 mm). The SEM images showed that the CMC-nZVI were spherical and present as aggregates ranging in size from nanoscale to microscale (Table 6-1). The presence of large aggregates is most likely due to the sample preparation (i.e. drying the aqueous suspension on the grid) and therefore SEM images are only used to provide information about the morphology of the primary particles and aggregates.

Finally, the specific activity of the stock solution was determined with a gamma radiation counter (2480 Wizard2-3, Perkin Elmer) and ICP-MS (Agilent 8800 Triple Quadrupole, Agilent Technologies, CA, USA). The stock solution was first acidified with HCl (99% purity) and then diluted (1:4) with MQ water before being analysed by both instruments.

Table 6-1: Characteristics of the lab-synthesised ^{59}Fe-CMC-nZVI (SEM image, Z-average hydrodynamic diameter and specific activity)
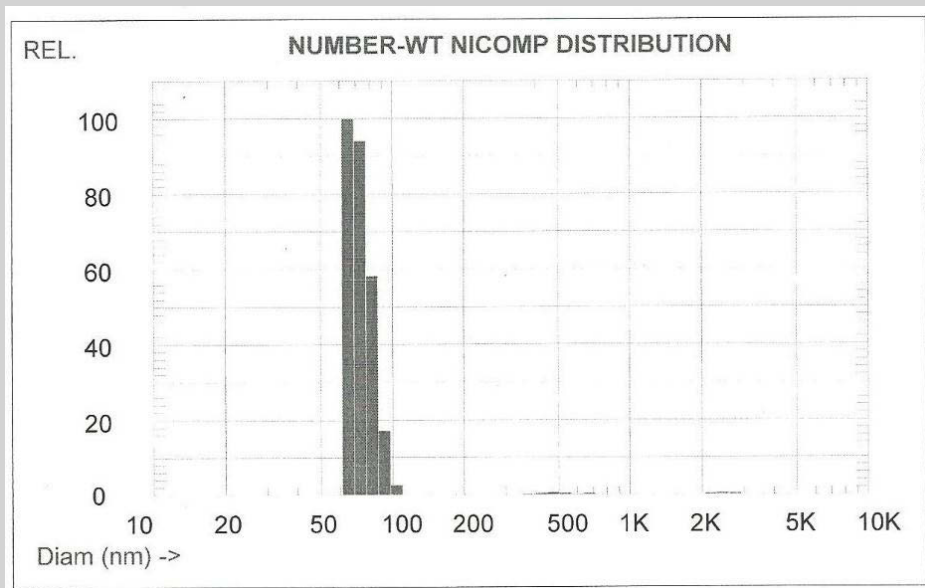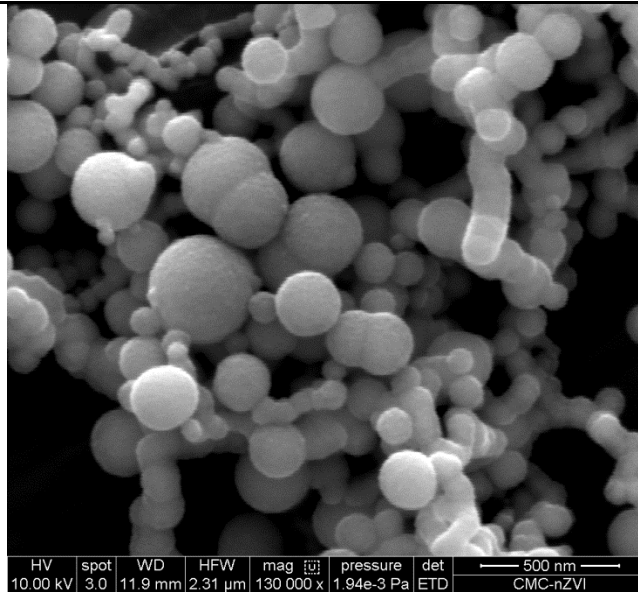
Z-average hydrodynamic diameter (number-weighted): **72.1 ± 7.8 nm**

Specific activity of the stock solution as measured by gamma counter analysis: **61.5 Bq/mg**

6.2.2 Column transport experiments

6.2.2.1 Soil type and experimental design

Two South Australian topsoils were collected for this study; an uncontaminated sand-loamy soil from Mount Compass (7 intact soil cores were extracted onsite) and a CCA-contaminated sand-loamy soil collected from a timber storage area in the Barossa Valley (3 intact soil cores were extracted onsite). CCA has been widely employed worldwide as a wood preservative to expand the lifespan of treated wooden structures exposed to weather (Hingston et al. 2001). Various studies have, however, demonstrated that the CCA metals/metalloids may leach when the treated wood is exposed to environmental conditions. This ultimately results in elevated concentration of chromium, copper and arsenic in the surrounding environment of the CCA-treated wooden structure (Hopp et al. 2008).

The detailed characteristics of these two soils can be found in Table 6-2. From this point forward, the two topsoils will be designated as MC and CCA soils.

Soil cores were 15 cm long with an inner diameter of 10 cm. A nylon mesh (200 μm opening size) was secured over the bottom of the column to hold the soil in place. The soil columns were first saturated from below for 24 hours using artificial soil pore water (Glæsner et al. 2012) and then drained and equilibrated overnight to ensure similar initial conditions for all columns. The soil cores were then connected to an irrigation system in which peristaltic pumps (Masterflex L/S, Cole Palmer, Australia) were used to ensure a constant flow rate of 1 mm/hr throughout the experiments. This low rate is common for extended rainfall events in South Australia (Glæsner et al. 2012). Artificial rainwater (Oorts et al. 2007) was used for leaching in this study. Baseline experiments (i.e. prior to injecting nZVI) were conducted for three days, after which the irrigation was stopped for 2 hours before applying the nZVI. Leachates from the baseline study were collected regularly and stored in the dark at 4°C until analysed. The nZVI suspensions (i.e. 50 g/L stock solution) were spiked uniformly on

top of the column (i.e. in the first 2 cm which represents about 200 g of soil considering a soil density of 1.3 g/cm^3) at the beginning of each experiment at an application rate of 1% (w/w) (i.e. approximately 2 g of nZVI injected). The irrigation system was started immediately after the injection of nZVI and leaching experiments were conducted for a further three days. Leachates were collected every three hours the first day and then twice a day for the rest of the experiment. A tracer test using potassium bromide (KBr) was conducted simultaneously as KBr (40 mg/L) was added to the artificial rainwater at the beginning of the experiment when nZVI was spiked; leachates were filtered through 0.2 μm filter (Regenerated cellulose, Thermofisher) and effluent bromide concentrations were analysed by ion chromatography (Dionex ICS 2000, Thermo Scientific, CA, USA).

Table 6-2: Physicochemical characteristics of the soil materials used for column experiments.

Soil	MC	CCA
Sand (%)	68.5 ± 0.7	70 ± 0.1
Silt (%)	13.8 ± 1.1	21.3 ± 0.4
Clay (%)	17.8 ± 0.4	8.8 ± 0.4
Texture	Sandy loam	Sandy loam
pH in water	5.68 ± 0.06	6.49 ± 0.04
pH in CaCl$_2$	5.04 ± 0.03	5.89 ± 0.08
Eh (mV)	213 ± 10	167 ± 3
EC (μS/cm)	51.9 ± 1.5	148.8 ± 0.5
Water holding capacity (%)	38.9 ± 2.2	47.5 ± 2.2
Porosity (%)	32 ± 2.8	39 ± 1.4
Permeability coefficient (K) in saturated condition (cm/s)	0.019 ± 0.003	0.003 ± 0.002
Moisture content (%)	2.7	4.5
Nitrogen (%)	0.17 ± 0.01	0.34 ± 0.04
Carbon (%)	2.10 ± 0.04	4.84 ± 0.62
Sulphur (%)	0.95 ± 0.04	0.93 ± 0.60

6.2.2.2 Mobility of commercialised N25S – ICP-MS method

As described above, 2 g of N25S were injected on the top of the MC soil columns before starting the irrigation system. Four soil columns were used for this experiment; three replicate columns to which nZVI was added and one control column to determine the background iron (Fe) concentration in the MC soil (in addition to the baseline study which also determined this). The collected effluent samples were acid digested and Fe concentration was determined using inductively coupled plasma mass spectrometry (ICP-MS) (Agilent 8800 Triple Quadrupole, Agilent Technologies, CA, USA). The data presented are the average of replicate experiments (n = 3).

6.2.2.3 Mobility of ^{59}Fe-CMC-nZVI – Gamma counting method

The mobility of radiolabelled nZVI was assessed in both MC and CCA soils. Three replicate columns of each soil were used for the transport study and data presented are the average of replicate measurements (n = 3). ^{59}Fe-CMC-nZVI (i.e. 2 g nZVI containing 0.123 MBq or 2,072K counts per minutes (CPM)) was added on top of each column and 2 ml aliquots of the collected effluent samples were analysed directly using a gamma radiation counter (2480 Wizard^2-3, Perkin Elmer) without any further sample preparation. Blank solutions (i.e. MQ water) were used to determine the average background radiation in each rack; which was then subtracted from the results obtained with the effluent samples. For this study, no control columns were needed as the gamma counter only detects the gamma emission from the radiolabelled ^{59}Fe-nZVI. This is one of the main advantages of this method as the background of naturally occurring Fe colloids present in the columns do not interfere with the results. The mass of eluted nZVI was then calculated by measuring the activity in solution (adjusted to time 0 – taking into consideration the radionuclide decay) and using the specific activity of the nZVI (i.e. at time 0).

To investigate the effect of wetting and drying on the mobility of nZVI, the irrigation system was stopped for one month after the first set of experiments and then started again for three consecutive days. Effluent samples were collected at the same frequency as for the first set of experiments and analysed directly with the gamma radiation counter.

Following the completion of the experiments, each column was dissected into different layers to determine the spatial distribution profile of retained nZVI. This gave a total of 10 soil layer samples, with 1 cm section for the top layer, 1.5 cm section for the following layer and 2.5 cm sections in the lower layers. Preliminary experiments were first conducted to assess the activity attenuation of each tested soil compared to water and results (Figure 6-1) showed that for the highest concentrations tested, the attenuation was less than 10 %. Therefore, three replicates of soil samples (i.e. 32 grams) were extracted from each layer and analysed directly with the gamma radiation counter (i.e. without any sample preparation). This is another advantage of this method over conventional elemental composition analysis (e.g. ICP-MS), with which, it would not have been possible to differentiate between the injected nZVI and the natural Fe present in the soil columns.
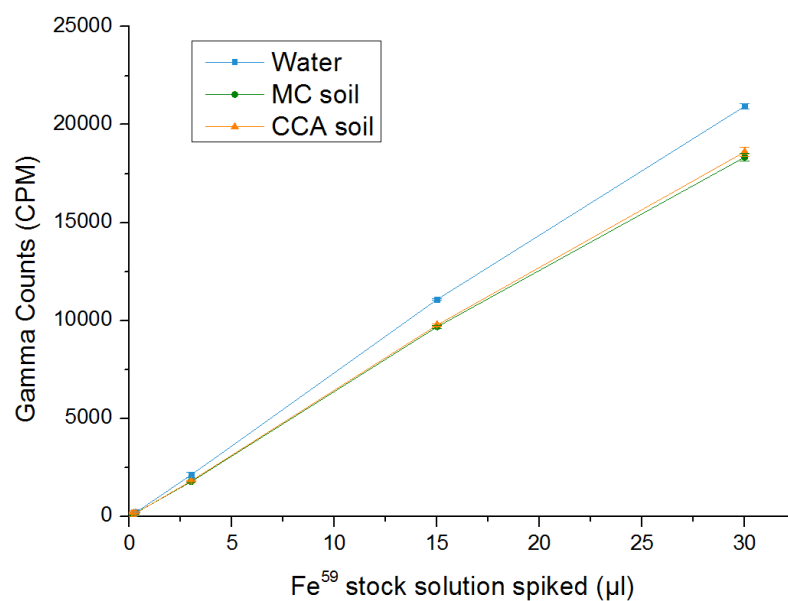
Figure 6-1: Comparison of gamma counts in soil and water solutions spiked with ^{59}Fe.

6.2.2.4   Co-transport of contaminants in CCA-contaminated soil

Eluted samples from the CCA soil columns were also acid digested and elemental concentrations of Fe, chromium (Cr), copper (Cu) and arsenic (As) were determined by ICP-MS. For this experiment, the initial leaching period (i.e. baseline study prior to adding nZVI) was used as control data for each column due to the heterogeneity in contaminant concentration between the different replicate columns. Leachates from the baseline study were acid digested and analysed with ICP-MS to determine the background concentration of Fe, Cr, Cu and As prior to the injection of nZVI. The data presented are the average of replicate measurements (n = 3).

6.3   Results and discussion

6.3.1   Evaluating the mobility of commercialised N25S based on ICP-MS analysis

The mobility of N25S was assessed in MC soil columns for 72 hours after injection of the nanomaterial and the results are presented in Figure 6-2 and Table 6-3.

The conservative tracer (i.e. KBr) breakthrough curve, shown in Figure 6-2a, indicated steady state effluent concentration by the end of the experiments suggesting that non-equilibrium processes, such as rate-limited mass transfer into regions of immobile water or preferential flow paths, were not significant during the transport of nZVI in the soil columns.

Figure 6-2b shows that the mass of Fe eluted from the control column (i.e. no N25S) was fairly steady (i.e. 0.42 mg ± 0.06 mg) while the mass of iron eluted from the spiked columns increased slowly, up to a maximum around 25 hours, and then slowly decreased until the end of the experiments. It is worth noting that the mass of Fe leached from the control column was quite low and steady throughout the experiment. This enabled us to assume that the enhanced Fe elution in the N25S treated column is due to nZVI, even though this cannot be unequivocally proved by simply analysing the eluate with ICP-MS. However, in the case of

a soil with higher and/or unevenly distributed Fe elution, ICP-MS would not have been sensitive enough to detect the spiked engineered nanomaterials.

The experimental breakthrough curve for N25S, shown in Figure 6-2c, indicates that only a small fraction of the initial injected mass was eluted from the MC soil columns (i.e. m/m_0 was less than 0.0004 at 25 hours); suggesting that most of the nZVI particles were retained in the column. Mass balance calculations, presented in Table 6-3, confirmed that less than 20 mg of N25S were eluted after 72 hours which represents less than 1% of the injected mass (2 g).
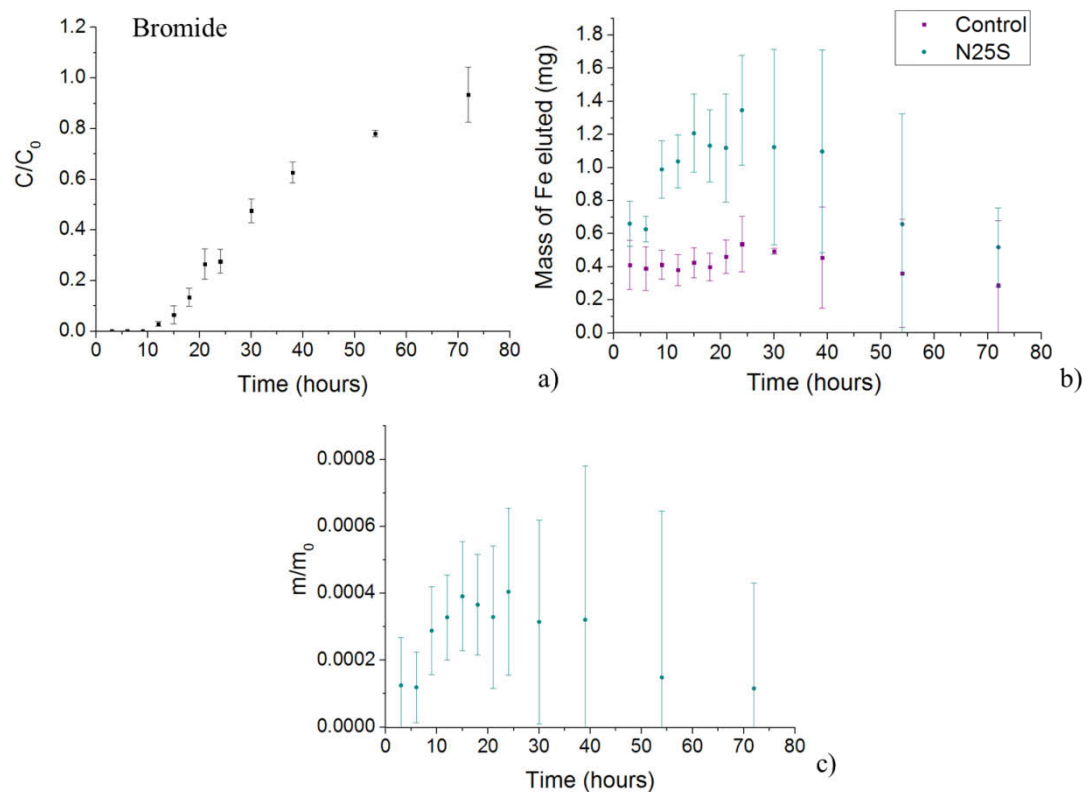
Figure 6-2: Summary results of N25S mobility in MC soil columns; (a) Experimental breakthrough curve of KBr; (b) Eluted mass of Fe from control (no nZVI) and spiked columns; (c) Experimental breakthrough curve of N25S. The error bars represent the standard deviation from three replicate columns.

There are several effects which can explain the limited transport behaviour of N25S: the ripening effect when the system is dominated by colloid-colloid attraction forces and attached particles can act as additional collectors for attachment by forming multilayer films

164

(Rajagopalan and Chu 1982; Ryde et al. 1991; Liu et al. 1995), the straining effect when the particles are trapped in down-gradient pore throats that are too small to allow particle passage (McDowell-Boyer et al. 1986) and deposition of the charged nanoparticles onto soil grains with opposite charge (Phenrat et al. 2010). Straining would cause the deposition of particles to decrease gradually since the smaller pores contributing to straining would fill up with time and restrict the other particles to larger pore networks; leading to an increase in effluent concentration. In this study, the eluted mass of Fe was not increasing with time (Figure 6-2b). However, straining cannot be excluded as it may be possible that, by the end of the experiments, all the smaller pores did not reach saturation. Ripening effect due to the aggregation of nanoparticles is likely to have caused the limited mobility of N25S. In fact, although surface modifiers were employed to reduce the aggregation of nZVI, there is still some residual aggregation (Phenrat et al. 2008; Fatisson et al. 2010; Raychoudhury et al. 2012). Furthermore, the high particle concentration (i.e. 50 g/L) used in this study may also promote the aggregation of nZVI (Phenrat et al. 2009). Finally, the sorption of polymer-coated nZVI onto soil grains through electrostatic attraction forces has been shown to significantly decrease its mobility (Liu et al. 1995; Fatisson et al. 2010; Kim et al. 2012; Raychoudhury et al. 2012; Laumann et al. 2013; Jung et al. 2014). It is therefore very probable that all three processes (i.e. straining, aggregation and sorption) contributed together to the limited mobility of nZVI.

Table 6-3: Mass of N25S eluted through 15-cm MC soil columns. The initial injected mass of N25S was 2 g, leaching period was 72 hours and flow rate was 1 mm/hr.

	Mass eluted (mg)	% eluted	% retained
Replicate 1	14.24	0.71	99.29
Replicate 2	26.72	1.33	98.66
Replicate 3	18.34	0.92	99.08
Average	**19.77**	**0.99**	**99.01**
SD	*6.36*	*0.32*	*0.32*

6.3.2 Evaluating the mobility of radiolabelled CMC-nZVI based on gamma counting analysis

6.3.2.1 *Transport of ^{59}Fe-CMC-nZVI in MC soil columns*

The mobility of radiolabelled CMC-nZVI was first assessed in MC soil columns. After an initial leaching period of 72 hours (similar to the N25S mobility study), the columns were left to dry for one month. The irrigation system was then started again for 72 hours to assess the effect of drying/wetting cycle on the mobility of nZVI. Results are presented in Figure 6-3 and Table 6-5.

The KBr tracer breakthrough (Figure 6-3a) was slightly delayed in comparison to the KBr breakthrough obtained in Figure 1a but, by the end of the 3 days the eluent concentrations approached C_0.

Similarly to the behaviour of N25S, experimental breakthrough of CMC-nZVI (Figure 6-3b-d) indicated limited mobility of the nanomaterials in the MC soil columns (i.e. m/m_0 was less than 0.0004 throughout the experiment). In replicate columns 2 and 3, however, some of the nanomaterials eluted very quickly, within a few minutes after the injection (i.e. $m/m_0 >$ 0.001 - Figure 6-3 c and 6-3d), which is most likely related to preferential flow down the edges of the columns. Results from the mass balance calculation in Table 6-5 confirmed that most of the particles (i.e. more than 98.9% of the total injected mass) were retained in the columns. Results in Table 6-5 also show the higher eluted mass in both columns 2 and 3 (i.e. about 3 mg eluted from column 1 compared to 20.99 mg and 14.81 mg from columns 2 and 3 respectively). Without considering the effect of preferential flows (i.e. excluding results from replicate columns 2 and 3), the mass of nZVI eluted from the MC soil columns was higher for N25S (i.e. about 20 mg compared to 5 mg for CMC-nZVI - Table 6-5). This is in

accordance with a previous study by Lin et al. (2010) where they found that the mobility of PAA-nZVI was superior to CMC-nZVI.
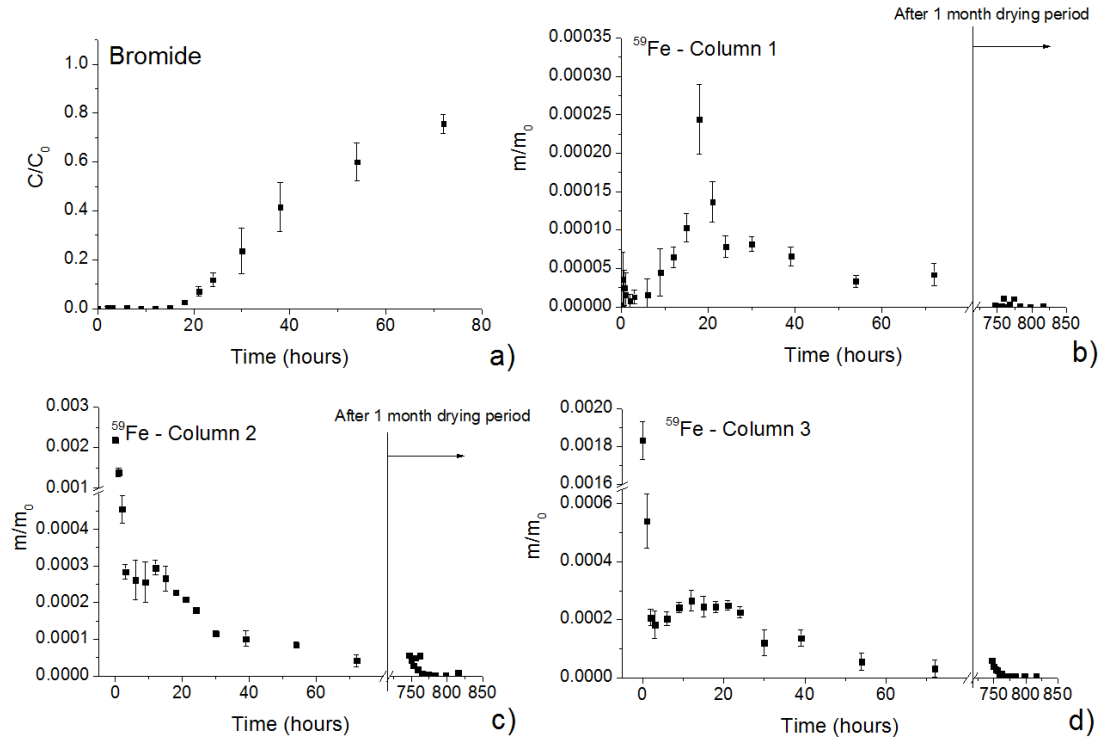
Figure 6-3: Summary results of ^{59}Fe-CMC-nZVI mobility in MC soil columns; (a) Experimental breakthrough curve of KBr; (b-d) Experimental breakthrough curve of ^{59}Fe-CMC-nZVI in replicate columns.

It has been demonstrated in previous studies that hydrodynamic perturbation such as rapid infiltration, episodic wetting and drying cycles or large increases in shear stress can cause the detachment of colloidal particles from the solid minerals (Saiers and Lenhart 2003; Zhuang et al. 2007). In the present study, Figure 6-3b-d show that wetting and drying events did not have any effect on the mobility of nZVI as the mass eluted during the second leaching period remained significantly low (i.e. less than 1 mg). This could be due to the fact that aggregates of nZVI had become trapped in down-gradient pore throats which restricted their subsequent mobility and/or degradation of the coating agents and oxidation of the nZVI core which would have promoted particles retention.

167

After completion of the mobility study, all three columns were dissected into 10 layers to determine the distribution of retained nZVI in the columns. The retention profiles of ^{59}Fe-CMC-nZVI in MC soil columns can be found in Figure 6-4. More detailed information, such as the mass of nZVI recovered from the dissected columns, can be found in Table 6-4. Results indicate that about 40 to 65% of the retained particles remained in the first few centimetres; which is most probably related to the rapid aggregation of the nZVI after their injection. The retention profiles of ^{59}Fe-CMC-nZVI in all three columns exhibit a hyperexponential shape with higher retention in the layers next to the column inlet and rapidly decreasing retention with depth. Hyperexponential retention profiles have also been observed in previous studies investigating the transport of nanoparticles in porous media (Wang et al. 2011; Liang et al. 2013). Some studies have suggested that hyperexponential retention profiles can be due to straining (Li et al. 2004), particle aggregation (Bradford et al. 2006), system hydrodynamics (Bradford et al. 2011; Liang et al. 2013) or surface charge heterogeneity on the porous media grains (Tufenkji and Elimelech 2005). It is likely that all these processes have contributed to some extent toward this result.

In both columns 2 and 3, some particles (i.e. about 5% of the total mass recovered) were found in the deepest layers; which is most likely associated with the early elution of particles in these two columns due to preferential flows.
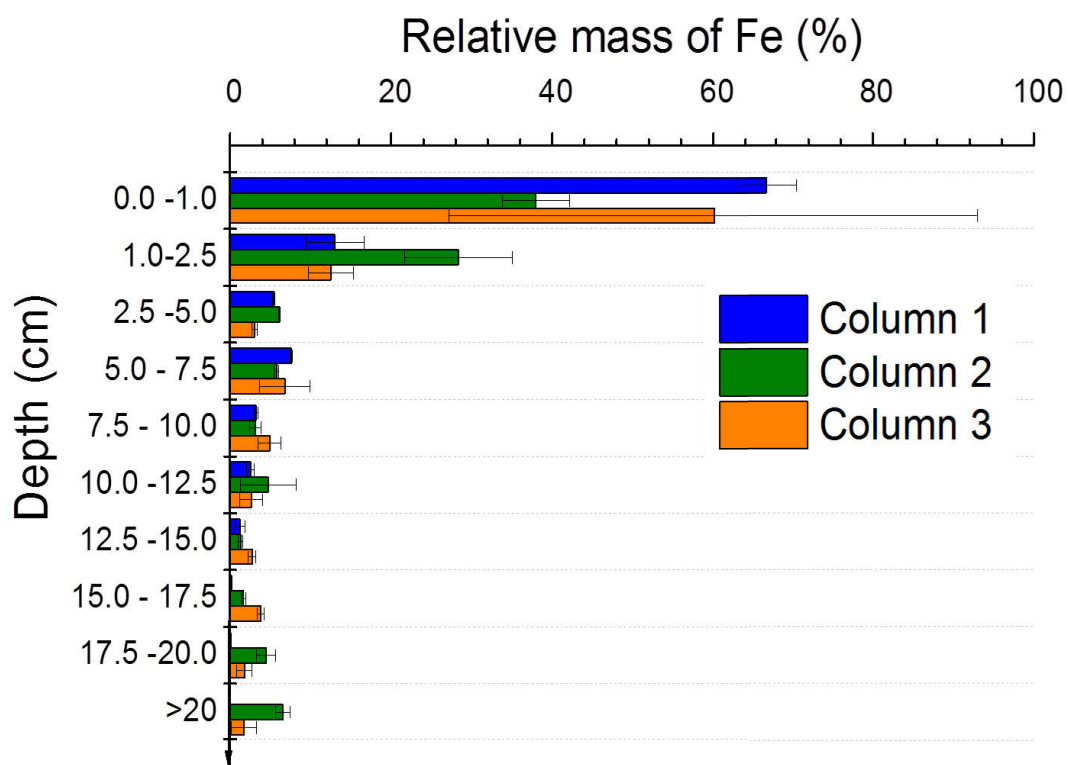
Figure 6-4: Retention profiles of ^{59}Fe-CMC-nZVI in MC soil columns. The relative mass of Fe is the mass of Fe per layer divided by the sum of the mass in each layer.

Table 6-4: Summary table of the dissection experiments for MC soil.

Columns	Depth (cm)	Mass of extracted soil per layer - dry (g)	Total mass of soil per layer - dry (g)	Fraction of the layer measured (%)	Total mass of ^{59}Fe-CMC-nZVI per measured soil layer (mg)	Estimated mass of ^{59}Fe-CMC-nZVI per soil layer (mg)
1	0.0 -1.0	34.4	60.5	56.9	493.7 ± 27.4	868.4 ± 48.2
	1.0-2.5	52.0	159.8	32.6	96.4 ± 26.4	296.3 ± 81.1
	2.5 -5.0	64.5	163.5	39.5	39.8 ± 1.2	100.9 ± 3.0
	5.0 - 7.5	65.0	208.5	31.2	56.1 ± 1.1	180.0 ± 3.5
	7.5 - 10.0	68.7	269.7	25.5	23.6 ± 1.8	92.8 ± 7.1
	10.0 -12.5	63.6	205.3	31.0	18.6 ± 3.4	60.1 ± 11.0
	12.5 -15.0	77.4	277.7	27.9	9.0 ± 4.3	32.4 ± 15.4
	15.0 - 17.5	71.6	280.8	25.5	1.4 ± 0.1	5.6 ± 0.4
	17.5 -20.0	70.3	274.8	25.6	0.6 ± 0.2	2.4 ± 0.8
	TOTAL	**567.5**	**1900.5**	**29.9**	**739.4 ± 66.0**	**1638.9 ± 170.5**
2	0.0 -1.0	32.0	49.9	64.2	217.4 ± 24.0	338.9 ± 37.4
	1.0-2.5	44.5	113.3	39.3	162.2 ± 38.4	412.8 ± 97.7
	2.5 -5.0	52.4	210.6	24.9	35.0 ± 0.4	140.8 ± 1.6
	5.0 - 7.5	57.7	234.3	24.6	32.9 ± 1.6	133.4 ± 6.5
	7.5 - 10.0	58.8	175.8	33.5	17.9 ± 4.2	53.4 ± 12.6
	10.0 -12.5	67.5	246.0	27.4	27.1 ± 19.7	98.7 ± 71.8
	12.5 -15.0	57.0	285.4	20.0	7.4 ± 1.7	37.2 ± 8.5
	15.0 - 17.5	69.9	285.5	24.5	9.4 ± 1.8	38.5 ± 7.4
	17.5 -20.0	54.9	201.3	27.3	25.7 ± 6.8	94.2 ± 24.9
	>20	61.4	64.3	95.5	37.4 ± 5.4	39.2 ± 5.7
	TOTAL	**556.3**	**1866.5**	**29.8**	**572.5 ± 103.9**	**1387.0 ± 274.0**
3	0.0 -1.0	35.8	88.2	40.6	330.8 ± 181.0	814.7 ± 445.8
	1.0-2.5	51.1	111.8	45.7	68.8 ± 15.4	150.5 ± 33.7
	2.5 -5.0	60.3	254.4	23.7	16.5 ± 1.7	69.8 ± 7.2
	5.0 - 7.5	67.7	174.8	38.7	37.3 ± 17.3	96.4 ± 44.7
	7.5 - 10.0	58.8	233.4	25.2	27.1 ± 7.8	107.5 ± 31.0
	10.0 -12.5	69.8	244.6	28.5	14.4 ± 7.9	50.6 ± 27.7
	12.5 -15.0	66.0	262.3	25.2	15.1 ± 2.5	59.8 ± 9.9
	15.0 - 17.5	62.8	231.9	27.1	20.9 ± 2.1	77.3 ± 7.8
	17.5 -20.0	65.3	306.9	21.3	9.8 ± 5.1	46.1 ± 24.0
	>20	61.0	144.8	42.1	9.4 ± 8.8	22.3 ± 20.9
	TOTAL	**598.6**	**2053.2**	**29.2**	**550.2 ± 249.8**	**1495.0 ± 652.5**

6.3.2.2 Transport behaviour of ^{59}Fe-CMC-nZVI in CCA-contaminated soil columns

The transport of radiolabelled CMC-nZVI in the CCA soil columns was also assessed and the results are presented in Figure 6-5 and Table 6-5. Similar to the behaviour in MC soil columns, ^{59}Fe-CMC-nZVI showed very poor mobility in CCA soil columns (i.e. $m/m_0 <$ 0.00015-0.0004 - Figure 6-5b-d) with less than 0.5% (i.e. 10 mg) of the mass injected eluted from the columns (Table 6-5). The breakthrough curves of ^{59}Fe-CMC-nZVI were almost identical in both soils with increasing mass eluted, up to a peak occurring at about 18 hours, and then slowly decreasing to the end of the first leaching period. In columns 1 and 3 (Figure 6-5b and 6-5d), however, the eluted mass of nanoparticles increased after 55 hours and 20 hours respectively; which may suggest that straining occurred in these columns. The second leaching period (i.e. after the columns were left to dry for one month) showed no improvement in particle mobility; which is similar to the trend observed in the MC soil columns.
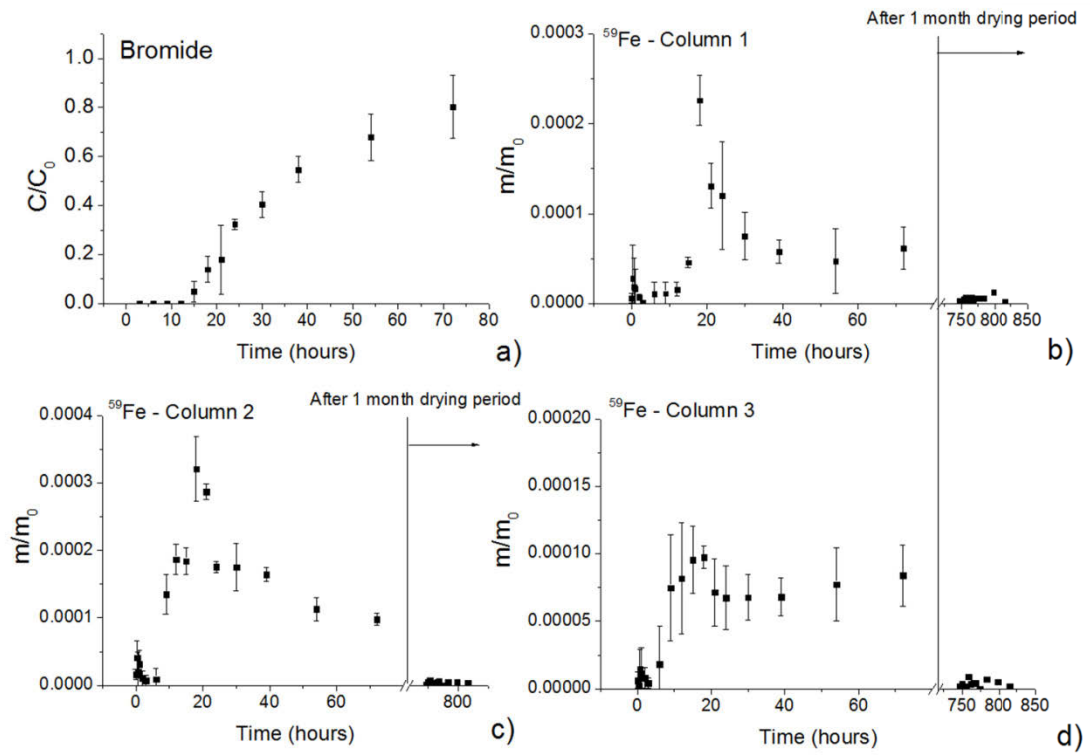
Figure 6-5: Summary results of ^{59}Fe-CMC-nZVI mobility in CCA soil columns; (a) Experimental breakthrough curve of KBr; (b-d) Experimental breakthrough curve of ^{59}Fe-CMC-nZVI in replicate columns.

172

Table 6-5: Mass of ^{59}Fe-CMC-nZVI eluted through 15-cm MC and CCA soil columns after one drying/wetting cycle (i.e. two 72-hours leaching periods separated by one month drying period). The initial injected mass of ^{59}Fe-CMC-nZVI was 2 g and flow rate was 1 mm/hr.

		Column 1			Column 2			Column 3		
		Mass eluted (mg)	% eluted	% retained	Mass eluted (mg)	% eluted	% retained	Mass eluted (mg)	% eluted	% retained
MC soil	Replicate 1	3.29	0.16	99.84	19.82	0.99	99.01	13.45	0.67	99.33
	Replicate 2	3.12	0.16	99.84	22.26	1.11	98.89	15.36	0.77	99.23
	Replicate 3	2.83	0.14	99.86	20.89	1.04	98.96	15.64	0.78	99.22
	Average	**3.08**	**0.15**	**99.85**	**20.99 (8.21)***	**1.05**	**98.95**	**14.81 (6.78)***	**0.74**	**99.26**
	SD	*0.23*	*0.01*	*0.01*	*1.22*	*0.06*	*0.06*	*1.19*	*0.06*	*0.06*
CCA soil	Replicate 1	2.80	0.14	99.86	6.61	0.33	99.67	4.02	0.20	99.80
	Replicate 2	3.97	0.20	99.80	6.91	0.35	99.65	7.63	0.38	99.62
	Replicate 3	3.06	0.15	99.85	6.94	0.35	99.65	4.41	0.22	99.78
	Average	**3.28**	**0.16**	**99.84**	**6.82**	**0.34**	**99.66**	**5.35**	**0.27**	**99.73**
	SD	*0.62*	*0.03*	*0.03*	*0.18*	*0.01*	*0.01*	*1.98*	*0.10*	*0.10*

* The values given in brackets are the mass of eluted iron without considering the effect of preferential flows (i.e. by removing the first two values)

173

The retention profiles of ^{59}Fe-CMC-nZVI in the CCA soil columns were similar to those observed in the MC soil columns; exhibiting a hyperexponential shape. Figure 6-6 shows that more than 90% of the particles were retained in the top centimetre of the columns; confirming the low mobility of the particles. This value rapidly decreased to 5-10% in the following layers (i.e. up to 5 cm deep) and less than 0.5% in the deepest layers.
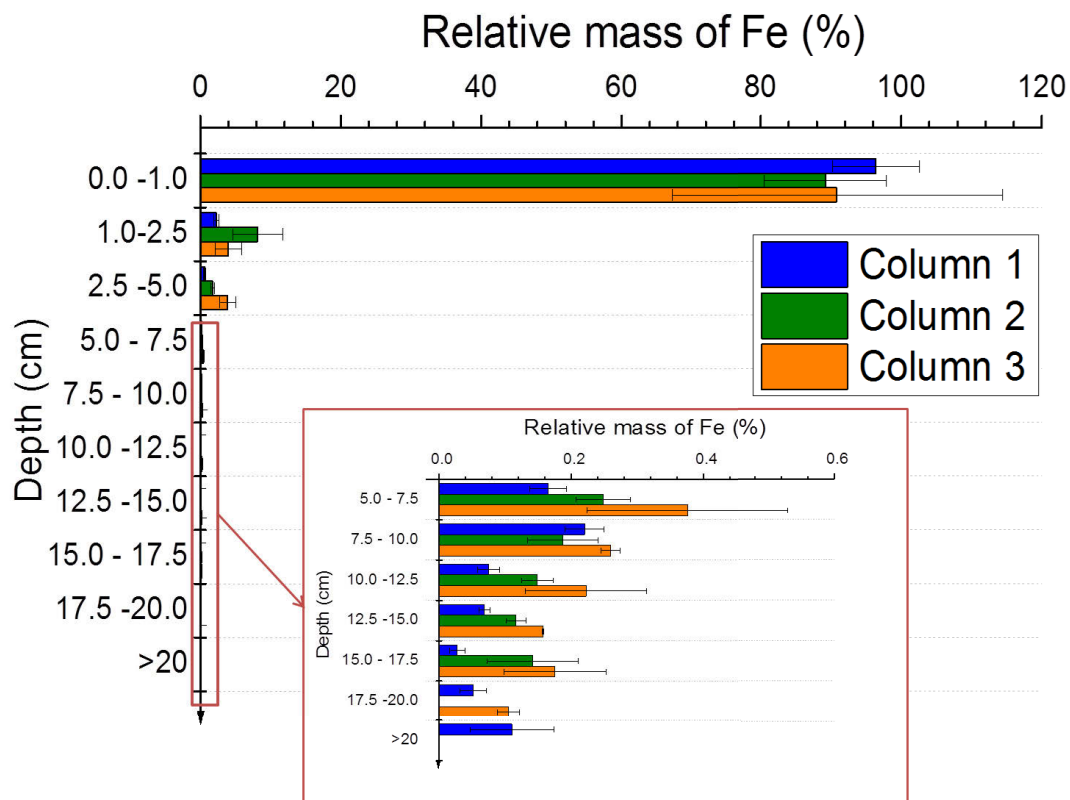
Figure 6-6: Retention profile of ^{59}Fe-CMC-nZVI in CCA soil columns. The relative mass of Fe is the mass of Fe per layer divided by the sum of the mass in each layer.

Table 6-6: Summary table of the dissection experiments for CCA soil.

Columns	Depth (cm)	Mass of extracted soil per layer (g)	Total mass of soil per layer (g)	Fraction of the layer measured (%)	Total mass of ^{59}Fe-CMC-nZVI per measured soil layer (mg)	Estimated mass of ^{59}Fe-CMC-nZVI per soil layer (mg)
1	0.0 -1.0	26.2	26.2	100.0	1282.9 ± 82.4	1282.9 ± 82.4
	1.0-2.5	39.8	152.6	26.1	30.7 ± 4.9	117.6 ± 18.9
	2.5 -5.0	53.6	225.0	23.8	7.8 ± 1.9	32.8 ± 8.1
	5.0 - 7.5	46.5	157.7	29.5	2.2 ± 0.4	7.43 ± 1.2
	7.5 - 10.0	53.0	249.4	21.2	2.9 ± 0.4	13.8 ± 1.8
	10.0 -12.5	57.8	286.4	20.2	1.0 ± 0.2	4.9 ± 1.1
	12.5 -15.0	62.5	195.7	31.9	0.9 ± 0.1	2.8 ± 0.4
	15.0 - 17.5	66.2	377.9	17.5	0.4 ± 0.1	2.1 ± 0.9
	17.5 -20.0	67.7	229.6	29.5	0.7 ± 0.3	2.3 ± 0.9
	>20	57.1	78.6	72.6	1.5 ± 0.8	2 ± 1.2
	TOTAL	**530.2**	**1979.3**	**26.8**	**1130.9 ± 91.6**	**1468.6 ± 116.9**
2	0.0 -1.0	41.0	60.8	67.3	887.0 ± 86.3	1317.3 ± 128.3
	1.0-2.5	37.8	67.8	55.7	81.1 ± 35.5	145.6 ± 63.8
	2.5 -5.0	54.8	195.5	28.0	17.5 ± 3.1	62.4 ± 10.9
	5.0 - 7.5	51.4	219.9	23.4	2.5 ± 0.4	10.6 ± 1.8
	7.5 - 10.0	59.7	192.7	31.0	1.9 ± 0.5	6 ± 1.7
	10.0 -12.5	64.4	236.8	27.2	1.5 ± 0.2	5.4 ± 0.9
	12.5 -15.0	61.8	350.8	17.6	1.2 ± 0.1	6.6 ± 0.8
	15.0 - 17.5	58.4	58.4	100.0	1.4 ± 0.7	1.4 ± 0.7
	TOTAL	**429.1**	**1382.7**	**31.0**	**994.0 ± 126.9**	**1555.3 ± 208.9**
3	0.0 -1.0	29.0	69.1	42.0	634.4 ± 165.1	1512.1 ± 393.3
	1.0-2.5	46.0	179.0	25.7	28.0 ± 13.2	108.9 ± 51.6
	2.5 -5.0	49.9	187.9	26.5	27.3 ± 7.7	102.8 ± 28.8
	5.0 - 7.5	46.7	175.9	26.6	2.6 ± 1.1	9.9 ± 4
	7.5 - 10.0	57.8	232.6	24.8	1.8 ± 0.1	7.3 ± 0.4
	10.0 -12.5	64.1	271.8	23.6	1.6 ± 0.6	6.6 ± 2.7
	12.5 -15.0	64.2	284.8	22.5	1.1 ± 0.01	4.9 ± 0.1
	15.0 - 17.5	71.2	314.1	22.7	1.2 ± 0.5	5.4 ± 2.4
	17.5 -20.0	48.0	88.1	54.5	0.7 ± 0.1	1.3 ± 0.2
	TOTAL	**476.9**	**1803.4**	**26.4**	**698.7 ± 188.5**	**1759.2 ± 483.5**

6.3.3   Co-transport of contaminants in CCA-contaminated soil

The potential for nZVI to co-transport inorganic contaminants (i.e. Cr, Cu and As) was assessed using the CCA soil columns and the results are presented in Figure 6-7. For this

experiment, the baseline data from the initial leaching period (i.e. prior to adding nZVI) was used as control data for each column. This was preferable to using separate control columns for comparison as it helps circumvent confounding effects caused by heterogeneity in contaminant concentrations within and between the different replicate columns (i.e. Column 1 released the highest concentration of all three contaminants - Figure 6-7). Results show that the eluted mass of all three contaminants was increasing with time during the baseline establishment period, suggesting that some of the contaminants were present in the mobile aqueous phase, either in dissolved form or bound to natural colloids. In fact, many previous studies focusing on contaminant transport in porous media demonstrated that contaminants are partitioned between an immobile solid phase (i.e. bound to immobile matrix), a mobile aqueous phase and a mobile colloidal phase (Massoudieh and Ginn 2010). The eluted mass of Fe during the baseline study was quite stable and homogeneous between the three replicate columns. After the injection of nZVI, the eluted mass of all three contaminants continued to increase for a short period of time and then gradually decreased. This may indicate that contaminants were effectively adsorbed on the surface of nZVI which reduced their mobility. In fact, many studies have already demonstrated that nZVI may be effective for the treatment of both chromium and arsenic (Dries et al. 2005; Kanel et al. 2005; Kanel et al. 2007; Schorr 2007; Ramos et al. 2009). In these studies, it was reported that nZVI can reduce both the mobility and toxicity of inorganic contaminants following surface-adsorption and/or a change in speciation induced by redox reactions. However, this implies that the contaminants remain in the environment but are changed to a less mobile and/or less toxic form.

After decreasing, the eluted mass of all three contaminants began to increase again, up to a peak at about 18 hours which corresponds to the peak observed for Fe in both Figure 6-7 (i.e. ICP-MS results) and Figure 6-5 (i.e. Gamma counter results). This may indicate the effective transport of contaminants following their adsorption on the surface of nZVI. Ryan

and Elimelech (1996) suggested that the following three criteria should be present to expect the effect of colloid-facilitated contaminant transport to be important: (i) colloids should be present in large enough concentration, (ii) the contaminant should be adsorbed to the colloids and (iii) the colloids should be mobile in the porous medium. As the eluted mass of all three contaminants was much lower (i.e. in the μg range - Figure 6-7) than the injected mass of nZVI (i.e. 2 g), and previous studies have already demonstrated that nZVI can effectively adsorbed heavy metals, both criteria (i) and (ii) for colloid-facilitated transport are met. However, we have demonstrated that the mobility of ^{59}Fe-CMC-nZVI in the CCA soil columns was very limited and that most of the retained particles were present in the top first centimetres of the columns. Nonetheless, the mass of eluted particles (i.e. about 3-7 mg) remained higher than the eluted mass of contaminants (i.e. less than 100 μg) which may indicate the effective transport of all three contaminants by the eluted nZVI.

Finally, as it was discussed in the previous section, the wetting/drying cycle did not have any effect on the mobility of both nZVI and all three contaminants. Figure 6-7 shows that the eluted mass of Cr, Cu, As and Fe was fairly steady and quite low during the second leaching period.
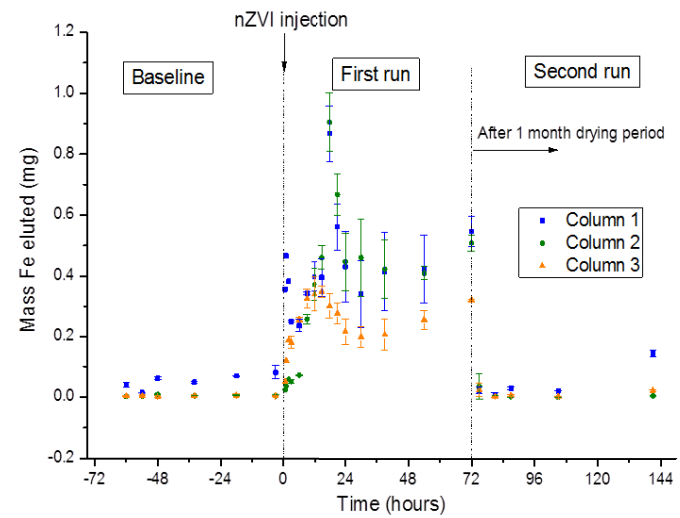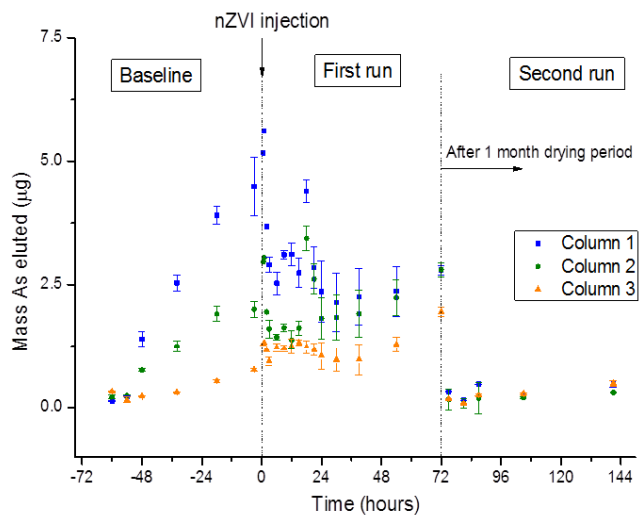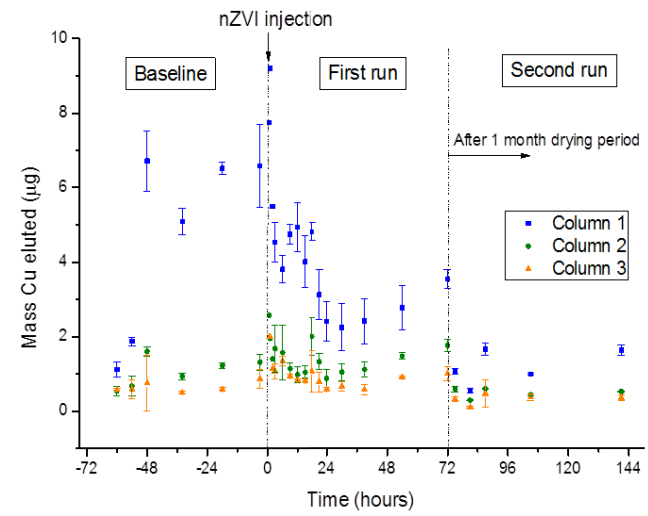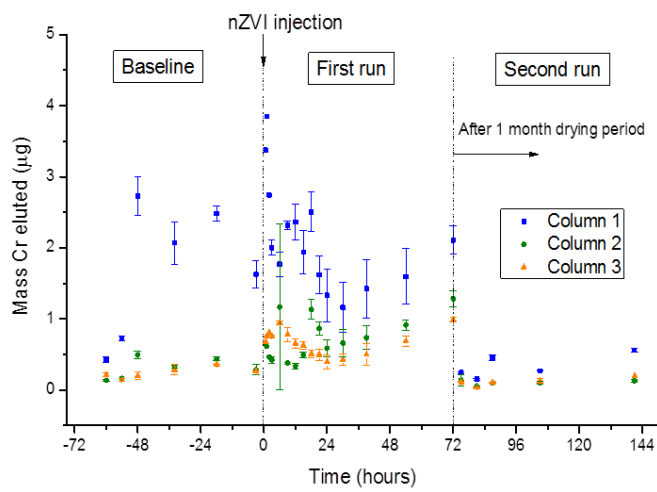
Figure 6-7: Effluent mass of inorganic contaminants (Cr, Cu and As) and Fe from CCA-soil columns.

6.4   Conclusions

The results obtained in this study have several implications. First, compared to previous research carried out in idealised systems, the results of the present study showed very little translocation of polymer-coated nZVI in intact soil cores. The retention profiles of retained particles showed that most of the particles remained in the first top layers demonstrating the limited volume that can be treated with this technology. Finally, if the nanoparticles are present in large enough concentration (i.e. much higher than the concentration of targeted contaminants), this will potentially promote the movement and dispersion of contaminants through colloidal-facilitated transport at least in the short term. However, considering that the concentrations in the eluent after nZVI application where similar to those obtained in the pre-treatment phase, the potential for contaminant mobilisation appears, at least in the soil investigated to be low.

University of Technology Sydney
FACULTY OF ENGINEERING

CHAPTER 7

DEVELOPMENT OF A NOVEL METHOD TO CHARACTERISE AGGREGATE STRUCTURE OF ENGINEERED NANOPARTICLES IN NATURAL WATERS USING ON-LINE LASER LIGHT SCATTERING

7.1 Introduction

Engineered nanoparticles (ENPs) used for environmental applications (e.g. soil and groundwater remediation) may ultimately end up in the entire aquatic environment. Besides, the rapid progress in nanomaterial research and development has led to industrial scale production and extensive commercialisation of nanoproducts. As a result, ENPs are increasingly released into the environment (Ju-Nam and Lead 2008). With several recent studies reporting potentially negative effects of ENPs (Handy et al. 2008; Chae et al. 2009; Gao et al. 2009; Poynton et al. 2010; Scown et al. 2010; Peralta-Videa et al. 2011), research into their environmental fate and behaviour is urgently needed to underpin risk assessment and policy development. However, until recently, few studies have investigated the behaviour of ENPs in real environmental samples, and little is known about their transport, fate, and probable concentrations in different environmental compartments. A recent modelling study by Keller et al. (Keller et al. 2013) estimated that in 2010, 63% to 91% of the global ENP production ended up in landfills; 8% to 28% was released into soils; 0.4% to 7% into water bodies; and 0.1% to 1.5% into the atmosphere. Among the ENPs considered, titanium dioxide (TiO_2) was released to the environment in the largest quantities, followed by iron and zinc (Keller et al. 2013). Gottschalk et al. developed a probabilistic material flow analysis model to predict the environmental concentrations of ENPs and found that silver NPs (Ag NPs) present in sewage treatment effluents and surface waters, and TiO_2 NPs and zinc oxide NPs (ZnO NPs) in sewage treatment effluents, may pose a risk to aquatic organisms (Gottschalk et al. 2009).

After entering the environment, the fate of ENPs greatly depends on their transport characteristics (i.e., aggregation, sedimentation or adsorption) and transformation (i.e., dissolution or chemical transformation) (Lowry et al. 2012). Agglomeration/aggregation and sedimentation are major processes affecting the behaviour of ENPs in aquatic systems and results suggest they are mainly controlled by the combined effects of pH, ionic strength, salt

composition and the presence and concentration of organic matter (Phenrat et al. 2007; Christian et al. 2008). Different experimental approaches have been tested to predict the behaviour of ENPs in aquatic systems. One approach is to consider the individual effects of different physical and chemical components (i.e., the effect of pH, a single electrolyte, organic matter, etc.) in order to identify the main factors affecting the stability of ENPs. A more realistic, yet more complex, approach investigates the behaviour of ENPs under environmentally-relevant conditions and ultimately in natural waters. Several recent studies have used these approaches to understand and predict the behaviour of ENPs once they enter the environment (Phenrat et al. 2007; Zhang et al. 2008; Baalousha 2009; Badawy et al. 2010; Hu et al. 2010; Keller et al. 2010; Huynh and Chen 2011; Ottofuelling et al. 2011; Baalousha et al. 2013; Brunelli et al. 2013; Dobias and Bernier-Latmani 2013; Romanello and de Cortalezzi 2013; Yang et al. 2013). Results from these studies confirmed the role of pH, electrolyte composition and the presence of organic matter in the aggregation or stabilization of ENPs. However, very few studies (e.g. (Baalousha et al. 2008; Baalousha 2009)) have focused on the structure and stability of the resulting aggregates and their potential for disaggregation. Aggregate structure (i.e. whether they are densely packed or loosely bound) is an important criteria to evaluate as it is likely to significantly influence aggregate behaviour and fate (Christian et al. 2008). Nevertheless, knowledge in this area is still lacking, partly because this type of investigation provides a significant analytical challenge.

Light scattering detectors are simple, robust and accurate tools that can be used to measure particle size, aggregation behaviour and aggregate structure. They are currently among the most widely used techniques worldwide for aggregation studies. Dynamic light scattering (DLS), in particular, has been applied in most nanoparticle aggregation studies in both synthetic and natural aquatic media (Phenrat et al. 2007; Zhang et al. 2008; Baalousha 2009; Ottofuelling et al. 2011; Baalousha et al. 2013; Chekli et al. 2013; Chowdhury et al. 2013).

In this study, we proposed an alternative way to characterise the aggregation behaviour and aggregate structure of various ENPs in complex environmental samples by performing continuous on-line light scattering analysis (i.e. combining both dynamic and static light scattering techniques) by using a pump to recirculate the sample inside the sample cell as shown in Figure 7-1. This simple set-up presents several advantages over conventional light scattering measurements. For instance, by recirculating the sample inside the measurement cell, it is possible to change the chemical or physical conditions of the sample and to directly observe and measure the effects of such changes on aggregate size. In addition, the fractal dimension (FD) of the aggregates can be studied using a static light scattering (SLS) instrument equipped with a series of photosensitive detectors positioned at different angles. Therefore, the method developed in this study can be useful to other researchers, working on fate of nanomaterials in the environment, to rapidly characterise the aggregation behaviour and aggregate structure of engineered nanoparticles (ENPs) formed in complex environmental system.

The overall objective of this chapter is to assess and compare the aggregation behaviour and aggregate structure of different ENPs in a range of natural water sources using on-line laser light scattering detectors. Aggregates will be characterised in terms of size, surface charge, DOM and Ca^{2+} adsorption capacity, fractal dimension, disaggregation and regrowth potential.
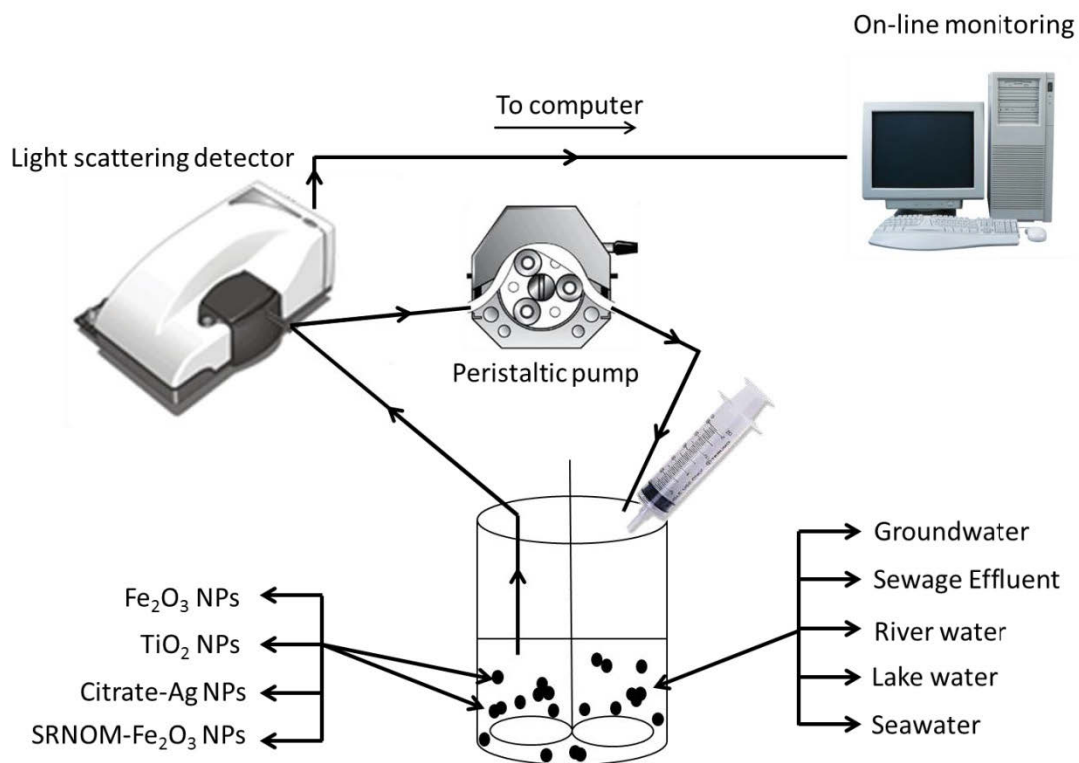
Figure 7-1: Experimental set-up used in this study.

This chapter is an extension of the research article published by the author in Journal of Hazardous Materials (Chekli et al. 2014).

7.2 Experimental

7.2.1 Chemicals and reagents

Commercially available Fe_2O_3 NPs and citrate coated-Ag NPs were supplied by Sigma-Aldrich, Australia. The Aeroxide P25 TiO_2 nanoparticles were provided by Evonik Degussa Corporation (Parsippany, NJ, USA). Further details are available in Table 7-1. Suwannee River natural organic matter (SRNOM), used as a model NOM, was obtained from the International Humic Substances Society (IHSS, St. Paul, USA).

7.2.2 Sample preparation

The methodology for the preparation of SRNOM-coated Fe_2O_3 NPs has been described in Chapter 5. SRNOM-coated Fe_2O_3 NPs were used in this study to mimic situations where ENPs are already coated with NOM before entering an aquatic system (e.g., pre-coated with DOM prior to subsurface injection for groundwater remediation).

A TiO_2 stock solution was prepared by mixing TiO_2 particles (10 g/L) with DI water for 1 hour, followed by 30 minutes of bath sonication (Model 800HD, Soniclean, Australia). Before each experiment, 200 mL of the stock solution was centrifuged for 10 min at 3500 rpm (Model 2040, Centurion Scientific Ltd, UK) and supernatant (100 mL) collected for the experiments. The final concentration of TiO_2 in the supernatant varied from 1.5 to 2.1 g/L. This concentration was determined by measuring the nephelometric turbidity as described in Chapter 3.

Table 7-1: Characteristics of the tested nanoparticles.

	Fe$_2$O$_3$ NPs	Citrate coated-Ag NPs	TiO$_2$ NPs	SRNOM-coated Fe$_2$O$_3$ NPs	Source
Average primary particle size (TEM)	< 30 nm	40 nm ± 4 nm	21 nm	-	Manufacturer
Density	1.17 g/mL ± 0.1 at 25°C	0.990 g/mL at 25°C	3.8 g/mL at 25°C	-	Manufacturer
pH	3.7 ± 0.3	7.1 ± 0.1	3.5-4.5 (40 g/L)	-	Manufacturer
Initial zeta potential (mV)	+35.4 ± 2.2 (pH 4)	-35.7 ± 2.4 (pH 4)	+20.7 ± 1.5 (pH 4)	-30.1 ± 1.8 (as prepared)	This study – Figure 7-2
Point of zero charge (PZC)	7.0 (200 mg/L)	< 2.0 (1 mg/L)	6.0 (25 mg/L)	< 2.0 (as prepared)	This study – Figure 7-2
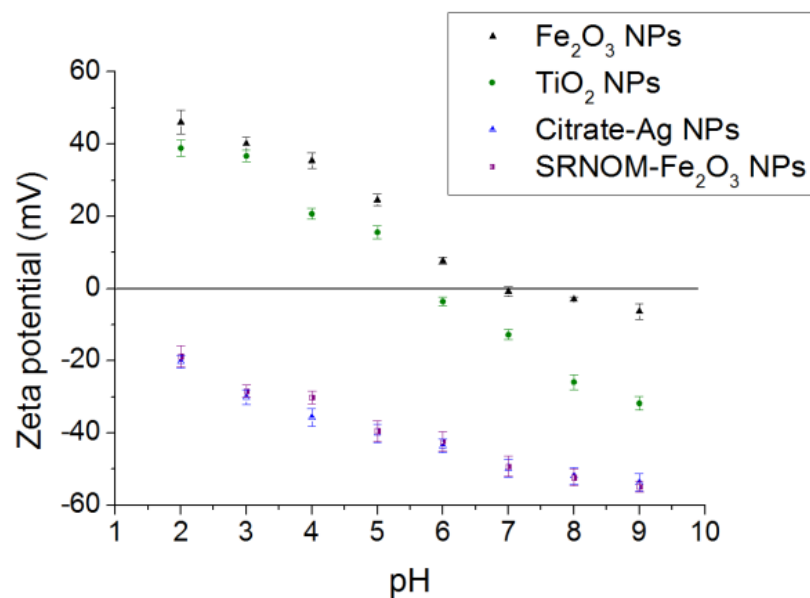
Figure 7-2: Zeta potential of Fe$_2$O$_3$NPs (200 mg/L), TiO$_2$ NPs (25 mg/L), Citrate Ag NPs (1 mg/L) and SRNOM-Fe$_2$O$_3$ NPs (as prepared) as a function of pH.

7.2.3 Natural waters

Five natural water samples were collected from a variety of sources across New South Wales, Australia: Sewage effluent (SewEff) from Sydney Olympic Park treatment plant, seawater (SeaW) from Chowder Bay (Sydney Harbour), lake water (LW) from Penrith, river water (RW) from Parramatta and groundwater (GW) from Williamstown. All water samples were filtered through a 0.2 μm polyethersulfone (PES) vacuum filtration unit (Vivascience AG, Germany), and stored at 4°C in the dark prior to use. Previous studies (Hyung et al. 2007; Quik et al. 2012) showed that this filtration method reduces the concentration of natural colloids to negligible levels. This procedure was further validated by checking the presence of natural colloids or large agglomerates of organic molecules in the filtered samples by use of the on-line DLS set-up. Particles were not detected by DLS in any of the natural waters meaning that either all the natural colloids/large agglomerates of organic molecules were effectively removed by the filtration method or the concentration and/or size of the remaining particles were below the detection limit of the instrument.

Dissolved organic carbon (DOC) was measured using a TOC analyser (Multi N/C 3100, Analytic Jena AG, Germany). The pH and electrical conductivity (EC) were measured using a portable pH/conductivity meter (Model WP-80, TPS Pty Ltd, Australia). Ion chromatography (IC) (850 Professional IC, Metrohm, Australia) was used to analyse major anions and cations. Ionic strength of the water samples was calculated using the following formula:

$$IS = \frac{1}{2} \sum C_i Z_i^2 \tag{1}$$

where IS is the ionic strength of the solution (mole/L), C_i is the concentration of the ith species (mole/L) and Z_i is the valence number of the ith species.

The detailed characteristics of the natural waters are gathered in Table 7-2.

Table 7-2: Water chemistry of the tested natural waters.

	Lake water (LW)	Sewage effluent (SewEff)	Seawater (SeaW)	Groundwater (GW)	River water (RW)
EC (μS/cm)	574	1126	49800	842	513
pH	7.09	7.80	7.86	6.53	6.89
DOC (mgC/L)	14.66	5.81	2.65	5.12	15.76
Ionic strength (mmol/L)	3.46	11.7	735	14.90	1.96
Ionic composition					
Cl^- (mg/L)	34.55	237.22	21442	267.40	17.23
NO_3^- (mg/L)	15.46	9.37	0.06	35.14	15.64
SO_4^{2-} (mg/L)	12.97	53.04	3055	39.31	6.67
PO_4^{3-} (mg/L)	0.39	3.73	0.02	1.43	n.d.
Na^+ (mg/L)	41.01	163.31	10756	122.02	40.62
K^+ (mg/L)	5.89	12.19	358	7.06	1.42
Ca^{2+} (mg/L)	16.51	28.89	415	59.23	2.40
Mg^{2+} (mg/L)	9.60	25.00	1338	52.11	5.22

n.d.: not detectable; all waters filtered through 0.2 μm vacuum filter

7.2.4 Aggregation study in natural waters

ENPs were introduced into each individual natural water samples in a variable-speed jar tester (ZR4-2, Zhongrun Water Industry Technology Development Co., Ltd., China) with a 37 mm x 23 mm flat paddle impeller in a 250 mL cylindrical jar. The final volume of sample in the jar tester was 150 mL. A slow mixing speed of 40 rpm (i.e. 25 g) was used throughout the aggregation study. This slow mixing speed was applied to prevent the aggregates from sedimenting in the jar tester in order to allow them to flow through the measurement cell and be analysed. Several mixing speeds were tested during preliminary experiments and 40 rpm was found to be the optimum mixing speed, not so fast as to break the aggregates and not so slow that the aggregates settled in the jar. This jar was connected to a peristaltic pump (Model 77521-47, Masterflex, Cole Palmer, Australia) which drew the sample directly to the light scattering instruments: a DLS system for measuring particle sizes in the 10 nm to 6 μm range (model ZEN3600; Malvern Instruments, Worcestershire, UK) and a static light scattering (SLS) instrument (Malvern Mastersizer 2000, Malvern Instruments,

Worcestershire, UK), with an array of photosensitive detectors, positioned at different angles between 0.01° and 40.6°, for the larger aggregates. After passing through the instruments, the samples were pumped back into the jar. Samples were pumped through the systems at a flow rate of 0.5 mL/min for the DLS instrument and 1.0 mL/min for the SLS instrument.

Preliminary tests using latex beads of 58 nm, 100 nm, 410 nm, 990 nm, 4900 nm and 8700 nm (Postnova Analytics, Germany) were carried out to determine the best flow rate for accurate detection of ENPs with the two different light scattering detectors (i.e. DLS and SLS). Figure 7-3 shows the results at a flow rate of 0.5 mL/min for DLS and 1.0 mL/min for SLS which were found to be the appropriate flow rates for ENPs detection. Tests with latex beads were run regularly (i.e. once a week) to check the accuracy of both instruments.

a)

b)
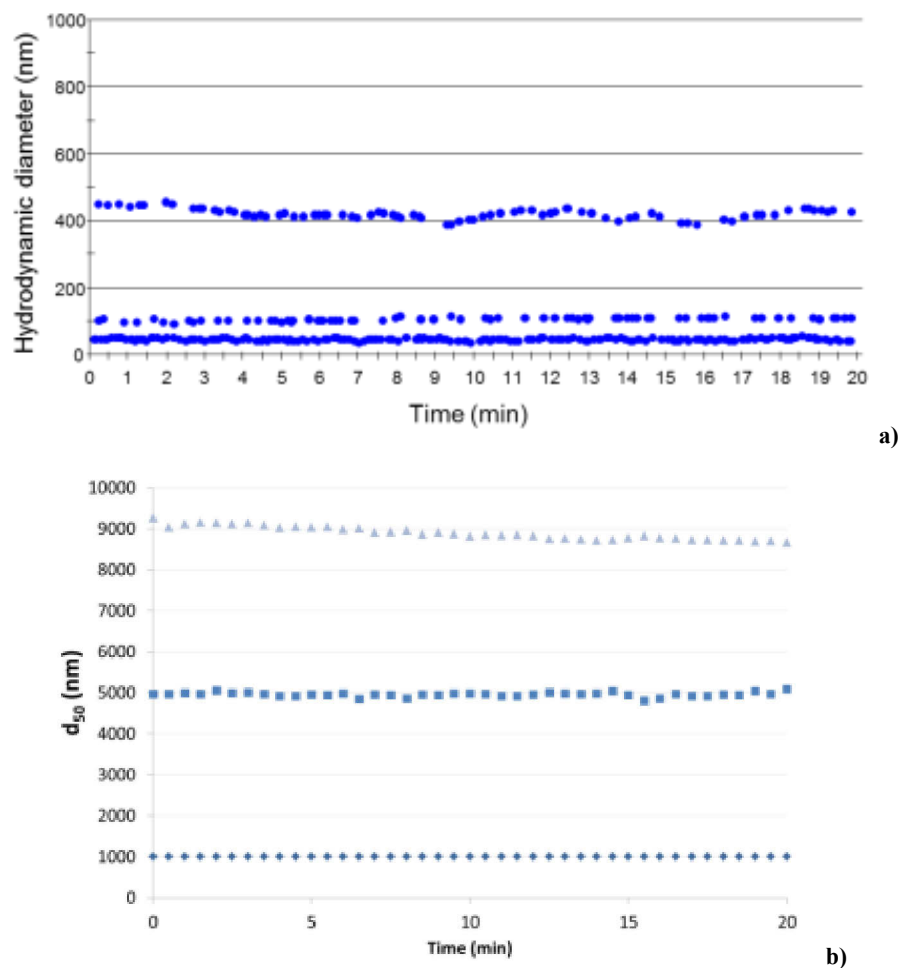
Figure 7-3: Hydrodynamic diameter of standard latex beads (10 mg/L) in DI water as measured by (a) DLS (flow rate: 0.5 mL/min) and (b) SLS (flow rate: 1mL/min) in continuous mode.

Final concentrations of ENPs in the natural waters were 200 mg/L, 25 mg/L and 1 mg/L for Fe_2O_3 NPs, TiO_2 NPs and citrate-Ag NPs, respectively. These concentrations were chosen as they are similar to those used in other studies involving the same ENPs (Baalousha 2009; Ottofuelling et al. 2011; Baalousha et al. 2013). Besides, these differences also relate to the expected relative concentrations of the different ENPs in the environment (e.g. Fe-based NPs used for remediation will be much more concentrated in the area surrounding the application zone than Ag NPs and TiO_2 NPs will be in the environment, as the release of both Ag NPs and TiO_2 NPs is more commonly due to unintentional release and hence subject to lower local release rates).

In addition to particle/aggregate size analysis, the zeta potential and surface-adsorbed DOM and Ca^{2+} were also measured at the end of the 60 minute aggregation experiments while the slow mixing speed of 40 rpm was maintained to avoid aggregates from settling at the bottom of the jar. Many recent studies have demonstrated the significant impact of DOM and divalent cations on both the aggregation behaviour and aggregate structure of ENPs (Hyung et al. 2007; Baalousha et al. 2008; Zhang et al. 2009; Hu et al. 2010; Thio et al. 2011; Li and Chen 2012; Baalousha et al. 2013; Chekli et al. 2013; Chowdhury et al. 2013; Liu et al. 2013; Romanello and de Cortalezzi 2013; Erhayem and Sohn 2014; Majedi et al. 2014). In these studies, the effect of DOM has been found to be concentration-dependent as, at sufficient concentration, DOM can effectively stabilise ENPs through electrosteric stabilisation. The presence of divalent cations, and especially Ca^{2+}, has been found to enhance the aggregation of ENPs through charge neutralisation by compressing the electrical double layer. In the presence of DOM, Ca^{2+} can further exacerbate the aggregation phenomena via the formation of calcium complexation with NOM.

Zeta potential was determined by DLS using 5 ml sample aliquots and a Zetasizer instrument (model ZEN3600; Malvern Instruments, Worcestershire, UK). Measurements

190

were performed in triplicate and the presented results are mean values and standard deviations.

For surface-adsorbed DOM analysis, 50 mL samples were centrifuged for 10 min at 2500 *g* (Model 2040, Centurion Scientific Ltd, UK) to separate the solution phase from the solid particles. The amount of DOM in the supernatant was measured using a TOC analyser (Multi N/C 3100, Analytic Jena AG, Germany). The amount of DOM adsorbed on the surface of the ENPs was then determined by calculating the difference between the initial and final DOM concentrations in solution.

The same protocol was followed to determine the amount of Ca^{2+} in the supernatant after sedimentation of the formed aggregates. The concentration of Ca^{2+} was measured by ion chromatography (IC) (850 Professional IC, Metrohm, Australia).

7.2.5   Aggregation kinetics

For colloidal systems where aggregation is governed by the DLVO theory (Derjaguin and Landau 1941; Verwey and Overbeek 1948), plots of the attachment efficiency against electrolyte concentration at a given experimental conditions can be used to characterize the aggregation kinetics:

$$\propto = \frac{1}{W} = \frac{k_{slow}}{k_{fast}} \tag{2}$$

Where α is the attachment efficiency, W is the stability ratio, k_{slow} and k_{fast} represent the aggregation rate constant under reaction-limited aggregation (RLA) and diffusion-limited aggregation (DLA) regimes. The aggregation rate constant k is proportional to the rate of change in the Z-average hydrodynamic diameter over time which corresponds to the slope of the hydrodynamic diameter growth, equation 2), and was determined by fitting a linear

correlation function to the experimental data during the early stage aggregation (Baalousha et al. 2013):

$$k = \frac{1}{oNd_0}\frac{d_r}{d_t}$$

(3)

Where N is the initial particle concentration, d_0 is the initial particle diameter and o is the optical factor.

The RLA regime occurs at counter ion concentrations below the critical coagulation concentration (CCC), whereas the DLA occurs at counter ion concentrations above the CCC. The CCC is frequently used to measure the stability of NP suspensions since it quantifies the minimum concentration of the counter ions that is required to completely destabilize the NP suspension (Elimelech and O'Melia 1990). The attachment efficiencies under RLA and DLA regimes were fitted by linear functions and their intersections yield the respective CCC.

In the present study, the attachment efficiencies of all ENPs were determined as a function of both NaCl and $CaCl_2$ concentration.

7.2.6   Disaggregation studies in natural waters

Disaggregation studies were conducted with the SLS detector (Malvern Mastersizer 2000, Malvern Instruments, Worcestershire, UK) with the same experimental set-up used for the aggregation study. Preliminary studies showed that this instrument does not give repeatable results for small aggregates (i.e., below 500 nm) and very low concentrated solutions (below 5 mg/L). Therefore, after an initial screening, TiO_2 NPs and Fe_2O_3 NPs were chosen for the disaggregation study in lake water, sewage effluent, groundwater and seawater as the concentration of citrate-Ag NPs and SRNOM-coated Fe_2O_3 NPs were below the detection limit of the instrument.

Upon the formation of stable aggregates (i.e. where the size of the aggregates was found to remain constant for more than 60 minutes) under conditions of slow mixing at 40 rpm (i.e. 25 g), the aggregates were then subjected to a high mixing speed of 200 rpm (i.e. 315 g) for 5 minutes to induce their disaggregation. After this breakage period, slow mixing (i.e. 40 rpm) was reintroduced for a further 30 minutes to allow regrowth of the aggregates. The size of the aggregates was measured by drawing the sample through the optical unit of the SLS detector and back into the jar using the peristaltic pump. Size measurements were taken every 30 seconds for the duration of the experiment and recorded on a computer. Samples were pumped through the system at a flow rate of 1 mL/min.

Aggregate strength factors (SF) and recovery factors (RF), which are used to evaluate the stability and propensity for formation of the aggregates were determined as follows (Yukselen and Gregory 2002; Jarvis et al. 2005; Zhao et al. 2012):

$$SF = \frac{d_2}{d_1} \times 100 \qquad (4)$$

$$RF = \frac{d_3 - d_2}{d_1 - d_2} \times 100 \qquad (5)$$

where d_1 is the average aggregate size of the plateau before applying the shear force, d_2 is the average aggregate size after aggregate breakage, and d_3 is the average aggregate size after regrowth to a new plateau.

7.2.7 Aggregate structural analysis

The highly disordered structure of colloidal aggregates can be characterised by its scaling behaviour, and is defined as the mass fractal dimension (FD) (Weitz et al. 1985; Rice and Lin 1993). The FD represents the actual space occupied by the system and defines the degree of "openness" of the colloidal aggregate structure.

Previous studies have reported the determination of aggregate FD using a Mastersizer 2000 as described in Chapter 3. Densely-packed aggregates will display a higher FD value, while lower FD values indicate linear and loosely bound aggregates.

7.2.8 Data analysis

Single and multiple linear regression analysis were performed to investigate the independent and combined effect of different variables (e.g., ionic strength, initial TOC concentration) on the aggregate size, surface-adsorbed DOM, strength factor and fractal dimension of the formed aggregates.

Preliminary screening showed that ionic strength, initial TOC and Ca^{2+} concentration of the natural waters tested were the three main variables controlling the aggregate size and surface-adsorbed DOM while ionic strength, surface-adsorbed DOM and Ca^{2+} were found to be the main variables affecting both the strength factor and fractal dimension of the formed aggregates.

The statistical significance of the effect of each variables (independently and combined) on each property tested was assessed by analysis of variance (one-way ANOVA, $p < .05$).

7.3 Results and discussion

7.3.1 Nanoparticles analysis in DI water prior to the aggregation study

Hydrodynamic diameters of the different ENPs were assessed in DI water by Dynamic Light Scattering (DLS) using a Zetasizer (model ZEN3600; Malvern Instruments, Worcestershire, UK) to ensure their stability prior to the aggregation study. Hydrodynamic diameters were recorded every 3 seconds for 30 minutes for all ENPs as shown in Figure 7-4.
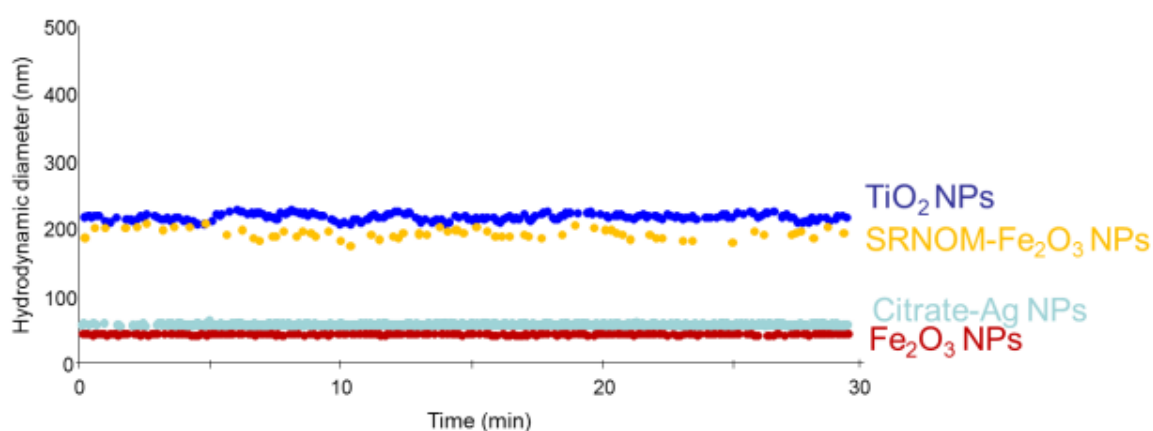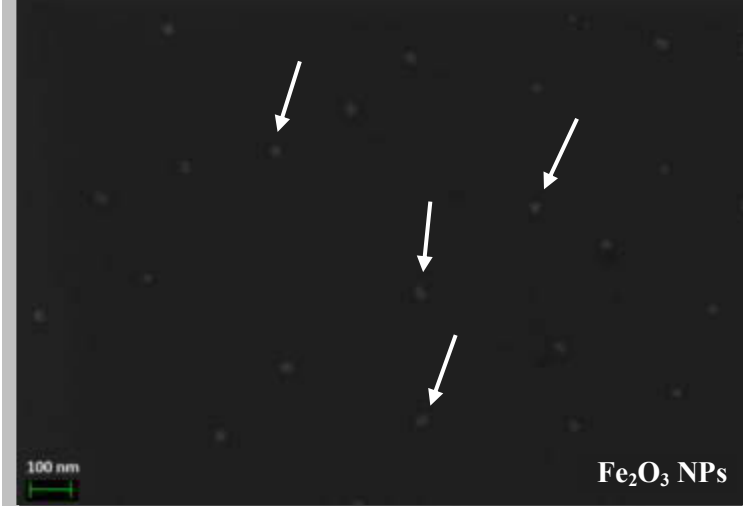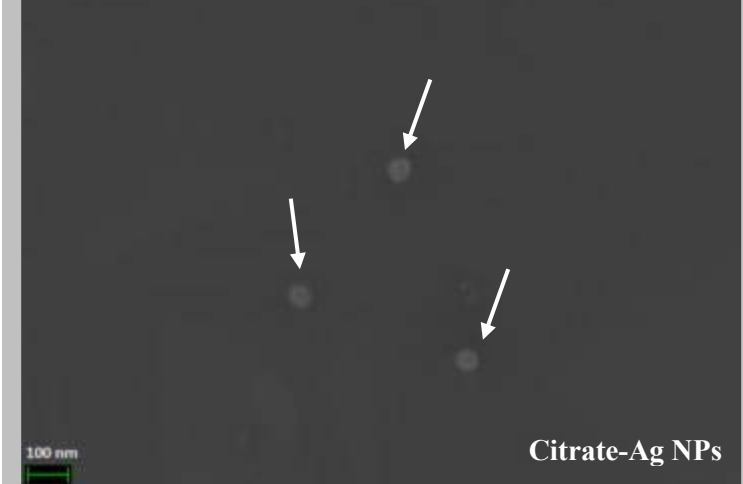
Figure 7-4: Hydrodynamic diameter of the different ENPs in DI water prior to the aggregation study measured by DLS in continuous mode.

SEM measurements were also carried out and images are gathered in Table 7-3. The mean equivalent circular diameter was determined from these images from the analysis of at least 200 nanoparticles. SRNOM-Fe_2O_3 NPs were not measured by SEM since samples likely to outgas at low pressures such as organic materials are unsuitable for examination in conventional SEM.

The results, presented in Figure 7-4 and Table 7-3 showed a good agreement among the different measurement techniques (i.e. on-line DLS and SEM). In general, the size measured by the on-line DLS setup was larger than the one determined from the SEM images. However, despite differing in absolute values, size measurements did show similar trends. All ENPs used in this experiment were stable (i.e., <5% variation in size over a 30-minute

period) and, with the exception of the TiO_2 NPs, size measurements were in agreement with the data reported by the manufacturers. TiO_2 NPs formed primary aggregates of around 200 nm in diameter (Table 7-3), rather than remaining as 21-nm particles indicated by the manufacturers. Attempts to break down the aggregates by various methods in order to obtain the primary particles were unsuccessful. These observations are consistent with previous studies suggesting that TiO_2 nanoparticles form strongly bound aggregates in aqueous solutions (Jiang et al. 2009; von der Kammer et al. 2010; Romanello and de Cortalezzi 2013). Hence, in this experiment, in the case of TiO_2, aggregation (or agglomeration) will occur between these aggregates, rather than between the primary particles.

Table 7-3: SEM images of the different ENPs in DI water (Magnification: x200K) and equivalent mean circular diameter (determined from the analysis of at least 200 nanoparticles).

SEM images	Mean circular diameter (nm)
Fe$_2$O$_3$ NPs (100 nm scale)	29.7 ± 3.2
TiO$_2$ NPs (100 nm scale)	204.1 ± 5.6
Citrate-Ag NPs (100 nm scale)	47.0 ± 4.8

7.3.2 Aggregation behaviour of engineered nanoparticles in natural waters

Table 7-4 shows the results of the aggregation studies in the different natural waters while Table 7-5 gathers the results of the linear regression analysis and one-way ANOVA test. Results from Table 7-5 show that more than 85% of the aggregate size variability is explained by the initial TOC concentration of the natural waters. The relation became stronger (i.e. $R^2 > 0.99$, $p < .05$) when combining the effect of both ionic strength (IS) and initial TOC concentration. These multiple regression analysis show that the aggregate size of all ENPs were positively related to the increase in IS and negatively related to the increase in TOC concentration (i.e. slope values in Table 3). Interestingly, when only considering the initial concentration of Ca^{2+} rather than the IS, the results of the multiple linear regression analysis (Table 7-5) are still statistically significant (i.e. $p < .005$) and the correlation between the aggregate size and the combined effect of initial TOC and Ca^{2+} concentration is even stronger (i.e. $R^2 > 0.995$) suggesting that the concentration of Ca^{2+} might dominate the behaviour of ENPs in most natural waters (von der Kammer et al. 2010).

Similarly, the amount of DOM adsorbed on the surface of ENPs was found to be strongly correlated (i.e. $R^2 > 0.97$, $p < .05$) to the combined effect of both IS and initial TOC concentration and initial Ca^{2+} and TOC concentration. According to the DLVO theory (Derjaguin and Landau 1941), an increase in ionic strength will lead to a significant decrease in the repulsive forces between particles, hence leading to the formation of larger particle aggregates. On the contrary, many studies (Mylon et al. 2004; Illes and Tombácz 2006; Baalousha 2009) have demonstrated that the presence of sufficiently high concentrations of DOM can stabilise the nanoparticles in solution and thus prevent them from aggregation.

Table 7-4[a]: Aggregation state of ENPs in natural waters (particle size, zeta potential and amount of DOM adsorbed onto the surface of ENPs).

Parameters		DI	River water	Lake water	Sewage effluent	Groundwater	Seawater
Characteristics	*pH*	-	6.89	7.09	7.8	6.53	7.86
	TOC (mgC/L)	-	15.76	14.66	5.81	5.12	2.65
	Ionic strength (mM)	-	1.96	3.46	11.7	14.9	735
	Ca^{2+} (mM)	-	*0.06*	*0.41*	*0.72*	*1.48*	*10.3*
Particle/aggregate size (nm)	*Fe_2O_3 NPs*	40.5 ± 0.3	225 ± 1.5	850 ± 10.7	2368 ± 34.4	2901 ± 12.5	4245 ± 47.9
	TiO_2 NPs	216.0 ± 3.0	819 ± 5.7	1416 ± 17.4	17049 ± 368[b]	19891 ± 714[b]	24136 ± 256[b]
	Citrate-Ag NPs	60.5 ± 0.3	61 ± 0.4	97 ± 1.6	1722 ± 4.5	2110 ± 17.2	4095 ± 43.1
	SRNOM-Fe_2O_3 NPs	202.6 ± 1.0	211 ± 3.0	538 ± 3.9	1642 ± 5.9	1826 ± 20.7	3140 ± 39.7
Zeta potential value (mV)	Fe_2O_3 NPs	35.4 ± 2.2	23.2 ± 0.9	18.4 ± 1.3	10.6 ± 1.5	8.3 ± 1.9	0.8 ± 1.1
	TiO_2 NPs	20.7 ± 1.5	15.4 ± 0.7	12.3 ± 1.1	2.7 ± 0.9	1.8 ± 1.2	-0.4 ± 1.3
	Citrate-Ag NPs	-35.7 ± 2.4	-33.5 ± 1.6	-22.6 ± 1.3	-13.4 ± 1.1	-12.5 ± 1.0	-1.6 ± 1.7
	SRNOM-Fe_2O_3 NPs	-30.1 ± 1.8	-29.4 ± 0.6	-20.8 ± 1.1	-11.7 ± 1.3	-7.6 ± 1.4	-4.6 ± 1.7
Amount of DOM adsorbed on the surface of ENPs (%)	*Fe_2O_3 NPs*	-	22.8 ± 1.1	21.5 ± 0.9	15.2 ± 0.6	11.5 ± 0.7	4.9 ± 1.77
	TiO_2 NPs	-	14.22 ± 1.2	13.9 ± 0.7	9.9 ± 0.6	7.6 ± 1.1	2.3 ± 0.9
	Citrate-Ag NPs	-	20.9 ± 1.0	19.9 ± 0.4	13.6 ± 0.6	10.0 ± 0.7	4.2 ± 0.8
	SRNOM-Fe_2O_3 NPs	-	n.d.	n.d.	n.d.	n.d.	n.d.

[a] The particle/aggregate size and amount of DOM adsorbed on the surface of ENPs are average of three replicates (n = 3) and ± 1SD [b] Size measured by SLS; n.d.: not detectable

Table 7-5^a: Summary of regression statistics analysis and one-way ANOVA test (95% confidence level) showing the independent and combined effect of IS (X$_1$), initial TOC concentration (X$_2$) and initial Ca^{2+} concentration (X$_3$) on both the aggregate size (Y$_1$) and amount of DOM adsorbed by the ENPs (Y$_2$).

	Y_1 = Aggregate size (nm)			
	Fe$_2$O$_3$ NPs		**TiO$_2$ NPs**	
Variables	Regression statistics (linear regression equation, R^2)	ANOVA (*F, p*)	Regression statistics (linear regression equation, R^2)	ANOVA (*F, p*)
X$_1$	$Y_1 = 1479.6 + 3.8X_1$, 0.551	3.68, n.s.	$Y_1 = 9568.2 + 20.2X_1$, 0.366	1.73, n.s.
X$_2$	$Y_1 = 4456.1 - 271.8X_2$, 0.95	56.70, ***	$Y_1 = 28567.3 - 1807.4X_2$, 0.995	568.21, ***
X$_3$	$Y_1 = 1264.7 + 308.1X_3$, 0.642	5.38, n.s.	$Y_1 = 8298.5 + 1682.2X_3$, 0.454	2.49, n.s.
X$_1$, X$_2$	$Y_1 = 3879.9 + 1.3X_1 - 229.5X_2$, 0.993	149.46, **	$Y_1 = 28159.7 + 0.9X_1 - 1777.4X_2$, 0.995	210.19, ***
X$_1$, X$_3$	$Y_1 = 257.4 - 25.3X_1 + 2189.9X_3$, 0.911	10.27, n.s.	$Y_1 = 558.3 - 194.1X_1 + 16142.6X_3$, 0.83	4.89, n.s.
X$_2$, X$_3$	$Y_1 = 3714.9 - 219.8X_2 + 109.3X_3$, 0.996	233.31, ***	$Y_1 = 27999.7 - 1767.6X_2 + 83.7X_3$, 0.995	215.77, ***
X$_1$, X$_2$, X$_3$	$Y_1 = 3133.7 - 5.4X_1 - 186.9X_2 + 538.9X_3$, 0.999	6687.24, **	$Y_1 = 26134.4 - 17.2X_1 - 1661.8X_2 + 1462.8X_3$, 0.996	92.68, n.s.
	Citrate-Ag NPs		**SRNOM-Fe$_2$O$_3$ NPs**	
Variables	Regression statistics (linear regression equation, R^2)	ANOVA (*F, p*)	Regression statistics (linear regression equation, R^2)	ANOVA (*F, p*)
X$_1$	$Y_1 = 956.3 + 4.3X_1$, 0.705	7.17, n.s.	$Y_1 = 1025.9 + 2.9X_1$, 0.66	5.83, n.s.
X$_2$	$Y_1 = 3899.0 - 259.3X_2$, 0.865	19.19, *	$Y_1 = 3090.0 - 183.9X_2$, 0.897	26.03, *
X$_3$	$Y_1 = 735.0 + 340.0X_3$, 0.783	10.81, *	$Y_1 = 873.0 + 230.7X_3$, 0.742	8.65, n.s.
X$_1$, X$_2$	$Y_1 = 2900.8 + 2.3X_1 - 185.9X_2$, 0.996	237.60, ***	$Y_1 = 2482.8 + 1.39X_1 - 139.3X_2$, 0.996	292.77, ***
X$_1$, X$_3$	$Y_1 = -2.2 - 18.5X_1 + 1717.4X_3$, 0.927	12.70, n.s.	$Y_1 = 306.5 - 14.2 X_1 + 1289.1X_3$, 0.918	11.20, n.s.
X$_2$, X$_3$	$Y_1 = 2642.2 - 171.1X_2 + 185.3X_3$, 0.997	346.83, ***	$Y_1 = 2323.7 - 130.2X_2 + 112.9X_3$, 0.998	513.43, ***
X$_1$, X$_2$, X$_3$	$Y_1 = 2556.0 - 0.8X_1 - 166.2X_2 + 249.0X_3$, 0.997	119.48, n.s.	$Y_1 = 2213.2 - 1.0X_1 - 123.9X_2 + 194.7X_3$, 0.998	204.23, n.s.

^{a} * : p < .05, ** : p < .01, *** : p < .005, ns: non-significant.

	Y$_2$ = Amount of DOM adsorbed on the surface of ENPs (%)			
	Fe$_2$O$_3$ NPs		**TiO$_2$ NPs**	
Variables	Regression statistics (linear regression equation, R^2)	ANOVA (*F, p*)	Regression statistics (linear regression equation, R^2)	ANOVA (*F, p*)
X$_1$	Y$_2$ = 17.9 - 0.02X$_1$, 0.623	4.96, n.s.	Y$_2$ = 11.5 -0.01X$_1$, 0.705	7.15, n.s.
X$_2$	Y$_2$ = 4.9 + 1.2X$_2$, 0.897	26.07, *	Y$_2$ = 2.9 + 0.7X$_2$, 0.842	15.98, *
X$_3$	Y$_2$ = 18.9 - 1.4X$_3$, 0.715	7.53, n.s.	Y$_2$ = 12.2 - 1.0X$_3$, 0.789	11.19, *
X$_1$, X$_2$	Y$_2$ = 8.4 - 0.008X$_1$ + 0.9X$_2$, 0.979	47.29, *	Y$_2$ = 5.95 - 0.007X$_1$ + 0.5X$_2$, 0.979	47.17, *
X$_1$, X$_3$	Y$_2$ = 23.1 + 0.1X$_1$ - 9.3X$_3$, 0.954	20.84, *	Y$_2$ = 14.6 + 0.06X$_1$ - 5.4X$_3$, 0.961	24.36, *
X$_2$, X$_3$	Y$_2$ = 9.4 + 0.8X$_2$ - 0.7X$_3$, 0.985	65.97, *	Y$_2$ = 6.8 + 0.48X$_2$ - 0.6X$_3$, 0.986	68.22, *
X$_1$, X$_2$, X$_3$	Y$_2$ = 14.1 + 0.04X$_1$ + 0.6X$_2$ -4.1X$_3$, 0.999	286.62, *	Y$_2$ = 9.3 + 0.02X$_1$ + 0.3X$_2$ - 2.4X$_3$, 0.995	61.49, n.s.

	Citrate-Ag NPs	
Variables	Regression statistics (linear regression equation, R^2)	ANOVA (*F, p*)
X$_1$	Y$_2$ = 16.3 - 0.02X$_1$, 0.6	4.49, n.s.
X$_2$	Y$_2$ = 3.9 + 1.1X$_2$, 0.907	29.33, *
X$_3$	Y$_2$ = 17.2 -1.3X$_3$, 0.693	6.77, n.s.
X$_1$, X$_2$	Y$_2$ = 7.0 - 0.007X$_1$ + 0.9X$_2$, 0.977	43.03, *
X$_1$, X$_3$	Y$_2$ = 21.3 + 0.1X$_1$ - 9.0X$_3$, 0.949	18.71, n.s.
X$_2$, X$_3$	Y$_2$ = 7.9 + 0.8X$_2$ - 0.6X$_3$, 0.983	56.93, *
X$_1$, X$_2$, X$_3$	Y$_2$ = 12.4 + 0.04X$_1$ + 0.6X$_2$ - 3.9X$_3$, 0.997	126.69, n.s.

[a] * : $p < .05$, ** : $p < .01$, *** : $p < .005$, ns: non-significant.

Despite differing in absolute values, both particle/aggregate size and DOM adsorption followed similar trends for all ENPs, although TiO_2 NPs appeared to be relatively more strongly affected by the IS and initial concentration of TOC and Ca^{2+}. This difference between TiO_2 NPs and the rest of the ENPs is revealed by comparison of the slope values in Table 3. This difference may be due to TiO_2 NPs occurring as small aggregates rather than single particles and exhibiting an initial lower zeta potential value (Table 7-1). Besides, Table 7-4, which reports the zeta potential values of the different ENPs in the natural waters, shows that the zeta potentials of TiO_2 aggregates are the smallest in magnitude indicating smaller repulsive forces between particles promoting their aggregation. The very distinct behaviour of TiO_2 NPs compared to the other ENPs becomes significant in the higher IS samples (i.e. sewage effluent, groundwater and seawater) and may indicate that the energy of interaction has been eliminated (i.e. there is no more repulsive forces between particles) and thus diffusion limited regime has been achieved for TiO_2 NPs.

Unexpectedly, citrate-Ag NPs effectively adsorbed DOM on their surfaces (Table 7-4) despite being negatively charged at the beginning of the aggregation experiments (Table 7-1). A recent study (Liu et al. 2013) indicated that negatively charged functional groups on NOM such as R-COO$^-$ and R-S$^-$ groups may facilitate NOM adsorption on gold NP surfaces by displacing weakly adsorbed citrate from the surface. This may also be the case for Ag-NPs in the present study. In fact, a recent study (Gondikas et al. 2012) showed that cysteine was adsorbed to citrate-Ag NP surfaces through the formation of Ag(+I)-sulfhydryl bonds.

In the case of SRNOM- Fe_2O_3 NPs, neither adsorption nor desorption of DOM were observed in the different natural waters as the initial and final measured TOC were similar (Table 7-4). However, these results could not indicate if there was an exchange between the SRNOM adsorbed on the surface of Fe_2O_3 NPs and the DOM present in the natural waters.

The citrate-Ag NPs and the SRNOM-Fe_2O_3 NPs were most stable (i.e. did not aggregate) in the low IS river water and their size remained quite similar to those obtained in DI water (i.e. increase in size of less than 5%) (Table 7-4); which is possibly due to their higher critical coagulation concentration (CCC) (Figure 7-5and Figure 7-6). In the relatively low IS lake water, however, both citrate-Ag NPs and SRNOM-Fe_2O_3 NPs aggregated. This is probably due to the presence of divalent ions (i.e., Ca^{2+}, 16.51 mg/L; Mg^{2+}, 9.60 mg/L; and SO_4^{2-}, 12.97 mg/L). These are known to promote ENP aggregation, even in the presence of NOM (Ottofuelling et al. 2011), due to bridging effects and/or charge neutralization (Chen et al. 2006). In seawater, because of the high ionic strength conditions, and especially the high concentration of divalent cations, the aggregates formation was mainly governed by diffusion (diffusion-limited aggregation mode) as the surface charge of the ENPs is partially or totally screened (i.e. Zeta potential values close to 0 in Table 7-4) through the compression of the electric double layer (Yan et al. 2000), giving a rise to weak physical particle-particle bonds such as van der Waals forces. Similar results were obtained in other recent studies (Keller et al. 2010; Ottofuelling et al. 2011) where electrophoretic mobility values were found to be close to zero in seawater samples.
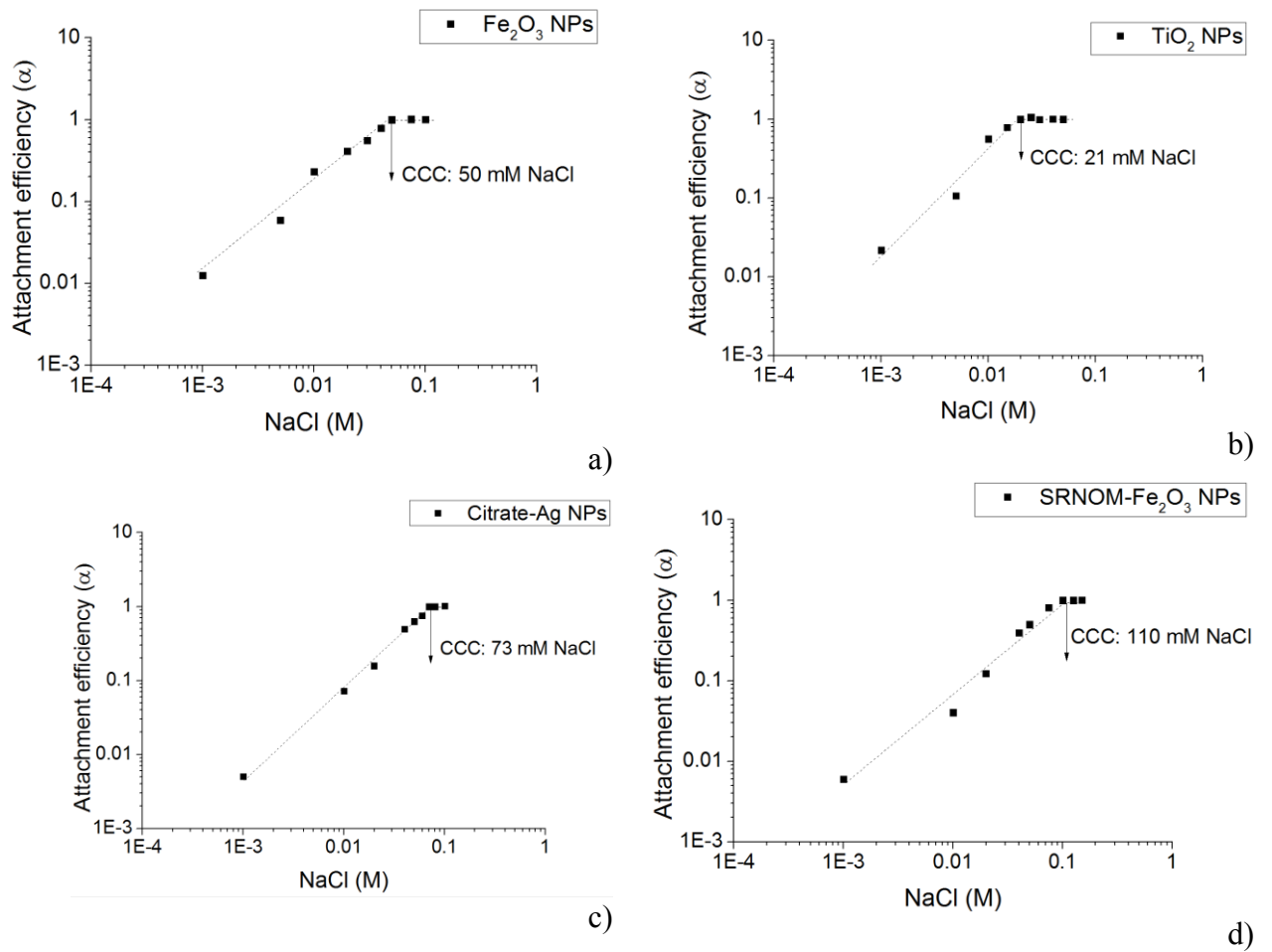
Figure 7-5: Attachment efficiencies of (a) Fe₂O₃NPs (200 mg/L), (b) TiO₂ NPs (25 mg/L), (c) Citrate Ag NPs (1 mg/L) and (d) SRNOM-Fe₂O₃ NPs (as prepared) as a function of NaCl concentration. The dashed line provides a visual guide to distinguish the two aggregation regime.
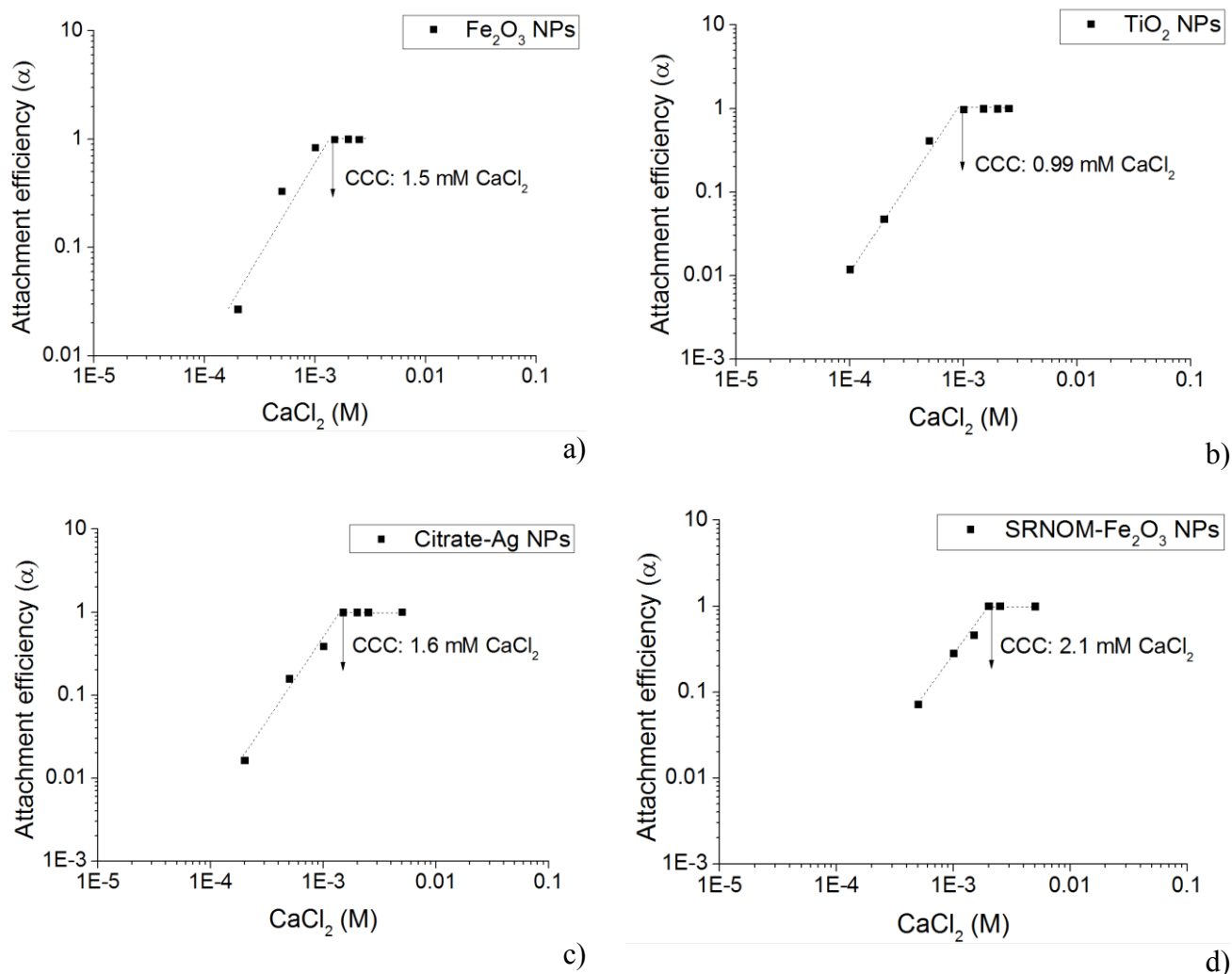
Figure 7-6: Attachment efficiencies of (a) Fe₂O₃NPs (200 mg/L), (b) TiO₂ NPs (25 mg/L), (c) Citrate Ag NPs (1 mg/L) and (d) SRNOM-Fe₂O₃ NPs (as prepared) as a function of CaCl₂ concentration. The dashed line provides a visual guide to distinguish the two aggregation regime.

7.3.3 Characterisation of aggregate structure: Comparison between Fe_2O_3 NPs and TiO_2 NPs

7.3.3.1 *Aggregate strength and recoverability*

In order to investigate aggregate structure, the aggregate strength and recoverability were evaluated using a high mechanical shear force to induce breakage of the aggregates, followed by a slow stirring to allow aggregate regrowth. The SF and RF of the aggregates

were then calculated using equations 4 and 5. These results are presented in Table 7-6, Table 7-7, Table 7-8 and Figure 7-7.
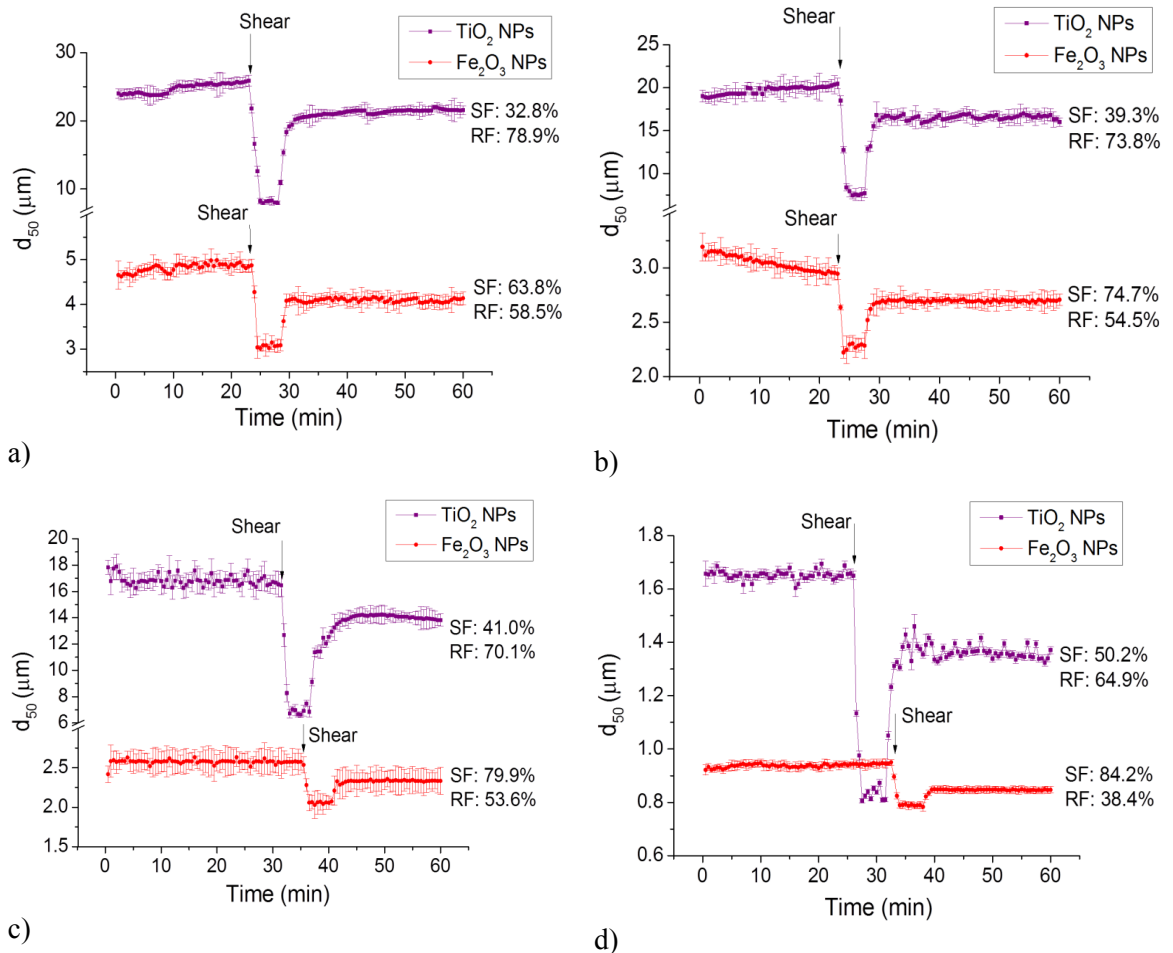
Figure 7-7: Breakage and regrowth profile of Fe_2O_3 NPs (200 mg/L) and TiO_2 NPs (25 mg/L) aggregates formed in (a) seawater, (b) groundwater, (c) sewage effluent and (d) lake water. Shear force applied: 200 rpm for 5 minutes. SF: Strength Factor; RF: Recovery Factor.

When the shear force was introduced, both Fe_2O_3 and TiO_2 NPs aggregates immediately decreased in size in all water samples (Figure 7-7). After slow stirring was reintroduced the aggregates began to grow again. Results for both Fe_2O_3 and TiO_2 NPs indicated the following order for SF: Lake water> Sewage effluent> Groundwater> Seawater, and the reverse order for RF (Table 7-6). In all waters, only partial aggregate recoverability was observed (i.e., RF < 100 %). Aggregate recoverability provides information about the internal bonding structure of the aggregates. In previous studies focusing on floc structure,

irreversible breakage of flocs was seen as evidence that floc formation was not caused by pure charge neutralisation mechanisms but was also associated with chemical bonds such as hydrogen bindings (Jarvis et al. 2005; Zhao et al. 2012). In the present study, chemical bonds could well arise from surface adsorption of DOM on ENPs as well as through intermolecular bridging via calcium complexation. In fact, Table 7-7 shows the amount of Ca^{2+} adsorbed within the formed aggregates in the different water samples which may suggest that calcium, together with NOM, plays a role in ENP aggregation. This statement is confirmed by the results obtained in Table 7-5 which shows that the aggregation of ENPs is strongly related to the combined effect of NOM and Ca^{2+} present in the natural waters (i.e. $R^2 > 0.99$, $p < .005$). Enhanced aggregation of ENPs due to a bridging mechanism by NOM was also observed in previous studies (Tipping and Ohnstad 1984; Chen et al. 2006; Chen et al. 2007; Baalousha et al. 2008).

Table 7-6: Summary of strength factor (SF), recovery factor (RF), fractal dimension (FD) of the formed aggregates.

| Sample | SF (%) | | RF (%) | | FD | | | |
| | | | | | Before breakage | | After regrowth | |
	Fe_2O_3 NPs	TiO_2 NPs	Fe_2O_3 NPs	TiO_2 NPs	Fe_2O_3 NPs	TiO_2 NPs	Fe_2O_3 NPs	TiO_2 NPs
LW	84.2 ± 0.9	50.2 ± 1.5	38.4 ± 0.9	64.9 ± 2.3	1.94 ± 0.02	1.75 ± 0.02	1.95 ± 0.02	1.77 ± 0.02
SewEff	79.9 ± 1.6	41.0 ± 1.9	53.6 ± 1.2	70.1 ± 2.0	1.86 ± 0.01	1.67 ± 0.02	1.87 ± 0.02	1.73 ± 0.01
GW	74.7 ± 1.3	39.3 ± 2.4	54.5 ± 1.5	73.8 ± 2.6	1.82 ± 0.01	1.65 ± 0.04	1.84 ± 0.01	1.72 ± 0.03
SeaW	63.8 ± 2.2	32.8 ± 3.1	58.5 ± 1.3	78.9 ± 2.9	1.69 ± 0.03	1.59 ± 0.02	1.75 ± 0.02	1.69 ± 0.03

In seawater, the aggregates were formed under high ionic strength conditions; much higher than the CCC of both Fe_2O_3 and TiO_2 NPs. This indicates that the ENPs aggregated in a diffusion limited aggregation mode or fast aggregation regime where aggregation is mainly governed by diffusion as the zeta potential values of the ENPs are close to 0 (Table 7-4) due the compression of the electric double layer (Yan et al. 2000). Therefore, it may be expected that these aggregates have low SF and proportionally high RF. In lake water, however,

aggregates of both ENPs had higher SF and lower RF. This can partly be explained by low IS water promoting reaction limited aggregation or a slow aggregation regime, giving rise to more compact aggregates. Furthermore, this could also be the result of DOM (present in higher concentrations in lake water) helping to bind the particles together through chemical bonds (Jarvis et al. 2005; Chowdhury et al. 2013). In fact, adsorption of DOM on the surface of both ENPs is more important in lake water where the recovery factor has the lowest value, suggesting that DOM plays a role in the aggregate recoverability. In fact, Table 7-8 shows a fairly strong correlation (i.e., $R^2 > 0.95$, $p < .05$ for both Fe_2O_3 NPs and TiO_2 NPs) between SF and the amount of DOM adsorbed by the NPs.. Furthermore, Table 7-4 shows that Fe_2O_3 NPs have a greater adsorption capacity for DOM than TiO_2 NPs. This can be explained by their higher initial zeta potential (+35.4 mV for Fe_2O_3 NPs vs. +20.7 mV for TiO_2 NPs) and higher surface area (because Fe_2O_3 NPs are initially present as primary, well-dispersed particles rather than small aggregates). Finally, the presence of calcium cations in lake water can also influence the strength and recoverability of the formed aggregates. In fact, Table 7-7 shows the amount of Ca^{2+} adsorbed within the formed aggregates. This amount was found to be more important in the waters with lower IS (i.e. river and lake waters) which can be seen as evidence of calcium complexation with DOM within the aggregates formed in these waters leading to more compact aggregates. Besides, Table 7-8 shows that there is a strong correlation (i.e. $R^2 > 0.99$, $p < .05$) between the SF and the combined effect of surface-adsorbed DOM and Ca^{2+} for Fe_2O_3 NPs only; which may explained the stronger SF values obtained for this ENP compared to TiO_2 NPs. In fact, as discussed earlier, strong chemical bindings can arise from the intermolecular bridging via calcium complexation with DOM leading to more compact aggregates.

Table 7-7: Amount of Ca²⁺ adsorbed within the ENPs aggregates in the different natural waters.

Sample	Amount of adsorbed Ca^{2+} (%)	
	Fe_2O_3 NPs	TiO_2 NPs
Lake water	27.2 ± 0.9	17.4 ± 1.0
Sewage effluent	12.1 ± 1.1	3.1 ± 1.3
Groundwater	7.6 ± 1.1	2.1 ± 1.0
Seawater	0.3 ± 0.1	0.2 ± 0.1

Table 7-8: Summary of regression statistics analysis and one-way ANOVA test (95% confidence level) showing the independent and combined effect of IS (X_1), amount of DOM (X_2) and Ca^{2+} adsorbed by the ENPs (X_3) on both the strength factor (SF, Y_3) and fractal dimension (FD, Y_4) of the formed aggregates.

	Y_3 = Strength Factor (%)			
	Fe_2O_3 NPs		TiO_2 NPs	
Variables	Regression statistics (linear regression equation, R^2)	ANOVA (*F, p*)	Regression statistics (linear regression equation, R^2)	ANOVA (*F, p*)
X_1	Y_3 = 79.8 - 0.02X_1, 0.815	8.83, n.s.	Y_3 = 43.7 - 0.01X_1, 0.568	2.63, n.s.
X_2	Y_3 = 59.2 + 1.2X_2, 0.957	44.18, *	Y_3 = 28.7 + 1.4X_2, 0.953	40.49, *
X_3	Y_3 = 67.3 + 0.7X_3, 0.829	9.72, n.s.	Y_3 = 35.9 + 0.8X_3, 0.873	13.79, n.s.
X_1, X_2	Y_3 = 65.0 - 0.008X_1 + 0.9X_2, 0.991	57.93, n.s.	Y_3 = 24.5 + 0.006X_1 + 1.8X_2, 0.976	20.05, n.s.
X_1, X_3	Y_3 = 73.1 - 0.01X_1 + 0.4X_3, 0.976	20.60, n.s.	Y_3 = 38.5 - 0.008X_1 + 0.7X_3, 0.997	154.40, n.s.
X_2, X_3	Y_3 = 52.1 + 2.4X_2 - 0.7X_3, 0.999	2451.55, *	Y_3 = 30.7 + 0.9X_2 + 0.3X_3, 0.997	167.08, n.s.
	Y_4 = Fractal Dimension			
	Fe_2O_3 NPs		TiO_2 NPs	
Variables	Regression statistics (linear regression equation, R^2)	ANOVA (*F, p*)	Regression statistics (linear regression equation, R^2)	ANOVA (*F, p*)
X_1	Y_4 = 1.9 - 0.0003X_1, 0.783	7.20, n.s.	Y_4 = 1.7 - 0.0001X_1, 0.585	2.83, n.s.
X_2	Y_4 = 1.6 + 0.01X_2, 0.981	101.39, **	Y_4 = 1.6 + 0.01X_2, 0.965	55.40, *
X_3	Y_4 = 1.7 + 0.009X_3, 0.89	16.15, n.s.	Y_4 = 1.6 + 0.008X_3, 0.857	11.94, n.s.
X_1, X_2	Y_4 = 1.7 - 0.00007X_1 + 0.01X_2, 0.999	1909.99, *	Y_4 = 1.5 + 0.00005X_1 + 0.02X_2, 0.985	31.82, n.s.
X_1, X_3	Y_4 = 1.8 - 0.0001X_1 + 0.006X_3, 0.997	175.13, n.s.	Y_4 = 1.6 - 0.00008X_1 + 0.006X_3, 0.993	69.28, n.s.
X_2, X_3	Y_4 = 1.6 + 0.02X_2 - 0.005X_3, 0.993	70.85, n.s.	Y_4 = 1.6 + 0.009X_2 + 0.003X_3, 0.999	440.84, *

[a] * : $p < .05$, ** : $p < .01$, *** : $p < .005$, ns: non-significant.

7.3.3.2 Aggregate structural analysis

The structure of the aggregates was also described by calculating their fractal dimension (FD) before breakage and after regrowth (Table 7-6). Fractal dimension can provide useful information about the morphology (i.e., porosity and compactness) of the aggregates (Christian et al. 2008). For both ENPs, the FD values remained fairly unchanged after regrowth, except in the samples with high IS (i.e. seawater). As discussed in the previous section, in seawater, the aggregates were formed under high ionic strength conditions and thus aggregation is mainly governed by diffusion giving rise to weak physical particle-particle bonds such as van der Waals forces. When the high shear force is applied, the aggregates will preferentially break at these weak points. When the slow mixing speed is then reintroduced, the aggregates will start to reform slowly and new bonds will be created at more favourable points (i.e. where the attractive forces will be greater or the repulsive forces lower) resulting in the formation of more compact aggregates with higher FD. (Yukselen and Gregory 2002). By comparing the FD of both ENPs in the different water samples (Table 7-6), it can be seen that the FD values followed the same trend as the SF values: increasing together with increasing quantities of DOM adsorbed on the ENPs (i.e., $R^2 > 0.96$, $p < .05$) (Table 7-8). Baalousha et al. (Baalousha et al. 2008) obtained similar findings, with the addition of humic acid (HA) molecules inducing a change in aggregate structure. In the absence of HA, the nanoparticles formed open porous aggregates with a low FD, whereas in the presence of HA, compact aggregates with higher FD were formed. The difference observed here between Fe_2O_3 and TiO_2 NPs may also be explained by the fact that Fe_2O_3 NPs adsorbed DOM more efficiently and therefore formed more compact aggregates. Furthermore, it can also be explained by the way ENP aggregates interact with DOM. Christian et al. (Christian et al. 2008) explained that HA (and therefore DOM) adsorption on NP aggregate surfaces could occur in two steps. Initially, DOM may cover the surfaces of NP aggregates in a fast adsorption step. This could be followed by slow diffusion of DOM

within the aggregate pores, leading to the formation of more compact aggregates. Finally, the difference in aggregate structure could also arise from the difference in initial particle surface area. A recent study (Chowdhury et al. 2013) showed that there is a linear relationship between NP surface area and fractal dimension, which suggests that smaller particles can form more compact aggregates.

SEM images of both ENPs in seawater (Figure 7-8) and in lake water (Figure 7-9) confirmed the difference in structure between the two extreme water samples (i.e., high IS and low TOC seawater versus low IS and high TOC lake water). Despite the difference in size, both Fe_2O_3 and TiO_2 NPs formed linear, chain-like aggregates in seawater, whereas in lake water, aggregates of both ENPs were more compact. In a recent study (Romanello and de Cortalezzi 2013) investigating the aggregation behaviour of TiO_2 NPs under relevant environmental conditions, similar findings were reached regarding the structure of the formed aggregates. In their study, Romanello et al. (2013) found that TiO_2 aggregates formed under favourable conditions (i.e. high IS) exhibited an open, porous morphology (based on SEM images analysis). Authors explained that under these unstable conditions, the total interaction energy between particles is positive which resulted in high attachment efficiency (Elimelech et al. 1995).
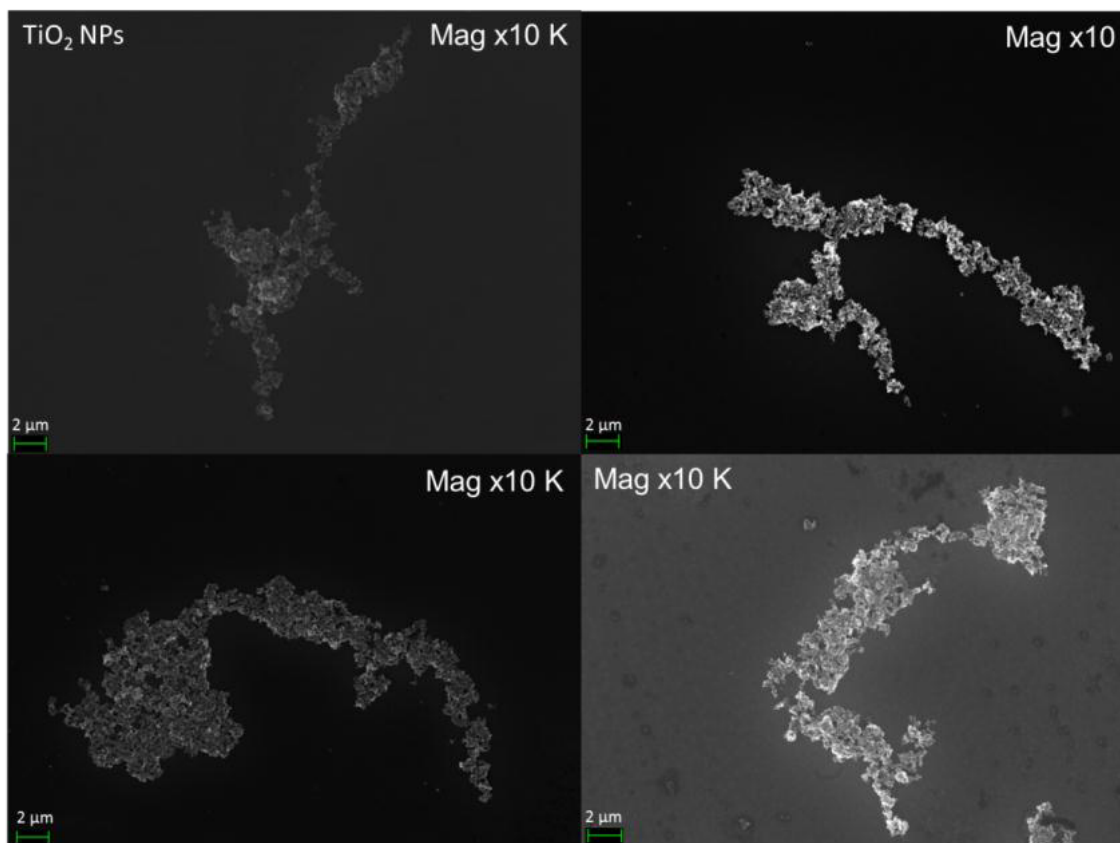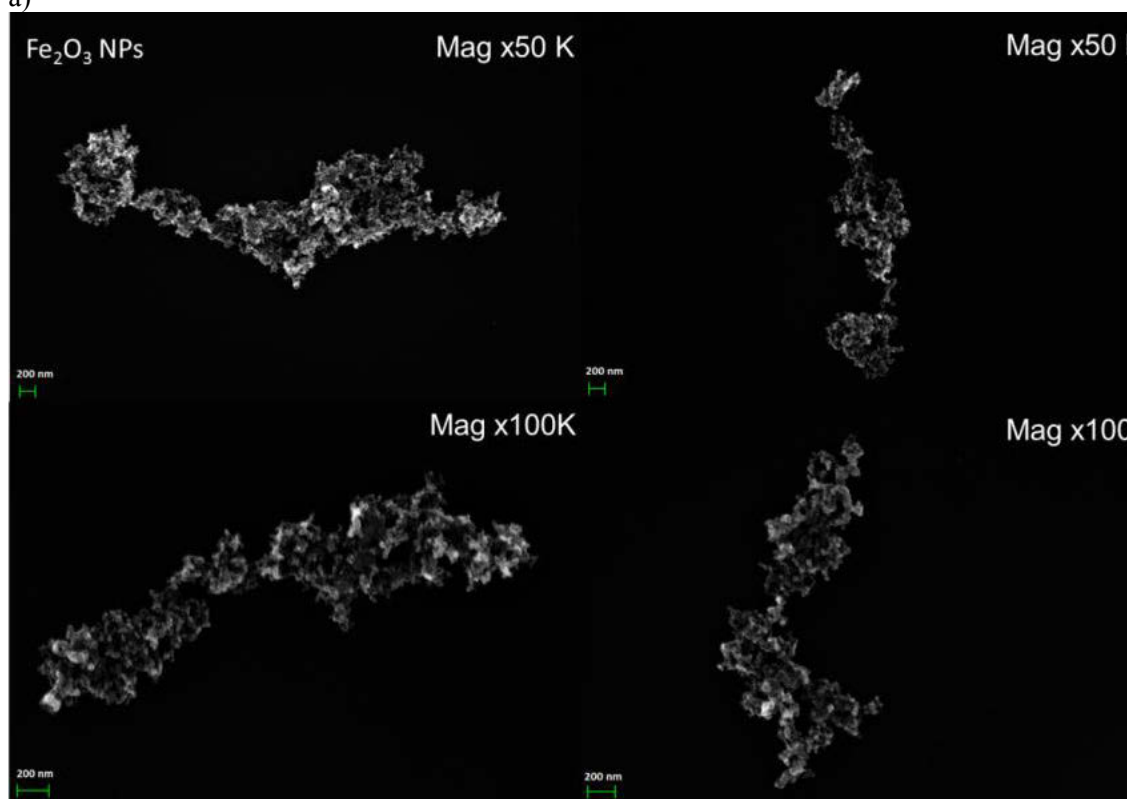
Figure 7-8: Representative SEM images of (a) TiO$_2$ and (b) Fe$_2$O$_3$ aggregates in seawater.
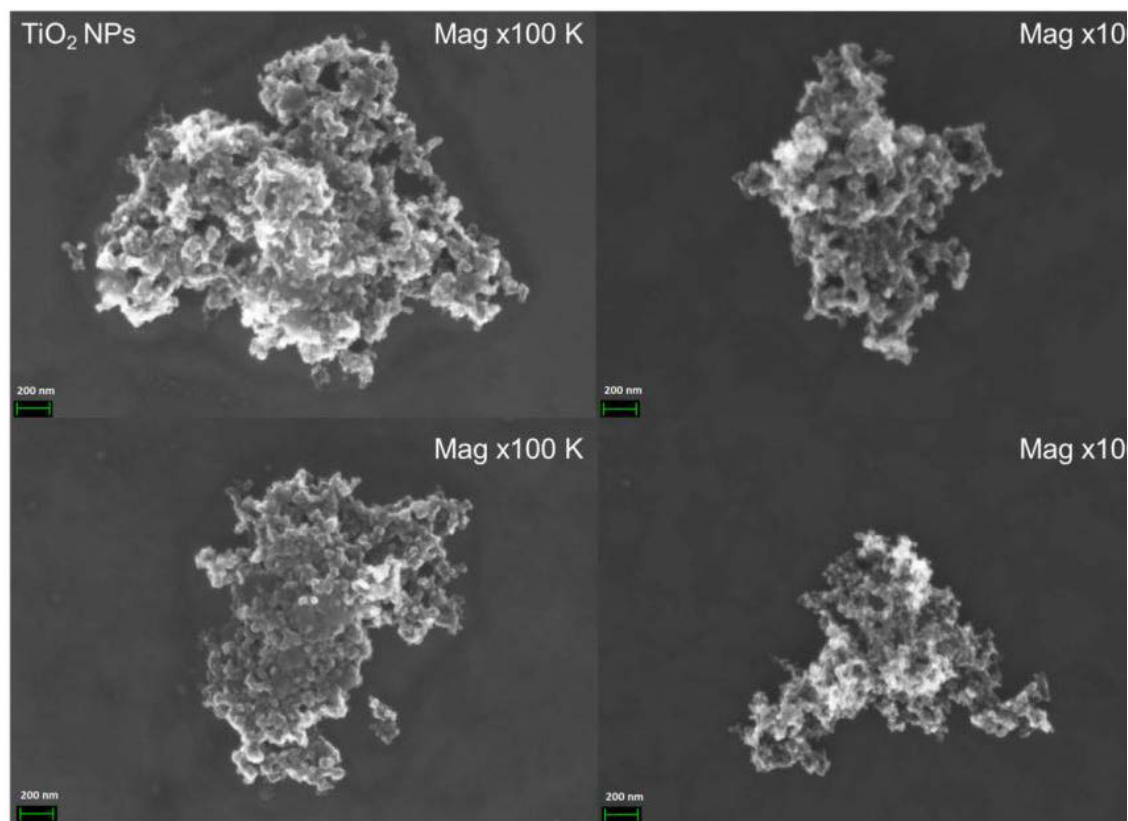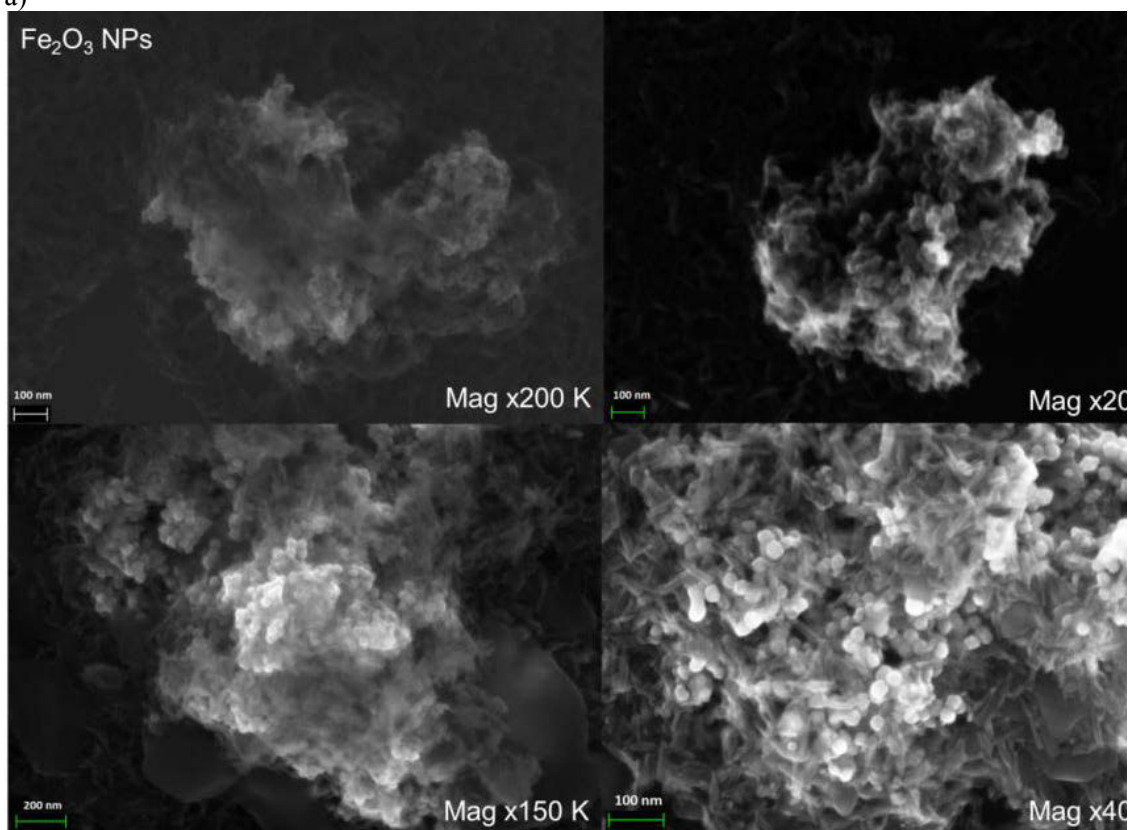
Figure 7-9: Representative SEM images of (a) TiO$_2$ and (b) Fe$_2$O$_3$ aggregates in lake water.

7.3.3.3 Correlation between SF and FD

Figure 7-10 shows that there is also a strong correlation (i.e., $R^2 > 0.98$) between aggregate FD and SF. This can be explained by the strong relationship between the aggregate structure and breakup mechanism. In fact, Jarvis et al. (Jarvis et al. 2005) explained that there are two mechanisms of aggregate breakup: surface erosion (slow) and large-scale fragmentation (fast). Highly-branched aggregates with low FD (e.g., in seawater) will breakup via a fragmentation mechanism, whereby aggregates split into pieces of comparable size, leading to a low SF. This suggests that these small aggregates were agglomerated rather than aggregated as they were only held by weak van der Waals forces (Jiang et al. 2009). However, compact aggregates with higher FD (e.g., in lake water) will preferentially breakup via a surface erosion mechanism, whereby small particles are separated from the surface of the aggregates, leading to higher SF. The high degree of compactness of these aggregates (i.e. high FD value) makes the disaggregation process more difficult (resulting in higher SF value) and this is mainly due to the presence of DOM within the aggregates (Baalousha et al. 2008). This finding is also supported by Wang et al. (Wang et al. 2009) who found a close relationship between floc structure (i.e., FD) and floc SF.
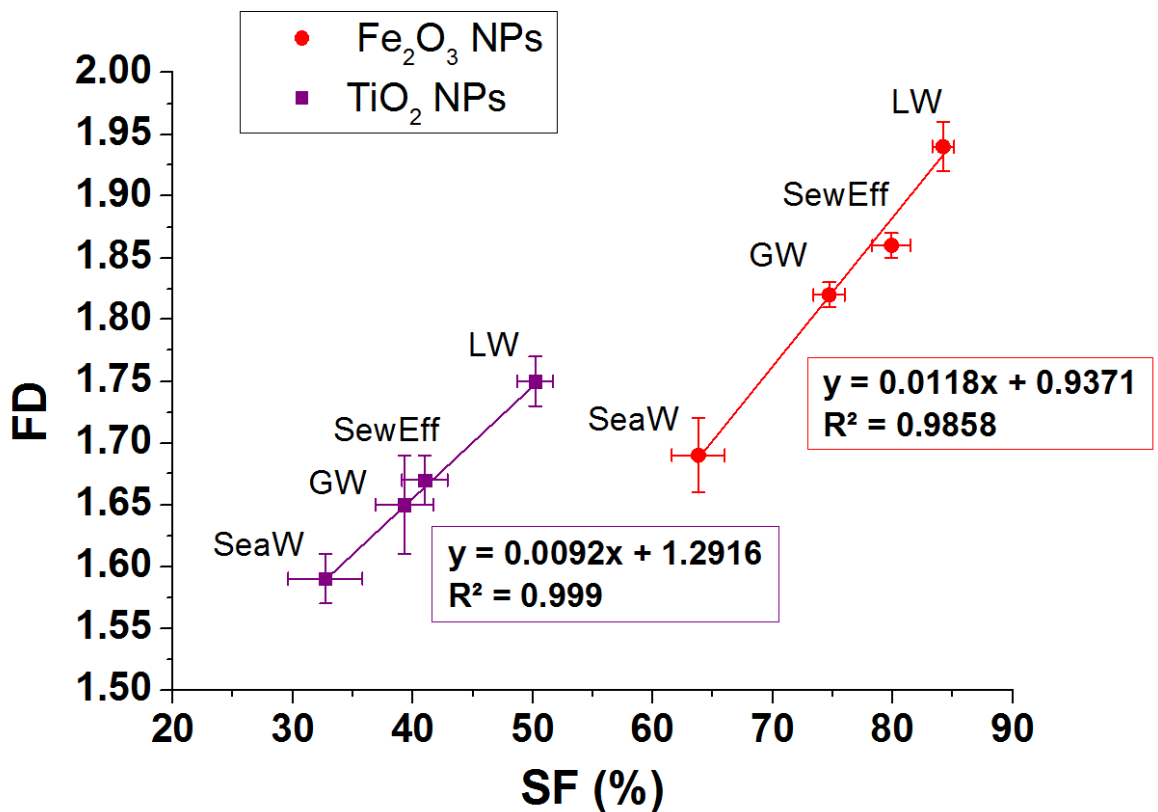
Figure 7-10: Correlations between the 1the strength factor SF and the fractal dimension FD of the formed aggregates. The error bars represent the standard deviation from triplicate measurements.

7.4 Conclusions

In this chapter, it was showed that aggregation behaviour and aggregate structure of ENPs are both strongly dependent on the physico-chemical characteristics of the environmental medium (i.e., ionic strength, ionic composition and presence and concentration of NOM). Aggregate structure of ENPs, in particular, is an important factor controlling their fate and behaviour in the aquatic environment. Results from this study also revealed a strong correlation between FD and SF. Compact aggregates (i.e. having high FD and SF) will more likely disaggregate via surface erosion which will likely lead to the formation of smaller aggregates that can potentially be resuspended in the water column where they can adsorb and transport pollutants, nutrients and/or natural colloids.

The method proposed and demonstrated in this chapter provides a simple and convenient way to characterise the aggregation behaviour and aggregate structure of ENPs in a range of different water types. With a rapidly multiplying suite of ENPs now identified as potential environmental contaminants, screening methods such as this are clearly required.
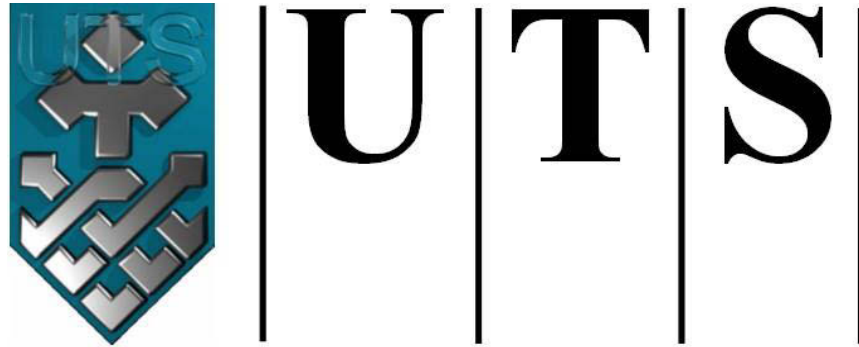
University of Technology Sydney
FACULTY OF ENGINEERING

CHAPTER 8

COUPLING LASER LIGHT SCATTERING WITH

FIELD FLOW FRACTIONATION TO ASSESS

THE AGGREGATION BEHAVIOUR AND

AGGREGATE STRUCTURE OF ENGINEERED

NANOPARTICLES IN NATURAL WATERS

8.1 Introduction

In the previous chapter (i.e. Chapter 7), we developed a novel set-up combining both dynamic and static laser light scattering techniques to study the aggregation behaviour and aggregate structure of ENPs in various natural water samples. Light scattering techniques are widely available but suffer from the strong particle size dependence of the scattering intensity (Hiemenz and Rajagopalan 1997). This leads to Z-average or intensity values being skewed toward larger particles/aggregates (Domingos et al. 2009). To circumvent this limitation, this on-line light scattering method was further developed by combining it with different off-line analytical techniques to better assess the polydispersity of the sample. The larger aggregates formed under a fast-aggregation regime were characterised in terms of size and structure by use of the on-line light scattering set-up. After sedimentation, the smaller particles/aggregates were collected and characterised by both dynamic light scattering (DLS) and flow field-flow fractionation (FlFFF).

Titanium dioxide (TiO_2) NPs were chosen for this study as they are among the most heavily commercialised ENPs, finding applications in paints, cosmetics, catalysts and food colorants (Joo et al. 2009; Robichaud et al. 2009). The principal pathway for TiO_2 NPs into the environment is through wastewater treatment plants (WWTPs) (Gottschalk et al. 2009; Kiser et al. 2009; Gottschalk et al. 2010; Kunhikrishnan et al. 2014). In some studies (Gottschalk et al. 2009; Kiser et al. 2009), it has been demonstrated that TiO_2 NPs are only partly removed in WWTPs and thus a large quantity can enter the natural water system. TiO_2 NPs have also been detected in freshwater in concentrations in the range of a few µg/L following runoff from painted-house facades (Kaegi et al. 2008). The release of TiO_2 NPs into the environment raises concerns about contamination, both by the nanoparticles themselves and by their potential to co-transport sorbed contaminants into surface and groundwaters. As river waters are an important source of drinking water and a major component of surface

waters, understanding the fate and behaviour of TiO_2 NPs in these natural systems is necessary to underpin robust risk assessment of these emerging contaminants.

The overall objectives of this study were therefore:

- To investigate the agglomeration behaviour of TiO_2 NPs in different river water samples using various analytical techniques. The benefit of using a multi-method approach to characterise ENPs in complex environmental samples has already been demonstrated (Domingos et al. 2009; Chekli et al. 2013) but has not been systematically applied in aggregation studies using natural waters;
- To assess the strength and recovery factors and the structure of the aggregates formed in the river waters.

This chapter is an extension of a research article published by the author in Journal of Environmental Management (Chekli et al. 2015).

8.2   Experimental

8.2.1 TiO_2 NPs

Commercial Aeroxide P25 TiO_2 NPs (average primary particle size reported by the manufacturer 21 nm) were purchased from the Evonik Degussa Corporation (Parsippany, NJ, USA). The detailed characteristics of this material can be found in Table 8-1. The zeta potential measurements and determination of CCC for both NaCl and $CaCl_2$ are described in Chapter 7.

Table 8-1: Characteristics of the tested TiO$_2$ NPs.

	TiO$_2$ NPs	Source
CAS-Nr	13463-67-7	Manufacturer
Powder content	> 99.5% TiO$_2$	Manufacturer
Average primary particle size (TEM)	21 nm	Manufacturer
Density	3.8 g/mL at 25°C	Manufacturer
pH	3.5-4.5 (40 g/L)	Manufacturer
Point of zero charge	pH 5.8	This study – Figure 8-1
CCC (mM NaCl)	18	This study – Figure 8-2
CCC (mM CaCl$_2$)	0.73	This study – Figure 8-2
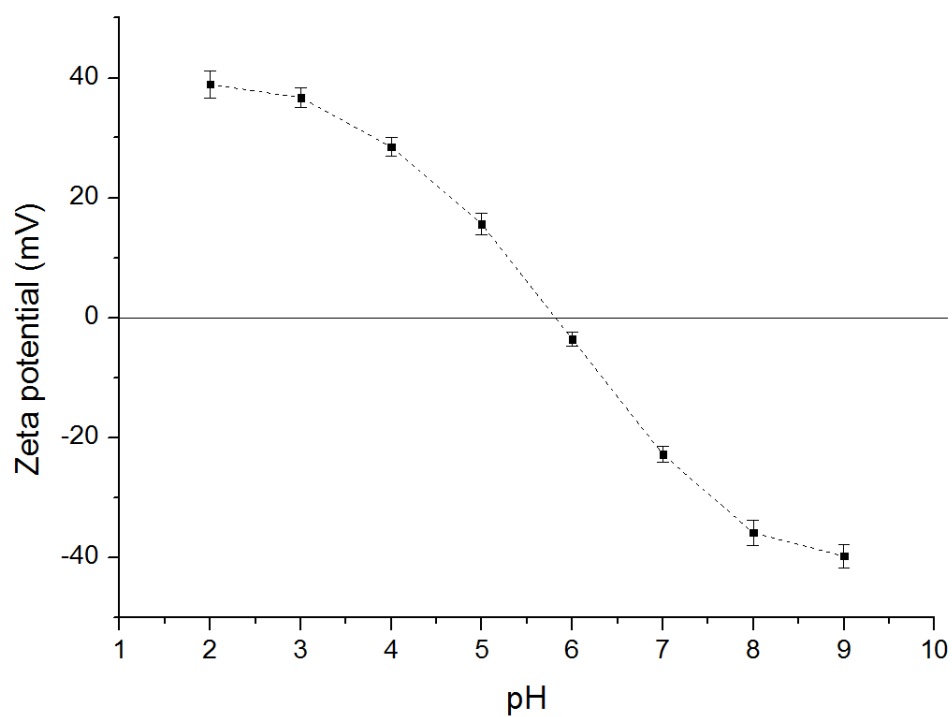
Figure 8-1: Zeta potential profile of TiO$_2$ NPs (12.5 mg/L) as a function of pH.
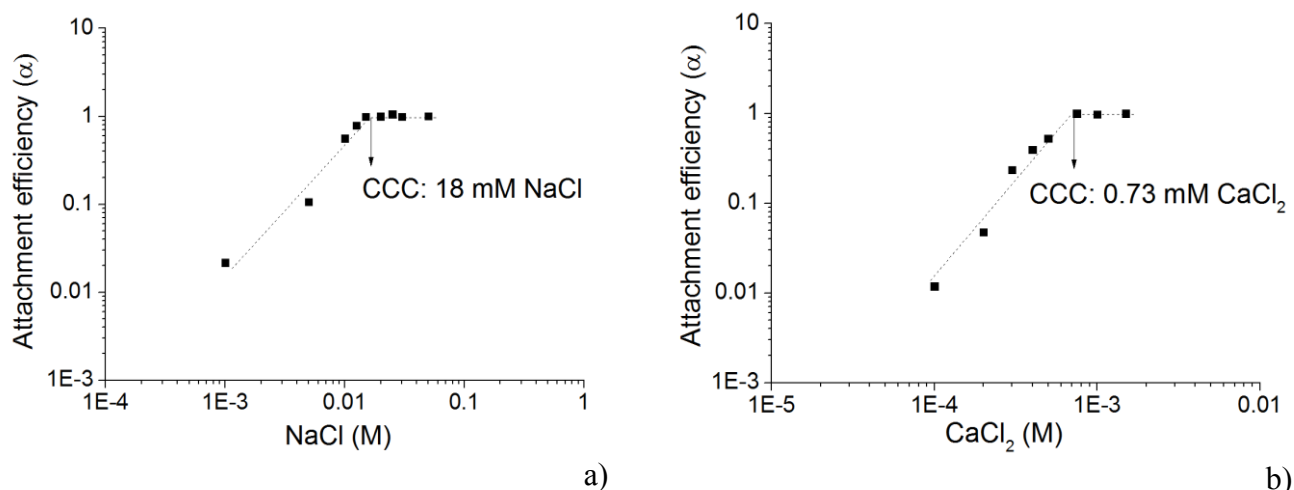
Figure 8-2: Attachment efficiencies of TiO$_2$ NPs (12.5 mg/L) as a function of (a) NaCl concentration and (b) CaCl$_2$ concentration. The dashed line provides a visual guide to distinguish the two aggregation regimes.

8.2.2 Sample preparation

TiO$_2$ stock solution was prepared by mixing TiO$_2$ particles (10 g/L) with DI water for 1 hour, followed by 30 minutes of bath sonication (Model 800HD, Soniclean, Australia). Before each experiment, 200 mL of the stock solution was centrifuged for 10 min at 3000 rpm (Model 2040, Centurion Scientific Ltd, UK) and supernatant (100 mL) collected for the experiments. The final concentration of TiO$_2$ in the supernatant varied from 1.5 to 2.1 g/L. This concentration was determined by measuring the nephelometric turbidity (NTU) as explained in Chapter 3.

8.2.3 Natural river water samples

Four river water samples were collected along the Parramatta River (NSW, Australia) at different distances from the sea to obtain a gradient in both DOM concentrations and solution IS. Physical and chemical characteristics of the water samples are given in Table 8-2. All water samples were filtered through a 0.2 μm membrane filter and stored at 4°C in the dark prior measurements as described in Chapter 7. Characterisation of the natural

waters (i.e. DOC, pH, EC and concentrations of the major anions and cations) is detailed in Chapter 7.

Table 8-2: Physico-chemical characteristics of the tested river waters.

	$R_{2.8}$	$R_{6.7}$	$R_{18.7}$	R_{342}
EC (µS/cm)	313	653	1850	26900
pH	7.36	7.64	8.04	7.96
DOC (mgC/L)	10.01	5.33	3.98	3.21
Ionic strength (mmol/L)	2.8	6.7	18.7	342.0
Ionic composition (mM)				
Cl^-	1.21	5.15	14.8	278.9
NO_3^-	0.01	0.05	0.07	2.16
SO_4^{2-}	0.24	0.27	0.82	14.7
PO_4^{3-}	0.07	n.d.	0.08	n.d.
Na^+	2.10	5.17	15.1	495.9
K^+	0.11	0.12	0.41	1.59
Ca^{2+}	n.d.	0.16	0.36	4.02
Mg^{2+}	0.30	0.30	0.56	8.61

*R_i: River sample with a ionic strength equal to i. n.d.: not detectable.

8.2.4 Aggregation study in river waters

The work of Phenrat et al. (2007) formed the basis for the study of the aggregation/sedimentation process. According to their study, there is a critical size (d_c) above which aggregates will sediment rapidly while aggregates having lower sizes ($d < d_c$) will remain suspended. Aggregation of the residual smaller aggregates will then occur slowly with time followed by sedimentation when their size reaches d_c. In this study, we firstly characterised the large aggregates ($d > d_c$) formed under a fast-aggregation regime or reaction-limited aggregation (RLA) (Weitz et al. 1985; Klein and Meakin 1989) using an on-line light scattering method. After this initial fast sedimentation process, the smaller aggregates remaining in suspension were collected and analysed by both DLS and FlFFF.

TiO$_2$ NPs were added to the different river water samples (final concentration in river waters of 12.5 mg/L) using a variable-speed jar tester (ZR4-2, Zhongrun Water Industry Technology Development Co., Ltd., China) which was connected to a peristaltic pump (Model 77521-47, Masterflex, Cole Palmer, Australia) as shown in Figure 7-1 (Chapter 7). Details on the experimental protocol of the on-line light scattering set-up can be found in Chapter 7. The water samples were pumped directly to the light scattering instrument for continuous particle/aggregate size analysis: a dynamic light scattering (DLS) instrument (model ZEN3600; Malvern Instruments, Worcestershire, UK) was used for particle size ranging from 10 nm to 6 µm and a static light scattering (SLS) system (Malvern Mastersizer 2000, Malvern Instruments, Worcestershire, UK) was utilised for measuring the larger particles.

In addition to particle size analysis, the amount of DOM adsorbed during the aggregation process was also measured at the end of the aggregation experiments. Surface-adsorbed DOM was measured by a TOC analyser (Multi N/C 3100, Analytic Jena AG, Germany) using 50 mL samples which were first centrifuged for 10 min at 2500 g (Model 2040, Centurion Scientific Ltd, UK) to separate the solution phase from the solid particles. The amount of DOM adsorbed on the surface of TiO$_2$ NPs during the aggregation process was calculated using the following equation:

$$q = (C_0 - C_f)\frac{V}{m} \tag{1}$$

where q (mg/g) is the amount of DOM (mg) adsorbed per mass (g) of TiO$_2$ NPs, C_0 and C_f (mg/L) are the initial and final concentration of DOM in solution, V (L) is the solution volume and m (g) is the mass of the TiO$_2$ NPs injected into the river water samples.

Measurements were performed in triplicate and the results presented are average values with standard deviations.

After the aggregation experiments, the larger aggregates were allowed to settle before the supernatant was collected following the protocol described in v.d. Kammer et al. (2010) (i.e. the supernatant should be collected after the fast aggregation reaction and before the most stable dispersion starts to settle). Concentration of the stable fraction of TiO_2 in the supernatant was determined by measuring the nephelometric turbidity as described earlier.

8.2.4.2 Dynamic light scattering – batch mode

After sedimentation of the larger aggregates, the supernatant (5 mL) was collected and analysed with a Zetasizer (model ZEN3600; Malvern Instruments, Worcestershire, UK) to determine both the zeta potential and hydrodynamic diameter of the different samples. Physical principles, mathematical treatment, and limitations of the DLS data can be found in Chapter 3.

8.2.4.3 Flow field-Flow Fractionation

The FlFFF system used in this study has been described in Chapter 3 (i.e. FlFFFb - Wyatt Technology, Dernbach, Germany) as well as the theory and principles of this instrument.

The operating conditions are summarised in Table 8-3. At least three independent replicates were run per sample and the data were averaged. In general, good agreement was observed between replicates (i.e. peak heights differed by less than 5 %). Samples used in FlFFF experiments were the same as for DLS experiments to ensure data comparability.

Table 8-3: Summary of the FFF operating conditions used in this study.

Sample	Channel flow (mL/min)	Cross Flow (mL/min)	Carrier liquid composition
$R_{2.8}$		1.5	
$R_{6.7}$	0.5		MilliQ water + 0.01% FL70*
$R_{18.7}$		0.3	
R_{342}			

*Fl-70 (SF105-1, Fisher Scientific, Fair Lawn, NJ) is an anionic surfactant composed with oleic acid, sodium carbonate, tergitol, tetrasodium EDTA, poly(ethylene glycol), and triethanolamine.

Polystyrene nanospheres with standard sizes of 100 nm, 300 nm and 400 nm (Thermo Scientific, Fremont, CA, USA) were used to create calibration curves from which hydrodynamic diameters of TiO_2 NPs were determined. An example of one such calibration curve is given in Figure 8-3.
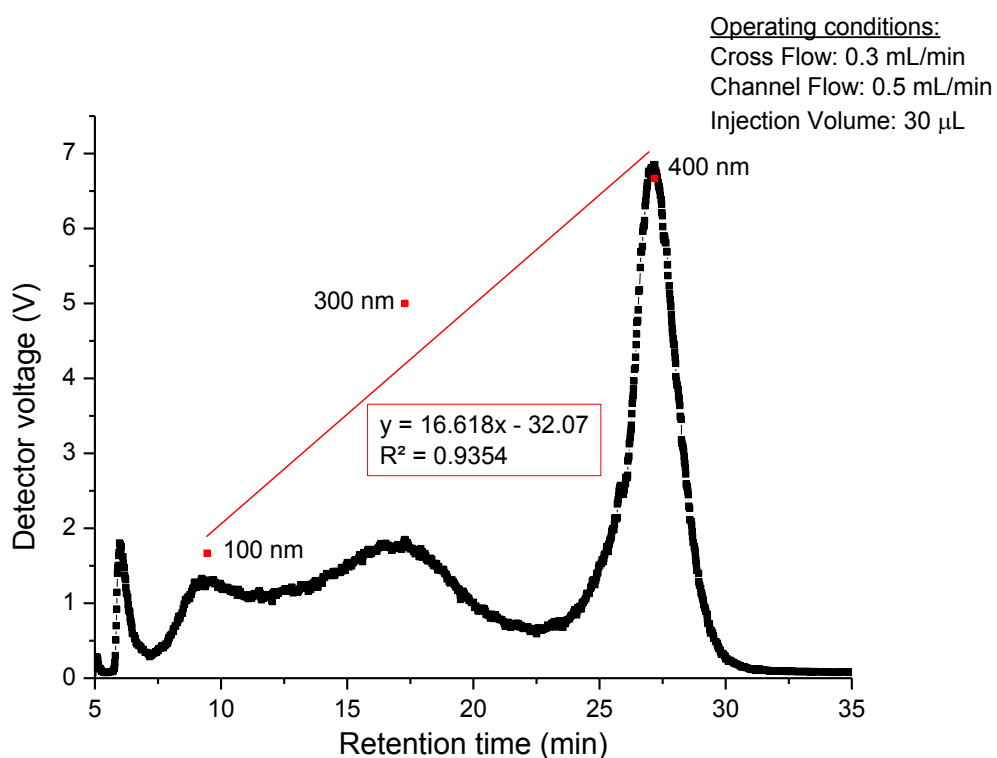
Figure 8-3: FFF calibration curve using polystyrene standard nanoparticles of 100 nm, 300 nm and 400 nm.

8.2.4.4   Data analysis

In order to assess the independent and combined effect of both the ionic strength and initial TOC concentration of the natural waters on the aggregate size and surface-adsorbed DOM;

single and multiple linear regression analysis were carried out. In fact, preliminary screening showed that both the ionic strength and initial TOC concentration of the natural waters tested were the two main variables controlling the aggregate size and surface-adsorbed DOM.

The statistical significance of the effect of each variables (independently and combined) on each property tested was assessed by analysis of variance (one-way ANOVA, $p < .05$).

8.2.5   Aggregate structure

8.2.5.1   *Strength and recovery factors*

The aggregates formed under the fast-aggregation regime were subjected to a high mixing speed of 200 rpm (i.e. 315 g) for 5 minutes to induce their disaggregation. After breakage, slow mixing (i.e. 40 rpm; 25 g) was reintroduced for 15 minutes to allow the aggregates to regrow. The size of the aggregates was measured by drawing the sample through the optical unit of the SLS detector and back into the jar using the peristaltic pump. Size measurements were taken every 30 seconds for the duration of the experiment and recorded on a computer.

To evaluate both the strength and recoverability of the formed aggregates, the strength factor (SF) and recovery factor (RF), were calculated as described in Chapter 7 (Yukselen and Gregory 2002; Jarvis et al. 2005; Zhao et al. 2012).

8.2.5.2   *Aggregate structural analysis*

There are two distinct regimes of irreversible colloid aggregation: reaction-limited aggregation (RLA) and diffusion-limited aggregation (DLA). The DLA regime will occur when there are no or negligible repulsive forces between particles, and aggregation is mainly controlled by diffusion (Klein and Meakin 1989), whereas the RLA regime will occur when

there are significant but not insurmountable repulsive forces between particles (Weitz et al. 1985; Klein and Meakin 1989; Lin et al. 1990).

The highly disordered structure of colloidal aggregates can be characterised by its scaling behaviour, defined as the mass fractal dimension (FD) (Weitz et al. 1985; Rice and Lin 1993). Typical FD values are FD ~ 1.8 for DLA, and FD ~ 2.1 for RLA, indicating a more compact structure for aggregates formed under the RLA regime (Klein and Meakin 1989).

The use of Mastersizer 2000 for the determination of FD has been previously reported (Rieker et al. 2000; Jarvis et al. 2005b) and detailed in Chapter 3.

8.3 Results and discussion

8.3.1 Characteristics of the river waters and stability of TiO_2 NPs in DI water

The characteristics of the tested river waters are presented in Table 1. The pH of the different river samples was restricted to a narrow range (i.e. 7.36 – 8.04). However, as expected, a gradient in both the DOC concentration (3.21 – 10.01 mgC/L) and solution IS (2.8 – 342.0 mmol/L) was obtained. The ionic composition and more specifically the ratio between mono- and divalent cations also varied significantly between the tested samples with monovalent cations (especially Na^+) becoming dominant in the highest IS river sample due to the vicinity of the ocean. This will have an important impact on the aggregation behaviour as the critical coagulation concentration (CCC) of mono- and divalent cations is approximately 1:0.033 (molar ratio) (Elimelech et al. 1998; Stumm and Morgan 2012). This suggests that, if only considering electrostatic interactions and neglecting the effects of specific adsorption (e.g. with NOM), the concentration of divalent cations should dominate the behaviour of ENPs in most surface waters (von der Kammer et al. 2010).

The hydrodynamic diameter of the TiO_2 NPs in DI water (pH 4) was measured to ensure their stability before being subjected to the natural river waters. The results are presented in Figure 8-4 and Table 8-4 and showed a small variation in size (< 5%) over the 30-minute test period. Size measurements by both on-line DLS and scanning electron microscope (SEM) were not in agreement with the data reported by the manufacturers. TiO_2 NPs were present in small aggregates of around 250 nm in diameter rather than well-dispersed as 21-nm primary particles. This is consistent with previous studies which found that TiO_2 NPs form strongly bound aggregates when dispersed in aqueous solutions (Jiang et al. 2009; von der Kammer et al. 2010; Romanello and de Cortalezzi 2013).
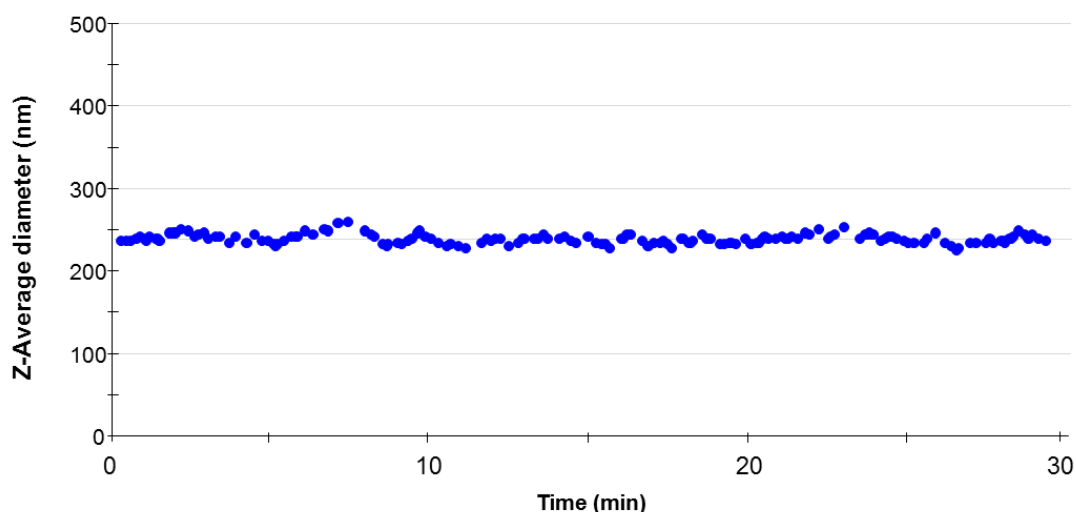
Figure 8-4: Hydrodynamic diameter of TiO$_2$ NPs in DI water (pH 4) prior to the aggregation study measured by DLS in continuous mode.

Table 8-4: SEM images of the TiO$_2$ NPs in DI water (Magnification: 200 000 ×).
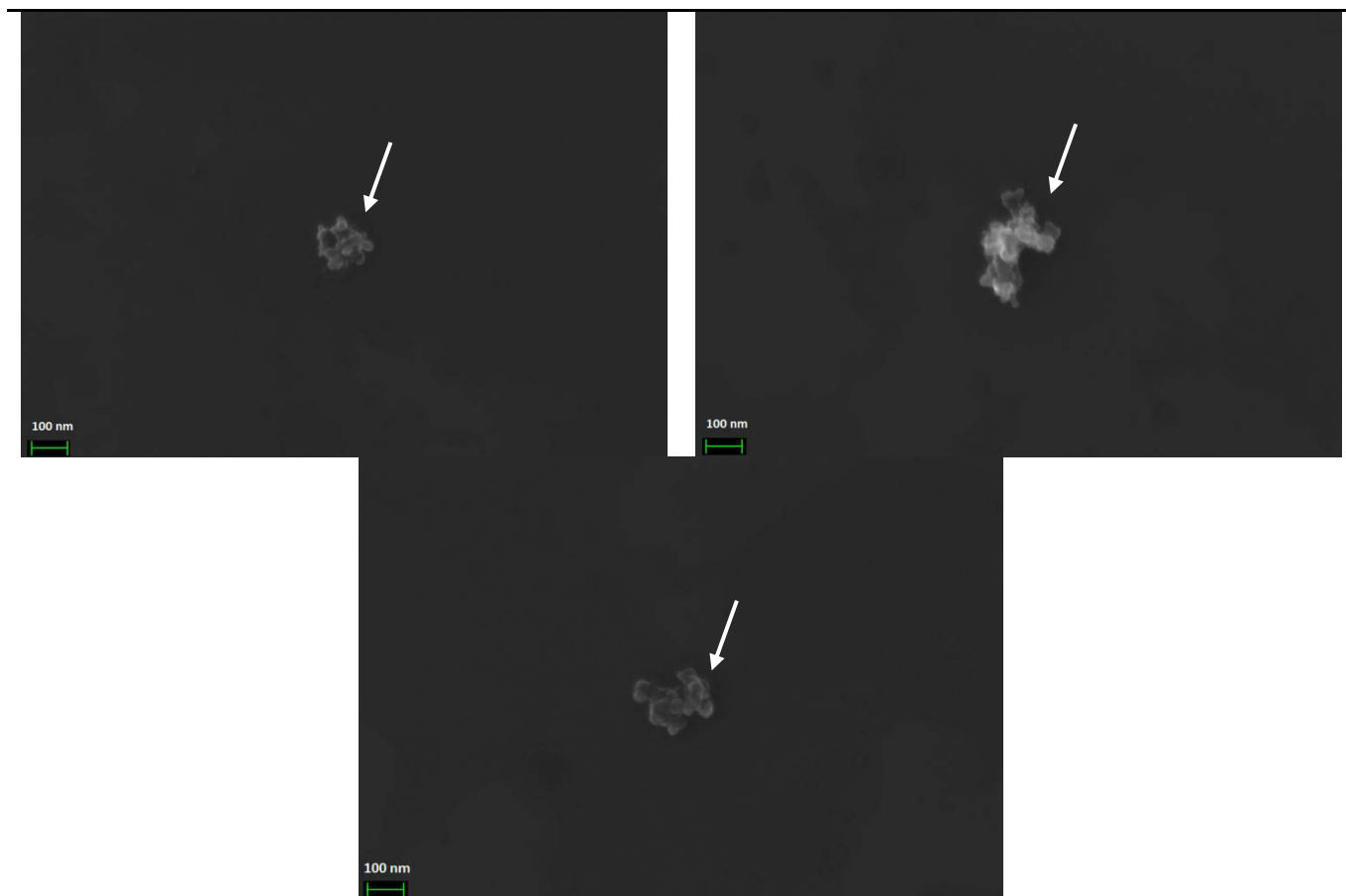
8.3.2 Characterisation of aggregate size and DOM adsorption capacity

Table 8-5 and Table 8-6 gather the results of the aggregation experiments. In all tested samples, TiO$_2$ NPs formed larger aggregates in river water than in DI water with aggregate sizes ranging from submicron (i.e. 987 nm ± 8 nm in R$_{2.8}$) to tens of micrometers in the higher IS river samples. These results are in agreement with previous studies by French et al. (2009) and Ridley et al. (2006) who measured TiO$_2$ NPs aggregate size through optical images and laser diffraction analyses respectively, and found aggregate sizes up to 30 μm in aqueous media at different IS and ionic composition.

Results from Table 8-5 also show that the aggregation of TiO$_2$ NPs and more specifically the aggregate size varied positively with the increase in IS and negatively with the amount of

DOM present in the natural waters. This is in accordance with the classical DLVO theory (Derjaguin and Landau 1941) which demonstrates that an increase in the IS will lead to a decrease in the repulsive forces between particles and thus enhance aggregation. Similarly, the amount of DOM adsorbed on the surface of TiO_2 aggregates (Table 8-5) decreased with increasing IS and increased with increasing amount of DOM present in the natural waters. Other recent studies reported the strong influence of both IS and DOM on the stability of TiO_2 NPs (French et al. 2009; Ottofuelling et al. 2011; Brunelli et al. 2013; Romanello and de Cortalezzi 2013; Erhayem and Sohn 2014).

Single and multiple linear regression analyses combined with one-way ANOVA tests were then performed to investigate the independent and combined effect of IS and initial TOC concentration on both the aggregate size and surface-adsorbed DOM in order to determine which variables influence the most on these 2 parameters. The results are gathered in Table 8-6.

These analyses show that 91% of the aggregate size variability was explained by the initial TOC concentration whereas the IS of the natural waters did not significantly affect the aggregate size (i.e. $R^2 = 0.58$, $p > .05$). This is in accordance with the results from Chapter 7 where it was found that 85% of the ENPs aggregate size variability was related to the initial TOC concentration of the natural waters. The multiple regression analysis (i.e. combining the effect of both IS and initial TOC concentration), even though not statistically significant (i.e. $p > .05$), confirmed that the aggregate size was positively related to the IS of the solution and negatively related to the initial TOC concentration (i.e. slope values on Table 8-6).

The amount of DOM adsorbed on the surface of TiO_2 NPs was also found to be strongly dependent (i.e. $R^2 > 0.99$, $p < .005$) to the initial TOC concentration of the river waters. The combined effect of IS and initial TOC concentration was also found to significantly affect

the surface-adsorbed DOM (i.e. $R^2 > 0.99$, p < .05) although the initial TOC concentration had much more influence than the IS of the solution (Table 8-6, slope values: 0.01 against 21.8 for IS and initial TOC concentration respectively).

Table 8-5*: Aggregation state (Particle size, DOM adsorption capacity, Strength and Recovery factors and Fractal dimension) of TiO2 NPs in the different river waters.

	DI	$R_{2.8}$	$R_{6.7}$	$R_{18.7}$	R_{342}
Ionic strength of the sample (mM)	-	2.8	6.7	18.7	342
Initial TOC concentration (mg/L)	-	10.01	5.33	3.98	3.21
Particle/Aggregate size (nm)	248 ± 5	987 ± 8	$10256 \pm 247^{**}$	$16532 \pm 429^{**}$	$23291 \pm 454^{**}$
Amount of DOM adsorbed on the surface (mg/g)	-	157.9 ± 7.7	51.7 ± 3.2	28.5 ± 2.8	13.1 ± 4.4
Strength Factor (%)	-	64.2 ± 1.2	45.9 ± 2.1	39.7 ± 2.3	34.0 ± 2.9
Recovery Factor (%)	-	56.7 ± 1.6	69.7 ± 1.9	73.8 ± 2.4	79.0 ± 3.2
Fractal Dimension	-	1.84 ± 0.02	1.69 ± 0.02	1.66 ± 0.01	1.59 ± 0.02

*The particle/aggregate size, amount of DOM adsorbed on the surface of TiO_2 NPs, SF, RF and FD values are average of three replicates (n = 3) and ± SD **Size measured by SLS

	Y_1 = Aggregate size (nm)	
Variables	Regression statistics (linear regression equation, R^2)	ANOVA (*F, p*)
X_1	$Y_1 = 8735 + 43.6X_1$, 0.58	2.81, n.s.
X_2	$Y_1 = 29454 - 2963X_2$, 0.91	19.17, *
X_1, X_2	$Y_1 = 24355 + 19.3X_1 - 2375X_2$, 0.98	31.6, n.s.
	Y_2 = Amount of DOM adsorbed on the surface of TiO_2 NPs (mg/g)	
Variables	Regression statistics (linear regression equation, R^2)	ANOVA (*F, p*)
X_1	$Y_2 = 82.2 - 0.2X_1$, 0.29	0.8, n.s.
X_2	$Y_2 = -57.9 + 21.4X_2$, 0.998	877.9, ***
X_1, X_2	$Y_2 = -61.3 + 0.01X_1 + 21.8X_2$, 0.998	329.7, *

[a] * : $p < .05$, ** : $p < .01$, *** : $p < .005$, ns: non-significant.

8.3.3 Characterisation of aggregate structure

8.3.3.1 Aggregate strength and recoverability

The strength and recoverability of the formed aggregates were firstly assessed by using a high mechanical shear force to induce their breakage followed by a 15-minute period of slow stirring to let the aggregates grow again. Results are presented in Figure 8-5 and Table 8-5.

Figure 8-5 shows that, when the aggregates were subjected to the high shear force, their size immediately decreased in all river waters. Following the breakage period, a slow stirring was reintroduced and aggregates started to regrow in all samples. The SF values were negatively correlated to the ionic strength of the samples whereas a positive correlation was observed between RF and IS. The recoverability of the aggregates in all river waters was only partial (i.e. RF < 100%). RF values generally provide information about the internal bonding structure. In previous studies focusing on the coagulation/flocculation process (Jarvis et al. 2005; Zhao et al. 2012), the irreversible breakage of the flocs was explained by their

formation mechanisms which were due not only to pure charge neutralisation (i.e. which would have caused complete recoverability) but also to the formation of internal chemical bonds such as hydrogen bonding. In the present study, internal chemical bonds could originate from the interaction between the negatively charged carboxylic groups of DOM (i.e. R-COO⁻) and the positively charged surface of TiO_2 NPs (i.e. + 28.5 mV at the beginning of the experiments). Table 8-5 shows the amount of DOM adsorbed during the aggregation process and it can be seen that this amount proportionally decreased with increasing IS. Simultaneously, the increase in RF correlates well with the increase in IS and thus with the decreasing amount of DOM adsorbed by the NPs during the aggregation process. These results suggest that DOM may play an important role in the aggregate recoverability.
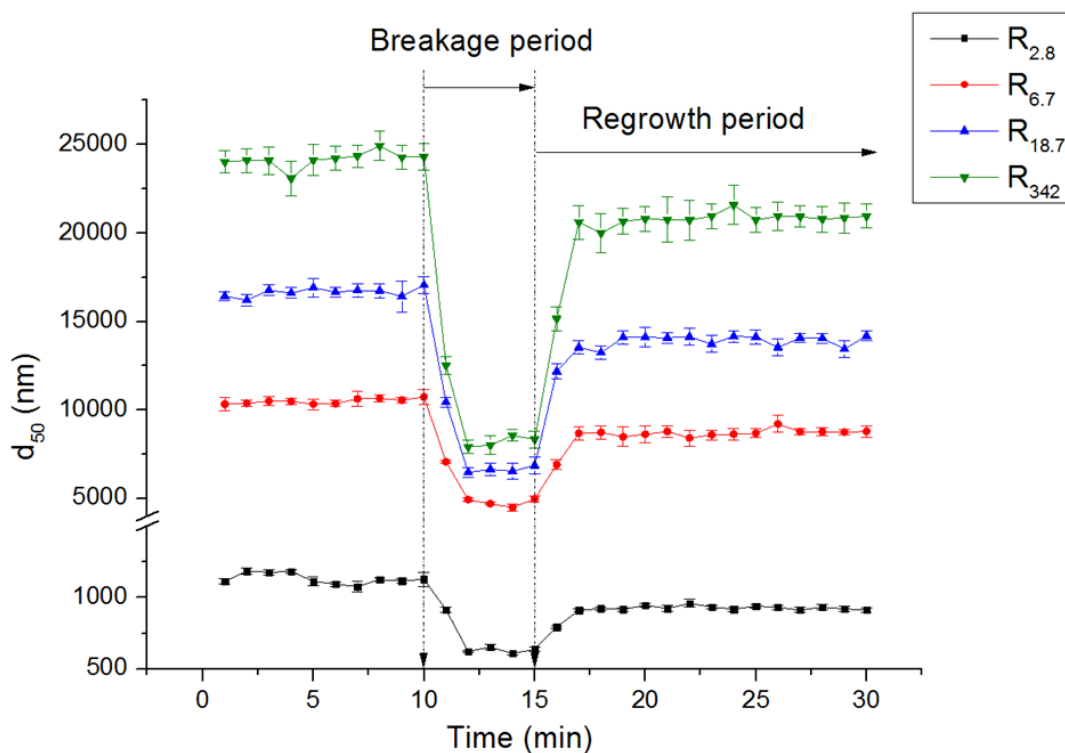
Figure 8-5: Breakage and regrowth profile of TiO_2 aggregates (12.5 mg/L) formed in the different river water samples. Shear force applied: 200 rpm for 5 minutes. Measurements were performed in triplicate and results show average size and standard deviation.

The SF values were also strongly correlated (linear relationship, $R^2 = 0.9809$) with the surface-adsorbed DOM as seen in Figure 8-6a; suggesting the formation of more compact aggregates when increasing quantities of DOM are adsorbed during the aggregation process. Similar findings were observed in a previous study (Baalousha et al. 2008) where it was found that the addition of humic acid (HA) induced a change in aggregate structure.
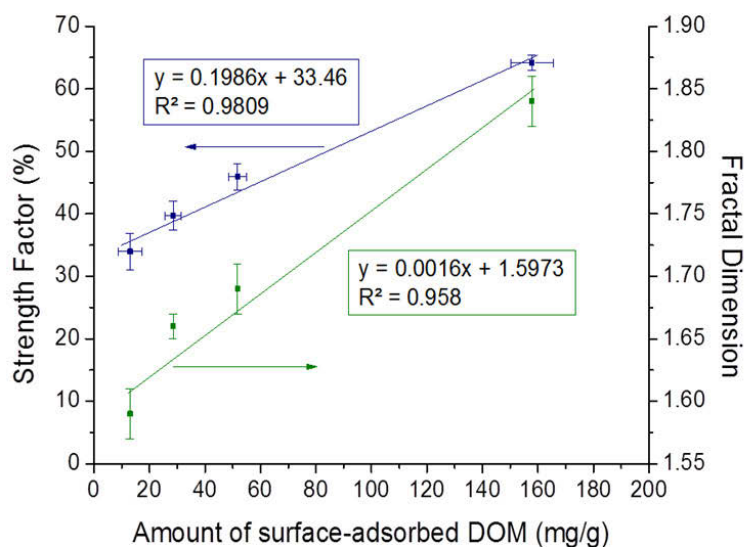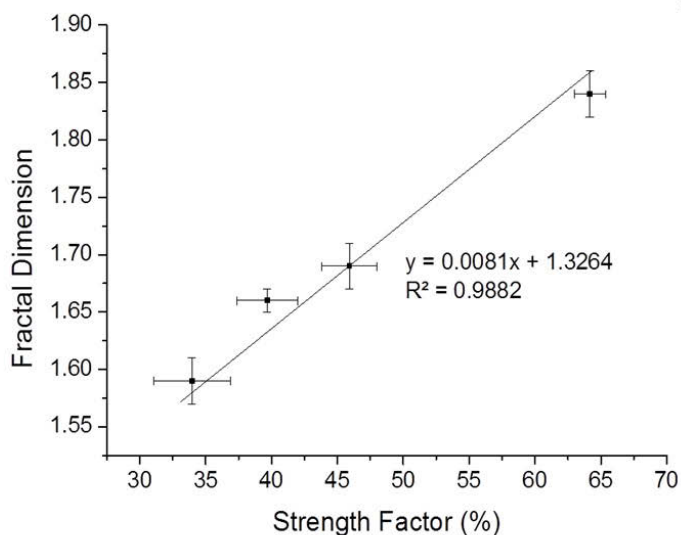
Figure 8-6: Correlations between (a) the amount of DOM adsorbed during the aggregation process and both the strength factor SF and fractal dimension FD of the formed aggregates and (b) the SF and FD. The error bars represent the standard deviation from triplicate measurements.

8.3.3.2   Aggregate structural analysis

The structure of nanoparticle aggregates can also be described by their mass FD (Weitz et al. 1985; Rice and Lin 1993) which can provide valuable information about the morphology of the aggregates (Christian et al. 2008). Table 8-5 shows the FD values obtained in the different river waters before the shear force was applied. These values decreased with increasing IS suggesting that aggregates formed under low IS conditions will have a more compact structure than the ones formed under higher IS. In fact, in R_{342}, aggregates were formed under high IS conditions, much higher than the CCC of TiO_2 for Ca^{2+} which resulted in fast aggregation or diffusion limited aggregation (DLA) under which linear and loosely bound aggregates are generally formed (Klein and Meakin 1989). However, in $R_{2.8}$, the low IS condition promoted reaction-limited aggregation (RLA) or slow aggregation giving rise to more compact aggregates.

The difference in aggregate compactness observed in the different river waters can also be explained by the amount of DOM adsorbed during the aggregation process. In fact, Baalousha et al. (2008) demonstrated that in the presence of HA, compact aggregates with high FD were formed, whereas in the absence of HA, the nanoparticles formed open porous aggregates with a lower FD. In another study, Christian et al. (2008) explained that the adsorption of HA on ENP surfaces may occur in two steps. First, HA will cover the ENPs surface in a fast adsorption step. This can be then followed by slow diffusion of HA molecules within the formed aggregates leading to a more compact structure. Results from this study confirmed the role of DOM adsorption in aggregate compactness as the highest FD values were observed in the samples where DOM adsorption was the highest.

Finally, Figure 8-6b also shows that there is a strong correlation (linear relationship, $R^2 = 0.9882$) between FD and SF values. This was already demonstrated in a previous study by Wang et al. (2009) where they observed a good relationship between floc SF and floc

structure. This is also in accordance with the results obtained in Chapter 7 where it was also found that the aggregate SF was strongly related to the aggregate FD. This correlation can be explained by the disaggregation kinetic which was found to be largely dominated by the compactness of the aggregates related to their FD (Jarvis et al. 2005; Christian et al. 2008; Chowdhury et al. 2013). Two disaggregation mechanisms were identified by Jarvis et al. (2005) and found to be dependent on the aggregates FD: low FD aggregates will breakup via fragmentation by splitting into smaller aggregates of comparable size leading to low SF value whereas high FD and thus more compact aggregates will preferentially disaggregate via surface erosion leading to higher SF values.

8.3.4 Characterisation of the stable fraction remaining after sedimentation: Particle concentration, size distribution and surface charge.

Following sedimentation of the larger aggregates, the supernatant (5 mL) in each river water sample was collected and analysed for particle concentration, size distribution and surface charge. The results are presented in Table 8-7 and Figure 8-7.

The size analysis showed significant differences among the measurement techniques, except for the lowest IS river samples (i.e. $R_{2.8}$). In fact, the PDI of this sample was quite low (Table 8-7); suggesting a relatively narrow monomodal particle size distribution (Basnet et al. 2013). The sizes reported by both DLS (Table 8-7) and FlFFF (Figure 8-7) were in close agreement to the size measured in DI water (i.e. 248 nm), indicating that most of the particles (i.e. 90.4 %) in this sample (i.e. $R_{2.8}$) did not undergo aggregation.

Table 8-7: Aggregation state of the stable fraction of TiO$_2$ NPs remaining after sedimentation of the larger aggregates (particle size and zeta potential were measured by DLS in batch mode).

	R$_{2.8}$	R$_{6.7}$	R$_{18.7}$	R$_{342}$
Colloidal stable fraction (mg/L)	11.3 (90.4%)	1.4 (11.2%)	1.2 (9.6%)	0.6 (4.8%)
Particle diameter (nm)	264 ± 14	1114 ± 23	1286 ± 36	1782 ± 62
Polydispersity Index (PDI)	0.125 ± 0.012	0.450 ± 0.018	0.624 ± 0.031	0.650 ± 0.042
Zeta potential (mV)	-23.8 ± 0.8	-10.5 ± 0.7	-7.3 ± 1.1	+ 3.7 ± 1.5

In the higher IS samples, the hydrodynamic diameters measured by DLS were larger than the particle size measured by FlFFF and varied from about 1100 nm to 1800 nm which is in accordance with previous studies reporting TiO$_2$ aggregates of similar size (measured by DLS) formed in both synthetic and natural waters (Zhang et al. 2009; Ottofuelling et al. 2011; Brunelli et al. 2013; Romanello and de Cortalezzi 2013). The high PDI of these samples may indicate some degree of polydispersity and because DLS is known to be very sensitive to larger particles, the size reported may be more representative of the large particles formed during the aggregation process (Domingos et al. 2009) whereas the size measured by FlFFF may be representative of the smaller particles/aggregates. These results clearly demonstrated the importance of using a multi-method approach when characterising ENPs in complex environmental samples.

In both samples R$_{6.7}$ and R$_{18.7}$, FlFFF results (Figure 8-7) showed that some of the particles did not aggregate as the measured size is close to the size measured in DI water (first peak in the fractogram). In sample R$_{6.7}$, the FlFFF fractogram showed that this fraction is higher than in R$_{18.7}$ while another peak (with smaller intensity) showed some particles at around 440 nm. In the fractogram of R$_{18.7}$, this trend is reversed as the second peak (i.e. representative of

particle size around 440 nm) was of higher intensity. In the highest IS samples (i.e. R_{342}), only the second peak was present in the fractogram suggesting that the physico-chemical conditions of this sample promoted the aggregation of all the particles. The zeta potential value measured in this sample (i.e. + 3.7 mV) may suggest that the high IS of this sample destabilised the nanoparticles through charge neutralisation.

The concentration of TiO_2 NPs remaining in the supernatant varied widely among the samples (i.e. from 11.3 mg/L to 0.6 mg/L) and decreased proportionally with both increasing IS and decreasing DOM concentration as previously observed in a recent study on TiO_2 stability in natural waters (Ottofuelling et al. 2011). This indicates that more aggregates were formed in the fast-aggregation regime under the highest IS conditions and their sizes were higher than the critical size d_c resulting in their sedimentation. In fact, in R_{342}, the combined effect of high IS and low DOM content promoted fast aggregation resulting in 95% aggregation and sedimentation (Table 8-7). Moreover the low FD observed in this sample (Table 8-7), resulting in the formation of more porous aggregates, will ultimately lead to faster sedimentation in comparison to higher fractal aggregates or impermeable spheres (Johnson et al. 1996; Li and Logan 2001). Finally, the presence of divalent cations and especially Ca^{2+} in this sample may further destabilise the nanoparticles via a bridging effect (Chen et al. 2006; Chowdhury et al. 2013). The high PDI observed in R_{342} (Table 8-7) can also be seen as evidence of the low stability of TiO_2 NPs in this high IS sample, even after sedimentation.
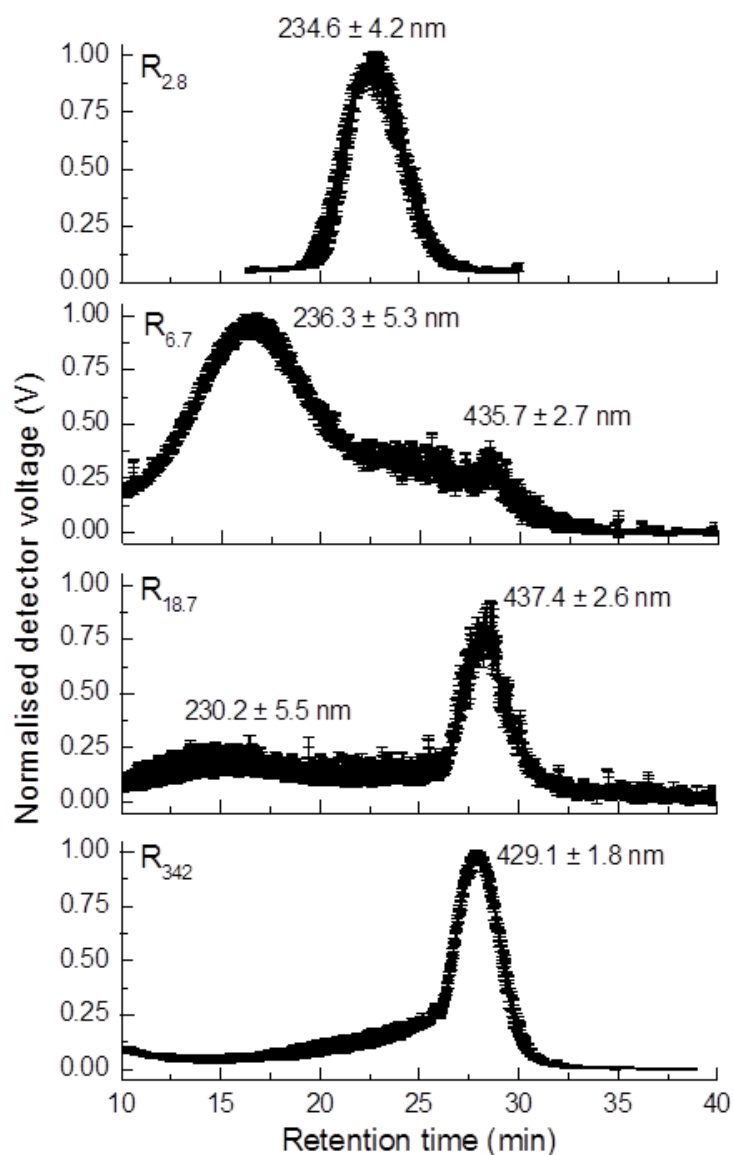
Figure 8-7: FlFFF fractograms of TiO$_2$ NPs (12.5 mg/L) stable fraction (i.e. remaining in the supernatant after sedimentation of the larger aggregates) in the different river water samples. Measurements were performed in replicate and results show average size and standard deviation. <u>Operating conditions:</u> Channel flow: 0.5 mL/min; Cross flow: 1.5 mL/min for R$_{2.8}$ and 0.3 mL/min for R$_{6.7\text{-}342}$.

8.4   Conclusions

In this chapter, we have demonstrated that the use of a multi-method approach is crucial to circumvent the limitations of each individual technique. While light scattering techniques can provide information on the larger aggregates (i.e. size and structure), FlFFF proved to be a very accurate technique for characterising the smaller particles remaining in suspension

after sedimentation. When combined, these techniques can offer complementary data on the particle size distribution of the samples.

The presented experimental method can, in principle, also be applied to other ENPs. However, the turbidity analysis would no longer be sufficiently specific and would need to be replaced, for instance, by elemental analysis (e.g. ICP-MS) or by radiolabelling as demonstrated in Chapter 6.

University of Technology Sydney
FACULTY OF ENGINEERING

CHAPTER 9   CONCLUSIONS AND

RECOMMENDATIONS

9.1 Conclusions

This research project aimed to reduce the uncertainties regarding the potential side effects of engineered nanomaterials designed for application in environmental remediation. This was achieved by developing novel methodologies to assess the behaviour (i.e. aggregation, mobility, potential to co-transport contaminants) of the nanomaterials upon their release to the environment.

9.1.1 Multi-method approach to characterise the behaviour of engineered nanoparticles in complex environmental samples

To date, one of the main challenges in the risk assessment of nanomaterials remains the difficulty of characterising the behaviour of ENPs once they are dispersed in complex environmental matrices. Besides, ENPs are also complex, and a multiple characterisation approach is therefore necessary to ensure the accuracy of the characterisation data. Although the benefit of using a multi-method approach to characterise ENPs in complex environmental samples has already been demonstrated (Domingos et al. 2009), it has not yet been systematically applied in aggregation studies.

The multi-method approach developed in this study (Chapter 4) combined several theoretical and analytical methods to investigate the stability of both bare and coated iron oxide ENPs under different environmental conditions. The need for such approach was demonstrated by highlighting the limitations of each method. For instance, one of the limitations of DLS was the polydispersity of the sample which leads to an over-estimation of the average particle size. With FlFFF, limitations arose from the interaction between the membrane and the particles; furthermore the pH dependent changes in the surface charge of the NPs, which controls the interaction with membrane, may limit the suitability of latex beads as references for particle size. Therefore, the use of FlFFF with mobile phases mimicking environmentally

relevant conditions may not provide definitive answers in terms of particle size as in this case most measurements will not be made using an optimised mode of operation. However, the versatility of FlFFF was demonstrated for the characterisation of HA-coated Fe_2O_3NPs by providing valuable information on the adsorption of HA onto Fe_2O_3NPs. Finally, the DLVO modelling approach is useful for the interpretation of the experimental results, but cannot predict the size of the aggregates. The presence of large aggregates (i.e. above 1 μm) and sedimentation of these aggregates during the analysis were also a significant limitation to the collection of accurate and reliable data. Therefore, this study shows that it is essential to deploy a number of analytical and theoretical techniques to investigate the behaviour of ENPs. Other analytical methods that can measure the size of aggregates in this size range with greater accuracy (e.g. low-angle laser light scattering (LALLS) techniques) should also be considered.

9.1.2 Application of the multi-method approach to characterise the stability of iron oxide ENPs coated with organic stabilisers

Organic coatings are now widely used as surface modifiers to reduce the aggregation of ENPs once applied to the environment and thereby increase their mobility. It is thus important to fully understand the interactions between the ENPs and the organic coating to be able to predict their fate and behaviour in the environment. To achieve that, a multi-method approach using a wide range of analytical techniques is crucial.

In this study (Chapter 5), DOM-coated iron oxide ENPs were characterised by various analytical methods including: flow field-flow fractionation, high performance size exclusion chromatography and Fourier transform infrared spectroscopy. The stability of the coated ENPs was also evaluated by assessing their aggregation and disaggregation behaviour over time. The advantage of combining several analytical methods is to understand with greater confidence the interaction between the ENPs and the organic surface modifier. For instance,

HPSEC allowed identifying which fraction(s) of the organic matter (i.e. high or low molecular weight components) is preferentially adsorbed onto the surface of the ENPs. FTIR results helped to investigate the type of chemical bonding arising from the interactions between ENPs and the organic coating. Finally, the use of FlFFF to study the long-term stability (i.e. aggregation/disaggregation) of the coated nanoparticles presented several advantages over conventional size-measurement techniques. In particular, compared to DLS which only measures an average particle size, FlFFF is a fractionation method and separation of the sample allows accurate determination of the particle size distribution which proved to be very useful for aggregation/disaggregation studies.

9.1.3 Radioisotope labelling combined with elemental analysis as a novel method to trace the mobility of iron-based ENPs in soil and their potential to co-transport contaminants

The two main obstacles limiting the widespread use of iron-based nanomaterials for environmental remediation are their limited mobility in porous systems and the uncertainties related to their potential to co-transport of contaminants. Developing novel methods to assess the behaviour of iron-based ENPs in intact soil cores would be crucial for the development of effective remediation materials. However, this task remains significantly challenging due to the high background of natural iron colloids present in soil.

In this study (Chapter 6), we developed a novel method based on radiolabelling to be able to differentiate the ENPs from the natural colloids. The radiolabelling process was performed during the nanoparticle synthesis by using a labelled precursor (i.e. $^{59}FeCl_3$). The mobility of radiolabelled nanoparticles and their potential to co-transport contaminants were successfully characterised in intact soil cores.

One of the main advantages of this method, compared to conventional ICP-MS measurements, is that the background of natural iron colloids do not interfere with the results as the gamma counter only detects the gamma radiation emitted from the radiolabelled nanoparticles. This method also permits to easily determine the spatial distribution profile of retained nanoparticles after completion of the mobility experiments. This is another benefit of this method over conventional elemental composition analysis, with which, it would not have been possible to differentiate between the injected nanomaterials and the natural iron colloids present in the soil columns. Finally, coupling this method with ICP-MS allows to successfully investigate the potential of iron-based nanomaterials to co-transport contaminants in CCA-contaminated soil columns.

9.1.4 Characterising aggregate structure using on-line laser light scattering

After entering the environment (e.g. through injection for environmental remediation), the fate of ENPs will depend on their mobility and transformation. Adsorption of NOM, aggregation/disaggregation have been identified as the main processes affecting the fate and behaviour of ENPs in aquatic environments. However, although several methods have been developed to study the aggregation behaviour of ENPs in natural waters, there are only a few studies focusing on the fate of such aggregates and their potential disaggregation behaviour. In this study (Chapter 7), we proposed and demonstrated a simple method, based on on-line light scattering analysis, for characterising the aggregation behaviour and aggregate structure of ENPs in different natural waters. The main advantages of this method over conventional light scattering measurements is the possibility to change the chemical or physical conditions of the sample or to apply external forces to induce nanoparticle disaggregation and to directly observe and measure the effects of such changes on aggregate size. In addition, the fractal dimension of the aggregates can be determined using a static light scattering instrument.

Results showed that, under high ionic strength conditions, aggregation is mainly governed by diffusion and the aggregates formed under these conditions showed the lowest stability and fractal dimension, forming linear, chain-like aggregates. In contrast, under low ionic strength conditions, the aggregate structure was more compact, most likely due to strong chemical binding with DOM and bridging mechanisms involving divalent cations formed during reaction-limited aggregation.

However, the method presented in this study only considers homo-aggregation. Hetero-aggregation process will more likely occur in real situations where the presence and concentration of natural nanoparticles and/or large agglomerates of organic molecules is much larger than the ENPs intentionally or unintentionally released into the environment. The characterisation of aggregation behaviour and aggregate structure in such complex and heterogeneous systems will then be more challenging and therefore the development of new analytical methods is still needed.

9.1.5 Multi method approach combining on-line light scattering measurement with FlFFF and DLS

On-line light scattering method developed in Chapter 7 was coupled with off-line analytical techniques (i.e. FlFFF ad DLS) to better assess the polydispersity of the sample. The larger aggregates formed under a fast-aggregation regime were characterised in terms of size and structure by use of the on-line light scattering set-up. After sedimentation, the smaller particles/aggregates were collected and characterised by both DLS and FlFFF.

In this study (Chapter 8), we have again demonstrated that the use of a multi-method approach is crucial to circumvent the limitations of each individual technique. While light scattering techniques can provide information on the larger aggregates (i.e. size and structure), FlFFF proved to be a very accurate technique for characterising the smaller

particles remaining in suspension after sedimentation. When combined, these techniques can offer complementary data on the particle size distribution of the samples.

9.2 Recommendations

Risk assessment of ENPs in the environment is urgently needed to support policy development and safe design of nanomaterials. In recent years, a large amount of information has been gathered regarding the behaviour of ENPs in the environment; which will help in the development of risk assessment for these materials. However, there are still some analytical challenges that need to be overcome in order to accurately assess the potential risks of ENPs:

- The behaviour of ENPs (e.g. transport, aggregation) is known to be concentration-dependent, and the predicted environmental concentrations for the incidental release of ENPs into the environment are currently estimated to be in the nanogram- to microgram- per litre range which is quite low compared to the current concentrations used in most studies including the present one. However, due to analytical challenges, very few instruments are capable of detecting, characterising and quantifying ENPs in complex environmental media at environmentally relevant concentrations. Therefore, there is a crucial need to develop standard analytical methods to detect, monitor, and quantify the nanomaterials in environmental media at relevant environmental concentration.

- As most of the existing analytical techniques are only adapted to the characterisation of pristine or "as-manufactured" nanoparticles, there is a need to develop standard methods for characterisation of ENPs in different environmental media with detailed procedure on sample preparation, instrumentation, key measurement parameters as well as data analysis. These methods will need to be validated through interlaboratory comparisons and then adopted by the nanoscience community. This

will be considerably helpful for data comparison between different laboratories and research centres.

REFERENCES

Abbas, K., I. Cydzik, R. Del Torchio, M. Farina, E. Forti, N. Gibson, U. Holzwarth, F. Simonelli and W. Kreyling (2010). "Radiolabelling of TiO2 nanoparticles for radiotracer studies." J. Nanopart. Res. **12**(7): 2435-2443.

Adeleye, A. S., A. A. Keller, R. J. Miller and H. S. Lenihan (2013). "Persistence of commercial nanoscaled zero-valent iron (nZVI) and by-products." J. Nanopart. Res. **15**(1).

Aiken, G. R., D. M. McKnight, R. L. Wershaw and P. MacCarthy (1985). Humic substances in soil, sediment, and water: geochemistry, isolation and characterization. New York, John Wiley & Sons.

Aitken, R., M. Chaudhry, A. Boxall and M. Hull (2006). "Manufacture and use of nanomaterials: current status in the UK and global trends." Occup. Med. **56**(5): 300-306.

Ali, M. A. and D. A. Dzombak (1996). "Competitive sorption of simple organic acids and sulfate on goethite." Environ. Sci. Technol. **30**(4): 1061-1071.

Allen, G. C., M. T. Curtis, A. J. Hooper and P. M. Tucker (1974). "X-Ray photoelectron spectroscopy of iron-oxygen systems." J. Chem. Soc., Dalton Trans. **0**(14): 1525-1530.

Alowitz, M. J. and M. M. Scherer (2002). "Kinetics of nitrate, nitrite, and Cr(vi) reduction by iron metal." Environ. Sci. Technol. **36**(3): 299-306.

Asharani, P. V., G. Low Kah Mun, M. P. Hande and S. Valiyaveettil (2008). "Cytotoxicity and genotoxicity of silver nanoparticles in human cells " ACS Nano **3**: 279-290.

Baalousha, M. (2009). "Aggregation and disaggregation of iron oxide nanoparticles: Influence of particle concentration, pH and natural organic matter." Sci. Total Environ. **407**(6): 2093-2101.

Baalousha, M., A. Manciulea, S. Cumberland, K. Kendall and J. R. Lead (2008). "Aggregation and surface properties of iron oxide nanoparticles: Influence of pH and natural organic matter." Environ. Toxicol. Chem. **27**(9): 1875-1882.

Baalousha, M., Y. Nur, I. Römer, M. Tejamaya and J. Lead (2013). "Effect of monovalent and divalent cations, anions and fulvic acid on aggregation of citrate-coated silver nanoparticles." Sci. Total Environ. **454**: 119-131.

Baalousha, M., B. Stolpe and J. R. Lead (2011). "Flow field-flow fractionation for the analysis and characterization of natural colloids and manufactured nanoparticles in environmental systems: A critical review." J. Chromatogr. A **1218**(27): 4078-4103.

Badawy, A. M. E., T. P. Luxton, R. G. Silva, K. G. Scheckel, M. T. Suidan and T. M. Tolaymat (2010). "Impact of environmental conditions (pH, ionic strength, and electrolyte type) on the surface charge and aggregation of silver nanoparticles suspensions." Environ. Sci. Technol. **44**(4): 1260-1266.

Baddeley, D., C. Batram, Y. Weiland, C. Cremer and U. J. Birk (2007). "Nanostructure analysis using spatially modulated illumination microscopy." Nat. Protocols **2**(10): 2640-2646.

Badireddy, A. R., M. R. Wiesner and J. Liu (2012). "Detection, Characterization, and Abundance of Engineered Nanoparticles in Complex Waters by Hyperspectral Imagery with Enhanced Darkfield Microscopy." Environ Sci Technol **46**(18): 10081-10088.

Baer, D. R., J. E. Amonette, M. H. Engelhard, D. J. Gaspar, A. S. Karakoti, S. Kuchibhatla, P. Nachimuthu, J. T. Nurmi, Y. Qiang, V. Sarathy, S. Seal, A. Sharma, P. G. Tratnyek and C. M. Wang (2008). "Characterization challenges for nanomaterials." Surf. Interface Anal. **40**(3-4): 529-537.

Baer, D. R. and M. H. Engelhard (2010). "XPS analysis of nanostructured materials and biological surfaces." J. Electron. Spectrosc. Relat. Phenom. **178–179**(0): 415-432.

Baer, D. R., D. J. Gaspar, P. Nachimuthu, S. D. Techane and D. G. Castner (2010). "Application of surface chemical analysis tools for characterization of nanoparticles." Anal Bioanal Chem **396**(3): 983-1002.

Baer, D. R., P. G. Tratnyek, Y. Qiang, J. E. Amonette, J. Linehan, V. Sarathy, J. T. Nurmi, C. Wang and J. Anthony (2012). Synthesis, Characterisation, and properties of zero-valent iron nanoparticles. Environmental applications of nanomaterials; synthesis, sorbents and sensors. G. E. Fryxell and G. Cao. London, Imperial College Press.

Barnes, R. J., O. Riba, M. N. Gardner, T. B. Scott, S. A. Jackman and I. P. Thompson (2010). "Optimization of nano-scale nickel/iron particles for the reduction of high concentration chlorinated aliphatic hydrocarbon solutions." Chemosphere **79**(4): 448-454.

Barnes, R. J., O. Riba, M. N. Gardner, A. C. Singer, S. A. Jackman and I. P. Thompson (2010). "Inhibition of biological TCE and sulphate reduction in the presence of iron nanoparticles." Chemosphere **80**(5): 554-562.

Barth, H. G. and B. E. Boyes (1992). "Size exclusion chromatography." Anal. Chem. **64**(12): 428R-442R.

Basnet, M., S. Ghoshal and N. Tufenkji (2013). "Rhamnolipid biosurfactant and soy protein act as effective stabilizers in the aggregation and transport of palladium-doped zerovalent iron nanoparticles in saturated porous media." Environ. Sci. Technol. **47**(23): 13355-13364.

Batley, G., M. McLaughlin and G. Batley (2008). Fate of manufactured nanomaterials in the Australian environment, CSIRO Niche Manufacturing Flagship Report.

Battin, T. J., F. v. Kammer, A. Weilhartner, S. Ottofuelling and T. Hofmann (2009). "Nanostructured TiO2: transport behavior and effects on aquatic microbial communities under environmental conditions." Environ. Sci. Technol. **43**(21): 8098-8104.

Beckett, R. and B. T. Hart (1993). Use of Field-Flow Fractionation Techniques to characterize aquatic particles, colloids and macromolecules. Environ. Part. J. Buffle and H. P. van Leeuwen. Boca Raton, Florida, Lewis Publishers. **2:** 165-205.

Bennett, P., F. He, D. Zhao, B. Aiken and L. Feldman (2010). "In situ testing of metallic iron nanoparticle mobility and reactivity in a shallow granular aquifer." J. Contam. Hydrol. **116**(1): 35-46.

Bezbaruah, A. N., S. Krajangpan, B. J. Chisholm, E. Khan and J. J. Elorza Bermudez (2009). "Entrapment of iron nanoparticles in calcium alginate beads for groundwater remediation applications." J. Hazard. Mater. **166**(2–3): 1339-1343.

Bleyl, S., F.-D. Kopinke and K. Mackenzie (2012). "Carbo-Iron®—Synthesis and stabilization of Fe(0)-doped colloidal activated carbon for in situ groundwater treatment." Chem. Eng. J. **191**(0): 588-595.

Bogner, A., G. Thollet, D. Basset, P. H. Jouneau and C. Gauthier (2005). "Wet STEM: A new development in environmental SEM for imaging nano-objects included in a liquid phase." Ultramicroscopy **104**(3–4): 290-301.

Bosi, S., T. Da Ros, G. Spalluto and M. Prato (2003). "Fullerene derivatives: an attractive tool for biological applications." European journal of medicinal chemistry **38**(11): 913-923.

Bradford, S. A., J. Simunek and S. L. Walker (2006). "Transport and straining of E. coli O157: H7 in saturated porous media." Water Resour. Res. **42**(12).

Bradford, S. A., S. Torkzaban and J. Simunek (2011). "Modeling colloid transport and retention in saturated porous media under unfavorable attachment conditions." Water Resour. Res. **47**(10).

Brunelli, A., G. Pojana, S. Callegaro and A. Marcomini (2013). "Agglomeration and sedimentation of titanium dioxide nanoparticles (n-TiO2) in synthetic and real waters." J. Nanopart. Res. **15**(6): 1-10.

Brust, M. and C. J. Kiely (2002). "Some recent advances in nanostructure preparation from gold and silver particles: a short topical review." Colloids Surf., A **202**(2): 175-186.

Buffle, J., K. J. Wilkinson, S. Stoll, M. Filella and J. Zhang (1998). "A generalized description of aquatic colloidal interactions: The three-colloidal component approach." Environ. Sci. Technol. **32**(19): 2887-2899.

Bystrzejewski, M. (2011). "Synthesis of carbon-encapsulated iron nanoparticles via solid state reduction of iron oxide nanoparticles." Journal of Solid State Chemistry **184**(6): 1492-1498.

Cain, M. and R. Morrell (2001). "Nanostructured ceramics: a review of their potential." Appl. Organomet. Chem. **15**(5): 321-330.

Cao, J., D. Elliott and W. X. Zhang (2005). "Perchlorate reduction by nanoscale iron particles." J. Nanopart. Res. **7**(4-5): 499-506.

Carpenter, E. E. (2001). "Iron nanoparticles as potential magnetic carriers." Journal of Magnetism and Magnetic Materials **225**(1-2): 17-20.

Carrillo-Carrión, C., Y. Moliner-Martínez, B. M. Simonet and M. Valcárcel (2011). "Capillary electrophoresis method for the characterization and separation of CdSe quantum dots." Anal. Chem. **83**(7): 2807-2813.

Celebi, O., C. Uzum, T. Shahwan and H. N. Erten (2007). "A radiotracer study of the adsorption behavior of aqueous Ba2+ ions on nanoparticles of zero-valent iron." J. Hazard. Mater. **148**(3): 761-767.

Cerqueira, B., F. Vega, C. Serra, L. Silva and M. Andrade (2011). "Time of flight secondary ion mass spectrometry and high-resolution transmission electron microscopy/energy dispersive spectroscopy: A preliminary study of the distribution of Cu< sup> 2+</sup> and Cu< sup> 2+</sup>/Pb< sup> 2+</sup> on a Bt horizon surfaces." J. Hazard. Mater. **195**: 422-431.

Cerqueira, B., F. A. Vega, L. F. Silva and L. Andrade (2012). "Effects of vegetation on chemical and mineralogical characteristics of soils developed on a decantation bank from a copper mine." Sci. Total Environ. **421**: 220-229.

Cha, H. G., Y. H. Kim, C. W. Kim and Y. S. Kang (2007). "Preparation of aqueous dispersion of colloidal α-Fe nanoparticle by phase transfer." Sensors Actuators B: Chem. **126**(1): 221-225.

Chae, Y. J., C. H. Pham, J. Lee, E. Bae, J. Yi and M. B. Gu (2009). "Evaluation of the toxic impact of silver nanoparticles on Japanese medaka (Oryzias latipes)." Aquat. Toxicol. **94**(4): 320-327.

Chekli, L., S. Phuntsho, M. Roy, E. Lombi, E. Donner and H. K. Shon (2013). "Assessing the aggregation behaviour of iron oxide nanoparticles under relevant environmental conditions using a multi-method approach." Water Res. **47**(13): 4585-4599.

Chekli, L., S. Phuntsho, M. Roy and H. K. Shon (2013). "Characterisation of Fe-oxide nanoparticles coated with humic acid and Suwannee River natural organic matter." Sci. Total Environ. **461–462**: 19-27.

Chekli, L., M. Roy, L. Tijing, E. Donner, E. Lombi and H. Shon (2015). "Agglomeration behaviour of titanium dioxide nanoparticles in river waters: A multi-method approach combining light scattering and field-flow fractionation techniques." Journal of Environmental Management **159**: 135-142.

Chekli, L., Y. X. Zhao, L. D. Tijing, S. Phuntsho, E. Donner, E. Lombi, B. Y. Gao and H. K. Shon (2014). "Aggregation behaviour of engineered nanoparticles in natural waters: Characterising aggregate structure using on-line laser light scattering." J. Hazard. Mater. **284**: 190-200.

Chen, J., Z. Xiu, G. V. Lowry and P. J. J. Alvarez (2011). "Effect of natural organic matter on toxicity and reactivity of nano-scale zero-valent iron." Water Res. **45**(5): 1995-2001.

Chen, K. L., S. E. Mylon and M. Elimelech (2006). "Aggregation kinetics of alginate-coated hematite nanoparticles in monovalent and divalent electrolytes." Environ. Sci. Technol. **40**(5): 1516-1523.

Chen, K. L., S. E. Mylon and M. Elimelech (2007). "Enhanced aggregation of alginate-coated iron oxide (hematite) nanoparticles in the presence of calcium, strontium, and barium cations." Langmuir **23**(11): 5920-5928.

Chen, S. S., H. D. Hsu and C. W. Li (2004). "A new method to produce nanoscale iron for nitrate removal." J. Nanopart. Res. **6**(6): 639-647.

Chi, F.-H. and G. L. Amy (2004). "Kinetic study on the sorption of dissolved natural organic matter onto different aquifer materials: the effects of hydrophobicity and functional groups." J. Colloid Interface Sci. **274**(2): 380-391.

Choa, Y. H., T. Nakayama, T. Sekino and K. Niihara (1999). "Synthesis and mechanical/magnetic properties of nano-grained iron-oxides prepared with an inert gas condensation and pulse electric current sintering process." Metals and Materials International **5**(2): 135-139.

Choe, S., Y. Y. Chang, K. Y. Hwang and J. Khim (2000). "Kinetics of reductive denitrification by nanoscale zero-valent iron." Chemosphere **41**(8): 1307-1311.

Choi, C.-J., X.-L. Dong and B.-K. Kim (2001). "Microstructure and Magnetic Properties of Fe Nanoparticles Synthesized by Chemical Vapor Condensation " Materials Transactions **42**(10): 2046-2049.

Choi, C. J., X. L. Dong and B. K. Kim (2001). "Characterization of Fe and Co nanoparticles synthesized by chemical vapor condensation." Scripta Materialia **44**(8-9): 2225-2229.

Choi, H.-C., A. B. M. Giasuddin and S. R. Kanel (2007). Method of synthesizing air-stable zero-valent iron nanoparticles at room temperature and applications, Google Patents.

Chorover, J. and M. K. Amistadi (2001). "Reaction of forest floor organic matter at goethite, birnessite and smectite surfaces." Geochimica et Cosmochimica Acta **65**(1): 95-109.

Chowdhury, I., M. C. Duch, N. D. Manuskhani, M. C. Hersam and D. Bouchard (2013). "Colloidal Properties and Stability of Graphene Oxide Nanomaterials in the Aquatic Environment." Environ. Sci. Technol. **47**(12): 6288-6296.

Chowdhury, I., S. L. Walker and S. E. Mylon (2013). "Aggregate morphology of nano-TiO2: role of primary particle size, solution chemistry, and organic matter." Environ. Sci. Process Impact **15**(1): 275-282.

Christian, P., F. Von der Kammer, M. Baalousha and T. Hofmann (2008). "Nanoparticles: structure, properties, preparation and behaviour in environmental media." Ecotoxicol. **17**(5): 326-343.

Chun, J., J. A. Fagan, E. K. Hobbie and B. J. Bauer (2008). "Size separation of single-wall carbon nanotubes by flow-field flow fractionation." Anal. Chem. **80**(7): 2514-2523.

Cirtiu, C. M., T. Raychoudhury, S. Ghoshal and A. Moores (2011). "Systematic comparison of the size, surface characteristics and colloidal stability of zero valent iron nanoparticles pre- and post-grafted with common polymers." Colloids Surf., A **390**(1-3): 95-104.

Contado, C. and A. Pagnoni (2008). "TiO2 in commercial sunscreen lotion: Flow field-flow fractionation and ICP-AES together for size analysis." Anal. Chem. **80**(19): 7594-7608.

Crane, R. A. and T. B. Scott (2012). "Nanoscale zero-valent iron: Future prospects for an emerging water treatment technology." J. Hazard. Mater. **211-212**: 112-125.

Croteau, M.-N., A. D. Dybowska, S. N. Luoma and E. Valsami-Jones (2011). "A novel approach reveals that zinc oxide nanoparticles are bioavailable and toxic after dietary exposures." Nanotoxicology **5**(1): 79-90.

Cundy, A. B., L. Hopkinson and R. L. D. Whitby (2008). "Use of iron-based technologies in contaminated land and groundwater remediation: A review." Sci. Total Environ. **400**(1-3): 42-51.

Dai, H. (2002). "Carbon nanotubes: synthesis, integration, and properties." Acc. Chem. Res. **35**(12): 1035-1044.

Dallimore, M. (1999). "Mechanochemical processing—A versatile, low cost technology for the manufacture of nano-powders." Mater. Technol **14**(1): 4-7.

De Gennes, P. (1987). "Polymers at an interface; a simplified view." Adv. Colloid Interface Sci. **27**(3): 189-209.

de Jonge, L. W., C. Kjærgaard and P. Moldrup (2004). "Colloids and Colloid-Facilitated Transport of Contaminants in Soils An Introduction." Vadose Zone Journal **3**(2): 321-325.

Del Bianco, L., A. Hernando, E. Navarro, E. Bonetti and L. Pasquini (1998). "Structural configuration and magnetic effects in as-milled and annealed nanocrystalline iron." Journal De Physique **8**(2): 107-110.

Deng, B. and S. Hu (2001). Reductive dechlorination of chlorinated solvents on zerovalent iron surfaces. Physicochemical groundwater remediation. B. S. Smith JA. New York, Kluwer Academic**:** 139–159.

Derjaguin, B. and L. Landau (1941). "Theory of the stability of strongly charged lyophobic sols and of the adhesion of strongly charged particles in solutions of electrolytes." Acta Physicochim URSS **14**(6): 633-662.

Dickinson, M. and T. B. Scott (2010). "The application of zero-valent iron nanoparticles for the remediation of a uranium-contaminated waste effluent." J. Hazard. Mater. **178**(1–3): 171-179.

Dickson, D., G. Liu, C. Li, G. Tachiev and Y. Cai (2012). "Dispersion and stability of bare hematite nanoparticles: Effect of dispersion tools, nanoparticle concentration, humic acid and ionic strength." Sci. Total Environ. **419**(0): 170-177.

Dobias, J. and R. Bernier-Latmani (2013). "Silver release from silver nanoparticles in natural waters." Environ. Sci. Technol. **47**(9): 4140-4146.

Domingos, R. F., M. A. Baalousha, Y. Ju-Nam, M. M. Reid, N. Tufenkji, J. R. Lead, G. G. Leppard and K. J. Wilkinson (2009). "Characterizing manufactured nanoparticles in the environment: multimethod determination of particle sizes." Environ Sci Technol **43**(19): 7277-7284.

Dong, H., X. Guan and I. M. C. Lo (2012). "Fate of As(V)-treated nano zero-valent iron: Determination of arsenic desorption potential under varying environmental conditions by phosphate extraction." Water Res. **46**(13): 4071-4080.

Dong, H. and I. Lo (2013). "Influence of humic acid on the colloidal stability of surface-modified nano zero-valent iron." Water Res. **47**(1): 419-427.

Dowling, A., R. Clift, N. Grobert, D. Hutton, R. Oliver, O. O'neill, J. Pethica, N. Pidgeon, J. Porritt and J. Ryan (2004). "Nanoscience and nanotechnologies: opportunities and uncertainties." London: The Royal Society & The Royal Academy of Engineering Report: 61-64.

Dries, J., L. Bastiaens, D. Springael, S. Kuypers, S. N. Agathos and L. Diels (2005). "Effect of humic acids on heavy metal removal by zero-valent iron in batch and continuous flow column systems." Water Res. **39**(15): 3531-3540.

Drouin, D., A. R. Couture, D. Joly, N. Poirier-Demers and H. Demers (2011). monte CArlo SImulations of electroN trajectory in sOlids, CASINO. Quebec, Canada, University de Sherbrooke.

Dubascoux, S., I. Le Hecho, M. Hassellov, F. Von Der Kammer, M. Potin Gautier and G. Lespes (2010). "Field-flow fractionation and inductively coupled plasma mass spectrometer coupling: History, development and applications." J. Anal. At. Spectrom. **25**(5): 613-623.

Dubascoux, S., F. Von Der Kammer, I. Le Hecho, M. P. Gautier and G. Lespes (2008). "Optimisation of asymmetrical flow field flow fractionation for environmental nanoparticles separation." J. Chromatogr. A **1206**(2): 160-165.

Duesberg, G., M. Burghard, J. Muster and G. Philipp (1998). "Separation of carbon nanotubes by size exclusion chromatography." Chemical Commununication(3): 435-436.

Dybowska, A. D., M.-N. Croteau, S. K. Misra, D. Berhanu, S. N. Luoma, P. Christian, P. O'Brien and E. Valsami-Jones (2011). "Synthesis of isotopically modified ZnO nanoparticles and their potential as nanotoxicity tracers." Environ. Pollut. **159**(1): 266-273.

Elimelech, M., J. Gregory, X. Jia and R. Williams (1995). Particle Deposition and Aggregation: Measurement, Modelling and Simulation. Boston, MA.

Elimelech, M., X. Jia, J. Gregory and R. A. Williams (1998). Particle deposition and aggregation: measurement, modelling and simulation Woburn, Massachusetts Butterworth-Heinemann 440.

Elimelech, M. and C. R. O'Melia (1990). "Kinetics of deposition of colloidal particles in porous media." Environ. Sci. Technol. **24**(10): 1528-1536.

Elliott, D. W. and W. X. Zhang (2001). "Field assessment of nanoscale bimetallic particles for groundwater treatment." Environ. Sci. Technol. **35**(24): 4922-4926.

EPA, U. (2005). "U.S. EPA Workshop on Nanotechnology for Site Remediation " Retrieved 26/02/2012, from http://epa.gov/ncer/publications/workshop/pdf/10 20 05 nanosummary.pdf

Erhayem, M. and M. Sohn (2014). "Stability studies for titanium dioxide nanoparticles upon adsorption of Suwannee River humic and fulvic acids and natural organic matter." Sci. Total Environ. **468**: 249-257.

Esfahani, A. R., A. F. Firouzi, G. Sayyad and A. Kiasat (2013). "Transport and retention of polymer-stabilized zero-valent iron nanoparticles in saturated porous media: Effects of initial particle concentration and ionic strength." J. Ind. Eng. Chem. **20**(5): 2671-2679.

Fang, Z., J. Chen, X. Qiu, X. Qiu, W. Cheng and L. Zhu (2011). "Effective removal of antibiotic metronidazole from water by nanoscale zero-valent iron particles." Desalination **268**(1–3): 60-67.

Farré, M., J. Sanchís and D. Barceló (2011). "Analysis and assessment of the occurrence, the fate and the behavior of nanomaterials in the environment." TrAC, Trends Anal. Chem. **30**(3): 517-527.

Fatisson, J., S. Ghoshal and N. Tufenkji (2010). "Deposition of carboxymethylcellulose-coated zero-valent iron nanoparticles onto silica: Roles of solution chemistry and organic molecules." Langmuir **26**(15): 12832-12840.

Febrianto, J., A. N. Kosasih, J. Sunarso, Y.-H. Ju, N. Indraswati and S. Ismadji (2009). "Equilibrium and kinetic studies in adsorption of heavy metals using biosorbent: A summary of recent studies." J. Hazard. Mater. **162**(2): 616-645.

Feldmann, J., P. Salaün and E. Lombi (2009). "Critical review perspective: elemental speciation analysis methods in environmental chemistry – moving towards methodological integration." Environmental Chemistry **6**(4): 275-289.

Ferguson, P. L., G. T. Chandler, R. C. Templeton, A. DeMarco, W. A. Scrivens and B. A. Englehart (2008). "Influence of sediment− amendment with single-walled carbon nanotubes and diesel soot on bioaccumulation of hydrophobic organic contaminants by benthic invertebrates." Environ. Sci. Technol. **42**(10): 3879-3885.

Fiedor, J. N., W. D. Bostick, R. J. Jarabek and J. Farrell (1998). "Understanding the Mechanism of Uranium Removal from Groundwater by Zero-Valent Iron Using X-ray Photoelectron Spectroscopy." Environ Sci Technol **32**(10): 1466-1473.

Filella, M., J. Zhang, M. E. Newman and J. Buffle (1997). "Analytical applications of photon correlation spectroscopy for size distribution measurements of natural colloidal suspensions: capabilities and limitations." Colloids Surf., A **120**(1): 27-46.

Filius, J. D., D. G. Lumsdon, J. C. L. Meeussen, T. Hiemstra and W. H. Van Riemsdijk (2000). "Adsorption of fulvic acid on goethite." Geochimica et Cosmochimica Acta **64**(1): 51-60.

Finsy, R. (1994). "Particle sizing by quasi-elastic light scattering." Adv. Colloid Interface Sci. **52**: 79-143.

French, R. A., A. R. Jacobson, B. Kim, S. L. Isley, R. L. Penn and P. C. Baveye (2009). "Influence of ionic strength, pH, and cation valence on aggregation kinetics of titanium dioxide nanoparticles." Environ. Sci. Technol. **43**(5): 1354-1359.

Gao, J., S. Youn, A. Hovsepyan, V. n. L. Llaneza, Y. Wang, G. Bitton and J.-C. J. Bonzongo (2009). "Dispersion and toxicity of selected manufactured nanomaterials in natural river water samples: effects of water chemical composition." Environ. Sci. Technol. **43**(9): 3322-3328.

Gao, X., Y. Cui, R. M. Levenson, L. W. Chung and S. Nie (2004). "In vivo cancer targeting and imaging with semiconductor quantum dots." Nat. Biotechnol. **22**(8): 969-976.

Geelhoed, J. S., T. Hiemstra and W. H. Van Riemsdijk (1998). "Competitive interaction between phosphate and citrate on goethite." Environ. Sci. Technol. **32**(14): 2119-2123.

Geng, B., Z. Jin, T. Li and X. Qi (2009). "Preparation of chitosan-stabilized Fe0 nanoparticles for removal of hexavalent chromium in water." Sci. Total Environ. **407**(18): 4994-5000.

Giasuddin, A. B. M., S. R. Kanel and H. Choi (2007). "Adsorption of humic acid onto nanoscale zerovalent iron and its effect on arsenic removal." Environ. Sci. Technol. **41**(6): 2022-2027.

Gibson, N., U. Holzwarth, K. Abbas, F. Simonelli, J. Kozempel, I. Cydzik, G. Cotogno, A. Bulgheroni, D. Gilliland and J. Ponti (2011). "Radiolabelling of engineered nanoparticles for in vitro and in vivo tracing applications using cyclotron accelerators." Arch. Toxicol. **85**(7): 751-773.

Giddings, J. C. (1993). "Field-flow fractionation: analysis of macromolecular, colloidal, and particulate materials." Science **260**(5113): 1456.

Giddings, J. C. (2000). Field flow fractionation handbook Chapter 1: The field-flow fractionation family: Underlying principles, Wiley-interscience.

Gillham, R. W. and S. F. Ohannesin (1994). "Enhanced degradation of halogenated aliphatics by zero valent iron." Ground Water **32**(6): 958-967.

Gimbert, L. J., R. E. Hamon, P. S. Casey and P. J. Worsfold (2007). "Partitioning and stability of engineered ZnO nanoparticles in soil suspensions using flow field-flow fractionation." Environ. Chem. **4**(1): 8-10.

Glæsner, N., E. Donner, J. Magid, G. H. Rubæk, H. Zhang and E. Lombi (2012). "Characterization of leached phosphorus from soil, manure, and manure-amended soil by physical and chemical fractionation and diffusive gradients in thin films (DGT)." Environ. Sci. Technol. **46**(19): 10564-10571.

Glavee, G. N., K. J. Klabunde, C. M. Sorensen and G. C. Hadjipanayis (1995). "Chemistry of borohydride reduction of iron(II) and iron(III) ions in aqueous and nonaqueous media. Formation of nanoscale Fe, FeB, and Fe2B powders." Inorganic Chemistry **34**(1): 28-35.

Glover, R. D., J. M. Miller and J. E. Hutchison (2011). "Generation of Metal Nanoparticles from Silver and Copper Objects: Nanoparticle Dynamics on Surfaces and Potential Sources of Nanoparticles in the Environment." ACS Nano **5**(11): 8950-8957.

Gondikas, A. P., A. Morris, B. C. Reinsch, S. M. Marinakos, G. V. Lowry and H. Hsu-Kim (2012). "Cysteine-induced modifications of zero-valent silver nanomaterials:

implications for particle surface chemistry, aggregation, dissolution, and silver speciation." Environ. Sci. Technol. **46**(13): 7037-7045.

Gottschalk, F., R. W. Scholz and B. Nowack (2010). "Probabilistic material flow modeling for assessing the environmental exposure to compounds: Methodology and an application to engineered nano-TiO2 particles." Environ. Modell. Softw. **25**(3): 320-332.

Gottschalk, F., T. Sonderer, R. W. Scholz and B. Nowack (2009). "Modeled environmental concentrations of engineered nanomaterials (TiO2, ZnO, Ag, CNT, fullerenes) for different regions." Environ. Sci. Technol. **43**(24): 9216-9222.

Gottschalk, F., T. Sonderer, R. W. Scholz and B. Nowack (2010). "Possibilities and limitations of modeling environmental exposure to engineered nanomaterials by probabilistic material flow analysis." Environ. Toxicol. Chem. **29**(5): 1036-1048.

Grafe, M., E. Donner, R. N. Collins and E. Lombi (2014). "Speciation of metal(loid)s in environmental samples by X-ray absorption spectroscopy: A critical review." Anal. Chim. Acta **822**: 22.

Grano, S. R., H. Cnossen, W. Skinner, C. A. Prestidge and J. Ralston (1997). "Surface modifications in the chalcopyrite-sulphite ion system, II. Dithiophosphate collector adsorption study." Int. J. Miner. Process. **50**(1): 27-45.

Grano, S. R., M. Sollaart, W. Skinner, C. A. Prestidge and J. Ralston (1997). "Surface modifications in the chalcopyrite-sulphite ion system. I. collectorless flotation, XPS and dissolution study." Int. J. Miner. Process. **50**(1): 1-26.

Greenlee, L. F., J. D. Torrey, R. L. Amaro and J. M. Shaw (2012). "Kinetics of Zero Valent Iron Nanoparticle Oxidation in Oxygenated Water." Environ Sci Technol **46**(23): 12913-12920.

Gregory, J. and J. Duan (2001). "Hydrolyzing metal salts as coagulants." Pure Appl. Chem. **73**(12): 2017-2026.

Grieger, K. D., A. Fjordboge, N. B. Hartmann, E. Eriksson, P. L. Bjerg and A. Baun (2010). "Environmental benefits and risks of zero-valent iron nanoparticles (nZVI) for in situ remediation: Risk mitigation or trade-off?" J. Contam. Hydrol. **118**(3-4): 165-183.

Grittini, C., M. Malcomson, Q. Fernando and N. Korte (1995). "Rapid dechlorination of polychlorinated biphenyls on the surface of a Pd/Fe bimetallic system." Environ. Sci. Technol. **29**(11): 2898-2900.

Gu, B., J. Schmitt, Z. Chen, L. Liang and J. F. McCarthy (1995). "Adsorption and desorption of different organic matter fractions on iron oxide." Geochimica et Cosmochimica Acta **59**(2): 219-229.

Guan, X. H., C. Shang and G. H. Chen (2006). "Competitive adsorption of organic matter with phosphate on aluminum hydroxide." J. Colloid Interface Sci. **296**(1): 51-58.

Gulson, B. and H. Wong (2006). "Stable isotopic tracing: A way forward for nanotechnology." Environmental health perspectives: 1486-1488.

Gustafsson, M. G. L. (2000). "Surpassing the lateral resolution limit by a factor of two using structured illumination microscopy." Journal of Microscopy **198**(2): 82-87.

Hajdú, A., E. Illés, E. Tombácz and I. Borbáth (2009). "Surface charging, polyanionic coating and colloid stability of magnetite nanoparticles." Colloids Surf., A **347**(1–3): 104-108.

Handy, R. D., R. Owen and E. Valsami-Jones (2008). "The ecotoxicology of nanoparticles and nanomaterials: current status, knowledge gaps, challenges, and future needs." Ecotoxicol. **17**(5): 315-325.

Handy, R. D., F. von der Kammer, J. R. Lead, M. Hassellöv, R. Owen and M. Crane (2008). "The ecotoxicology and chemistry of manufactured nanoparticles." Ecotoxicol. **17**(4): 287-314.

Hanus, L. H. and H. J. Ploehn (1999). "Conversion of intensity-averaged photon correlation spectroscopy measurements to number-averaged particle size distributions. 1. Theoretical development." Langmuir **15**(9): 3091-3100.

Hassellöv, M. and R. Kaegi (2009). Environmental and Human Health Effects of Nanoparticles. Chichester, Wiley.

Hassellöv, M., J. W. Readman, J. F. Ranville and K. Tiede (2008). "Nanoparticle analysis and characterization methodologies in environmental risk assessment of engineered nanoparticles." Ecotoxicol. **17**(5): 344-361.

Hassellöv, M. and F. von der Kammer (2008). "Iron oxides as geochemical nanovectors for metal transport in soil-river systems." Elements **4**(6): 401-406.

He, C., J. Yang, L. Zhu, Q. Zhang, W. Liao, S. Liu, Y. Liao, M. Abou Asi and D. Shu (2013). "pH-dependent degradation of acid orange II by zero-valent iron in presence of oxygen." Separation and Purification Technology **117**(0): 59-68.

He, F. and D. Zhao (2005). "Preparation and characterization of a new class of starch-stabilized bimetallic nanoparticles for degradation of chlorinated hydrocarbons in water." Environ. Sci. Technol. **39**(9): 3314-3320.

He, F. and D. Zhao (2007). "Manipulating the size and dispersibility of zerovalent iron nanoparticles by use of carboxymethyl cellulose stabilizers." Environ. Sci. Technol. **41**(17): 6216-6221.

He, F., D. Zhao, J. Liu and C. B. Roberts (2007). "Stabilization of Fe - Pd nanoparticles with sodium carboxymethyl cellulose for enhanced transport and dechlorination of trichloroethylene in soil and groundwater." Ind. Eng. Chem. Res. **46**(1): 29-34.

He, F., D. Zhao and C. Paul (2010). "Field assessment of carboxymethyl cellulose stabilized iron nanoparticles for in situ destruction of chlorinated solvents in source zones." Water Res. **44**(7): 2360-2370.

He, Y. T., J. Wan and T. Tokunaga (2008). "Kinetic stability of hematite nanoparticles: the effect of particle sizes." J. Nanopart. Res. **10**(2): 321-332.

Helfrich, A., W. Brüchert and J. Bettmer (2006). "Size characterisation of Au nanoparticles by ICP-MS coupling techniques." J. Anal. At. Spectrom. **21**(4): 431-434.

Henderson, A. D. and A. H. Demond (2007). "Long-term performance of zero-valent iron permeable reactive barriers: a critical review." Environ. Eng. Sci. **24**: 401-423.

Henglein, A. and M. Giersig (1999). "Formation of colloidal silver nanoparticles: capping action of citrate." The Journal of Physical Chemistry B **103**(44): 9533-9539.

Henn, K. W. and D. W. Waddill (2006). "Utilization of nanoscale zero-valent iron for source remediation: A case study." Remediation Journal **16**(2): 57-77.

Hiemenz, P. C. and R. Rajagopalan (1997). Principles of Colloid and Surface Chemistry, revised and expanded, CRC Press.

Hildebrand, H. and K. Franke (2012). "A new radiolabeling method for commercial Ag0 nanopowder with 110mAg for sensitive nanoparticle detection in complex media." J. Nanopart. Res. **14**(10): 1-7.

Hingston, J., C. Collins, R. Murphy and J. Lester (2001). "Leaching of chromated copper arsenate wood preservatives: a review." Environ. Pollut. **111**(1): 53-66.

Hoag, G. E., J. B. Collins, J. L. Holcomb, J. R. Hoag, M. N. Nadagouda and R. S. Varma (2009). "Degradation of bromothymol blue by 'greener' nano-scale zero-valent iron synthesized using tea polyphenols." Journal of Materials Chemistry **19**(45): 8671-8677.

Hoch, L. B., E. J. Mack, B. W. Hydutsky, J. M. Hershman, J. M. Skluzacek and T. E. Mallouk (2008). "Carbothermal synthesis of carbon-supported nanoscale zero-valent iron particles for the remediation of hexavalent chromium." Environ. Sci. Technol. **42**(7): 2600-2605.

Honetschlagerova, L., P. Janouskovcova and Z. Soffer (2012). NANOSCALE ZERO VALENT IRON COATING FOR SUBSURFACE APPLICATION. Nanocon 2012. Brno, Czech Republic.

Hong, S. and M. Elimelech (1997). "Chemical and physical aspects of natural organic matter (NOM) fouling of nanofiltration membranes." Journal of Membrane Science **132**(2): 159-181.

Hopp, L., P. S. Nico, M. A. Marcus and S. Peiffer (2008). "Arsenic and chromium partitioning in a podzolic soil contaminated by chromated copper arsenate." Environ. Sci. Technol. **42**(17): 6481-6486.

Hu, J.-D., Y. Zevi, X.-M. Kou, J. Xiao, X.-J. Wang and Y. Jin (2010). "Effect of dissolved organic matter on the stability of magnetite nanoparticles under different pH and ionic strength conditions." Sci. Total Environ. **408**(16): 3477-3489.

Huynh, K. A. and K. L. Chen (2011). "Aggregation kinetics of citrate and polyvinylpyrrolidone coated silver nanoparticles in monovalent and divalent electrolyte solutions." Environ. Sci. Technol. **45**(13): 5564-5571.

Hwang, W.-M., C.-Y. Lee, D. W. Boo and J.-G. Choi (2003). "Separation of nanoparticles in different sizes and compositions by capillary electrophoresis." Bull. Korean Chem. Soc. **24**(5): 684-686.

Hwang, Y. H., D. G. Kim and H. S. Shin (2011). "Effects of synthesis conditions on the characteristics and reactivity of nano scale zero valent iron." Appl. Catal., B **105**(1-2): 144-150.

Hyung, H., J. D. Fortner, J. B. Hughes and J.-H. Kim (2007). "Natural organic matter stabilizes carbon nanotubes in the aqueous phase." Environ. Sci. Technol. **41**(1): 179-184.

Iijima, S. (1991). "Helical microtubules of graphitic carbon." Nature **354**: 56-58.

Illes, E. and E. Tombácz (2006). "The effect of humic acid adsorption on pH-dependent surface charging and aggregation of magnetite nanoparticles." J. Colloid Interface Sci. **295**(1): 115-123.

Illés, E. and E. Tombácz (2004). "The role of variable surface charge and surface complexation in the adsorption of humic acid on magnetite." Colloids Surf., A **230**(1–3): 99-109.

Imae, T., K. Muto and S. Ikeda (1991). "The pH dependence of dispersion of TiO2 particles in aqueous surfactant solutions." Colloid and Polymer Science **269**(1): 43-48.

Isaacson, C. W. and D. Bouchard (2010). "Asymmetric flow field flow fractionation of aqueous C< sub> 60</sub> nanoparticles with size determination by dynamic light scattering and quantification by liquid chromatography atmospheric pressure photo-ionization mass spectrometry." J. Chromatogr. A **1217**(9): 1506-1512.

Jamei, M. R., M. R. Khosravi and B. Anvaripour (2014). "A novel ultrasound assisted method in synthesis of NZVI particles." Ultrasonics Sonochemistry **21**(1): 226-233.

Jarvis, P., B. Jefferson, J. Gregory and S. A. Parsons (2005). "A review of floc strength and breakage." Water Res. **39**(14): 3121-3137.

Jarvis, P., B. Jefferson and S. A. Parsons (2005). "Breakage, regrowth, and fractal nature of natural organic matter flocs." Environ. Sci. Technol. **39**(7): 2307-2314.

Jekel, M. R. (1986). "The stabilization of dispersed mineral particles by adsorption of humic substances." Water Res. **20**(12): 1543-1554.

Jiang, J., G. Oberdörster and P. Biswas (2009). "Characterization of size, surface charge, and agglomeration state of nanoparticle dispersions for toxicological studies." J. Nanopart. Res. **11**(1): 77-89.

Jiemvarangkul, P., W. X. Zhang and H. L. Lien (2011). "Enhanced transport of polyelectrolyte stabilized nanoscale zero-valent iron (nZVI) in porous media." Chem. Eng. J. **170**(2-3): 482-491.

Jillavenkatesa, A., S. J. Dapkunas and L.-S. H. Lum (2001). Special Publication 960-1: Partice Size Characterisation. NIST Recommended Practice Guide, National Institute of Standards and Technology.

Johnson, C. P., X. Li and B. E. Logan (1996). "Settling velocities of fractal aggregates." Environ. Sci. Technol. **30**(6): 1911-1918.

Johnson, R. L., G. O. B. Johnson, J. T. Nurmi and P. G. Tratnyek (2009). "Natural organic matter enhanced mobility of nano zerovalent iron." Environ Sci Technol **43**(14): 5455-5460.

Johnson, R. L., G. O. B. Johnson, J. T. Nurmi and P. G. Tratnyek (2009). "Natural organic matter enhanced mobility of nano zerovalent iron." Environ. Sci. Technol. **43**(14): 5455-5460.

Johnson, R. L., J. T. Nurmi, G. S. O'Brien Johnson, D. Fan, R. L. O'Brien Johnson, Z. Shi, A. J. Salter-Blanc, P. G. Tratnyek and G. V. Lowry (2013). "Field-scale transport and transformation of carboxymethylcellulose-stabilized nano zero-valent iron." Environ. Sci. Technol. **47**(3): 1573-1580.

Joo, S. H., S. R. Al-Abed and T. Luxton (2009). "Influence of carboxymethyl cellulose for the transport of titanium dioxide nanoparticles in clean silica and mineral-coated sands." Environ. Sci. Technol. **43**(13): 4954-4959.

Jortner, J. and C. N. R. Rao (2002). "Nanostructured advanced materials. Perspectives and directions." Pure Appl. Chem. **74**(9): 1491-1506.

Ju-Nam, Y. and J. R. Lead (2008). "Manufactured nanoparticles: An overview of their chemistry, interactions and potential environmental implications." Sci. Total Environ. **400**(1–3): 396-414.

Ju-Nam, Y. and J. R. Lead (2008). "Manufactured nanoparticles: An overview of their chemistry, interactions and potential environmental implications." Sci. Total Environ. **400**(1): 396-414.

Jung, B., D. O'Carroll and B. Sleep (2014). "The influence of humic acid and clay content on the transport of polymer-coated iron nanoparticles through sand." Sci. Total Environ. **496**(0): 155-164.

Kadar, E., G. A. Tarran, A. N. Jha and S. N. Al-Subiai (2011). "Stabilization of engineered zero-valent nanoiron with Na-acrylic copolymer enhances spermiotoxicity." Environ. Sci. Technol. **45**(8): 3245-3251.

Kaegi, R., A. Ulrich, B. Sinnet, R. Vonbank, A. Wichser, S. Zuleeg, H. Simmler, S. Brunner, H. Vonmont, M. Burkhardt and M. Boller (2008). "Synthetic TiO2 nanoparticle emission from exterior facades into the aquatic environment." Environ. Pollut. **156**(2): 233-239.

Kammer, F. V. D., S. Legros, T. Hofmann, E. H. Larsen and K. Loeschner (2011). "Separation and characterization of nanoparticles in complex food and environmental samples by field-flow fractionation." TrAC - Trends in Analytical Chemistry **30**(3): 425-436.

Kanel, S. R., R. R. Goswami, T. P. Clement, M. O. Barnett and D. Zhao (2008). "Two dimensional transport characteristics of surface stabilized zero-valent iron nanoparticles in porous media." Environ. Sci. Technol. **42**(3): 896-900.

Kanel, S. R., J.-M. Grenèche and H. Choi (2006). "Arsenic(V) Removal from Groundwater Using Nano Scale Zero-Valent Iron as a Colloidal Reactive Barrier Material." Environmental Science & Technology **40**(6): 2045-2050.

Kanel, S. R., B. Manning, L. Charlet and H. Choi (2005). "Removal of arsenic (III) from groundwater by nanoscale zero-valent iron." Environ. Sci. Technol. **39**(5): 1291-1298.

Kanel, S. R., B. Manning, L. Charlet and H. Choi (2005). "Removal of arsenic(III) from groundwater by nanoscale zero-valent iron." Environ. Sci. Technol. **39**(5): 1291-1298.

Kanel, S. R., D. Nepal, B. Manning and H. Choi (2007). "Transport of surface-modified iron nanoparticle in porous media and application to arsenic (III) remediation." J. Nanopart. Res. **9**(5): 725-735.

Kang, S. and B. Xing (2008). "Humic acid fractionation upon sequential adsorption onto goethite." Langmuir **24**(6): 2525-2531.

Karabelli, D., C. a. r. Üzüm, T. Shahwan, A. E. Eroğlu, T. B. Scott, K. R. Hallam and I. Lieberwirth (2008). "Batch Removal of Aqueous Cu2+ Ions Using Nanoparticles of Zero-Valent Iron: A Study of the Capacity and Mechanism of Uptake." Industrial & Engineering Chemistry Research **47**(14): 4758-4764.

Karakoti, A. S., L. L. Hench and S. Seal (2006). "The potential toxicity of nanomaterials—The role of surfaces." JOM **58**(7): 77-82.

Kaur, M., J. S. McCloy, W. Jiang, Q. Yao and Y. Qiang (2012). "Size Dependence of Inter- and Intracluster Interactions in Core–Shell Iron–Iron Oxide Nanoclusters." The Journal of Physical Chemistry C **116**(23): 12875-12885.

Keller, A. A., S. McFerran, A. Lazareva and S. Suh (2013). "Global life cycle releases of engineered nanomaterials." J. Nanopart. Res. **15**(6): 1-17.

Keller, A. A., H. Wang, D. Zhou, H. S. Lenihan, G. Cherr, B. J. Cardinale, R. Miller and Z. Ji (2010). "Stability and aggregation of metal oxide nanoparticles in natural aqueous matrices." Environ. Sci. Technol. **44**(6): 1962-1967.

Kempson, I. M., W. M. Skinner and P. Kirkbride (2003). "Calcium distributions in human hair by ToF-SIMS." Biochim. Biophys. Acta-General Subjects **1624**(1): 1-5.

Kim, H.-J., T. Phenrat, R. D. Tilton and G. V. Lowry (2012). "Effect of kaolinite, silica fines and pH on transport of polymer-modified zero valent iron nano-particles in heterogeneous porous media." J. Colloid Interface Sci. **370**(1): 1-10.

Kim, H.-S., J.-Y. Ahn, K.-Y. Hwang, I.-K. Kim and I. Hwang (2010). "Atmospherically stable nanoscale zero-valent iron particles formed under controlled air contact: characteristics and reactivity." Environ. Sci. Technol. **44**(5): 1760-1766.

Kim, J. H., P. G. Tratnyek and Y. S. Chang (2008). "Rapid dechlorination of polychlorinated dibenzo-p-dioxins by bimetallic and nanosized zerovalent iron." Environ. Sci. Technol. **42**(11): 4106-4112.

Kirchner, C., T. Liedl, S. Kudera, T. Pellegrino, A. Muñoz Javier, H. E. Gaub, S. Stölzle, N. Fertig and W. J. Parak (2005). "Cytotoxicity of colloidal CdSe and CdSe/ZnS nanoparticles." Nano Lett. **5**(2): 331-338.

Kiruba Daniel, S. C. G., G. Vinothini, N. Subramanian, K. Nehru and M. Sivakumar (2012). "Biosynthesis of Cu, ZVI, and Ag nanoparticles using Dodonaea viscosa extract for antibacterial activity against human pathogens." J. Nanopart. Res. **15**(1): 1-10.

Kiser, M., P. Westerhoff, T. Benn, Y. Wang, J. Perez-Rivera and K. Hristovski (2009). "Titanium nanomaterial removal and release from wastewater treatment plants." Environ. Sci. Technol. **43**(17): 6757-6763.

Klein, C. L., Comero, B. Stahlmecke, J. Romazanov, T. A. J. Kuhlbusch, E. Van Doren, P.-J. De Temmerman, J. Mast, P. Wick, H. F. Krug, G. Locoro, K. Hund-Rinke, W. Kördel, S. Friedrichs, G. Maier, J. Werner, T. Linsinger and B. M. Gawlik (2011). NM-300 Silver Characterisation, Stability, Homogeneity. NM-Series of Representative Manufactured Nanomaterials. Luxembourg, JRS Institute for Health and Consumer Protection.

Klein, R. and P. Meakin (1989). "Universality in colloid aggregation." Nature **339**: 360−362.

Kocur, C. M., A. I. Chowdhury, N. Sakulchaicharoen, H. K. Boparai, K. P. Weber, P. Sharma, M. M. Krol, L. M. Austrins, C. Peace and B. E. Sleep (2014). "Characterization of nZVI mobility in a field scale test." Environ. Sci. Technol.

Kocur, C. M., D. M. O'Carroll and B. E. Sleep (2012). "Impact of nZVI stability on mobility in porous media." J. Contam. Hydrol.

Kopinke, F.-D. and K. Mackenzie. (2012). "Carbo Iron." Retrieved 28/02/2012, from http://www.ufz.de/index.php?de=7038.

Kosmulski, M. (2006). "pH-dependent surface charging and points of zero charge: III. Update." J. Colloid Interface Sci. **298**(2): 730-741.

Kowalkowski, T., B. Buszewski, C. Cantado and F. Dondi (2006). "Field-flow fractionation: Theory, techniques, applications and the challenges." Critical Reviews in Analytical Chemistry **36**(2): 129-135.

Kroto, H. W., J. R. Health, S. C. O'Brien, R. F. Curl and R. E. Smalley (1985). "C60: Buckminsterfullerene." Nature **318**: 162-163.

Kunhikrishnan, A., H. K. Shon, N. S. Bolan, I. El Saliby and S. Vigneswaran (2014). "Sources, distribution, environmental fate and ecological effects of nanomaterials in wastewater streams." Crit. Rev. Env. Sci. Technol.(just-accepted).

Larlus, O., S. Mintova and T. Bein (2006). "Environmental syntheses of nanosized zeolites with high yield and monomodal particle size distribution." Microporous and Mesoporous Materials **96**(1): 405-412.

Latham, A. H. and M. E. Williams (2008). "Transmission Electron Microscope-Induced Structural Evolution in Amorphous Fe, Co, and Ni Oxide Nanoparticles." Langmuir **24**(24): 14195-14202.

Laumann, S., V. Micić and T. Hofmann (2014). "Mobility enhancement of nanoscale zero-valent iron in carbonate porous media through co-injection of polyelectrolytes." Water Res. **50**: 70-79.

Laumann, S., V. Micić, G. V. Lowry and T. Hofmann (2013). "Carbonate minerals in porous media decrease mobility of polyacrylic acid modified zero-valent iron nanoparticles used for groundwater remediation." Environ. Pollut. **179**: 53-60.

Lead, J. R. and K. J. Wilkinson (2006). "Aquatic colloids and nanoparticles: current knowledge and future trends." Environ. Chem. **3**(3): 159-171.

Ledin, A., S. Karlsson, A. Düker and B. Allard (1994). "Measurements< i> in situ</i> of concentration and size distribution of colloidal matter in deep groundwaters by photon correlation spectroscopy." Water Res. **28**(7): 1539-1545.

Lee, Y.-C., C.-W. Kim, J.-Y. Lee, H.-J. Shin and J.-W. Yang (2009). "Characterization of nanoscale zero valent iron modified by nonionic surfactant for trichloroethylene removal in the presence of humic acid: A research note." Desalination and Water Treatment **10**(1-3): 33-38.

Leveneur, J., G. I. N. Waterhouse, J. Kennedy, J. B. Metson and D. R. G. Mitchell (2011). "Nucleation and Growth of Fe Nanoparticles in SiO2: A TEM, XPS, and Fe L-Edge XANES Investigation." The Journal of Physical Chemistry C **115**(43): 20978-20985.

Li, F., C. Vipulanandan and K. K. Mohanty (2003). "Microemulsion and solution approaches to nanoparticle iron production for degradation of trichloroethylene." Colloids Surf., A **223**(1-3): 103-112.

Li, K. and Y. Chen (2012). "Effect of natural organic matter on the aggregation kinetics of CeO2 nanoparticles in KCl and CaCl2 solutions: Measurements and modeling." J. Hazard. Mater. **209–210**(0): 264-270.

Li, L., M. Fan, R. C. Brown, J. Van Leeuwen, J. Wang, W. Wang, Y. Song and P. Zhang (2006). "Synthesis, properties, and environmental applications of nanoscale iron-based materials: A review." Crit. Rev. Env. Sci. Technol. **36**(5): 405-431.

Li, P., M. Hansen and J. C. Giddings (1997). "Separation of lipoproteins from human plasma by flow field-flow fractionation." J. Liq. Chromatogr. Related Technol. **20**(16-17): 2777-2802.

Li, S., W. Yan and W.-x. Zhang (2009). "Solvent-free production of nanoscale zero-valent iron (nZVI) with precision milling." Green Chemistry **11**(10): 1618-1626.

Li, X.-Y. and B. E. Logan (2001). "Permeability of fractal aggregates." Water Res. **35**(14): 3373-3380.

Li, X., T. D. Scheibe and W. P. Johnson (2004). "Apparent decreases in colloid deposition rate coefficients with distance of transport under unfavorable deposition conditions: A general phenomenon." Environ. Sci. Technol. **38**(21): 5616-5625.

Li, X. Q., D. W. Elliott and W. X. Zhang (2006). "Zero-valent iron nanoparticles for abatement of environmental pollutants: Materials and engineering aspects." Crit. Rev. Solid State Mater. Sci. **31**(4): 111-122.

Liang, L., G. R. Moline, W. Kamolpornwijit and O. R. West (2005). "Influence of hydrogeochemical processes on zero-valent iron reactive barrier performance: A field investigation." J. Contam. Hydrol. **80**(1-2): 71-91.

Liang, Y., S. A. Bradford, J. Simunek, M. Heggen, H. Vereecken and E. Klumpp (2013). "Retention and remobilization of stabilized silver nanoparticles in an undisturbed loamy sand soil." Environ. Sci. Technol. **47**(21): 12229-12237.

Lien, H. L. and W. Zhang (1999). "Transformation of chlorinated methanes by nanoscale iron particles." Journal of environmental engineering **125**(11): 1042-1047.

Lien, H. L. and W. Zhang (2005). "Hydrodechlorination of chlorinated ethanes by nanoscale Pd/Fe bimetallic particles." Journal of environmental engineering **131**(1): 4-10.

Lien, H. L. and W. X. Zhang (2007). "Nanoscale Pd/Fe bimetallic particles: catalytic effects of palladium on hydrodechlorination." Appl. Catal., B **77**(1-2): 110-116.

Limbach, L. K., R. Bereiter, E. Müller, R. Krebs, R. Gälli and W. J. Stark (2008). "Removal of oxide nanoparticles in a model wastewater treatment plant: influence of agglomeration and surfactants on clearing efficiency." Environ. Sci. Technol. **42**(15): 5828-5833.

Lin, K.-S., N.-B. Chang and T.-D. Chuang (2008). "Fine structure characterization of zero-valent iron nanoparticles for decontamination of nitrites and nitrates in wastewater and groundwater." Science and Technology of Advanced Material **9**(2): 9.

Lin, M., H. Lindsay, D. Weitz, R. Klein, R. Ball and P. Meakin (1990). "Universal diffusion-limited colloid aggregation." J. Phys.: Condens. Matter **2**(13): 3093-3113.

Lin, Y.-T., C.-H. Weng and F.-Y. Chen (2008). "Effective removal of AB24 dye by nano/micro-size zero-valent iron." Sep. Purif. Technol. **64**(1): 26-30.

Lin, Y. H., H. H. Tseng, M. Y. Wey and M. D. Lin (2010). "Characteristics of two types of stabilized nano zero-valent iron and transport in porous media." Sci. Total Environ. **408**(10): 2260-2267.

Ling, L. and W.-x. Zhang (2014). "Reactions of Nanoscale Zero-Valent Iron with Ni(II): Three-Dimensional Tomography of the "Hollow Out" Effect in a Single Nanoparticle." Environmental Science & Technology Letters **1**(3): 209-213.

Litzen, A. and K. G. Wahlund (1991). "Zone broadening and dilution in rectangular and trapezoidal asymmetrical flow field-flow fractionation channels." Anal. Chem. **63**(10): 1001-1007.

Liu, D., P. R. Johnson and M. Elimelech (1995). "Colloid deposition dynamics in flow-through porous media: Role of electrolyte concentration." Environ. Sci. Technol. **29**(12): 2963-2973.

Liu, F.-K., F.-H. Ko, P.-W. Huang, C.-H. Wu and T.-C. Chu (2005). "Studying the size/shape separation and optical properties of silver nanoparticles by capillary electrophoresis." J. Chromatogr. A **1062**(1): 139-145.

Liu, F.-K. and G.-T. Wei (2004). "Adding sodium dodecylsulfate to the running electrolyte enhances the separation of gold nanoparticles by capillary electrophoresis." Anal. Chim. Acta. **510**(1): 77-83.

Liu, J., S. Legros, F. Von Der Kammer and T. Hofmann (2013). "Natural organic matter concentration and hydrochemistry does influence aggregation kinetics of functionalized engineered nanoparticles." Environ. Sci. Technol. **47**(9): 4113-4120.

Liu, J., Z. Zhao and G. Jiang (2008). "Coating Fe3O4 magnetic nanoparticles with humic acid for high efficient removal of heavy metals in water." Environ. Sci. Technol. **42**(18): 6949-6954.

Liu, Y., H. Choi, D. Dionysiou and G. V. Lowry (2005). "Trichloroethene hydrodechlorination in water by highly disordered monometallic nanoiron." Chem. Mater. **17**(21): 5315-5322.

Liu, Y., S. A. Majetich, R. D. Tilton, D. S. Sholl and G. V. Lowry (2005). "TCE dechlorination rates, pathways, and efficiency of nanoscale iron particles with different properties." Environ. Sci. Technol. **39**(5): 1338-1345.

Liu, Y. and B. Yan (2011). "Characterizing the Surface Chemistry of Nanoparticles: An Analogy to Solid-Phase Synthesis Samples." Combinatorial Chemistry & High Throughput Screening **14**(3): 191-197.

Liu, Z. L., H. B. Wang, Q. H. Lu, G. H. Du, L. Peng, Y. Q. Du, S. M. Zhang and K. L. Yao (2004). "Synthesis and characterization of ultrafine well-dispersed magnetic nanoparticles." Journal of Magnetism and Magnetic Materials **283**(2-3): 258-262.

Lo, I. M. C., R. Y. Surampalli and K. C. K. Lai (2007). Zero-valent iron reactive materials for hazardous waste and inorganics removal. Reston, Virginia, American Society of Civil Engineers (ASCE).

Lombi, E. and J. Susini (2009). "Synchrotron-based techniques for plant and soil science: opportunities, challenges and future perspectives." Plant Soil **320**(1-2): 1-35.

Lowry, G. V., K. B. Gregory, S. C. Apte and J. R. Lead (2012). "Transformations of nanomaterials in the environment." Environ. Sci. Technol. **46**(13): 6893-6899.

Majedi, S. M., B. C. Kelly and H. K. Lee (2014). "Role of combinatorial environmental factors in the behavior and fate of ZnO nanoparticles in aqueous systems: A multiparametric analysis." J. Hazard. Mater. **264**(0): 370-379.

Makela, J. M., H. Keskinen, T. Forsblom and J. Keskinen (2004). "Generation of metal and metal oxide nanoparticles by liquid flame spray process." Journal of Materials Science **39**(8): 2783-2788.

Malik, M. A., P. O'Brien and N. Revaprasadu (2002). "A simple route to the synthesis of core/shell nanoparticles of chalcogenides." Chem. Mater. **14**(5): 2004-2010.

Malow, T. R., C. C. Koch, P. Q. Miraglia and K. L. Murty (1998). "Compressive mechanical behavior of nanocrystalline Fe investigated with an automated ball indentation technique." Materials Science and Engineering A **252**(1): 36-43.

Manna, L., E. C. Scher and A. P. Alivisatos (2000). "Synthesis of soluble and processable rod-, arrow-, teardrop-, and tetrapod-shaped CdSe nanocrystals." Journal of the American Chemical Society **122**(51): 12700-12706.

Martin, J. E., A. A. Herzing, W. Yan, X.-q. Li, B. E. Koel, C. J. Kiely and W.-x. Zhang (2008). "Determination of the Oxide Layer Thickness in Core−Shell Zerovalent Iron Nanoparticles." Langmuir **24**(8): 4329-4334.

Masciangioli, T. and W. X. Zhang (2003). "Environmental technologies at the nanoscale." Environ. Sci. Technol. **37**(5): 102A-108A.

Massoudieh, A. and T. R. Ginn (2010). "Colloid-facilitated contaminant transport in unsaturated porous media." Modelling of Pollutants in Complex Environmental Systems **2**: 263-292.

Maurice, P. and K. Namjesnik-Dejanovic (1999). "Aggregate structures of sorbed humic substances observed in aqueous solution." Environ. Sci. Technol. **33**(9): 1538-1541.

McDowell-Boyer, L. M., J. R. Hunt and N. Sitar (1986). "Particle transport through porous media." Water Resour. Res. **22**(13): 1901-1921.

McKnight, D. M., K. E. Bencala, G. W. Zellweger, G. R. Aiken, G. L. Feder and K. A. Thorn (1992). "Sorption of dissolved organic carbon by hydrous aluminum and iron oxides occurring at the confluence of Deer Creek with the Snake River, Summit County, Colorado." Environ. Sci. Technol. **26**(7): 1388-1396.

Mie, G. (1976). "Contributions to the optics of turbid media, particularly of colloidal metal solutions." Contributions to the optics of turbid media, particularly of colloidal metal solutions Transl. into ENGLISH from Ann. Phys.(Leipzig), v. 25, no. 3, 1908 p 377-445 **1**: 377-445.

Miehr, R., P. G. Tratnyek, J. Z. Bandstra, M. M. Scherer, M. J. Alowitz and E. J. Bylaska (2004). "Diversity of Contaminant Reduction Reactions by Zerovalent Iron: Role of the Reductate." Environ. Sci. Technol. **38**(1): 139-147.

Mori, S. and H. G. Barth (1999). Size exclusion chromatography, Springer Verlag.

Morones, J. R., J. L. Elechiguerra, A. Camacho, K. Holt, J. B. Kouri, J. T. Ramírez and M. J. Yacaman (2005). "The bactericidal effect of silver nanoparticles." Nanotechnol. **16**(10): 2346.

Morrison, S. J., P. S. Mushovic and P. L. Niesen (2006). "Early breakthrough of molybdenum and uranium in a permeable reactive barrier." Environ. Sci. Technol. **40**(6): 2018-2024.

Mueller, N. C. and B. Nowack (2009). Report on nanotechnology in the technology sector: Environment, European Commission, ObservatoryNano.

Müeller, N. C. and B. Nowack. (2010). "Nano zero valent iron - THE solution for water and soil remediation? Report of the ObservatoryNANO " Retrieved 27/02/2012, from http://www.observatorynano.eu/project/filesystem/files/nZVI_final_vsObservatory.pdf.

Murphy, E. M., J. M. Zachara and S. C. Smith (1990). "Influence of mineral-bound humic substances on the sorption of hydrophobic organic compounds." Environ. Sci. Technol. **24**(10): 1507-1516.

Mylon, S. E., K. L. Chen and M. Elimelech (2004). "Influence of natural organic matter and ionic composition on the kinetics and structure of hematite colloid aggregation: Implications to iron depletion in estuaries." Langmuir **20**(21): 9000-9006.

Nakayama, T., Y. H. Choa, T. A. Yamamoto and K. Niihara (1998). "The Iron Oxide Nanocrystalline Manufactured by IGC-PECS Process." Funtai Oyobi Fummatsu Yakin/Journal of the Japan Society of Powder and Powder Metallurgy **45**(12): 1207-1210.

Nakayama, T., T. A. Yamamoto, Y. H. Choa and K. Niihara (2000). "Synthesis and magnetic properties of nanocluster composite." Cera. Trans. **108**: 257.

Natter, H., M. Schmelzer, M. S. Loffler, C. E. Krill, A. Fitch and R. Hempelmann (2000). "Grain-growth kinetics of nanocrystalline iron studied in situ by synchrotron realtime X-ray diffraction." Journal of Physical Chemistry B **104**: 2467-2476.

Niyogi, S., M. Hamon, H. Hu, B. Zhao, P. Bhowmik, R. Sen, M. Itkis and R. Haddon (2002). "Chemistry of single-walled carbon nanotubes." Acc. Chem. Res. **35**(12): 1105-1113.

Nowack, B. and T. D. Bucheli (2007). "Occurrence, behavior and effects of nanoparticles in the environment." Environ. Pollut. **150**(1): 5-22.

Nurmi, J. T., P. G. Tratnyek, V. Sarathy, D. R. Baer, J. E. Amonette, K. Pecher, C. Wang, J. C. Linehan, D. W. Matson, R. L. Penn and M. D. Driessen (2005). "Characterization and properties of metallic iron nanoparticles: Spectroscopy, electrochemistry, and kinetics." Environ. Sci. Technol. **39**(5): 1221-1230.

Nutt, M. O., J. B. Hughes and M. S. Wong (2005). "Designing Pd-on-Au bimetallic nanoparticle catalysts for trichloroethene hydrodechlorination." Environ. Sci. Technol. **39**(5): 1346-1353.

O'Carroll, D., B. Sleep, M. Krol, H. Boparai and C. Kocur (2012). "Nanoscale zero valent iron and bimetallic particles for contaminated site remediation." AdWR(0).

Oorts, K., U. Ghesquiere and E. Smolders (2007). "Leaching and aging decrease nickel toxicity to soil microbial processes in soils freshly spiked with nickel chloride." Environ. Toxicol. Chem. **26**(6): 1130-1138.

Ottofuelling, S. (2010). Engineered Nanoparticles in the Environment: Behavior of Titanium Dioxide in Aquatic Systems. PhD, University of Vienna.

Ottofuelling, S., F. Von Der Kammer and T. Hofmann (2011). "Commercial titanium dioxide nanoparticles in both natural and synthetic water: comprehensive multidimensional testing and prediction of aggregation behavior." Environ. Sci. Technol. **45**(23): 10045-10052.

Oughton, D. H., T. Hertel-Aas, E. Pellicer, E. Mendoza and E. J. Joner (2008). "Neutron activation of engineered nanoparticles as a tool for tracing their environmental fate and uptake in organisms." Environ. Toxicol. Chem. **27**(9): 1883-1887.

Panacek, A., L. Kvitek, R. Prucek, M. Kolar, R. Vecerova, N. Pizurova, V. K. Sharma, T. Nevecna and R. Zboril (2006). "Silver colloid nanoparticles: Synthesis, characterization, and their antibacterial activity." Journal of Physical Chemistry B **110**(33): 16248-16253.

Peng, X., Z. Luan, F. Chen, B. Tian and Z. Jia (2005). "Adsorption of humic acid onto pillared bentonite." Desalination **174**(2): 135-143.

Peralta-Videa, J. R., L. Zhao, M. L. Lopez-Moreno, G. de la Rosa, J. Hong and J. L. Gardea-Torresdey (2011). "Nanomaterials and the environment: A review for the biennium 2008–2010." J. Hazard. Mater. **186**(1): 1-15.

Petersen, E. J., Q. Huang and J. Weber, Walter J (2008). "Bioaccumulation of radio-labeled carbon nanotubes by Eisenia foetida." Environ. Sci. Technol. **42**(8): 3090-3095.

Phenrat, T., A. Cihan, H. J. Kim, M. Mital, T. Illangasekare and G. V. Lowry (2010). "Transport and deposition of polymer-modified Fe0 nanoparticles in 2-D heterogeneous porous media: Effects of particle concentration, Fe 0 content, and coatings." Environ. Sci. Technol. **44**(23): 9086-9093.

Phenrat, T., H. J. Kim, F. Fagerlund, T. Illangasekare, R. D. Tilton and G. V. Lowry (2009). "Particle size distribution, concentration, and magnetic attraction affect transport of polymer-modified Fe0 nanoparticles in sand columns." Environ. Sci. Technol. **43**(13): 5079-5085.

Phenrat, T., Y. Liu, R. D. Tilton and G. V. Lowry (2009). "Adsorbed polyelectrolyte coatings decrease Fe0 nanoparticle reactivity with TCE in water: conceptual model and mechanisms." Environ. Sci. Technol. **43**(5): 1507-1514.

Phenrat, T., T. C. Long, G. V. Lowry and B. Veronesi (2008). "Partial oxidation (aging) and surface modification decrease the toxicity of nanosized zerovalent iron." Environ. Sci. Technol. **43**(1): 195-200.

Phenrat, T., G. Lowry, N. Savage, D. Mamadou, J. Duncan, A. Street and R. Sustich (2009). "Physicochemistry of polyelectrolyte coatings that increase stability, mobility, and contaminant specificity of reactive nanoparticles used for groundwater remediation." Nanotechnology Applications for Clean Water: 249-267.

Phenrat, T., N. Saleh, K. Sirk, H.-J. Kim, R. D. Tilton and G. V. Lowry (2008). "Stabilization of aqueous nanoscale zerovalent iron dispersions by anionic polyelectrolytes: adsorbed anionic polyelectrolyte layer properties and their effect on aggregation and sedimentation." J. Nanopart. Res. **10**(5): 795-814.

Phenrat, T., N. Saleh, K. Sirk, R. D. Tilton and G. V. Lowry (2007). "Aggregation and sedimentation of aqueous nanoscale zerovalent iron dispersions." Environ. Sci. Technol. **41**(1): 284-290.

Phenrat, T., N. Saleh, K. Sirk, R. D. Tilton and G. V. Lowry (2007). "Aggregation and sedimentation of aqueous nanoscale zerovalent iron dispersions." Environ. Sci. Technol. **41**(1): 284-290.

Phillips, D. H., D. B. Watson, Y. Roh and B. Gu (2003). "Mineralogical Characteristics and Transformations during Long-Term Operation of a Zerovalent Iron Reactive Barrier." Journal of Environmental Quality **32**(6): 2033-2045.

Phuntsho, S., H. Shon, S. Vigneswaran and J. Cho (2011). "Assessing membrane fouling potential of humic acid using flow field-flow fractation." Journal of Membrane Science **373**(1-2): 64-73.

Plathe, K. L. (2010). Nanoparticle - Heavy metal associations in river sediments. PhD thesis PhD thesis, Virginia Polytechnic Institute.

Poda, A. R., A. J. Bednar, A. J. Kennedy, A. Harmon, M. Hull, D. M. Mitrano, J. F. Ranville and J. Steevens (2011). "Characterization of silver nanoparticles using flow-field flow fractation interfaced to inductively coupled plasma mass spectrometry." J. Chromatogr. A **1218**(27): 4219-4225.

Pokropivny, V. V. (2001). "Non-carbon nanotubes (Review). Part 2. Types and structure." Powder Metall. Met. Ceram. **40**(11-12): 582-594.

Ponder, S. M., J. G. Darab, J. Bucher, D. Caulder, I. Craig, L. Davis, N. Edelstein, W. Lukens, H. Nitsche, L. Rao, D. K. Shuh and T. E. Mallouk (2001). "Surface Chemistry and Electrochemistry of Supported Zerovalent Iron Nanoparticles in the Remediation of Aqueous Metal Contaminants." Chem. Mater. **13**(2): 479-486.

Ponder, S. M., J. G. Darab and T. E. Mallouk (2000). "Remediation of Cr(VI) and Pb(II) aqueous solutions using supported, nanoscale zero-valent iron." Environ. Sci. Technol. **34**(12): 2564-2569.

Poynton, H. C., J. M. Lazorchak, C. A. Impellitteri, M. E. Smith, K. Rogers, M. Patra, K. A. Hammer, H. J. Allen and C. D. Vulpe (2010). "Differential gene expression in Daphnia magna suggests distinct modes of action and bioavailability for ZnO nanoparticles and Zn ions." Environ. Sci. Technol. **45**(2): 762-768.

Prato, M. (1999). Fullerene materials. Fullerenes and Related Structures, Springer**:** 173-187.

Prietzel, J., J. Thieme, K. Eusterhues and D. Eichert (2007). "Iron speciation in soils and soil aggregates by synchrotron-based X-ray microspectroscopy (XANES,μ-XANES)." Eur. J. Soil Sci. **58**(5): 1027-1041.

Pyell, U. (2010). "Characterization of nanoparticles by capillary electromigration separation techniques." Electrophoresis **31**(5): 814-831.

Qiu, S., J. Dong and G. Chen (1999). "Preparation of Cu nanoparticles from water-in-oil microemulsions." J. Colloid Interface Sci. **216**(2): 230-234.

Qiu, S. R., H. F. Lai, M. J. Roberson, M. L. Hunt, C. Amrhein, L. C. Giancarlo, G. W. Flynn and J. A. Yarmoff (2000). "Removal of Contaminants from Aqueous Solution by Reaction with Iron Surfaces." Langmuir **16**(5): 2230-2236.

Quik, J. T., M. C. Stuart, M. Wouterse, W. Peijnenburg, A. J. Hendriks and D. van de Meent (2012). "Natural colloids are the dominant factor in the sedimentation of nanoparticles." Environ. Toxicol. Chem. **31**(5): 1019-1022.

Quinn, J., C. Geiger, C. Clausen, K. Brooks, C. Coon, S. O'Hara, T. Krug, D. Major, W. S. Yoon, A. Gavaskar and T. Holdsworth (2005). "Field demonstration of DNAPL dehalogenation using emulsified zero-valent iron." Environ. Sci. Technol. **39**(5): 1309-1318.

Rajagopalan, R. and R. Q. Chu (1982). "Dynamics of adsorption of colloidal particles in packed beds." J. Colloid Interface Sci. **86**(2): 299-317.

Ramos, M. A., W. Yan, X.-q. Li, B. E. Koel and W.-x. Zhang (2009). "Simultaneous oxidation and reduction of arsenic by zero-valent iron nanoparticles: understanding the significance of the core− shell structure." The J. Phy. Chem., C **113**(33): 14591-14594.

Rasband, W. S. (1997-2012). ImageJ. Bethesda, Maryland, USA, U.S. National Institutes of Health.

Ravel, B. and M. Newville (2005). "ATHENA, ARTEMIS, HEPHAESTUS: data analysis for x-ray absorption spectroscopy using IFEFFIT." J. Synchrotron Radiat. **12**: 537-541.

Raychoudhury, T., N. Tufenkji and S. Ghoshal (2012). "Aggregation and deposition kinetics of carboxymethyl cellulose-modified zero-valent iron nanoparticles in porous media." Water Res. **46**(6): 1735-1744.

Raychoudhury, T., N. Tufenkji and S. Ghoshal (2014). "Straining of polyelectrolyte-stabilized nanoscale zero valent iron particles during transport through granular porous media." Water Res. **50**: 80-89.

Reinsch, B. C., B. Forsberg, R. L. Penn, C. S. Kim and G. V. Lowry (2010). "Chemical Transformations during Aging of Zerovalent Iron Nanoparticles in the Presence of Common Groundwater Dissolved Constituents." Environ Sci Technol **44**(9): 3455-3461.

Rempel, J. Y., B. L. Trout, M. G. Bawendi and K. F. Jensen (2006). "Density functional theory study of ligand binding on CdSe (0001),(0001), and (1120) single crystal

relaxed and reconstructed surfaces: implications for nanocrystalline growth." The Journal of Physical Chemistry B **110**(36): 18007-18016.

Ressler, T. (1998). "WinXAS: a program for X-ray absorption spectroscopy data analysis under MS-Windows." J. Synchrotron Radiat. **5**(2): 118-122.

Rice, J. A. and J. S. Lin (1993). "Fractal nature of humic materials." Environ. Sci. Technol. **27**(2): 413-414.

Ridley, M. K., V. A. Hackley and M. L. Machesky (2006). "Characterization and surface-reactivity of nanocrystalline anatase in aqueous solutions." Langmuir **22**(26): 10972-10982.

Rieker, T. P., M. Hindermann-Bischoff and F. Ehrburger-Dolle (2000). "Small-angle X-ray scattering study of the morphology of carbon black mass fractal aggregates in polymeric composites." Langmuir **16**(13): 5588-5592.

Robichaud, C. O., A. E. Uyar, M. R. Darby, L. G. Zucker and M. R. Wiesner (2009). "Estimates of upper bounds and trends in nano-TiO2 production as a basis for exposure assessment." Environ. Sci. Technol. **43**(12): 4227-4233.

Rojas, T. C., J. C. Sánchez-López, J. M. Greneche, A. Conde and A. Fernández (2004). "Characterization of oxygen passivated iron nanoparticles and thermal evolution to γ-Fe2O3." Journal of Materials Science **39**(15): 4877-4885.

Romanello, M. B. and M. M. F. de Cortalezzi (2013). "An experimental study on the aggregation of TiO2 nanoparticles under environmentally relevant conditions." Water Res. **47**(12): 3887-3898.

Rust, M. J., M. Bates and X. Zhuang (2006). "Sub-diffraction-limit imaging by stochastic optical reconstruction microscopy (STORM)." Nat. Methods **3**(10): 793-796.

Ryan, J. N. and M. Elimelech (1996). "Colloid mobilization and transport in groundwater." Colloids Surf., A **107**: 1-56.

Ryde, N., N. Kallay and E. Matijević (1991). "Particle adhesion in model systems. Part 14.—Experimental evaluation of multilayer deposition." J. Chem. Soc., Faraday Trans. **87**(9): 1377-1381.

Saiers, J. E. and J. J. Lenhart (2003). "Colloid mobilization and transport within unsaturated porous media under transient-flow conditions." Water Resour. Res. **39**(1).

Saleh, N., H. J. Kim, T. Phenrat, K. Matyjaszewski, R. D. Tilton and G. V. Lowry (2008). "Ionic strength and composition affect the mobility of surface-modified Fe0 nanoparticles in water-saturated sand columns." Environ. Sci. Technol. **42**(9): 3349-3355.

Saleh, N., T. Phenrat, K. Sirk, B. Dufour, J. Ok, T. Sarbu, K. Matyjaszewski, R. D. Tilton and G. V. Lowry (2005). "Adsorbed triblock copolymers deliver reactive iron nanoparticles to the oil/water interface." Nano Lett. **5**(12): 2489-2494.

Saleh, N., T. Sarbu, K. Sirk, G. V. Lowry, K. Matyjaszewski and R. D. Tilton (2005). "Oil-in-water emulsions stabilized by highly charged polyelectrolyte-grafted silica nanoparticles." Langmuir **21**(22): 9873-9878.

Saleh, N., K. Sirk, Y. Liu, T. Phenrat, B. Dufour, K. Matyjaszewski, R. D. Tilton and G. V. Lowry (2007). "Surface modifications enhance nanoiron transport and NAPL targeting in saturated porous media." Environ. Eng. Sci. **24**(1): 45-57.

Sánchez-González, J., N. García-Otero, A. Moreda-Piñeiro and P. Bermejo-Barrera (2012). "Multi-walled carbon nanotubes — Solid phase extraction for isolating marine dissolved organic matter before characterization by size exclusion chromatography." Microchem. J. **102**(0): 75-82.

Sanchez-Lopez, J. C., A. Justo, A. Fernandez, C. F. Conde and A. Conde (1997). "Preparation and thermal evolution of vapour-condensed nanocrystalline iron." Philosophical Magazine B: Physics of Condensed Matter; Statistical Mechanics, Electronic, Optical and Magnetic Properties **76**(4): 663-667.

Sau, T. K., A. Pal and T. Pal (2001). "Size regime dependent catalysis by gold nanoparticles for the reduction of eosin." The Journal of Physical Chemistry B **105**(38): 9266-9272.

Scherer, M. M., S. Richter, R. L. Valentine and P. J. J. Alvarez (2000). "Chemistry and microbiology of permeable reactive barriers for in situ groundwater clean up." Crit. Rev. Env. Sci. Technol. **30**(3): 363-411.

Schorr, J. R. (2007) "Promise of Nanomaterials for Water Cleanup. Water Conditioning & Purification."

Schrick, B., J. L. Blough, A. D. Jones and T. E. Mallouk (2002). "Hydrodechlorination of trichloroethylene to hydrocarbons using bimetallic nickel-iron nanoparticles." Chem. Mater. **14**(12): 5140-5147.

Schrick, B., B. W. Hydutsky, J. L. Blough and T. E. Mallouk (2004). "Delivery vehicles for zerovalent metal nanoparticles in soil and groundwater." Chem. Mater. **16**(11): 2187-2193.

Schurtenberger, P. and M. E. Newman (1993). "Characterization of biological and environmental particles using static and dynamic light scattering." Environ. Part. **2**: 37-115.

Scott, T. B. (2011). Inorganic nanoparticles for remediation Inorganic Nanoparticles: Synthesis, Applications, and Perspectives C. Altavilla and E. Ciliberto. Boca Raton, FL CRC Press 393-441

Scott, T. B., M. Dickinson, R. A. Crane, O. Riba, G. M. Hughes and G. C. Allen (2010). "The effects of vacuum annealing on the structure and surface chemistry of iron nanoparticles." J. Nanopart. Res. **12**(5): 1765-1775.

Scown, T., R. Van Aerle and C. Tyler (2010). "Review: Do engineered nanoparticles pose a significant threat to the aquatic environment?" Crit. Rev. Toxicol. **40**(7): 653-670.

Shaw, D. J. (1992). Colloid and surface science. Oxford, UK, Butterworth-Heinemann Ltd.

Shi, L.-n., Y.-M. Lin, X. Zhang and Z.-l. Chen (2011). "Synthesis, characterization and kinetics of bentonite supported nZVI for the removal of Cr(VI) from aqueous solution." Chem. Eng. J. **171**(2): 612-617.

Shih, Y.-h., C.-y. Hsu and Y.-f. Su (2011). "Reduction of hexachlorobenzene by nanoscale zero-valent iron: kinetics, pH effect, and degradation mechanism." Sep. Purif. Technol. **76**(3): 268-274.

Shimmin, R. G., A. B. Schoch and P. V. Braun (2004). "Polymer size and concentration effects on the size of gold nanoparticles capped by polymeric thiols." Langmuir **20**(13): 5613-5620.

Shon, H., S. Vigneswaran, I. S. Kim, J. Cho and H. Ngo (2004). "The effect of pretreatment to ultrafiltration of biologically treated sewage effluent: a detailed effluent organic matter (EfOM) characterization." Water Res. **38**(7): 1933-1939.

Shon, H., S. Vigneswaran, H. Ngo and J. H. Kim (2005). "Chemical coupling of photocatalysis with flocculation and adsorption in the removal of organic matter." Water Res. **39**(12): 2549-2558.

Shon, H. K., S. Puntsho, K. Chon, R. Aryal, S. Vigneswaran, I. S. Kim and J. Cho (2009). "A study on the influence of ionic strength on the elution behaviour of membrane organic foulant using advanced separation tools." Desalination and Water Treatment **11**(1-3): 38-45.

Shon, H. K., S. Vigneswaran and H. H. Ngo (2006). "Effect of partial flocculation and adsorption as pretreatment to ultrafiltration." AIChE Journal **52**(1): 207-216.

Signorini, L., L. Pasquini, L. Savini, R. Carboni, F. Boscherini, E. Bonetti, A. Giglia, M. Pedio, N. Mahne and S. Nannarone (2003). "Size-dependent oxidation in iron/iron oxide core-shell nanoparticles." Phys. Rev. B **68**(19): 195423.

Silva, L., C. Sampaio, A. Guedes, S. Fdez-Ortiz de Vallejuelo and J. Madariaga (2012). "Multianalytical approaches to the characterisation of minerals associated with coals

and the diagnosis of their potential risk by using combined instrumental microspectroscopic techniques and thermodynamic speciation." <u>Fuel</u> **94**: 52-63.

Silva, L. F., K. DaBoit, C. H. Sampaio, A. Jasper, M. L. Andrade, I. J. Kostova, F. B. Waanders, K. R. Henke and J. C. Hower (2012). "The occurrence of hazardous volatile elements and nanoparticles in Bulgarian coal fly ashes and the effect on human health exposure." <u>Sci. Total Environ.</u> **416**: 513-526.

Silva, L. F., A. Jasper, M. L. Andrade, C. H. Sampaio, S. Dai, X. Li, T. Li, W. Chen, X. Wang and H. Liu (2012). "Applied investigation on the interaction of hazardous elements binding on ultrafine and nanoparticles in Chinese anthracite-derived fly ash." <u>Sci. Total Environ.</u> **419**: 250-264.

Singh, C., S. Friedrichs, M. Levin, R. Birkedal, K. A. Jensen, G. Pojana, W. Wohlleben, S. Schulte, K. Wiench, T. Turney, O. Koulaeva, D. Marshall, K. Hund-Rinke, W. Kördel, E. Van Doren, P.-J. De Temmerman, M. Abi Daoud Francisco, J. Mast, N. Gibson, R. Koeber, T. Linsinger and C. L. Klein (2011). Zinc Oxide NM-110, NM-111, NM-112, NM-113 Characterisation and Test Item Preparation. <u>NM-Series of Representative Manufactured Nanomaterials</u>, JRS Institute for Reference Materials and Measurements.

Sirk, K. M., N. B. Saleh, T. Phenrat, H. J. Kim, B. Dufour, J. Ok, P. L. Golas, K. Matyjaszewski, G. V. Lowry and R. D. Tilton (2009). "Effect of adsorbed polyelectrolytes on nanoscale zero valent iron particle attachment to soil surface models." <u>Environ. Sci. Technol.</u> **43**(10): 3803-3808.

Song, G., J. Bo and R. Guo (2004). "The characterization and property of polystyrene compounding of Î±-Fe2O3 in the nano-scale." <u>Colloid and Polymer Science</u> **282**(6): 656-660.

Stern, O. (1924). "Theory of the electrical double layer." <u>Electrochemistry</u> **30**: 508-516.

Stolpe, B., M. Hassellov, K. Andersson and D. R. Turner (2005). "High resolution ICPMS as an on-line detector for flow field-flow fractionation; multi-element determination of colloidal size distributions in a natural water sample." <u>Anal. Chim. Acta.</u> **535**(1-2): 109-121.

Stumm, W. and J. J. Morgan (2012). <u>Aquatic chemistry: chemical equilibria and rates in natural waters</u>, John Wiley & Sons.

Su, J., S. Lin, Z. Chen, M. Megharaj and R. Naidu (2011). "Dechlorination of p-chlorophenol from aqueous solution using bentonite supported Fe/Pd nanoparticles: Synthesis, characterization and kinetics." <u>Desalination</u> **280**(1–3): 167-173.

Sun, Y.-P., X.-q. Li, J. Cao, W.-x. Zhang and H. P. Wang (2006). "Characterization of zero-valent iron nanoparticles." <u>Adv. Colloid Interface Sci.</u> **120**(1-3): 47-56.

Sun, Y. P. (2006). <u>Dispersion of nanocale iron particles</u>. Doctorate degree, Lehigh University.

Sun, Y. P., X. Q. Li, W. X. Zhang and H. P. Wang (2007). "A method for the preparation of stable dispersion of zero-valent iron nanoparticles." <u>Colloids Surf., A</u> **308**(1-3): 60-66.

Sus-Ryszkowska, M., T. Wejrzanowski, Z. Pakiela and K. J. Kurzydlowski (2004). "Microstructure of ECAP severely deformed iron and its mechanical properties." <u>Materials Science and Engineering A</u> **369**(1-2): 151-156.

Takahashi, K., H. Kato, T. Saito, S. Matsuyama and S. Kinugasa (2008). "Precise measurement of the size of nanoparticles by dynamic light scattering with uncertainty analysis." <u>Particle & Particle Systems Characterization</u> **25**(1): 31-38.

Tang, N., W. Chen, W. Zhong, H. Jiang, S. Huang and Y. Du (2006). "Highly stable carbon-coated Fe/SiO2 composites: Synthesis, structure and magnetic properties." <u>Carbon</u> **44**(3): 423-427.

Tao, N. R., M. L. Sui, J. Lu and K. Lua (1999). "Surface nanocrystallization of iron induced by ultrasonic shot peening." <u>Nanostruct. Mater.</u> **11**(4): 433-440.

Tee, Y. H., L. Bachas and D. Bhattacharyya (2009). "Degradation of Trichloroethylene by Iron-Based Bimetallic Nanoparticles." The J. Phy. Chem., C **113**(22): 9454-9464.

Theron, J., J. Walker and T. Cloete (2008). "Nanotechnology and water treatment: applications and emerging opportunities." Crit. Rev. Microbiol. **34**(1): 43-69.

Thio, B. J. R., D. Zhou and A. A. Keller (2011). "Influence of natural organic matter on the aggregation and deposition of titanium dioxide nanoparticles." J. Hazard. Mater. **189**(1–2): 556-563.

Tiller, C. L. and C. R. O'Melia (1993). "Natural organic matter and colloidal stability: Models and measurements." Colloids Surf., A **73**: 89-102.

Tipping, E. and D. Higgins (1982). "The effect of adsorbed humic substances on the colloid stability of haematite particles." Colloids and Surfaces **5**(2): 85-92.

Tipping, E. and M. Ohnstad (1984). "Colloid stability of iron oxide particles from a freshwater lake."

Tiraferri, A., K. L. Chen, R. Sethi and M. Elimelech (2008). "Reduced aggregation and sedimentation of zero-valent iron nanoparticles in the presence of guar gum." J. Colloid Interface Sci. **324**(1-2): 71-79.

Tiraferri, A. and R. Sethi (2009). "Enhanced transport of zerovalent iron nanoparticles in saturated porous media by guar gum." J. Nanopart. Res. **11**(3): 635-645.

Tombácz, E., Z. Libor, E. Illés, A. Majzik and E. Klumpp (2004). "The role of reactive surface sites and complexation by humic acids in the interaction of clay mineral and iron oxide particles." Organic Geochemistry **35**(3): 257-267.

Treubig Jr, J. M. and P. R. Brown (2002). "Analysis of C$_{60}$ and C$_{70}$ fullerenes using high-performance liquid chromatography–Fourier transform infrared spectroscopy." J. Chromatogr. A **960**(1): 135-142.

Tufenkji, N. and M. Elimelech (2005). "Breakdown of colloid filtration theory: Role of the secondary energy minimum and surface charge heterogeneities." Langmuir **21**(3): 841-852.

Tungittiplakorn, W., L. W. Lion, C. Cohen and J.-Y. Kim (2004). "Engineered polymeric nanoparticles for soil remediation." Environ. Sci. Technol. **38**(5): 1605-1610.

Turner, N. H., B. I. Dunlap and R. J. Colton (1984). "Surface analysis: x-ray photoelectron spectroscopy, Auger electron spectroscopy and secondary ion mass spectrometry." Anal. Chem. **56**(5): 373R-416R.

Uegami, M., J. Kawano, K. Kakuya, T. Okita and K. Okinaka (2004). Iron composite particles for purifying soil or groundwater. E. P. Application.

Üzüm, Ç., T. Shahwan, A. Eroğlu, I. Lieberwirth, T. Scott and K. Hallam (2008). "Application of zero-valent iron nanoparticles for the removal of aqueous Co2+ ions under various experimental conditions." Chem. Eng. J. **144**(2): 213-220.

Üzüm, Ç., T. Shahwan, A. E. Eroglu, K. R. Hallam, T. B. Scott and I. Lieberwirth (2009). "Synthesis and characterization of kaolinite-supported zero-valent iron nanoparticles and their application for the removal of aqueous Cu2+ and Co2+ ions." Applied Clay Science **43**(2): 172-181.

Üzüm, Ç., T. Shahwan, A. E. Eroğlu, I. Lieberwirth, T. B. Scott and K. R. Hallam (2008). "Application of zero-valent iron nanoparticles for the removal of aqueous Co2+ ions under various experimental conditions." Chemical Engineering Journal **144**(2): 213-220.

Valiev, R. Z., R. K. Islamgaliev and I. V. Alexandrov (2000). "Bulk nanostructured materials from severe plastic deformation." Progress in Materials Science **45**(2): 103-189.

Vecchia, E. D., M. Luna and R. Sethi (2009). "Transport in porous media of highly concentrated iron micro-and nanoparticles in the presence of xanthan gum." Environ. Sci. Technol. **43**(23): 8942-8947.

Venezia, A. M. (2003). "X-ray photoelectron spectroscopy (XPS) for catalysts characterization." Catal. Today **77**(4): 359-370.

Vermeer, A. and L. Koopal (1998). "Adsorption of humic acids to mineral particles. 2. Polydispersity effects with polyelectrolyte adsorption." Langmuir **14**(15): 4210-4216.

Verwey, E. and J. T. G. Overbeek (1948). "Theory of the stability of lyophobic colloids." Amserdam: Elsevier.

Verwey, E. J. W. (1947). "Theory of the stability of lyophobic colloids." The Journal of Physical Chemistry **51**(3): 631-636.

von der Kammer, F., P. L. Ferguson, P. A. Holden, A. Masion, K. R. Rogers, S. J. Klaine, A. A. Koelmans, N. Horne and J. M. Unrine (2012). "Analysis of engineered nanomaterials in complex matrices (environment and biota): General considerations and conceptual case studies." Environ. Toxicol. Chem. **31**(1): 32-49.

von der Kammer, F., S. Ottofuelling and T. Hofmann (2010). "Assessment of the physico-chemical behavior of titanium dioxide nanoparticles in aquatic environments using multi-dimensional parameter testing." Environ. Pollut. **158**(12): 3472-3481.

Wang, C.-B. and W.-X. Zhang (1997). "Synthesizing nanoscale iron particles for rapid and complete dechlorination of TCE and PCBs." Environ. Sci. Technol. **31**(7): 2154-2156.

Wang, C., D. R. Baer, J. E. Amonette, M. H. Engelhard, J. Antony and Y. Qiang (2009). "Morphology and Electronic Structure of the Oxide Shell on the Surface of Iron Nanoparticles." J Am Chem Soc **131**(25): 8824-8832.

Wang, C. M., D. R. Baer, J. E. Amonette, M. H. Engelhard, J. J. Antony and Y. Qiang (2007). "Electron beam-induced thickening of the protective oxide layer around Fe nanoparticles." Ultramicroscopy **108**(1): 43-51.

Wang, C. M., D. R. Baer, J. E. Amonette, M. H. Engelhard, Y. Qiang and J. Antony (2007). "Morphology and oxide shell structure of iron nanoparticles grown by sputter-gas-aggregation." Nanotechnology **18**(25): 255603.

Wang, D., M. Paradelo, S. A. Bradford, W. J. G. M. Peijnenburg, L. Chu and D. Zhou (2011). "Facilitated transport of Cu with hydroxyapatite nanoparticles in saturated sand: Effects of solution ionic strength and composition." Water Res. **45**(18): 5905-5915.

Wang, H., J. Zhang and T. Y. Hsu (2004). "Internal friction associated with phase transformation of nanograined bulk Fe-25 at.% Ni alloy." Materials Science and Engineering A **380**(1): 408-413.

Wang, L. S. and R. Y. Hong (2011). Synthesis, Surface Modification and Characterisation of Nanoparticles. Advances in Nanocomposites - Synthesis, Characterization and Industrial Applications. D. B. Reddy.

Wang, Q., S. Kanel, H. Park, A. Ryu and H. Choi (2009). "Controllable synthesis, characterization, and magnetic properties of nanoscale zerovalent iron with specific high Brunauer–Emmett–Teller surface area." J Nanopart Res **11**(3): 749-755.

Wang, Q., S. Lee and H. Choi (2010). "Aging Study on the Structure of Fe0-Nanoparticles: Stabilization, Characterization, and Reactivity." The Journal of Physical Chemistry C **114**(5): 2027-2033.

Wang, Q., S. Snyder, J. Kim and H. Choi (2009). "Aqueous Ethanol modified Nanoscale Zerovalent Iron in Bromate Reduction: Synthesis, Characterization, and Reactivity." Environmental Science & Technology **43**(9): 3292-3299.

Wang, T., J. S. Hu, W. Yang and H. M. Zhang (2008). "Electrodeposition of monodispersed metal nanoparticles in a nafion film: Towards highly active nanocatalysts." Electrochemistry Communications **10**(5): 814-817.

Wang, W., Z.-h. Jin, T.-l. Li, H. Zhang and S. Gao (2006). "Preparation of spherical iron nanoclusters in ethanol/water solution for nitrate removal." Chemosphere **65**(8): 1396-1404.

Wang, Y., B.-Y. Gao, X.-M. Xu, W.-Y. Xu and G.-Y. Xu (2009). "Characterization of floc size, strength and structure in various aluminum coagulants treatment." J. Colloid Interface Sci. **332**(2): 354-359.

Ward, B., J. A. Notte and N. Economou (2006). "Helium ion microscope: A new tool for nanoscale microscopy and metrology." J. Vac. Sci. Technol., B **24**(6): 2871-2874.

Wei, Y.-T., S.-C. Wu, C.-M. Chou, C.-H. Che, S.-M. Tsai and H.-L. Lien (2010). "Influence of nanoscale zero-valent iron on geochemical properties of groundwater and vinyl chloride degradation: a field case study." Water Res. **44**(1): 131-140.

Weinberg, H., A. Galyean and M. Leopold (2011). "Evaluating engineered nanoparticles in natural waters." TrAC Trends in Analytical Chemistry **30**(1): 72-83.

Weitz, D., J. Huang, M. Lin and J. Sung (1985). "Limits of the fractal dimension for irreversible kinetic aggregation of gold colloids." Phys. Rev. Lett. **54**(13): 1416.

Wiesner, M. R. and J.-Y. Bottero (2007). Applications and Impacts of Nanomaterials. Environmental Nanotechnology. New York, The McGraw-Hill Companies.

Wiggins, J., E. E. Carpenter and C. J. O'Connor (2000). "Phenomenological magnetic modeling of Au:Fe:Au nano-onions." Journal of Applied Physics **87**(9 II): 5651-5653.

Wilson, J., P. Poddar, N. Frey, H. Srikanth, K. Mohomed, J. Harmon, S. Kotha and J. Wachsmuth (2004). "Synthesis and magnetic properties of polymer nanocomposites with embedded iron nanoparticles." Journal of Applied Physics **95**(3): 1439-1443.

WooáLee, J. and S. BináKim (2011). "Enhanced Cr (vi) removal using iron nanoparticle decorated graphene." Nanoscale **3**(9): 3583-3585.

Wu, F.-C., R.-L. Tseng and R.-S. Juang (2001). "Enhanced abilities of highly swollen chitosan beads for color removal and tyrosinase immobilization." J. Hazard. Mater. **81**(1): 167-177.

Wu, L., M. Shamsuzzoha and S. Ritchie (2005). "Preparation of cellulose acetate supported zero-valent iron nanoparticles for the dechlorination of trichloroethylene in water." J. Nanopart. Res. **7**(4): 469-476.

Wu, X., Q. Yang, D. Xu, Y. Zhong, K. Luo, X. Li, H. Chen and G. Zeng (2013). "Simultaneous Adsorption/Reduction of Bromate by Nanoscale Zerovalent Iron Supported on Modified Activated Carbon." Industrial & Engineering Chemistry Research **52**(35): 12574-12581.

Xi, Y., M. Mallavarapu and R. Naidu (2010). "Reduction and adsorption of Pb2+ in aqueous solution by nano-zero-valent iron—A SEM, TEM and XPS study." Mater. Res. Bull. **45**(10): 1361-1367.

Xie, Y. and D. M. Cwiertny (2010). "Use of Dithionite to Extend the Reactive Lifetime of Nanoscale Zero-Valent Iron Treatment Systems." Environmental Science & Technology **44**(22): 8649-8655.

Xie, Y. and D. M. Cwiertny (2012). "Influence of anionic cosolutes and pH on nanoscale zerovalent iron longevity: time scales and mechanisms of reactivity loss toward 1, 1, 1, 2-tetrachloroethane and Cr (VI)." Environ. Sci. Technol. **46**(15): 8365-8373.

Xu, J., A. Dozier and D. Bhattacharyya (2005). "Synthesis of nanoscale bimetallic particles in polyelectrolyte membrane matrix for reductive transformation of halogenated organic compounds." J. Nanopart. Res. **7**(4-5): 449-467.

Xu, Y. and W. Zhang (2000). "Subcolloidal Fe/Ag particles for reductive dehalogenation of chlorinated benzenes." Industrial & engineering chemistry research **39**(7): 2238-2244.

Yan, W., A. A. Herzing, C. J. Kiely and W.-x. Zhang (2010). "Nanoscale zero-valent iron (nZVI): Aspects of the core-shell structure and reactions with inorganic species in water." J. Contam. Hydrol. **118**(3–4): 96-104.

Yan, W., R. Vasic, A. I. Frenkel and B. E. Koel (2012). "Intraparticle Reduction of Arsenite (As(III)) by Nanoscale Zerovalent Iron (nZVI) Investigated with In Situ X-ray

Absorption Spectroscopy." <u>Environmental Science & Technology</u> **46**(13): 7018-7026.

Yan, Y.-d., J. L. Burns, G. J. Jameson and S. Biggs (2000). "The structure and strength of depletion force induced particle aggregates." <u>Chem. Eng. J.</u> **80**(1): 23-30.

Yang, Y., N. Nakada, R. Nakajima, M. Yasojima, C. Wang and H. Tanaka (2013). "pH, ionic strength and dissolved organic matter alter aggregation of fullerene C60 nanoparticles suspensions in wastewater." <u>J. Hazard. Mater.</u> **244–245**(0): 582-587.

Yang, Y., L. Xie, Z. Chen, M. Liu, T. Zhu and Z. Liu (2005). "Purification and length separation of single-walled carbon nanotubes using chromatographic method." <u>Synth. Met.</u> **155**(3): 455-460.

Yantasee, W., C. L. Warner, T. Sangvanich, R. S. Addleman, T. G. Carter, R. J. Wiacek, G. E. Fryxell, C. Timchalk and M. G. Warner (2007). "Removal of heavy metals from aqueous systems with thiol functionalized superparamagnetic nanoparticles." <u>Environ. Sci. Technol.</u> **41**: 5114-5119.

Yaron-Marcovich, D., Y. Chen, S. Nir and R. Prost (2005). "High resolution electron microscopy structural studies of organo-clay nanocomposites." <u>Environ. Sci. Technol.</u> **39**(5): 1231-1238.

Yegin, B. A. and A. Lamprecht (2006). "Lipid nanocapsule size analysis by hydrodynamic chromatography and photon correlation spectroscopy." <u>Int. J. Pharm.</u> **320**(1–2): 165-170.

Yin, K., I. Lo, H. Dong, P. Rao and M. S. Mak (2012). "Lab-scale simulation of the fate and transport of nano zero-valent iron in subsurface environments: Aggregation, sedimentation, and contaminant desorption." <u>J. Hazard. Mater.</u> **227**: 118-125.

Yoo, J. S. (1998). "Selective gas-phase oxidation at oxide nanoparticles on microporous materials." <u>Catalysis Today</u> **41**(4): 409-432.

Yukselen, M. A. and J. Gregory (2002). "Breakage and re-formation of alum flocs." <u>Environ. Eng. Sci.</u> **19**(4): 229-236.

Yuvakkumar, R., V. Elango, V. Rajendran and N. Kannan (2011). "Preparation and characterization of zero valent Iron nanoparticles." <u>Dig. J. Nano. Biost.</u> **6**(4): 1771-1776.

Zänker, H. and A. Schierz (2012). "Engineered nanoparticles and their identification among natural nanoparticles." <u>Annual review of analytical chemistry</u> **5**: 107-132.

Zattoni, A., D. C. Rambaldi, P. Reschiglian, M. Melucci, S. Krol, A. M. C. Garcia, A. Sanz-Medel, D. Roessner and C. Johann (2009). "Asymmetrical flow field-flow fractionation with multi-angle light scattering detection for the analysis of structured nanoparticles." <u>J. Chromatogr. A</u> **1216**(52): 9106-9112.

Zhang, D., S. Wei, C. Kaila, X. Su, J. Wu, A. B. Karki, D. P. Young and Z. Guo (2010). "Carbon-stabilized iron nanoparticles for environmental remediation." <u>Nanoscale</u> **2**(6): 917-919.

Zhang, H., X. Quan, S. Chen and H. Zhao (2006). "Fabrication and characterization of silica/titania nanotubes composite membrane with photocatalytic capability." <u>Environ. Sci. Technol.</u> **40**(19): 6104-6109.

Zhang, P., X. Tao, Z. Li and R. S. Bowman (2002). "Enhanced perchloroethylene reduction in column systems using surfactant-modified zeolite/zero-valent iron pellets." <u>Environ. Sci. Technol.</u> **36**(16): 3597-3603.

Zhang, W.-X. (2003). "Nanoscale iron particles for environmental remediation: An overview." <u>J. Nanopart. Res.</u> **5**: 323-332.

Zhang, W.-x., C.-B. Wang and H.-L. Lien (1998). "Treatment of chlorinated organic contaminants with nanoscale bimetallic particles." <u>Catalysis Today</u> **40**(4): 387-395.

Zhang, W. x. and D. W. Elliott (2006). "Applications of iron nanoparticles for groundwater remediation." <u>Remediation Journal</u> **16**(2): 7-21.

Zhang, X., P. Zhang, Z. Wu, L. Zhang, G. Zeng and C. Zhou (2013). "Adsorption of Methylene Blue onto Humic Acid-Coated Fe3O4 Nanoparticles." <u>Colloids Surf., A</u>.

Zhang, Y., Y. Chen, P. Westerhoff and J. Crittenden (2009). "Impact of natural organic matter and divalent cations on the stability of aqueous nanoparticles." Water Res. **43**(17): 4249-4257.

Zhang, Y., Y. Chen, P. Westerhoff, K. Hristovski and J. C. Crittenden (2008). "Stability of commercial metal oxide nanoparticles in water." Water Res. **42**(8): 2204-2212.

Zhang, Y., Y. Chen, P. Westerhoff, K. Hristovski and J. C. Crittenden (2008). "Stability of commercial metal oxide nanoparticles in water." Water Res. **42**(8-9): 2204-2212.

Zhang, Y., Y. Su, X. Zhou, C. Dai and A. A. Keller (2013). "A new insight on the core–shell structure of zerovalent iron nanoparticles and its application for Pb(II) sequestration." Journal of Hazardous Materials **263, Part 2**(0): 685-693.

Zhao, Y., B. Gao, H. Shon, Y. Wang, J.-H. Kim, Q. Yue and X. Bo (2012). "Anionic polymer compound bioflocculant as a coagulant aid with aluminum sulfate and titanium tetrachloride." Bioresour. Technol. **108**: 45-54.

Zheng, T., J. Zhan, J. He, C. Day, Y. Lu, G. L. McPherson, G. Piringer and V. T. John (2008). "Reactivity Characteristics of Nanoscale Zerovalent Iron−Silica Composites for Trichloroethylene Remediation." Environ Sci Technol **42**(12): 4494-4499.

Zhou, J., J. Ralston, R. Sedev and D. A. Beattie (2009). "Functionalized gold nanoparticles: Synthesis, structure and colloid stability." J. Colloid Interface Sci. **331**: 251-262.

Zhou, Q., S. E. Cabaniss and P. A. Maurice (2000). "Considerations in the use of high-pressure size exclusion chromatography (HPSEC) for determining molecular weights of aquatic humic substances." Water Res. **34**(14): 3505-3514.

Zhu, S.-N., G.-h. Liu, Z. Ye, Q. Zhao and Y. Xu (2012). "Reduction of dinitrotoluene sulfonates in TNT red water using nanoscale zerovalent iron particles." Environ Sci Pollut Res **19**(6): 2372-2380.

Zhuang, J., J. F. McCarthy, J. S. Tyner, E. Perfect and M. Flury (2007). "In situ colloid mobilization in Hanford sediments under unsaturated transient flow conditions: Effect of irrigation pattern." Environ. Sci. Technol. **41**(9): 3199-3204.